NASA/TM-2020-5006765/Volume I NESC-RP-16-01183





Composite Overwrapped Pressure Vessel (COPV) Damage Tolerance Life Analysis Methodology and Test Best Practices

Heather K. Hickman/NESC, and Richard W. Russell/NESC Langley Research Center, Hampton, Virginia

David S. Dawicke Analytical Services and Materials, Hampton, Virginia

William Leser, Patrick E. Leser, and Russell A. Wincheski Langley Research Center, Hampton, Virginia

Jacob D. Hochhalter University of Utah, Salt Lake City, Utah

Lorie R. Grimes Ledesma Jet Propulsion Laboratory, Pasadena, California

Kauser S. Imtiaz Johnson Space Center, Houston, Texas

NASA STI Program . . . in Profile

Since its founding, NASA has been dedicated to the advancement of aeronautics and space science. The NASA scientific and technical information (STI) program plays a key part in helping NASA maintain this important role.

The NASA STI program operates under the auspices of the Agency Chief Information Officer. It collects, organizes, provides for archiving, and disseminates NASA's STI. The NASA STI program provides access to the NTRS Registered and its public interface, the NASA Technical Reports Server, thus providing one of the largest collections of aeronautical and space science STI in the world. Results are published in both non-NASA channels and by NASA in the NASA STI Report Series, which includes the following report types:

- TECHNICAL PUBLICATION. Reports of completed research or a major significant phase of research that present the results of NASA Programs and include extensive data or theoretical analysis. Includes compilations of significant scientific and technical data and information deemed to be of continuing reference value. NASA counter-part of peerreviewed formal professional papers but has less stringent limitations on manuscript length and extent of graphic presentations.
- TECHNICAL MEMORANDUM. Scientific and technical findings that are preliminary or of specialized interest, e.g., quick release reports, working papers, and bibliographies that contain minimal annotation. Does not contain extensive analysis.
- CONTRACTOR REPORT. Scientific and technical findings by NASA-sponsored contractors and grantees.

- CONFERENCE PUBLICATION.
 Collected papers from scientific and technical conferences, symposia, seminars, or other meetings sponsored or co-sponsored by NASA.
- SPECIAL PUBLICATION. Scientific, technical, or historical information from NASA programs, projects, and missions, often concerned with subjects having substantial public interest.
- TECHNICAL TRANSLATION.
 English-language translations of foreign scientific and technical material pertinent to NASA's mission.

Specialized services also include organizing and publishing research results, distributing specialized research announcements and feeds, providing information desk and personal search support, and enabling data exchange services.

For more information about the NASA STI program, see the following:

- Access the NASA STI program home page at http://www.sti.nasa.gov
- E-mail your question to help@sti.nasa.gov
- Phone the NASA STI Information Desk at 757-864-9658
- Write to: NASA STI Information Desk Mail Stop 148 NASA Langley Research Center Hampton, VA 23681-2199

NASA/TM-2020-5006765/Volume I NESC-RP-16-01183





Composite Overwrapped Pressure Vessel (COPV) Damage Tolerance Life Analysis Methodology and Test Best Practices

Heather K. Hickman/NESC, and Richard W. Russell/NESC Langley Research Center, Hampton, Virginia

David S. Dawicke Analytical Services and Materials, Hampton, Virginia

William Leser, Patrick E. Leser, and Russell A. Wincheski Langley Research Center, Hampton, Virginia

Jacob D. Hochhalter University of Utah, Salt Lake City, Utah

Lorie R. Grimes Ledesma Jet Propulsion Laboratory, Pasadena, California

Kauser S. Imtiaz Johnson Space Center, Houston, Texas

National Aeronautics and Space Administration

Langley Research Center Hampton, Virginia 23681-2199

Acknowledgments

This assessment is dedicated to our team member and friend, Roy Hampton, who passed away before seeing its completion. Roy was a persistent voice of safety and engineering excellence, always providing keen insights, timely suggestions, and exemplary technical leadership. His warm collegiality and outstanding expertise will be sincerely missed.

We thank the following people and organizations for their collaborations and insights:

- Samuel Angier, ArianeGroup
- Matthias Thielen, Airbus
- Gerben Sinnema, European Space Agency
- Daniel Samson, John Ostrander, General Dynamics
- Andrew Pritchard, Nicole Walsh, and Mason Woish, Lockheed Martin
- Kirk Sneddon, ARDÉ

We thank John Cervoni and Larry Starritt at WSTF and John Savage and Johnnie West at LaRC for their dedication, flexibility, and meticulous work on hundreds of test coupons.

We thank our peer reviewers for their detailed review, questions, and comments: Mark McElroy, Ken Hamm, Ken Johnson, Jim McMahon, Ian Juby, Azita Valinia, Bill Prosser, Don Parker, Tim Brady, Steve Gentz, and Steve Smith.

Finally, we thank our additional September 2018 and January 2020 Technical Interchange Meeting participants for their technical discussion and guidance: Bob Piascik, Pravin Aggarwal, Brian Jensen, Jim McMahon, Joachim Beek, Preston McGill, Doug Wells, Joel Hobbs, Gerry Widmar, and James Smith.

The use of trademarks or names of manufacturers in the report is for accurate reporting and does not constitute an official endorsement, either expressed or implied, of such products or manufacturers by the National Aeronautics and Space Administration.

Available from:

NASA STI Program / Mail Stop 148 NASA Langley Research Center Hampton, VA 23681-2199 Fax: 757-864-6500



NASA Engineering and Safety Center Technical Assessment Report

Volume I

Composite Overwrapped Pressure Vessel (COPV) Damage Tolerance Life Analysis Methodology and Test Best Practices

June 4, 2020

Report Approval and Revision History

Approved:	Original Signature on File	7/31/20
	NESC Director	Date

Version	Description of Revision	Office of Primary Responsibility	Effective Date
1.0	Initial Release	Heather Hickman, Associate Principal Engineer, GRC	6/4/2020
1.1	Revised Acknowledgements section and acronym correction in Section 7.2. (Director's signature not required)	Heather Hickman, Associate Principal Engineer, GRC	8/3/2020

Table of Contents

Tech	nical A	Assessment Report	
1.0	Notifi	cation and Authorization	8
2.0	Signat	ure Page	9
3.0	_	List	
	3.1	Acknowledgements	
4.0	Execu	tive Summary	12
5.0		ment Plan	
6.0	Backg	round and Problem Description	17
7.0	_	nd Analysis	
	7.1	Evaluation of the Limitations of LEFM Computational Methods	
	7.1.1	Evaluation of LEFM Crack Growth and Life Predictions	
	7.1.2	Analysis Approach to Add Conservatism to LEFM Based Life Prediction	29
	7.2	Test-Based Methodology for Validating Damage Tolerance Life Requirements	38
	7.2.1	Liner Material Evaluation	
	7.2.2	Autofrettage Crack Growth Tests	
	7.2.3	Damage Tolerance Tests	87
	7.3	Best Practices for Complying with AIAA/ANSI S-081B Damage Tolerance Life	404
	7.4	Requirements	
	7.4	Other Considerations	
8.0		ngs, Observations, and NESC Recommendations	
	8.1	Findings	
	8.2	Observations	
0.0	8.3	NESC Recommendations	
9.0		active Viewpoint(s)	
10.0		Deliverables	
11.0		ns Learned	
12.0		nmendations for NASA Standards and Specifications	
13.0	Defini	tion of Terms	125
14.0	Acron	yms and Nomenclature List	125
15.0	Refere	ences	126
Appen	idices		128
		List of Figures	
Figure	6.0-1.	Images of a Metal-Lined, Carbon-Fiber Overwrapped COPV	17
Figure		Fracture Surface Resulting from a Fatigue Crack that was Initiated from a Surfac	
Ü		Notch and Grown almost to the Back Face of the Thin-walled coupon	
Figure	7.1.1-1.	-	
Figure	7.1.1-2.	Example of (a) CMOD and (b) Back Face Strain as Measured with DIC	22
Figure	7.1.1-3.	•	
		Sharpie® Pen Stained Precrack, and the Final Fatigue Crack	23
Figure	7.1.1-4.	•	
		with a Surface Crack with $a/t = 0.55$. (b) a Normalized by Thickness at which	22
Figure	7 1 1-5	Point Plasticity was Observed on the Back Face for all Surface Crack Tests Far-field Strain vs CMODEFM	23 24
CIVILLA	. / - 7	CAL-DERU MIANI VS CIVICIDEEJVI	//1

Figure 7.1.1-6.	CMOD And J Vs A For An Elastic And Elastic-Plastic FEM	.25
Figure 7.1.1-7.	Example Comparison of (a) a and (b) Crack Length between NASGRO	
-	Simulation and Test Data.	.25
Figure 7.1.1-8.	Percent Error between NASGRO Simulation and Test Data as a Function of a	
-	Normalized Precrack Ligament Size	.27
Figure 7.1.1-9.	<i>a/c</i> vs. a Normalized by Precrack Ligament	
Figure 7.1.1-10.	Cross-Section At Snapshots Of A Semi-Elliptical Crack (1/4 Symmetry) Growing	
	Toward the Liner Back Face	.29
Figure 7.1.2-1.	Schematic of a Surface Crack Growth Simulation and Applicable Limits on a,	
	including the Irwin Limit, <i>ai</i> , the LEFM Limit, <i>aL</i> , and the Modified Limit,	
	ai *	.30
Figure 7.1.2-2.	Crack depth (a) Normalized to Thickness (t) at which Back Face Plasticity was	
8	Observed during Test as Compared to Calculated Irwin and LEFM Limits	.32
Figure 7.1.2-3.	Plastic Zone Size from FEA comparing LEFM Limit Calculated according to	
8	ASTM E2899-15 and the Irwin Limit.	.32
Figure 7.1.2-4.	Comparison of NASGRO and Penalized NASGRO a Predictions Normalized by	
C	Observed a for all Coupon Tests	.34
Figure 7.1.2-5.	Example NASGRO Analysis and Identification of a Limits for M-Lifetimes Equal	
8		.36
Figure 7.1.2-6.	Example NASGRO Analysis and Identification of a Limits for M-Lifetimes Equal	
8	to 2,500 Cycles	.37
Figure 7.1.2-7.	Example NASGRO Analysis and Identification of a Limits for M-Lifetimes Equal	
C	to 3,000 Cycles	.38
Figure 7.2.1.1-1.	(left) AA6061-T6 Liner with (middle) Upper and Lower Dome EBSD Results	
8	and (right) Cylinder EBSD Results	.40
Figure 7.2.1.1-2.	EBSD Results from (left) AA6061-T6 Liner Cylinder and (right) Rolled Sheet	
Figure 7.2.1.1-3.	Second-phase Particle Distribution and SEM Image from (a) Rolled Sheet	
8	(b) Liner Dome and (c) Liner Cylinder	.41
Figure 7.2.1.1-4.	AA6061-T6 EBSD Result from Dome of Second Thicker Liner	
Figure 7.2.1.1-5.	EBSD Result from IN718 (a) Sheet Material on TL Surface and (b) Dome Material	
8	Extracted in Radial Direction.	
Figure 7.2.1.1-6.	AA6061-T6 Liner with Coupons Extracted along Entire Length	
Figure 7.2.1.1-7.	Small-scale Coupon (left) Geometry (middle) Displacement Contour under	
8	Uniaxial Load and (right) the Resulting Horizontal (S11) and Vertical (S22)	
	Components of Stress.	.44
Figure 7.2.1.1-8.	DIC Results with Virtual Strain Gage during Testing (a) Edge Localization Effect	
8	and (b) Failed Coupon	
Figure 7.2.1.1-9.	(a) Tensile Test Results for Small-scale Liner and Sheet Coupons. (b) Uniaxial	
118010 /121111 /1	Tensile Data for Similar Material and Heat-treatment	.46
Figure 7.2.1.1-10.	Engineering Stress-strain Curve with Uncertainty Bars for Small-scale IN718	•
8	Tensile Test.	.47
Figure 7.2.1.1-11.	Engineering Stress-strain Curve for all IN718 Tensile Tests	
	Line Plots for Summarizing the IN718 Tensile Test Results for (a) Yield Stress,	• • •
116010 7.2.1.1 12.	(b) Ultimate Tensile Strength, and (c) Modulus	48
Figure 7.2.1.1-13	Thin AA6061 Coupon Fracture Surface with Measurements of Initial and Final	. 10
116010 7.2.1.1 13.	Crack Depths	49
Figure 7 2 1 1-14	Thick AA6061-T6 Coupon Fracture Surface with Measurements of Initial and Fina	
- 15010 / 12.11.1 1T.	Crack Depths	
Figure 7.2.1.1-15	Analyzed CMOD from the Virtual Gage at Periodic Cycle Counts During the Test.	
•	Thin AA6061 Aggregated Initial and Final as with Corresponding CMOD	
	Thick AA6061 Aggregated Initial and Final as with Corresponding CMOD	

Figure 7.2.1.1-18.	Thin AA6061 Processed Crack Growth Data	51
Figure 7.2.1.1-19.	Thick AA6061 Processed Crack Growth Data	52
Figure 7.2.1.1-20.	All AA6061-T6 Processed Crack Growth Data with Large-scale Surface Crack Results	53
Figure 7.2.1.1-21.	AA6061-T6 Fatigue Crack Growth Observations from (a) Rolled Sheet and (b) AA6061-T6 Liner	
Figure 7.2.1.1-22.	Thin IN718 Coupon Fracture Surface with Measurements of Initial and Final Cracl Depths	k
Figure 7.2.1.1-23.	Analyzed CMOD from the Virtual Gage at Periodic Cycle Counts during the Test.	
	Thin IN718 Aggregated Initial and Final a with Corresponding CMOD	
	Liner #35 IN718 Processed Crack Growth Data	
	All IN718 Processed Crack Growth Data	
Figure 7.2.2-1.	Illustration of a Test Coupon used for Autofrettage Testing	
Figure 7.2.2-2.	Example of Strain Measurements (DIC virtual extensometers on edges) for an AA6061-T6 Autofrettage test at 1.5% Far-field Strain	
Figure 7.2.2-3.	SEM Photograph of the Fracture Surface of an AA6061-T6 Single Autofrettage Cycle Test (1.5% strain)	
Figure 7.2.2-4.	High Magnification SEM Photograph of the Autofrettage Region of an AA6061-T6 Single Autofrettage Cycle Test (1.5% strain)	
Figure 7.2.2-5.	SEM Photograph of the Fracture Surface of an IN718 Single Autofrettage Cycle Test (1.72% strain)	
Figure 7.2.2-6.	High Magnification SEM Photograph of the Autofrettage Region of an IN718 Single Autofrettage Cycle Test (1.72% strain)	
Figure 7.2.2-7.	SEM Photograph of the Fracture Surface of a Ti Single Autofrettage Cycle Test (2.65% strain)	
Figure 7.2.2-8.	High Magnification SEM Photograph of the Autofrettage Region of a Ti Single Autofrettage Cycle Test (2.65% strain)	
Figure 7.2.2-9.	High Magnification SEM Photograph of the autofrettage Region of an AA6061-T6 Single Autofrettage Cycle Test (2% strain)	
Figure 7.2.2-10.	High Magnification SEM Photograph of the autofrettage Region of a Ti 6Al-4V Single Autofrettage Cycle Test (2.65% strain)	
Figure 7.2.2-11.	Topography Measurements of the Fatigue and Blunted Regions of two AA6061-T6 Autofrettage Tests (1.75% strain)	
Figure 7.2.2-12.	Edge View Schematic based on Interpretation of the Topographic Measurements and Fracture Surface Photographs	
Figure 7.2.2-13.	Photograph of the 4xAF Testing Setup	
Figure 7.2.2-14.	Stress-strain Curve from a 4xAF Test of a 0.082-inch Thick Ti6Al-44 Coupon	
Figure 7.2.2-15.	Measured Autofrettage Crack Growth for the AA6061-T6 Coupons	
Figure 7.2.2-16.	Fracture Surface Photographs for a 0.09-inch thick AA6061-T6 Coupon Subjected to an Autofrettage Strain of 2.25%	
Figure 7.2.2-17.	Fracture Surface Photographs for a 0.032-inch Thick AA6061-T6 Coupon Subjected to an Autofrettage Strain of 1.5%	
Figure 7.2.2-18.	Fracture Surface Photographs for a 0.032-inch Thick AA6061-T6 Coupon Subjected to an Autofrettage Strain of 2%	
Figure 7.2.2-19.	CMOD vs. Strain Curves for Coupons that Did and Did Not Exhibit Stable Tearing	
Figure 7.2.2-20.	Difference in CMOD vs. Strain Behavior in LT and TL Coupons	
Figure 7.2.2-21.	Fracture surface Photographs for a 0.030-inch Thick IN178 (AMS 5663) Coupon Subjected to an Autofrettage Strain of 1.72% Without Stable Tearing	
Figure 7.2.2-22.	Fracture Surface Photographs for a 0.030-inch thick IN178 (AMS 5663) Coupon Subjected to an Autofrettage Strain of 1.72% with Stable Tearing	
	Subjected to all Autorichage Shall of 1.72/0 with Stable Tearing	/ +

Figure 7.2.2-23.	CMOD for Two IN718 (AMS 5663) Coupons with Slightly different Initial Crack	
Figure 7.2.2-24.	Depths	
F: 7.2.2.25	F-LT-030-19	75
Figure 7.2.2-25.	Axial Strain Field at 1.4% Far-field Strain for Two IN718 (AMS 5663) Coupons with Slightly Different Initial Crack Depths	76
Figure 7.2.2.26	Axial Strain Field at 1.72% Far-field Strain for Two IN718 (AMS 5663) Coupons	70
Figure 7.2.2-26.	with Slightly Different Initial Crack Depths	76
Figure 7.2.2-27.	Autofrettage Crack Growth in the 0.03-inch Thick IN718 (AMS 5663) Coupons	/ 0
11guie 7.2.2-27.	Subjected to a Strain Level of 1.72%	77
Figure 7.2.2-28.	Autofrettage Crack Growth in the 0.05-inch Thick IN718 (AMS 5662) Coupons	
Figure 7.2.2-29.	Location on the Tank Dome where the Coupons were Extracted	
Figure 7.2.2-30.	Amount of Autofrettage Crack Growth in the 0.082-inch thick Ti 6Al-4V	1 >
1 iguie 7.2.2 50.	Coupons Subjected to a Strain Level of 2.65%	80
Figure 7.2.2-31.	Fracture Surface Photographs for a 0.082-inch thick Ti 6Al-4V Coupon	00
1 1guic 7.2.2 31.	Subjected to an Autofrettage Strain of 2.65% (without stable tearing)	80
Figure 7.2.2-32.	Fracture Surface Photographs for a 0.082-inch thick Ti 6Al-4V Coupon Subjected	
	to an Autofrettage Strain of 2.65% (with stable tearing)	
Figure 7.2.2-33.	Fracture Surface Photographs for a 0.082-inch Thick Ti 6Al-4V Coupon	
	Subjected to an Autofrettage Strain of 2.65% (with stable tearing)	81
Figure 7.2.2-34.	Strain at Failure as a Function of a for the $a/c = 1$, 0.082-inch Thick Ti 6Al-4V	
118010 /1212 0 11	Autofrettage Tests	82
Figure 7.2.2-35.	Schematic of the Notch Pattern used for the $a/c = 0.2$ Cracks	
Figure 7.2.2-36.	Long, Shallow Crack that was Nucleated from 5 Co-linear Notches	
Figure 7.2.2-37.	Region of Autofrettage Crack Growth in Ti 6Al-4V Coupon Ti-Dome-02-02-82	
Figure 7.2.2-38.	Stress-strain Curve from a 4xAF test of a 0.06-inch Thick Ti 6Al-4V Coupon	
Figure 7.2.2-39.	Amount of Autofrettage Crack Growth in the 0.06-inch Thick Ti 6Al-4V Coupons	
8	Subjected to a Strain Level of 1%	85
Figure 7.2.2-40.	Fracture Surface Photographs for a 0.06-inch Thick Ti6Al-4V Coupon Subjected	
8	to an Autofrettage Strain of 1% (without stable tearing)	85
Figure 7.2.2-41.	Fracture Surface Photographs for a 0.06-inch thick Ti 6Al-4V Coupon Subjected	
	to an Autofrettage Strain of 1% (with stable tearing)	86
Figure 7.2.2-42.	Fracture Surface Photographs for a 0.06-inch Thick Ti 6Al-4V Coupon Subjected	
C	to Four Consecutive Autofrettage Cycles of 1% to 0% Strain	86
Figure 7.2.3-1.	Schematic of AA6061-T6 Liners	
Figure 7.2.3-2.	Schematic Describing the Location of the EDM Notches Placed in the Liners	
Figure 7.2.3-3.	Wrapping of the Liners with the Composite	
Figure 7.2.3-4.	Design Behavior of the COPV Liner	91
Figure 7.2.3-5.	Fracture Surface of OML crack N9 for COPV 18074	92
Figure 7.2.3-6.	Autofrettage Crack Growth In Crack N1 of COPV 18074	92
Figure 7.2.3-7.	Eddy Current Response for the IML Crack that Leaked During the COPV 18086	
		93
Figure 7.2.3-8.	Deepest Section of the Long, Shallow Crack that Leaked during the Autofrettage	
	of Tank 18086	93
Figure 7.2.3-9.	Crack Growth for an OML Crack in COPV 18099 (4xAF & 800 MDP)	94
Figure 7.2.3-10.	Fracture Surface for Crack C4 of COPV 18072	
Figure 7.2.3-11.	Autofrettage Crack Growth Region in Crack C4 of COPV 18072	95
Figure 7.2.3-12.	Coupon Design for the Uniaxial Fatigue crack Growth Tests	98
Figure 7.2.3-13.	Uniaxial coupon Testing Setup	
Figure 7.2.3-14.	Predicted Stress-strain Behavior for the COPVs and the Measured Stress-strain	
	Behavior for the Uniaxial Coupons	100

Figure 7.2.3-15.	DIC Measurement of the CMOD for the Uniaxial Coupons	.100
Figure 7.2.3-16.	Applied Stresses for the Two Uniaxial Coupon Loading Spectra	.101
Figure 7.2.3-17.	CMOD Measurements for the Autofrettage Cycles of the Two Spectra	.101
Figure 7.2.3-18.	Fracture Surfaces for Two Uniaxial Coupon Tests	
Figure 7.2.3-19.	Higher Magnification Images of the Fracture Surfaces	.102
Figure 7.2.3-20.	Crack Growth Rate Data from the Pressurized COPV and Uniaxial Coupon Tests.	.104
Figure 7.4-1.	Fracture Surface Resulting from a Fatigue Crack that was Initiated from a Surface	
_	Notch and Grown Almost to the Back Face of the Thin-walled Coupon	.115
Figure 7.4-2.	Measured CMOD as a Function of Applied Strain for a Uniaxial Simulation of a	
_	COPV Liner Strain History	.118
Figure 7.4-3.	Measured ΔCMOD as a Function of Applied Strain for MDP Cycles With and	
C	Without Autofrettage	.119
Figure 7.4-4.	Measured Crack Length and NASGRO Predictions for Three Tests with 800 MDF)
_	Cycles following Autofrettage Cycles and One Test with 800 MDP Cycles	
	Without an Autofrettage Cycle	.120
Figure 7.4-5.	Ratio of Predicted Final Crack Depth to Measured Crack Depth as a Function of	
	Initial Crack Depth is Plotted for the COPV and Coupon Tests	.121
	List of Tables	
Table 7.2.2-1.	Summary of AA6061-T6 Autofrettage Results	71
Table 7.2.2-2.	COPV Manufacturing Information	
Table 7.2.3-1.	Summary of Pressurized COPV Tests	95

Technical Assessment Report

1.0 Notification and Authorization

Mr. Michael Kirsch, NASA Engineering and Safety Center (NESC) Deputy Director, requested an independent assessment to develop data to understand the limitations of linear elastic fracture mechanics (LEFM) computational methods used to predict fatigue crack growth rate (da/dN) behavior of small detectable cracks in thin metal liners for composite overwrapped pressure vessels (COPVs). The NESC assessment team was also requested to demonstrate a test-based methodology for validating damage tolerance requirements for COPVs with elastically responding metal liners where LEFM methods are not appropriate.

The key stakeholders for this assessment are all NASA programs that use fracture-critical COPVs and the NASA Fracture Control Methodology Panel.

2.0 Signature Page

Submitted by:			
Team Signature Page on File – 8	8/10/2020		
Ms. Heather K. Hickman	Date		
Significant Contributors:			
Dr. David S. Dawicke	Date	Dr. William Leser	Date
Dr. Patrick E. Leser	Date	Dr. Jacob D. Hochhalter	Date
Dr. Lorie R. Grimes Ledesma	Date	Dr. Russell A. Wincheski	Date
Mr. Richard W. Russell	Date	Mr. Kauser S. Imtiaz	Date

Signatories declare the findings, observations, and NESC recommendations compiled in the report are factually based from data extracted from program/project documents, contractor reports, and open literature, and/or generated from independently conducted tests, analyses, and inspections.

3.0 Team List

Name	Discipline	Organization
Core Team		
Rick Russell	Lead, NASA Technical Fellow for	NESC/KSC
	Materials	
Heather Hickman	Deputy Lead, NESC Associate Principal	NESC/GRC
	Engineer	
Eric Baker	COPV Analysis Subject Matter Expert	GRC/Connecticut Reserve
		Technologies
Jim Baughman	SEM/PFIB Technician	LaRC/AMA
Matthew Buchholz	Business Development Manager	Hexagon Masterworks
John Cervoni	Material Fabrication	JSC WSTF/Jacobs
Harold "Clay" Claytor	Materials Technician	LaRC/AMA
Joseph Cochran	Student	University of Utah
Lorie Grimes-Ledesma	COPV Working Group Lead	JPL
David Dawicke	Technical Lead, Durability and Damage	LaRC/AS&M
	Tolerance	
James Harris	Managing Director	Hexagon Masterworks
Jacob Hochhalter	Micromechanical Fracture Mechanics	University of Utah
Patrick Leser	Experimental Testing	LaRC
William Paul Leser	Experimental Testing	LaRC
Jonas Merrell	LaRC Intern	University of Utah
Michael O'Neill	LaRC Intern	Georgia Tech
Tim Ruggles	Micromechanical Materials Analysis	NIA
Greg Shanks	Senior Engineering Technician	LaRC
Victor Stewart	Experimental Testing	LaRC
John Thesken	COPV Analysis Subject Matter Expert	GRC
Russell "Buzz"	NDE	LaRC
Wincheski		
Consultants		
Bill Prosser	NASA Technical Fellow for	LaRC
	Nondestructive Evaluation (NDE)	
Ken Hamm	Structures TDT	LaRC
Roy Hampton	Materials TDT, Fracture Mechanics	Owl Analytics, LLC
Kauser Imtiaz	NASA Technical Fellow for Structures	JSC
Bob Piascik	Materials (retired)	LaRC
Ed Glaessgen	Materials TDT, Computational	LaRC
Brian Jensen	Materials TDT	LaRC
Jim McMahon	Fracture Control	JSC
Pravin Aggarwal	Fracture Control	MSFC
Business Management		
Linda Moore	Program Analyst	LaRC/MTSO
Assessment Support		
Linda Burgess	Planning and Control Analyst	LaRC/AMA
Terri Derby	Project Coordinator	LaRC/AMA
Erin Moran	Technical Writer	LaRC/AMA

3.1 Acknowledgements

This assessment is dedicated to our team member and friend, Roy Hampton, who passed away before seeing its completion. Roy was a persistent voice of safety and engineering excellence, always providing keen insights, timely suggestions, and exemplary technical leadership. His warm collegiality and outstanding expertise will be sincerely missed.

We thank the following people and organizations for their collaborations and insights:

- Samuel Angier, ArianeGroup
- Matthias Thielen, Airbus
- Gerben Sinnema, European Space Agency
- Daniel Samson, John Ostrander, General Dynamics
- Andrew Pritchard, Nicole Walsh, and Mason Woish, Lockheed Martin
- Kirk Sneddon, ARDÉ

We thank John Cervoni and Larry Starritt at WSTF and John Savage and Johnnie West at LaRC for their dedication, flexibility, and meticulous work on hundreds of test coupons.

We thank our peer reviewers for their detailed review, questions, and comments: Mark McElroy, Ken Hamm, Ken Johnson, Jim McMahon, Ian Juby, Azita Valinia, Bill Prosser, Don Parker, Tim Brady, Steve Gentz, and Steve Smith.

Finally, we thank our additional September 2018 and January 2020 Technical Interchange Meeting participants for their technical discussion and guidance: Bob Piascik, Pravin Aggarwal, Brian Jensen, Jim McMahon, Joachim Beek, Preston McGill, Doug Wells, Joel Hobbs, Gerry Widmar, and James Smith.

4.0 Executive Summary

This assessment was requested by Mr. Michael Kirsch, NASA Engineering and Safety Center (NESC) deputy director, to address the concern that linear elastic fracture mechanics (LEFM) computational methods are not providing conservative damage tolerance life predictions and the intended level of safety for composite overwrapped pressure vessels (COPVs). LEFM methods have traditionally been used to successfully characterize the damage tolerance life of elastically responding components that contain cracks that are small relative to the thickness or other structural features; parameters like fracture toughness or net section stress can conservatively provide limitations that define the end-of-life. However, prediction of part-through cracks in thin metal materials, where break-through is an end-of-life condition (e.g., COPV liners), present unique problems: breakthrough may occur before fracture toughness and net section stress limits are exceeded. Traditional plastic zone limits that bound the use of LEFM (e.g., Irwin plastic zone model) are based on cracks in semi-infinite bodies and may be unconservative for a part-through crack approaching the back surface. Furthermore, existing standards (e.g., ANSI/AIAA S-081B [ref. 3]) do not provide guidelines for end-of-life limits in damage tolerance life analysis. The scope of this assessment was to develop data to define the limitations of LEFM computational methods used to predict fatigue crack growth rate behavior (i.e., damage tolerance life) of cracks in thin metal liners for COPVs.

To define the limitations of LEFM computational methods used to predict fatigue crack growth rate behavior in elastically responding COPV liners, the NESC assessment team evaluated the underlying assumptions associated with this method. LEFM Assumptions [ref. 1]:

- The size of the cyclic plastic zone around the crack tip is small relative to the crack size.
- The crack-tip plasticity is completely surrounded by elastically responding material.
- The material is a homogeneous continuum and governing microstructural features are small relative to the crack size

The first two LEFM assumptions, relating to plasticity and referred to as the plasticity assumptions, were addressed by defining mechanics- and evidence-based criteria to set quantitative limits on the use of LEFM computational methods used to predict fatigue crack growth rate behavior of detectable cracks in thin metal liners for elastically-responding COPVs. The third LEFM assumption, relating to microstructural features, manifests in the determination of the stress intensity factor solutions required for LEFM predictions and was addressed by evaluating material equivalence for damage tolerance life analysis and coupon level tests.

In addressing the LEFM plasticity assumptions, the NESC assessment team:

- Performed fatigue and fracture testing to generate crack growth data and crack mouth opening displacement (CMOD) data.
- Performed LEFM analyses with the tool, NASGRO v8.2 [ref. 24], to compare crack growth test data to LEFM computations.
- Developed a validated finite element model (FEM) that compares elastic-plastic crack behavior to elastic crack behavior.

This evaluation considered variation in crack size, liner thickness, stress level, and material stress-strain behavior. The test and analysis data demonstrated a gradual divergence in elastic-plastic and elastic crack behavior. As a result, the NESC assessment team:

- Developed a criteria that expands on the concepts developed in ASTM E2899 [ref. 4] to determine when LEFM plasticity assumptions are invalid (i.e., LEFM limit).
- Provided a modified failure criterion for continued use of LEFM analyses beyond the LEFM limit.

The modified failure criterion was based on test and analyses that account for the gradual divergence and is more conservative than failure criteria used in the LEFM damage tolerance life state-of-practice prediction methods. The modified failure criterion uses a knockdown factor to add conservatism to analyses that exceed the LEFM limit based on the degree of exceedance, elastic-plastic finite element analysis (FEA), and applicable test data.

Second, the NESC assessment team developed and demonstrated a test-based methodology validating the damage tolerance life requirements for COPVs with elastically responding metal liners. The focus on damage tolerance of COPV liners drove the team to perform tests and analyses on surface cracks. The test methodology used in this assessment reflects the AIAA S-081B [ref. 3] requirements for damage tolerance life verification by test. Findings and associated best practices for complying with damage tolerance life requirements of AIAA S-081B were identified from the following tests and analyses:

- Material state evaluation
 - Evaluation of microstructure-sensitive crack growth mechanism and crack growth rates
 - Direct comparisons of coupons extracted directly from COPV liners and sheet material
- Autofrettage crack growth testing
 - o Measurement of autofrettage crack growth
 - o Identification of onset of stable tearing
- Damage tolerance life coupon testing
 - o Evaluation of influence of loading sequence
 - o Evaluation of influence of truncating compressive stresses in loading sequence
- Models of crack behavior in coupons
 - Surface crack FEMs
 - o Fracture parameter evaluation (e.g., CMOD, crack tip opening displacement, J)
 - o NASGRO v9.0 [ref. 9] and v8.2 [ref.24] crack growth evaluation compared to tests
- Pressurized COPV tests
 - o Process development for nucleating multiple cracks in a COPV liner
 - Damage tolerance life test demonstration
 - o Nondestructive evaluation (NDE) of COPV liners via eddy current inspection

In summary, the NESC assessment team defined an analysis approach to identify where LEFM small-scale and constrained plasticity assumptions are violated and found that measured crack growth behavior gradually diverges from LEFM predictions as the crack depth (a) approaches the liner thickness. The NESC recommends damage tolerance assessments evaluate whether or not the LEFM limit has been exceeded and identify if the modified failure criterion (i.e., knockdown) was employed. A damage tolerance life analysis that predicts a final crack depth that is larger than allowed by the modified failure criterion must be considered to have failed analysis qualification. This approach quantifies violation of LEFM assumptions and is more conservative than the state-of-practice LEFM analyses, but does not eliminate all risk associated with damage tolerance life analysis. Thus, the LEFM limit and modified failure criterion should be considered as elements in the overall fracture control risk assessment.

The NESC assessment team demonstrated a test-based methodology for validating damage tolerance life requirements by performing material evaluation, autofrettage crack growth tests, and damage tolerance life tests. These tests and analyses provided evidence to support best practices to comply with the damage tolerance requirements in AIAA A-081B [ref 3]. The NESC recommends the use of best practices for complying with damage tolerance life requirements of AIAA S-081B. The evaluation of autofrettage crack growth found that unstable crack growth occurred at conditions almost immediately beyond the onset of stable tearing. Thus, small changes in crack size or strain level can result in a crack going from an apparent safe condition (i.e., little autofrettage crack extension) to failure (i.e., leak). The NESC recommends to programs that qualify COPVs for damage tolerance life, that stable tearing be demonstrated to not occur during any load cycle in the service life, including autofrettage. This demonstration can be by test or validated elastic-plastic analysis. A test approach for identifying the onset of stable tearing is documented.

Finally, the NESC assessment team documented four additional topics that arose during the testing and analyses that could influence damage tolerance tolerance life of COPV liners, but were beyond the scope of this assessment. These topics are: an analysis limit for grain size relative to crack size and remaining ligament, uniaxial coupon simulations of biaxial COPV liners, predicting crack aspect ratio (a/c) evolution in NASGRO, and prediction of fatigue crack growth following autofrettage in NASGRO.

5.0 **Assessment Plan**

This assessment was initiated when concern was raised over the potentially inappropriate use of LEFM computational methods to demonstrate damage tolerance life of fracture critical components (e.g., COPV liners) [ref. 2].

The scope of this assessment was to develop data to define the limitations of LEFM computational methods used to predict fatigue crack growth (i.e., damage tolerance life) of cracks in thin metal liners for COPVs. To meet this scope, the NESC assessment team developed an analysis methodology, anchored with test data, for identifying violation of LEFM plasticity assumptions and for adding conservatism to the life prediction. This evaluation was completed considering variations in a, a/c, liner thickness, stress level, and material. The team developed and demonstrated a test-based methodology for validating the damage tolerance life¹ requirements for COPVs with elastically responding metal liners. The focus on cracks in COPV liners drove the team to perform tests and analyses on surface cracks (i.e., part-through cracks). The test methodology used in this assessment reflects the AIAA S-081B requirements for damage tolerance life verification by test [ref. 3].

To develop the analysis methodology for identifying exceedance of LEFM plasticity assumptions and adding conservatism to the life prediction, the NESC assessment team:

- Performed fatigue crack growth testing and LEFM analysis with the tool, NASGRO v8.2 [ref. 24], to compare crack growth test data to LEFM computations in various test conditions
 - o Uniaxial coupons with and without simulated autofrettage strain application
 - Standard fatigue crack growth testing for comparison to NASGRO database values
- Performed FEA that simulated both elastic and elastic-plastic response of a cracked structure and provided quantification of divergence between elastic and elastic-plastic response
 - o A material model calibrated using local tensile measurements (i.e., in the necking region) was used to describe the elastic-plastic material behavior at the crack tip
 - High precision, near crack measurements validated the FEA
- Developed criterion that expands on concepts developed in ASTM E2899 [ref. 4] to determine when LEFM plasticity assumptions are violated
- Developed a damage tolerance life analysis method and modified failure criteria that is more conservative than the current state-of-practice LEFM damage tolerance life prediction methods

¹ Note 1: Damage Tolerance Life is used rather than 'safe-life' in COPV requirements. Damage tolerance life is the required period of time and number of cycles that the metal liner of a COPV, containing the largest undetected crack, flaw, or discontinuity, must survive without leak or burst in the expected service environment).

The NESC assessment team identified test-based best practices for complying with the damage tolerance life requirements of AIAA-S-081B [ref. 3]. The tests and analyses performed in developing best practices were:

- Material state evaluation
 - Evaluation of microstructure-sensitive crack growth mechanism and crack growth rates
 - o Direct comparison of coupons extracted from COPV liners and sheet material
- Autofrettage crack growth testing
 - o Measurement of autofrettage crack growth
 - o Identification of onset of stable tearing
- Damage tolerance life coupon testing
 - o Evaluation of influence of loading sequence
 - o Evaluation of influence of truncating compressive stresses in loading sequence
- Models of crack behavior in coupons
 - Surface crack FEMs
 - o Fracture parameter evaluation (e.g., CMOD, crack tip opening displacement, J)
 - o NASGRO v9.0 [ref. 9] and v8.2 [ref. 24]
- Pressurized COPV tests
 - o Process development for nucleating multiple cracks in a COPV liner
 - o Damage tolerance life test demonstration
 - o NDE of COPV liners via eddy current inspection

Scanning electron microscopy (SEM) and optical profilometry were used to evaluate fracture surfaces. Digital image correlation (DIC) was used to measure material behavior during most tensile and crack growth coupon tests. Tests were performed using the COPV liner materials: aluminum alloy (AA) 6061-T6, titanium (Ti) 6Al-4V, and Inconel® 718 (IN718). The evaluation of the limitation of LEFM computational methods and development of a method to add conservatism to LEFM predictions are demonstrated for AA6061-T6 sheet materials. AA6061-T6 sheet was selected because the alloy is the same as used in some COPV liners and the sheet material allows for efficient testing of multiple thicknesses to evaluate LEFM limitations. The approach is applicable to other liner materials and tensile data on IN718 and Ti 6Al-4V are included in the appendices to facilitate developing the LEFM limit and modified failure criteria for these materials. The test-based methodology for validating damage tolerance life requirements was demonstrated with AA6061-T6 and IN718 liner and sheet, and Ti 6Al-4V liner materials. AA6061-T6 COPVs were used to demonstrate COPV damage tolerance life testing. These materials were selected because they are often used in COPV liners. Material forms (i.e., sheet or forging) were guided by the Composite Pressure Vessel Working Group (CPVWG) and by other requests for assessment of a specific application. In addition to the specific test results, coupon notching and precracking, fracture surface marking, coupon design, and test methodology are addressed for the different test types. In the development of best practices, examples in the main body of the report use a subset of the identified materials and results of all material tests are included in the appendices (Volume II).

6.0 Background and Problem Description

COPVs with metal liners are used in human spaceflight applications, often to store pressurized fluids for propulsion or environmental control and life support systems. Images of a COPV being wrapped and a cross-section are shown in Figure 6.0-1. The left image shows the metal liner in a mid-stage of having a carbon fiber overwrap applied. The right image shows a section of COPV with the metal liner and overwrap. The tapering of the metal liner can be observed as the COPV transitions from the dome to cylinder sections. AA6061-T6, IN718, and Ti 6Al-4V are common metals used in COPV liners. [refs. 5, 6]



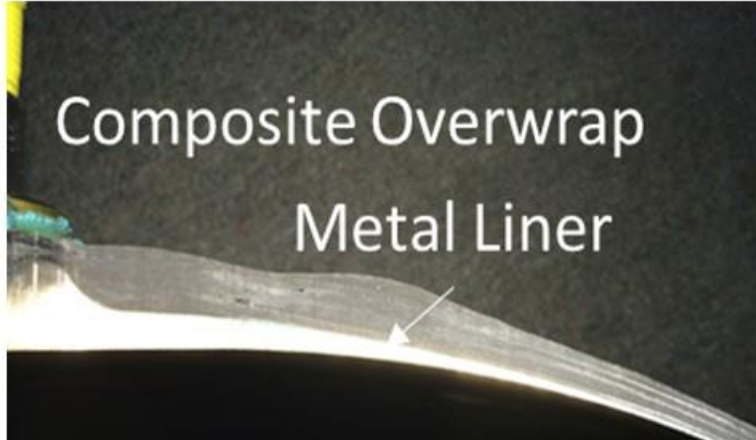


Figure 6.0-1. Images of a metal-lined, carbon-fiber overwrapped COPV.

The COPV liner and overwrap material selection allows for reduced mass compared to an all metal tank. To minimize mass in a COPV, the metal COPV liners are often chemically or mechanically thinned where the final thickness can approach 0.03 inch. Depending on design requirements, COPV liners may have a wide range of thicknesses (e.g., typically 0.5 to 0.02 inch). Liner thicknesses of 0.03 to 0.09 inch are addressed in this report. The minimum NDE detectable flaw size for these vessels can be on the order of 0.025-inch deep, and can result in a remaining ligament (between the crack front and the opposite surface) of approximately 0.005 inch and fewer than 10 grains. Figure 6.0-2 shows a fracture surface resulting from a fatigue crack that was initiated from a surface notch and grown almost to the coupon back face. The material is 0.03-inch thick AA6061-T6 and the figure shows the 0.028-inch deep crack relative to the material thickness and the grain size.

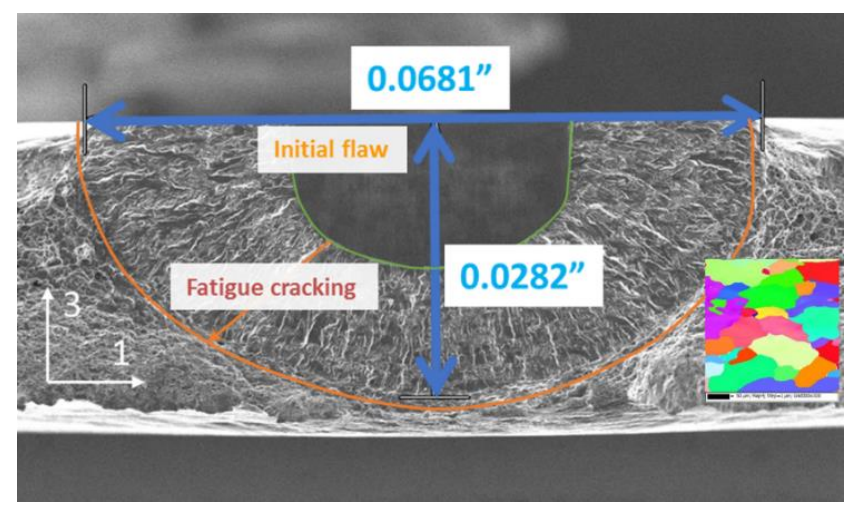


Figure 6.0-2. Fracture surface resulting from a fatigue crack that was initiated from a surface notch and grown almost to the back face of the thin-walled coupon. Grain size image is same scale as fracture surface image.

Most COPVs used in human spaceflight applications are required to comply with the standard AIAA/ANSI S-081² [ref. 3], and the failure mode of crack growth in liner is addressed by damage tolerance life requirements. Damage tolerance life is defined as:

The required period of time and number of cycles that the metal liner of a COPV, containing the largest undetected crack, flaw, or discontinuity, must survive without leak or burst in the expected service environment.

AIAA/ANSI S-081 provides requirements on how to verify the damage tolerance by analysis or test. Excerpts from AIAA/ANSI S-081B are provided in Appendix A for convenience. To demonstrate damage tolerance life in worst-case scenarios, initial flaws are inserted within representative vessels with strategic placement at worst-case locations (i.e., combined high fatigue crack driving force and representative material that considers any low resistance to crack growth due to undesirable microstructural features).

The damage tolerance life of a COPV with a plastically responding liner is required to be verified by test. The damage tolerance life of a COPV with an elastically responding liner³ that is also characterized by LEFM can be verified by analysis or test [ref. 3]. Approaches for damage tolerance life testing have been established for plastically responding liners [ref. 8]. A concern for COPVs with elastically responding liners is that the limits for using LEFM analysis tools are not clearly defined and could result in unconservative damage tolerance life predictions if underlying LEFM assumptions become violated as the crack grows close to the back surface [ref. 2]. LEFM methods have traditionally been used to successfully characterize the damage tolerance life of elastically responding components that contain cracks that are small relative to the thickness or other structural features; parameters such as fracture toughness or net section

_

² Multi-Purpose Crew Vehicle, Space Launch System, and Commercial Crew Programs require COPV compliance with ANSI/AIAA S-081. Several robotic missions (e.g., Mars 2020, Europa Clipper, James Webb Space Telescope) also require compliance to this standard. Some COPVs used in payloads for the International Space Station are required to comply with Department of Transportation (DOT) standards, which are more stringent than ANSI/AIAA S-081 with respect to structural factors of safety.

³ Elastically responding refers to the liner far-field stresses in cycles post autofrettage.

stress can conservatively provide limitations that define the end-of-life. However, prediction of part-through cracks in thin metal materials, where break-through is an end-of-life condition (e.g., COPV liners), present a unique problem: breakthrough may occur before fracture toughness and net section stress limits are exceeded. Traditional plastic zone limits that bound the use of LEFM (e.g., Irwin plastic zone model) are based on cracks in semi-infinite bodies and may be unconservative for a part-through crack approaching the back surface. Furthermore, existing standards (e.g., ANSI/AIAA S-081B [ref. 3]) do not provide guidelines for end-of-life limits in damage tolerance life analysis. If LEFM analyses are used inappropriately and the life prediction is unconservative, then the result could be a catastrophic failure of leak or burst of the COPV. This assessment was requested to develop data to define the limitations of LEFM computational methods in the prediction of damage tolerance life.

To address the limitation of LEFM computational methods, the NESC assessment team evaluated the underlying LEFM assumptions [ref. 1]:

- 1. The size of the cyclic plastic zone around the crack tip is small relative to the crack size.
- 2. The crack-tip plasticity is completely surrounded by elastically responding material.
- 3. The material is a homogeneous continuum and governing microstructural features are small relative to the crack size.

In addressing the LEFM assumptions relating to plastic zone size and constrained plasticity, referred to as plasticity assumptions, the NESC assessment team defined mechanics- and evidence-based criteria to set quantitative limits on the use of LEFM computational methods used to predict growth of detectable fatigue cracks in thin metal liners for elastically-responding COPVs. Second, the team developed a test-based methodology for experimental validation of damage tolerance life qualifications. The test methodology follows AIAA/ANSI S-081B requirements for test. The third LEFM assumption relating to grain size is addressed in developing best practices for evaluating the behavior of the liner material in comparison to more standard material forms (i.e., sheet).

7.0 Test and Analysis

Section 7.1 documents the tests and analyses used to understand the limitations of LEFM computational methods that are used to predict fatigue crack growth in thin metal liners for COPVs. Section 7.2 documents the tests and analyses used to develop a test-based methodology for validating damage tolerance life requirements in elastically responding COPV liners. Section 7.3 summarizes best practices based on data collected in this assessment for complying with AIAA S-081B damage tolerance life requirements. Section 7.4 addresses other considerations for complying with damage tolerance life requirements.

7.1 Evaluation of the Limitations of LEFM Computational Methods

The NESC assessment team's evaluation of the LEFM computational method limitations focuses on the assumptions related to small-scale constrained plasticity at the crack tip. Assuming material homogeneity, the size of the plastic zone, the state of the material around the plastic zone, and crack front driving force are functions of crack depth (a), crack length (2c), liner thickness (t), applied stress (σ) , and liner material. Crack growth simulation typically involves numerical integration of a crack growth rate (da/dN) equation over the service life, discretized by cycle or blocks of cycles with identical applied far-field stresses. Values of a, a/c, and material state are updated at each of these discrete times, referred to as crack growth steps, and an analysis is conducted to determine crack front driving force. In this assessment, the violation of LEFM assumptions are identified using the simulated crack growth step at which LEFM plasticity assumptions are no longer valid. The a at this crack growth step is referred to as the LEFM limit throughout the remainder of this section and associated appendices.

An approach for identifying the LEFM limit in the a, a/c, t, σ , and liner material parameter space is presented in Section 7.1.1. This section also includes a discussion on the impact of invalid LEFM assumptions on the error accumulation during crack growth simulation after the LEFM limit has been exceeded. The LEFM limit identifies the crack growth step (defined by a specific a, associated a/c, and applied stress) during a crack growth simulation beyond which LEFM analyses are no longer valid. Violation of LEFM assumptions result in a gradually increasingly non-conservative accumulation of error. A knockdown factor to be applied to standards damage tolerance life failure criterion was developed and is introduced in Section 7.1.2. The knockdown factor failure criterion adds conservatism to analyses that exceed the LEFM limit based on the degree of exceedance and a driving force ratio computed using elastic and elastic-plastic FEA. The data, analysis, observations and recommendations contained in Section 7.1 apply to damage tolerance life assessment of COPV liners in the context of constant amplitude loading. The load history effects of autofrettage are not considered here (see Section 7.4 for a discussion of these effects).

NESC Document No.: NESC-RP-16-01183, Vol. I, V.1.1

⁴ Evaluation of grain size with respect to crack size is not easily achieved with simulation nor is it common practice. The evaluation of impact of grain size is critical in selecting material parameters for an analysis or representative test. The impact of grain size and best practices on the selection of material parameters for analysis and test are addressed in Section 7.2.1.

⁵ The COPV life LEFM limit and knockdown failure criteria outlined in Section 7.1 can be expanded to variable amplitude, elastic load cycles. See Appendix F.2 for details.

7.1.1 Evaluation of LEFM Crack Growth and Life Predictions

A common tool used for LEFM-based damage tolerance life analysis is NASGRO and the applicability for LEFM-based predictions and overall NASGRO use limitations is discussed in the manual [ref. 9]. COPV damage tolerance life analysis assumes that the largest crack that can be missed by an NDE inspection will exist at the worst location. The initial crack is a part-through crack and the end-of-life condition is when the crack breaks through the back surface. NASGRO models the part-through crack with a semi-elliptical shape and simulates crack growth in both the surface and maximum depth locations. A NASGRO analysis will continue to advance the surface and depth crack growth to the point that the crack breaks through the back face (i.e., leakage in context of a COPV liner).

Alternative failure mechanisms for general fracture problems can be predicted (e.g., net-section yielding and exceedance of the material surface-crack fracture toughness or through-crack fracture toughness). However, these mechanisms typically apply to cracks with surface areas that are large with respect to the in-plane cross-section of the structure, regardless of the remaining ligament size for a surface crack. In the context of COPV liners where the surface area of the crack is not a significant portion of the liner cross-section (i.e., the entire circumference of the liner), these are less likely to occur. While any of the aforementioned failure mechanisms can be flagged in a NASGRO analysis, the violation of LEFM plasticity assumptions (e.g., the plasticity in the ligament ahead of the crack tip at the maximum depth location interacts with the back surface, violating the requirement that the crack tip be surrounded by elastic material) is not explicitly flagged.⁶ Therefore, users can mistakenly continue the analysis after the tool's underlying LEFM assumptions are violated. This allows the tool to be used outside of the intended scope and on cracks that are no longer characterized by LEFM, in violation of NASA-STD-7009A on the use of models and simulations and AIAA S-081B requirements on the use of analysis for damage tolerance life verification. In applications where leak is not an end-of-life condition, the breakdown of LEFM assumptions is mitigated by transition to a through-crack. The LEFM assumptions are again valid after transition to a through-crack because, with the ligament gone, the crack tip is once again surrounded by elastic material. However, for the application of thin COPV liners where leak is considered an end-of-life condition, the prediction of crack growth prior to breakthrough is critical and an unconservative prediction could lead to catastrophic failure.

Mechanical testing and elastic-plastic FEA were used to identify the conditions under which LEFM plasticity assumptions (i.e., underlying assumptions of NASGRO analysis) may be violated for a subset of crack sizes, liner thicknesses, applied stresses, and materials used in COPV designs. While AA6061-T6, Ti 6Al-4V, and In718 were studied in this assessment and the approach can be applied to them all, the results presented in this section were based on AA6061-T6.

- **O-1.** The NASGRO user's manual discusses its limitations and provides guidance on its use.
- **O-2.** LEFM plasticity assumption violations are not always flagged in a NASGRO analysis, allowing users to mistakenly continue the analysis.

NESC Document No.: NESC-RP-16-01183, Vol. I, V.1.1

⁶ The violation of plasticity assumptions is not flagged in the NASGRO SC30 and SC31 crack cases, which are the NASGRO recommended stress intensity factor models for semi-elliptical surface cracks.

7.1.1.1 Surface Crack Fatigue Tests

Surface cracks were grown in sheet material to look for indications that LEFM assumptions were being violated and to provide test data to be compared to NASGRO results. Test coupons were machined from rolled sheet with thicknesses: 0.032, 0.048, and 0.090 inch. The coupons were dogbone-shaped with a 2.0 inch-wide gage section with an electrical discharge machined (EDM) notch (i.e., for crack nucleation) with dimensions 0.02-inch wide x 0.01-inch deep as shown in Figure 7.1.1-1. The far-field applied stresses investigated were intended to represent typical COPV liner stresses (i.e., 30, 35, and 40 ksi for an AA6061-T6 liner). The specimens were precracked to a crack size of approximately 2c = 0.04 inch and a = 0.02 inch. This precrack size was selected such that data were gathered starting below the NDE limit for the special penetrant that is commonly used. The precracked surface was marked with Sharpie® pen ink to allow for a post-test measurement, and then the coupon was cycled in load control with a stress ratio R = 0.1 defined as:

$$R = \frac{\sigma_{min}}{\sigma_{max}}$$

DIC was used to measure CMOD and back face strain at approximately 1000 cycle intervals, as shown in Figure 7.1.1-2. A distribution of crack sizes between the NDE limit and breakthrough was obtained by applying different number of precrack and fatigue test cycles to each coupon. The actual crack depth, a, size and shape, a/c, could not be measured during the test, so the CMOD measurements were used as a surrogate for the depth, a. The specimens were then fractured to expose the fatigue crack surfaces and measurements were then made as shown in Figure 7.1.1-3. This approach provided measurements of a range of crack sizes for model validation. See Appendix B for full testing details and a listing of all results generated.

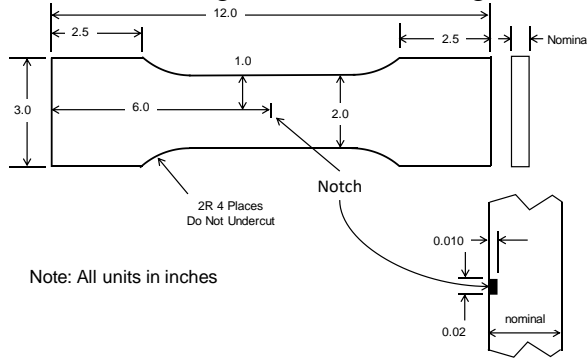


Figure 7.1.1-1. Coupon dimensions for uniaxial surface crack tests.

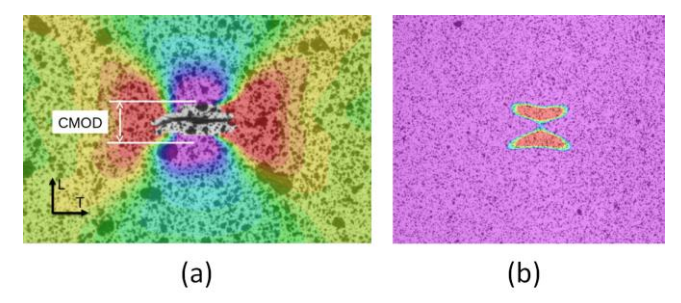


Figure 7.1.1-2. Example of (a) CMOD and (b) back face strain as measured with DIC.

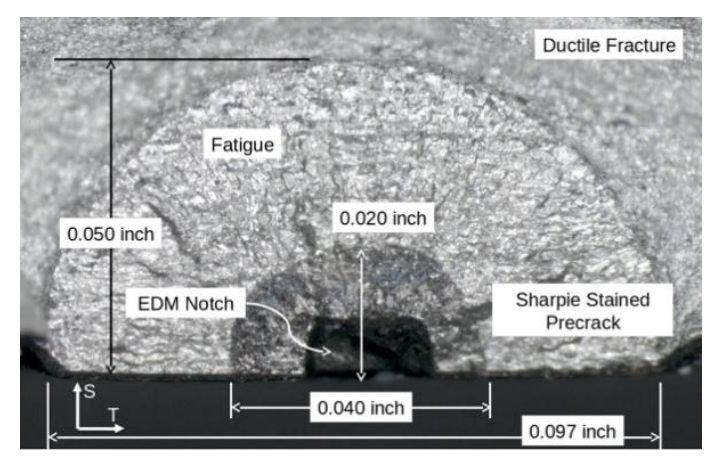


Figure 7.1.1-3. An example of a post-test crack measurement showing the EDM notch, the Sharpie® pen stained precrack, and the final fatigue crack.

Plastic strain was observed on the back face as the crack grew through the thickness, as shown by the DIC results presented in Figure 7.1.1-4a. In this figure, the scale bar is set such that purple represents the elastic far-field strain and red indicates plastic strain (as determined from uniaxial tension tests) in the loading direction. At a minimum, these test results demonstrate a violation of the second assumption of LEFM provided in Section 6.0 (i.e., constrained crack tip plasticity). Figure 7.1.1-4b shows the crack depth to thickness ratio (a/t) value at which the plastic strain made contact with the back face for all available test coupons. This indicates that the plastic zone size at the point of back face contact is typically between 20-50% of the specimen thickness. The effect of applied stress is also shown as cracks growing under higher stresses will violate LEFM plasticity assumptions at smaller a. Testing was primarily conducted on AA6061, but the result was also observed also in limited testing of IN718.

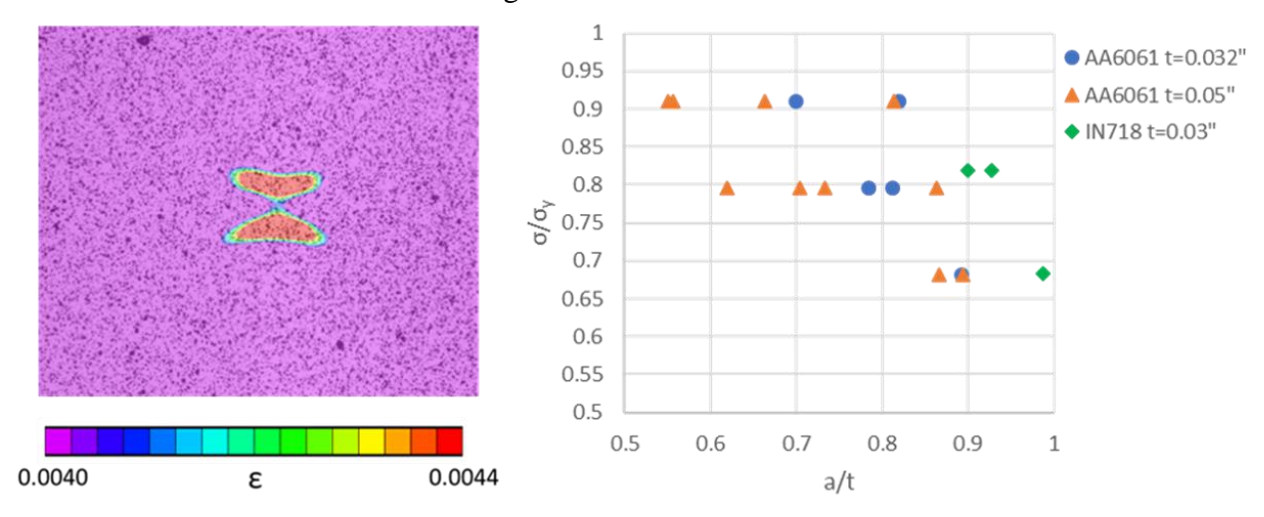


Figure 7.1.1-4. (a) Example of plasticity observed with DIC on the back face of a specimen with a surface crack with a/t = 0.55. (b) The a normalized by thickness at which point plasticity was observed on the back face for all surface crack tests.

Mechanical testing revealed multiple instances where LEFM plasticity assumptions were violated before the surface crack transitioned to a through-crack. At this point, it was important to understand (i) how the violation of LEFM assumptions affects predictions of crack growth

(i.e., whether error accumulation follows a step function or is gradual) and (ii) for what crack depths, aspect ratios, thicknesses, stresses, and materials are LEFM assumptions invalid. Expanding on (ii), the goal was to identify a quantitative measure where the violation occurs during a LEFM-based crack growth simulation. The crack growth step (defined by a specific a, associated a/c, and applied stress) beyond which the assumptions of LEFM breakdown during the simulation is referred to as the LEFM limit.

F-1. LEFM plasticity assumptions are violated before the transition from a surface crack to a through-crack (i.e., before COPV liner leakage).

7.1.1.2 Analyzing the Impact of Invalid LEFM Assumptions on Predicted Crack Growth

The conditions at the crack-tip can be modeled using FEA. An elastic-plastic FEM was created (see Appendix C) to compare simulated CMOD to those observed in testing. When compared to a linear-elastic material model, the elastic-plastic material model more closely captures the observed CMOD behavior of a surface crack under tension, as shown in Figure 7.1.1-5. These results are typical for all tests conducted. See Appendix C for more details on model validation with test data. CMOD is an indication of crack driving force, therefore if linear-elastic FEA is not accurately capturing CMOD, then LEFM is not likely to accurately predict crack growth in these cases. Furthermore, it was observed that the linear-elastic, simulated CMOD gradually diverges from the nonlinear test and elastic-plastic FEA data. This divergence is also reflected in Figure 7.1.1-6. Here, CMOD and J are shown for crack growth steps for a simulated crack growing at a constant a/c = 1.0, with a maximum load of 80% of yield stress (σ_{vs}) (i.e., a representative loading condition for a liner). Results are normalized by thickness and are representative of the divergence expected in an AA6061 liner. In Figure 7.1.1-6a, elastic and elastic-plastic normalized CMODs, neglecting stress history effects, were computed for each step and plotted versus normalized a. The elastic and elastic-plastic *J*-integrals were computed for each step, as shown in Figure 7.1.1-6b, and demonstrate the divergence in crack front driving forces.

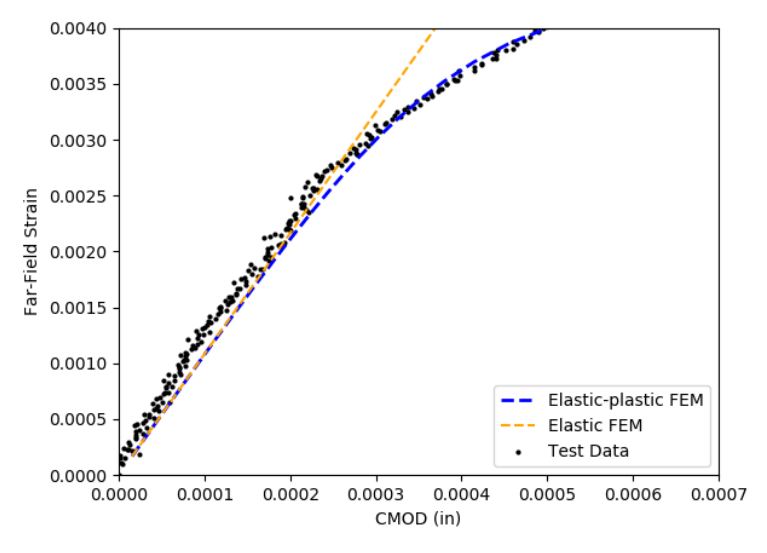


Figure 7.1.1-5. Far-field strain vs CMOD; test data compared to an elastic and elastic-plastic FEM.

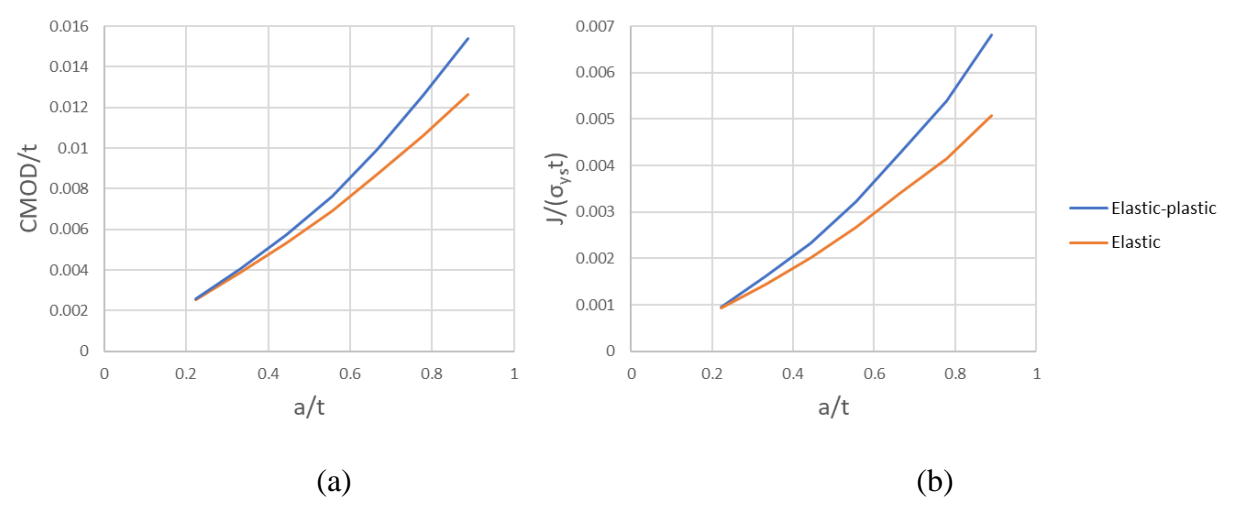


Figure 7.1.1-6. CMOD and J vs a for an elastic and elastic-plastic FEM.

The simulation of fatigue crack growth, da/dN is typically modeled as a power law function of a parameter representative of the crack driving force. A driving force error that increases gradually as a function of crack size will result in a smooth accumulation of error in predicted crack growth due to mathematical integration of this da/dN equation during simulation. In Figure 7.1.1-7, data from a single mechanical test is compared to a single NASGRO simulation with the initial crack size equal to that of the precrack size that was measured post-mortem using optical microscopy. The NASGRO material model, specifically da/dN, was calibrated using the long crack data presented in Appendix E, as is currently a common practice. A gradual divergence between the test data and simulated data is observed.

F-2. There is a gradual divergence between LEFM predicted behavior and measured crack behavior as cracks grow through the uncracked ligament.

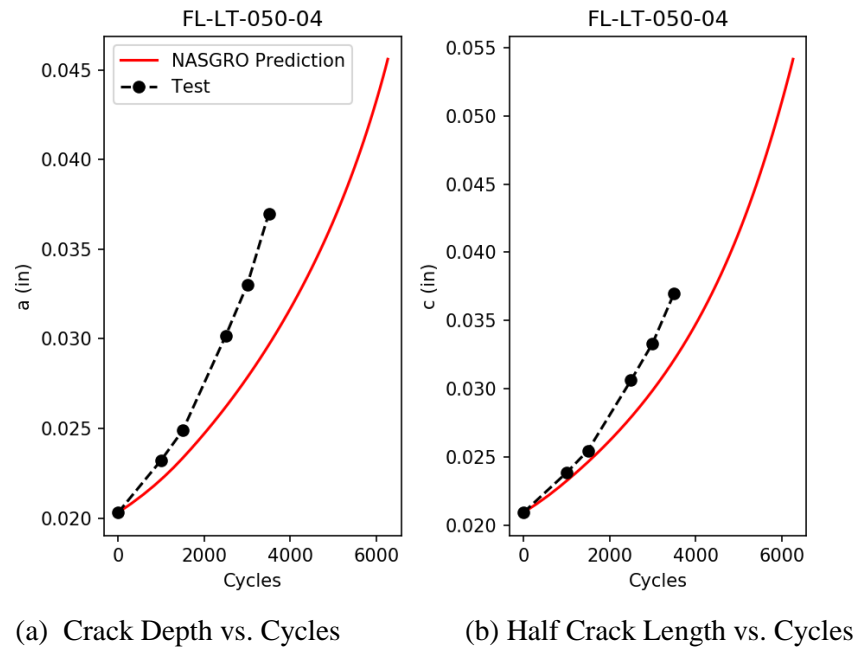


Figure 7.1.1-7. Example comparison of (a) a and (b) crack length between NASGRO simulation and test data.

The percent error between NASGRO simulations and test data is shown in Figure 7.1.1.-8. Percent error was calculated as $(y_{sim} - y_{test})/y_{test}$ where y_{test} is the observed crack dimension (i.e., a or c) and y_{sim} is the simulated crack dimension interpolated at N_{test} , or the cycle count when y_{test} was observed. A negative percent error indicates that the NASGRO simulation is unconservative. The x-axes of Figure 7.1.1-8 are the crack growth as a percentage of the remaining ligament, measured in-plane with and perpendicular to the crack front (i.e., = $(a_{test} - a_{test,0})/(t - a_{test,0})$). Here, $a_{test,0}$ is the a measured in the precracked condition, and t is the liner thickness.

Figure 7.1.1-8 shows that NASGRO simulations typically exhibited slower (unconservative) crack growth than what was observed during testing. Possible sources of error include inaccurate measurement of the initial crack size, material uncertainty (e.g., da/dN behavior, including differences in shielding mechanisms between long and surface cracks), inaccurate evolution of crack a/c, and errors due to linear-elastic assumptions. It has been observed that the precrack dimensions may have been measured inaccurately, in some cases, due to Sharpie® pen ink bleeding during fatigue cycling (see Appendix B). However, this bleeding would result in an over-estimate of crack size, meaning that the NASGRO simulations would have started from a more conservative initial crack size. The AA6061-T6 da/dN vs. ΔK equation parameters from the NASGRO database (M6AB13AB1) were estimated from tests conducted at higher ΔK values than in most of the tests in this assessment. Thus, the use of this equation for the tests herein would require an extrapolation beyond the underlying data. Standard, long crack tests were conducted for a more representative ΔK range and a piecewise linear fit was applied to allow determination of da/dN through interpolation of the standard test data results, as described in Appendix E. A more accurate representation of the crack growth rate behavior should reduce uncertainty in the crack growth behavior of the material. The a/c was observed to vary from 1.1 to 0.8, as shown in Figure 7.1.1-9. The a/c is shown for initial and final cracks for tests with the AA6061-T6 material at stress levels of 30, 35, and 40 ksi. Corresponding evolution of a/c predicted by NASGRO is also shown.

- **F-3** Measured crack growth in 0.032-, 0.048-, and 0.090-inch thick AA6061-T6 sheet material (i.e., representative of COPV liner thickness) was predominantly higher than predicted by common practice LEFM-based methods (e.g., NASGRO).
- **O-3.** The crack growth scatter for a/c ranging from 1.1 to 0.8, with NASGRO consistently predicting smaller than observed a/c, was greater than expected given the test coupons were extracted from the same material lot using the identical cracking process.

While it is acknowledged by the NESC assessment team that multiple factors are contributing to the error in the NASGRO predictions compared to test data in Figure 7.1.1-8, it was observed that LEFM assumptions were violated before breakthrough. Therefore, the errors in LEFM predictions due to invalid linear-elastic assumptions are the focus of this report. Furthermore, it was observed that these errors accumulate gradually, implying that LEFM tools do not immediately lose their utility once associated assumptions have been violated. This is the motivation for: (i) identifying a limit that defines the point during a simulation that these assumptions become invalid, and (ii) developing an approach for adding conservatism to the LEFM analysis once this limit has been surpassed.

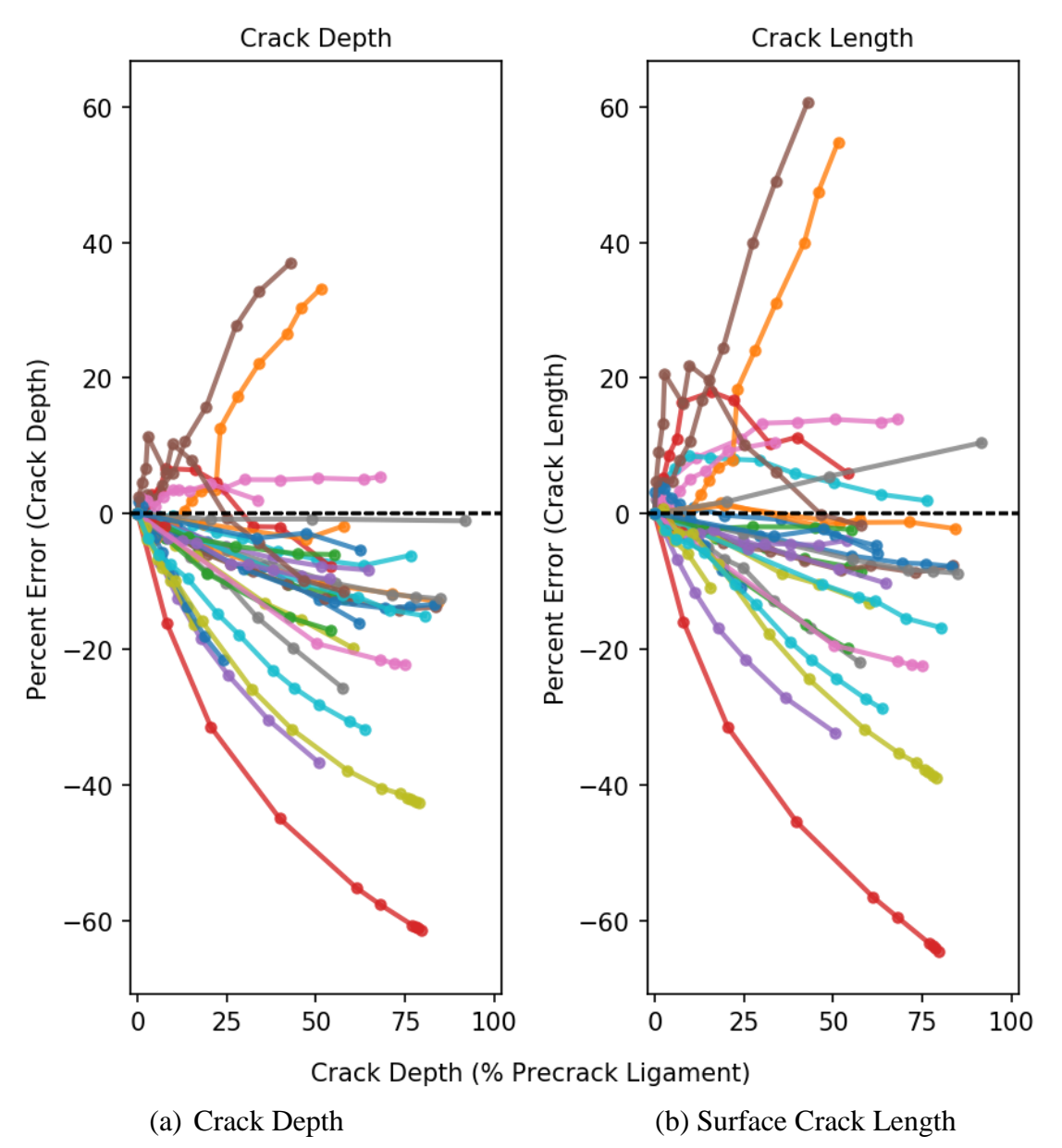


Figure 7.1.1-8. Percent error between NASGRO simulation and test data as a function of a normalized precrack ligament size. Each color represents a different fatigue test.

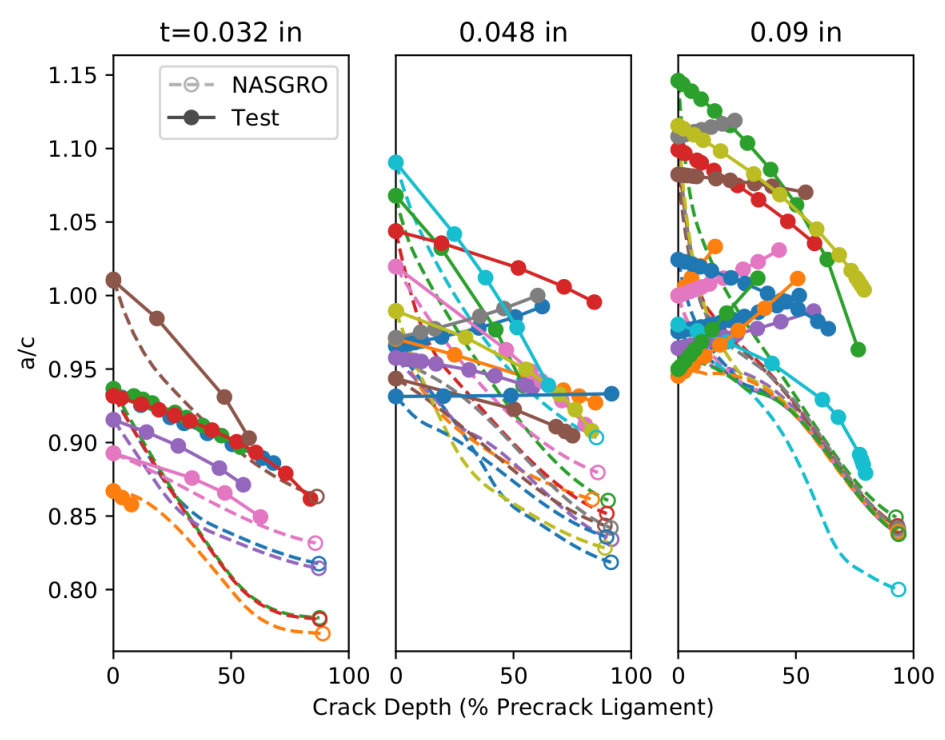


Figure 7.1.1-9. a/c vs. a normalized by precrack ligament. Solid symbols and lines represent test data and dashed lines represent NASGRO predictions. Each color represents a different fatigue test.

7.1.1.3 Quantifying the LEFM Limit

Small-scale and constrained plasticity assumptions are the underlying basis of an LEFM simulation. Thus, it is critical to be able to identify the LEFM limit in a quantitative, repeatable manner in the context of these fundamental assumptions. The approach for identifying the LEFM limit for COPVs with thin-walled, metal liners must consider the relevant parameter space (i.e., crack depth, crack length, liner thickness, applied stress, and material) and be based on the violation of the LEFM plasticity assumptions presented in Section 6.

Elastic-plastic FEA can be used to estimate the size of the plastic zone near a semi-elliptical surface crack. Figure 7.1.1-10 shows cross-sectional snapshots of the modeled semi-elliptical surface crack growing from left to right toward the liner back face. The plastic zone is highlighted in red. This sequence of crack growth steps shows the evolution of the plastic zone and the development of back-face plasticity. These two plastic zones eventually link up as the crack grows.

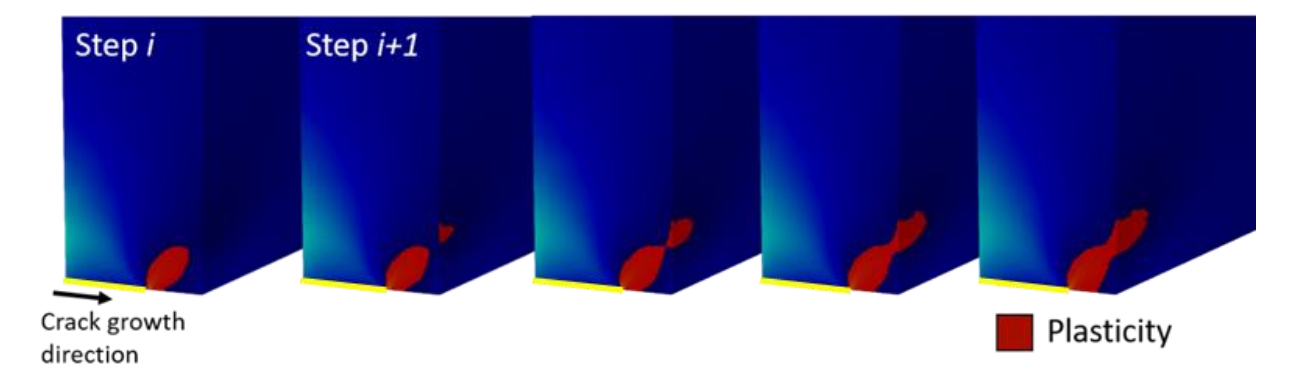


Figure 7.1.1-10. Cross-section at snapshots of a semi-elliptical crack (1/4 symmetry) growing toward the liner back face. The crack tip plastic zone at each step is highlighted in red. The crack is highlighted in yellow.

The ASTM E2899-15 [ref. 4] standard for determining fracture toughness of surface-cracked panels via mechanical testing was adopted to ensure repeatable identification of the LEFM limit. This standard provides a quantitative definition of various fracture toughness analysis regimes based on local crack tip conditions. Specifically, the standard identifies a regime that fracture toughness can be accurately described by a single linear-elastic parameter, the stress intensity factor (K). This regime corresponds to the definition of LEFM investigated in this report to determine whether the maximum stress intensity factors in a given fatigue cycle is an accurate descriptor of crack driving force.

ASTM E2899-15 is a test-based standard so the procedure was modified for the identification of the LEFM limit as outlined in Appendix F. This limit can be determined by identifying the a and a/c that the requirements for the single-parameter linear-elastic analysis regime outlined in ASTM E2899-15 are violated for a given liner thickness, applied stress, and material.

7.1.2 Analysis Approach to Add Conservatism to LEFM Based Life Prediction

The error in predicted crack growth accumulates gradually, as shown in Section 7.1.1, and is not a step-function after the LEFM plasticity assumptions are violated. Therefore, LEFM tools (e.g., NASGRO) may maintain engineering utility. A modified failure criteria is proposed for LEFM analyses of surface cracks growing in thin structures where crack breakthrough (i.e., leakage) is considered an end-of-life condition. The modification is a knockdown intended to provide conservatism over the state-of-the-practice techniques when LEFM assumptions are violated in the analysis and associated errors are accumulating.

The knockdown is based on a penalty function applied to the crack size regime that violates LEFM assumptions. The derivation of this penalty is based on elastic-plastic FEA of the cracked body and involves the computation of a ratio of an elastic-plastic driving force to the corresponding linear-elastic driving force. In this way, the penalty scales with the magnitude of deviation from LEFM assumptions (i.e., small deviations result in smaller penalty). This approach is in contrast to: (a) prohibiting the use of LEFM beyond its limit outright, or (b) applying an additional safety factor, that may be overly conservative for small deviations.

Though potentially applicable to a wider range of topics, the target audience for the modified analysis procedure is designers and analysts of thin-walled COPV liners for the purposes of damage tolerance life verification. As such, ease of use was a concern and the proposed modification has been designed to interface with existing analysis methods and LEFM tools

(e.g., NASGRO). The penalty function associated with violation of LEFM assumptions was converted into a limit to be used in place of state-of-the-practice failure criteria. If the limit is exceeded, the crack is not characterized by LEFM and the AIAA S-081B requirements for damage tolerance life verification by test apply. The remainder of this section discusses the new limit, beginning with a review of state-of-the-practice failure criteria and closing with an example application of the methodology. To aid understanding of subsequent notation, a schematic diagram of a surface crack and applicable limits on *a* is provided in Figure 7.1.2-1.

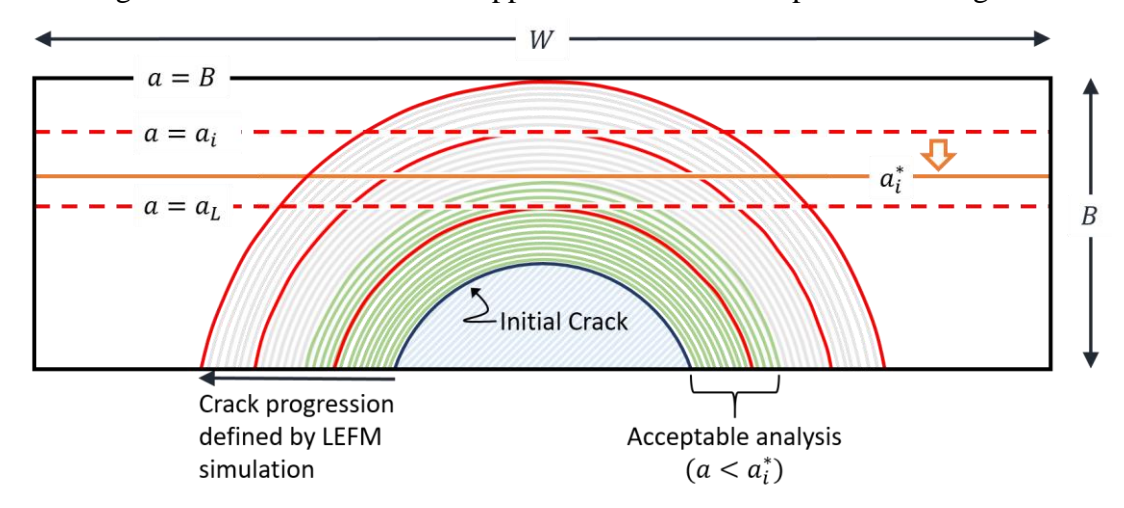


Figure 7.1.2-1. Schematic of a surface crack growth simulation and applicable limits on a, including the Irwin limit, a_i , the LEFM limit, a_L , and the modified limit, a_i^* .

Current practice allows use of LEFM as long as the a at the end of simulated service life (including safety factors in the form of M-lifetimes; typically M=4) does not exceed the liner thickness. This limit will be referred to as the $breakthrough \ limit$ and is defined mathematically as:

$$a_F < B$$
,

where a_F is the predicted a after application of M-lifetimes, measured from the cracked surface toward the liner back surface, and B is the liner thickness. Variations of the breakthrough limit exist; for example, using semi-elliptical surface crack cases SC30 or SC31 in NASGRO results in the modified limit:

$$a_{\rm F} < 0.95B$$
.

An additional limit on net-section yielding is defined such that the net-section stress in the cracked liner must remain below the material flow stress. However, this limit is rarely applicable in pressure vessel liners where crack surface area is a small percentage of overall cross-sectional area.

While not explicitly enforced by NASGRO, a limit addressing plasticity in the uncracked ligament immediately ahead of and in-plane with the crack front can be defined using the Irwin plastic zone⁷ [refs. 9, 17, 18]. This limit will be referred to as the *Irwin limit*, and is defined as

$$a_F < a_i$$

NESC Document No.: NESC-RP-16-01183, Vol. I, V.1.1

⁷ Currently, this limit is used in NASGRO to select the appropriate fracture toughness (i.e., surface crack toughness if not exceeded or through-crack toughness if exceeded) but does not correspond to crack transition to a through-crack, distinguishing it from the breakthrough limit.

where a_i is the *a* that the Irwin plastic zone size is equal to the size of the remaining uncracked ligament; i.e., the solution to the following equation:

$$\rho(a) + a = B$$

for a given crack growth simulation. Here, a denotes the crack depth during the analysis, and the Irwin plastic zone size as a function of a is given by:

$$\rho(a) = \frac{1}{2\pi} \left(\frac{K_{max}}{\sigma_{vs}} \right)^2,$$

where σ_{ys} is the material yield stress and K_{max} is the maximum stress intensity factor computed for a and the associated crack length and stress state obtained from the crack growth simulation.

Exceedance of this Irwin limit can provide an initial approximation of when LEFM assumptions have been violated, although it was observed that LEFM assumptions break down before this limit is reached. Figure 7.1.2-2 shows a comparison of the Irwin limit to the LEFM limit calculated according to ASTM-E2899-15 and the a that plasticity was first observed on the back face during a series of tests. Plasticity was observed on the back face of the specimen before the crack had reached the calculated Irwin limit in more than 50% of the tests. In contrast, the LEFM limit, denoted as a_L and defined using ASTM-E2899-15, was conservative in all cases. This conservatism can be seen in the plastic zone size at the limits as calculated by FEA. Figure 7.1.2-3 shows a comparison of the plastic zone size at the two limits from FEA. The ASTM E2899-15 limit shows a small amount of plasticity starting to appear on the back face. Conversely, at the Irwin limit, there is a significant amount of back face plasticity that is fully connected to the crack front plastic zone. By definition, the Irwin limit is equal to or more conservative than the standard breakthrough limit. Figure 7.1.2-2 suggests the Irwin limit is also more conservative than the modified 0.95B breakthrough limit. Thus, the Irwin limit will be used in place of the breakthrough limit in the following discussion.

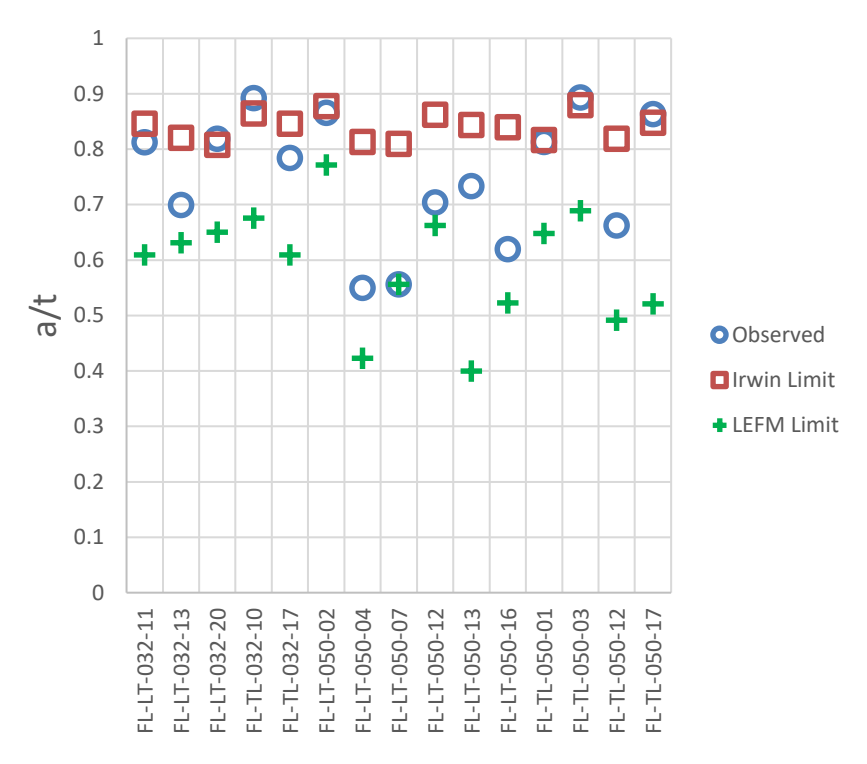


Figure 7.1.2-2. Crack depth (a) normalized to thickness (t) at which back face plasticity was observed during test as compared to calculated Irwin and LEFM limits.

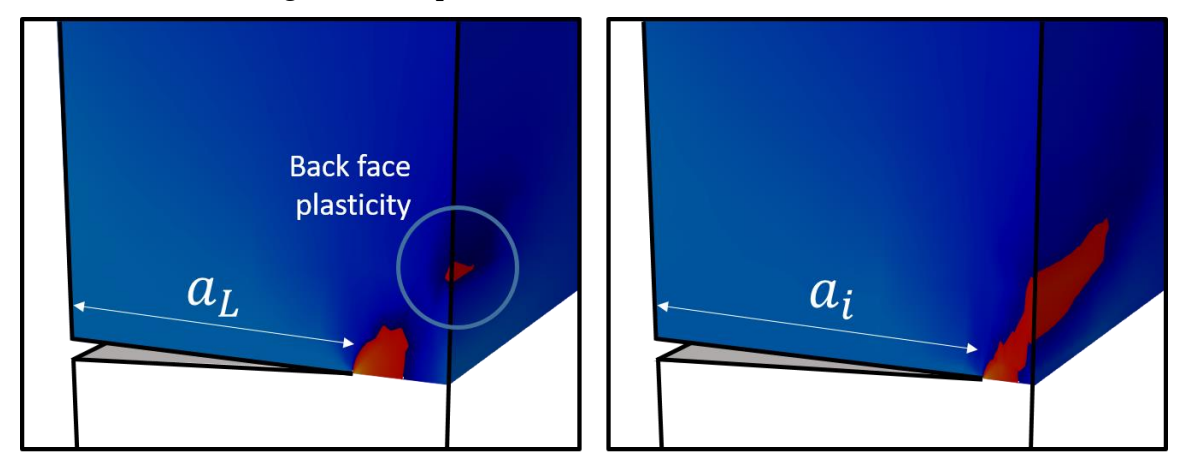


Figure 7.1.2-3. Plastic zone size from FEA comparing LEFM limit calculated according to ASTM E2899-15 and the Irwin limit.

The crack tip plastic zone is highlighted in red.

Other failure mechanisms exist and are reported by LEFM tools such as fracture due to exceedance of material fracture toughness. For the case where a at fracture is predicted to be less than the Irwin limit, set a_i equal to the fracture a (i.e., a_i becomes the minimum of all failure criteria).

The state-of-the-practice damage tolerance life verification analysis is a two-step process: (i) a LEFM-based simulation to determine a_F and (ii) verification that a_F does not exceed the breakthrough limit or, more conservatively, a_i . The proposed modification requires the computation of two additional limits. The first is based on ASTM E2899-15 and is referred to as

the *LEFM limit* (a_L) that is the crack depth where the LEFM assumptions are violated. No additional consideration is required if the predicted crack depth is below the LEFM limit (i.e., $a_F < a_L$). The LEFM limit has been shown to be more conservative than the Irwin limit (Figure 7.1.2-2) and details regarding the interpretation and calculation of a_L are provided in Section 7.1.1 and Appendix F.1, respectively. The second limit involves a knockdown applied to the Irwin limit to add conservatism relative to the state-of-the-practice LEFM analysis. This knockdown acknowledges that error is accumulating at an unknown rate beyond the LEFM limit. This limit is referred to as the *modified Irwin limit* (a_i^*). A predicted crack depth that is above the LEFM limit and below the modified Irwin limit (i. e., $a_L < a_F < a_i^*$) is acknowledged to be in a regime that the LEFM assumptions are violated, but the associated errors in predicted behavior is small due to the gradual deviation from LEFM behavior. The modified Irwin limit is defined as:

$$a_i^* = \frac{a_i - a_L}{\left(\frac{J_{\max \phi_i}^*}{J_{\phi_i}}\right)^n} + a_L.$$

where, a_L is the a defining the LEFM limit, n is the exponent of the LEFM-based crack growth rate equation, and J_{ϕ_i} and $J_{\phi_i}^*$ are measures of the predicted driving forces along the crack front estimated using elastic and elastic plastic FEA, respectively. See Appendix F for details on how these driving forces are computed. The amount of knockdown is dictated by the ratio of the driving forces that is assumed to be greater than or equal to one. Therefore, a_i^* always lies between the Irwin and LEFM limits,

$$\lim_{\substack{J_{\max\phi_i}^* \to J_{\max\phi_i} \\ \bigcup_{\phi_i}^* \to \infty}} a_i^* = a_i - a_L + a_L = a_i$$

It is important to note that the modification is calculated based on the portion of the simulation exceeding the LEFM limit. If the predicted a_F is less than a_L , then a_i^* does not apply and LEFM assumptions are understood to be valid for the entire analysis.

To eliminate the computational burden imposed on the designer, future software could be developed to automatically calculate the new limits given a NASGRO output file (or other properly formatted LEFM simulation output). The software would interrogate a response surface to compute a_i , a_L , and a_i^* automatically. The construction of the response surface would be similar to that of the Tool for Analysis of Surface Cracks (TASC) [ref. 10]. In this way, the COPV designer would not be required to perform elastic-plastic FEA or interpret results beyond comparison of a_F to the additional limits (i.e., rather than just the breakthrough limit).

The modified analysis procedure involves the following steps:

- 1. Simulate crack growth to failure (i.e., breakthrough)⁸ using an approved LEFM tool.
- 2. Identify the predicted a after M-lifetimes, a_F .
- 3. Identify the limits a_i , a_L , and a_i^* .

⁸ This is in contrast to current practice of only simulating *M*-lifetimes. This step is required to compute a_i , and, thus, the modified Irwin limit, a_i^* (see Appendix F.2 for details). It is argued that the running of ∞-lifetimes until the LEFM tool predicts breakthrough is a relatively simple addition to the workflow.

- 4. Verify that $a_F < a_i^*$, otherwise the design does not meet recommended requirements for damage tolerance life by analysis.
- 5. Report a_F , a_i , a_L , and a_i^* to fracture control engineering technical authority.

Details regarding the calculation of a_L and the derivation of a_i^* are provided in Appendix F.1 and F.2, respectively. As discussed previously and documented in Appendix F.2, a_i^* is based on a penalty applied to the NASGRO-computed a_F . While the limit-form of the penalty (i.e., a_i^*) is easier to interpret in the context of a damage tolerance life assessment, the penalized a can be used to investigate the performance of the proposed approach on real NASGRO predictions through a comparison to test data. The procedure was applied to the analysis of all available test data from Section 7.1.1.1. A comparison of the NASGRO prediction to the penalized NASGRO prediction is shown in Figure 7.1.2-4. The predictions are normalized by the measured test result such that results <1 are non-conservative predictions and >1 are conservative. Of the cases where $a_F > a_L$, 82% of the original NASGRO predictions were non-conservative while 81% of the predictions were conservative after the penalty was applied. It is important to note that the penalization approach is not predictive; a predictive tool would be expected to produce normalized predictions \approx 1. Instead, the goal of the approach was to force this ratio to positive values.

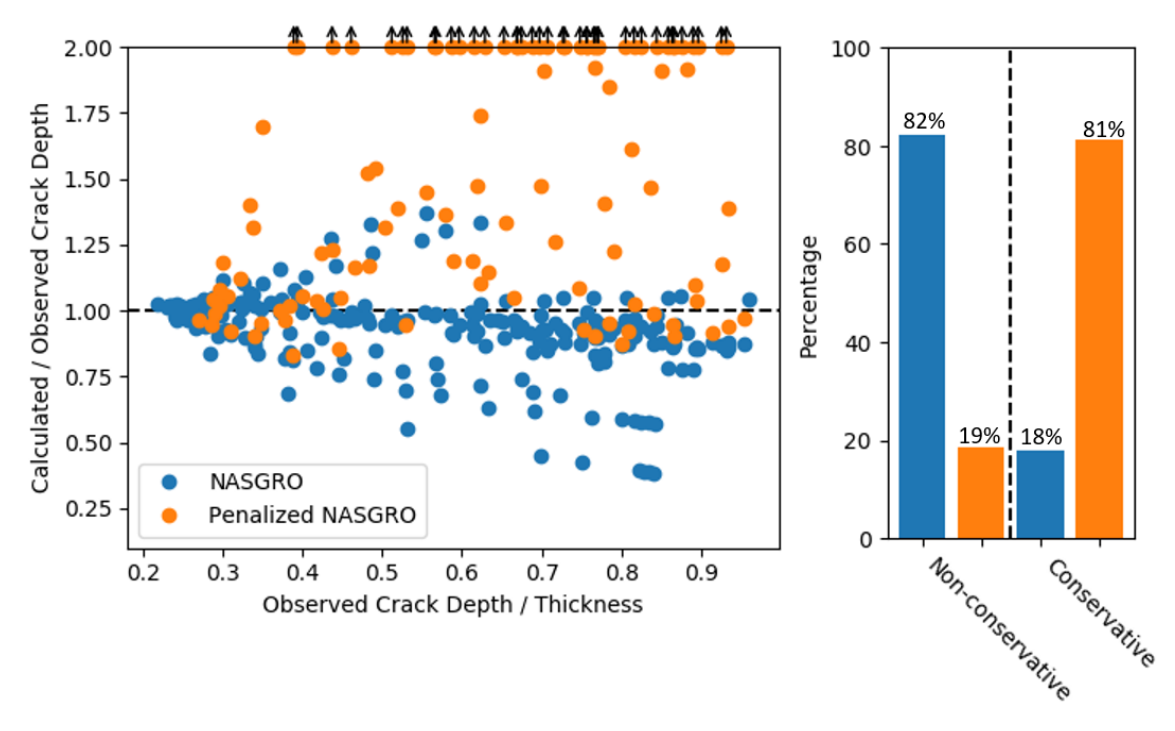


Figure 7.1.2-4. Comparison of NASGRO and penalized NASGRO a predictions normalized by observed a for all coupon tests.

F-4. The COPV life LEFM limit and knockdown failure criterion is a more conservative damage tolerance life analysis approach than the state-of-the-practice damage tolerance life analysis approach.

7.1.2.1 Statement of Intended Usage

The approach outlined in Sections 7.1, Appendix F.1, and Appendix F.2 is intended to add conservatism when performing damage tolerance life analysis of thin-walled, homogeneous,

metal COPV liners when the amount of growth of semi-elliptical surface cracks is the quantity of interest. This approach is more conservative than the state-of-the-practice LEFM analyses, but does not eliminate uncertainty associated with damage tolerance life analysis. Thus, risk analysis associated with damage tolerance life should consider all sources of uncertainty. The approach is not intended to serve as an EPFM predictive tool. At this time, the models used to generate the data presented here have been experimentally validated for AA6061 in wall thickness ranging from 0.032 to 0.090 inch. Details regarding these models are provided in Appendix C.

7.1.2.2 Example Application of the Methodology

Graphical demonstrations of the limit modification procedure for cases where (i) $a_F < a_L$, (ii) $a_F < a_i^*$, and (iii) $a_F > a_i^*$ are shown in Figures 7.2.1-5, 7.2.1-6 and 7.2.1-7, respectively. Each case is based on the same fatigue crack growth test that was conducted using a surface cracked specimen (i.e., AA6061 with thickness, B=0.048 inch) according to the process outlined in Section 7.1.1.1. The test served as ground truth for comparison with the LEFM analysis. Starting from the initial precrack shape (a=0.0335 inch and c=0.0345 inch), the crack was grown under load control with an applied cyclic stress of 30 ksi with R=0.1.

For each case, a_F was modified such that a new outcome (i, ii, or iii) was achieved. Each chosen a_F corresponds to a cycle count at which a was measured. In the figures, a measured from test data are represented by black triangles while a_F is represented by a yellow star. For the first case depicted in Figure 7.2.1-5, M-lifetimes was 1,000 constant amplitude cycles. Per the recommended analysis procedure, the following steps were conducted:

- 1. Crack growth was simulated using NASGRO v8.2 to breakthrough (i.e., failure) as indicated by the dotted blue line.
- 2. The *M*-lifetime crack depth, a_F , was found to be 0.0351 inch, as indicated by the yellow star
- 3. Using the NASGRO output file, the following limits were computed:⁹
 - a. Irwin limit, $a_i = 0.0421$ inch
 - b. LEFM limit, $a_L = 0.0370$ inch
- 4. Since $a_F < a_L$, the additional limit was not computed; damage tolerance life requirements were met.

NESC Document No.: NESC-RP-16-01183, Vol. I, V.1.1

⁹ As discussed previously, software for automatically processing NASGRO output files using a response surface could be built and made available to designers to remove FEA from the workflow. There is currently no such response surface, so the analysis was conducted manually by analyzing each NASGRO crack growth step (i.e., a specific crack depth, a/c, applied stress, liner thickness and material) using finite elements and computing both elastic and elastic-plastic crack driving forces. Data were post-processed using a Python implementation of the procedures outlined in Appendix F.

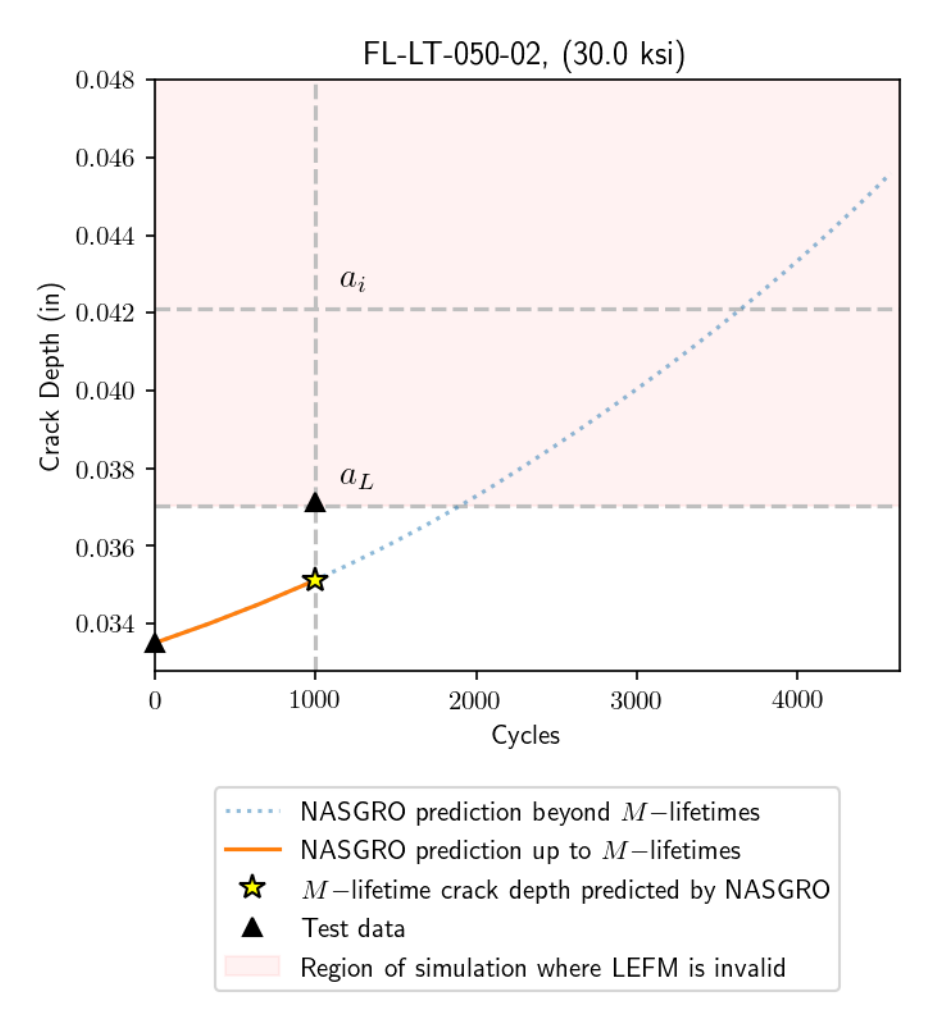


Figure 7.1.2-5. Example NASGRO analysis and identification of a limits for M-lifetimes equal to 1,000 cycles.

The second case is shown in Figure 7.2.1-6. Here, M-lifetimes was increased to 2,500 constant amplitude cycles and $a_F = 0.0386$ inch. In this case, a_L was exceeded at approximately 2,000 cycles. Thus, the remaining 500 cycles were subjected to a penalty based on the amount of crack growth beyond a_L and the difference between elastic-plastic and elastic driving force parameters (see Appendix F.2 for details on how the penalty is calculated). The penalty was converted to a knockdown of the Irwin limit, represented by the dotted red line in Figure 7.2.1-6. Thus, steps 1-3 of the analysis procedure were executed as before, and steps 4 and 5 were executed as follows:

- 4. Since $a_F > a_L$, the following additional limit was computed:
 - a. Modified Irwin limit, $a_i^* = 0.0396$ inch
- 5. Since $a_F < a_i^*$, the analysis was considered valid (i.e., it is suggested that this analysis meets damage tolerance life requirements).

The measured a at 2,500 cycles was 0.0438 inch, meaning that the measured a was approximately 91.3% of the liner thickness.

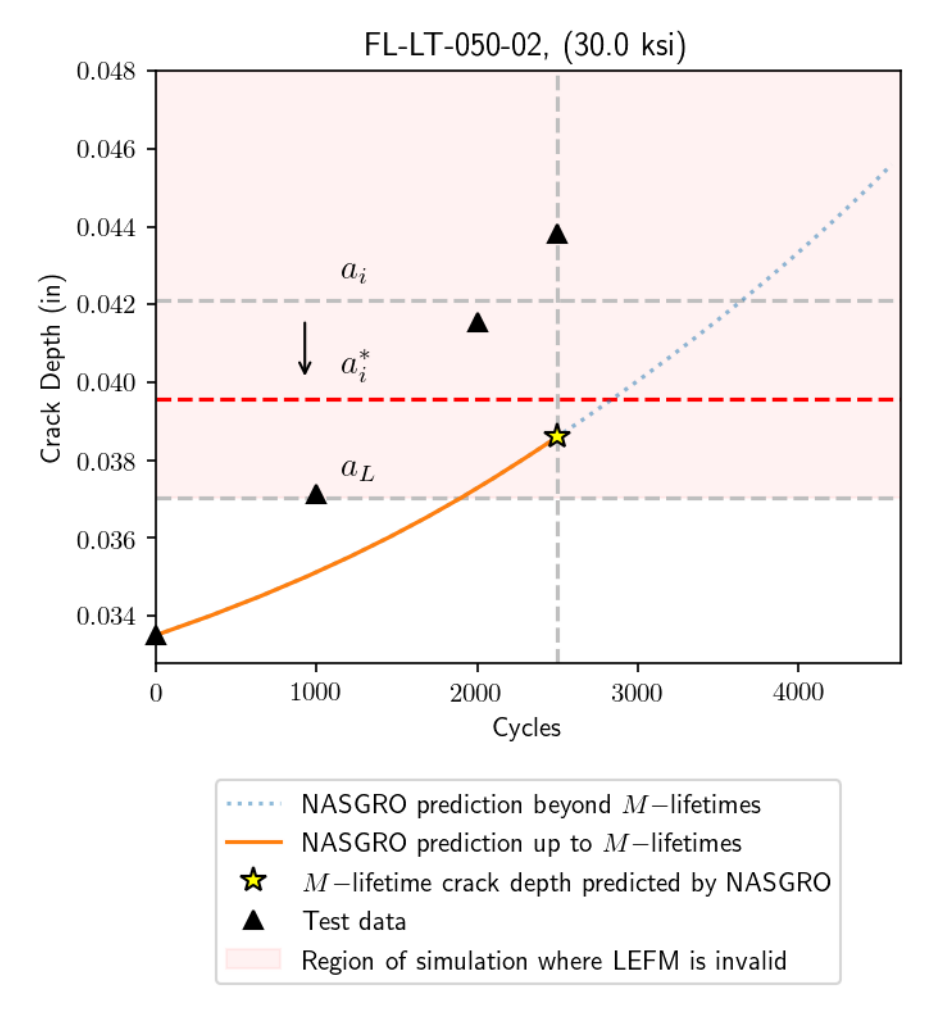


Figure 7.1.2-6. Example NASGRO analysis and identification of a limits for M-lifetimes equal to 2,500 cycles.

The third and final case is shown in Figure 7.2.1-7 and the *M*-lifetimes is 3,000 constant amplitude cycles and $a_F = 0.0400$ inch. Again, a_L is exceeded at approximately 2,000 cycles, meaning the penalty is applied for the final 1,000 cycles. Steps 4 and 5 were modified as follows:

- 4. Since $a_F > a_L$, the following additional limit was computed:
 - a. Modified Irwin limit, $a_i^* = 0.0391$ inch
- 5. Since $a_F > a_i^*$, the analysis was rejected; AIAA S-081B requirements for damage tolerance life verification by test must now be met or the tank must be redesigned.

Comparing to test data, a_F is non-conservative and, at 3,000 cycles, the measured a was 0.0458 inch or 95.4% of the liner thickness.

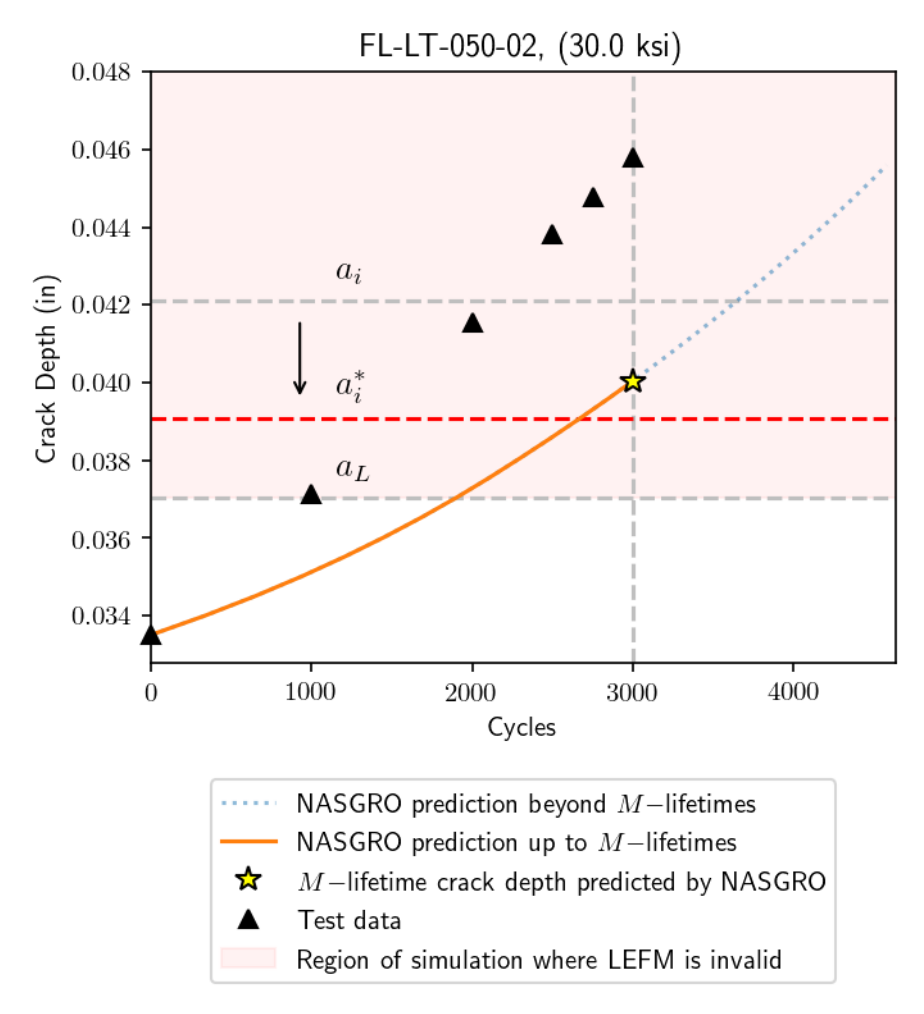


Figure 7.1.2-7. Example NASGRO analysis and identification of a limits for M-lifetimes equal to 3,000 cycles.

7.2 Test-Based Methodology for Validating Damage Tolerance Life Requirements

This section documents a test-based methodology for validating damage tolerance life requirements. Damage tolerance life verification has several test-based requirements, whether performing the overall demonstration by analysis or coupon or COPV test. When performing damage tolerance life analysis, it is required to have an understanding of the liner material to develop nominal fracture properties. Crack growth measurements during high strain cycles (e.g., autofrettage) are needed to supplement the LEFM computations in a damage tolerance life analysis. Crack growth measurements during high strain cycles is part of damage tolerance life coupon testing and test methods used to measure crack growth in these conditions are directly applicable to coupon level damage tolerance life testing. Liner material evaluation, autofrettage crack growth, and damage tolerance life testing by coupon or COPV are addressed.

7.2.1 Liner Material Evaluation

The demonstration of damage tolerance life in worst-case scenarios requires that the initial flaws are inserted within representative vessels with placement at worst-case locations (i.e., combined

high fatigue crack driving force or reduced thickness in representative material that considers any low resistance to crack growth due to undesirable microstructural features).

As discussed in Section 6.0, thin COPV liners (i.e., 0.030 inch) with an NDE minimum detectable crack depth of 0.025 inch can result in a ligament of less than 10 grains. Furthermore, COPV liners can be manufactured using spin forming or forging methods that have been shown to produce large grain structures (relative to the liner thickness) and widely varying microstructure throughout the final product. [ref. 7]. In these cases, additional testing has been performed for evaluation of compliance with damage tolerance requirements. While regions of increased driving force are likely known from structural-scale models (e.g., FEA), they currently do not capture the impact of microstructure variation. Therefore, the material-scale stress concentrations and inherent resistance to cracking are sources of bias and uncertainty that must be considered. Data presented in Section 7.2.1.1 provide evidence that important microstructure features vary significantly throughout individual COPVs. This means that deformation and crack growth behavior variation is expected within a COPV liner, among COPVs in the same lot and, especially, COPVs from different lots. To understand this effect on reliable service life of these COPVs, numerous COPVs would need to be tested for each material lot and/or tank design, such that the corresponding variability in service life could be quantified.

Extracting standard size test coupons from thin and doubly-curved COPV liners causes a significant barrier to fatigue crack growth rate testing using as-manufactured materials. Consequently, the LEFM-based prediction tools will use crack growth rate data obtained from a surrogate: new data on similar, flat-sheet material or existing databases (i.e., NASGRO material library). However, crack growth data available in such libraries are mainly comprised of standard coupons and material pedigrees (processing and/or forming) that are conducive to standard coupon testing (i.e., the employed surrogate materials). Consequently, the library option that most closely fits the as-manufactured material in a tank would be chosen for analysis, where the material composition might be equivalent, but likely has a different pedigree.

Violation of LEFM plasticity assumptions is discussed in Section 7.1.1. Those studies focus on the structural-scale aspects, where grain size is not typically considered in the determination of the plastic zone size. To better understand the effect of grain-scale variability on fatigue crack growth behavior in COPV liners, coupons were extracted from AA6061-T6 and IN718 as manufactured liners and rolled sheet (surrogate) materials. The coupons were analyzed to acquire supporting data regarding inherent variations in microstructural features and fatigue crack growth rates to identify any potential impact of material selection on damage tolerance life test or analysis. First, the variation of microstructure within representative liner materials is presented with comparison to standard rolled sheet materials. Second, a subscale coupon was designed to enable a more explicit study of as-manufactured materials. Next, the measured tensile behavior in the longitudinal and circumferential directions of these coupons is presented. Finally, the measured fatigue da/dN are presented and compared with the structure-scale fatigue da/dN.

7.2.1.1 Liner Microstructure Variation

Metallographic specimens were removed from various locations of the AA6061-T6 spun-formed liner. The grain size was observed to vary throughout the liner as shown in Figure 7.2.1.1-1. The images in Figure 7.2.1.1-1 were generated using electron backscattered diffraction (EBSD). Each color in the inset images indicates a grain orientation and the provided legend, known as an inverse pole figure (IPF) map, correlates the color to the relative rotation of the sample

coordinate system with respect to the crystallographic unit vectors (e.g., [111]). Larger grain sizes were observed in samples taken from the dome regions, where a greater amount of heat and forming were needed to create the curved shape. Smaller grain sizes were observed in the cylinder regions. The mid-cylinder grain size was similar to that found in rolled AA6061-T6 sheet, see Figure 7.2.1.1-2. Furthermore, it was observed that the liner microstructure (grains and particles) followed the flow lines of the spin-forming process. While there was a strong correlation between grain size and shape with location on the liner, it was observed that the crystallographic texture did not vary significantly.

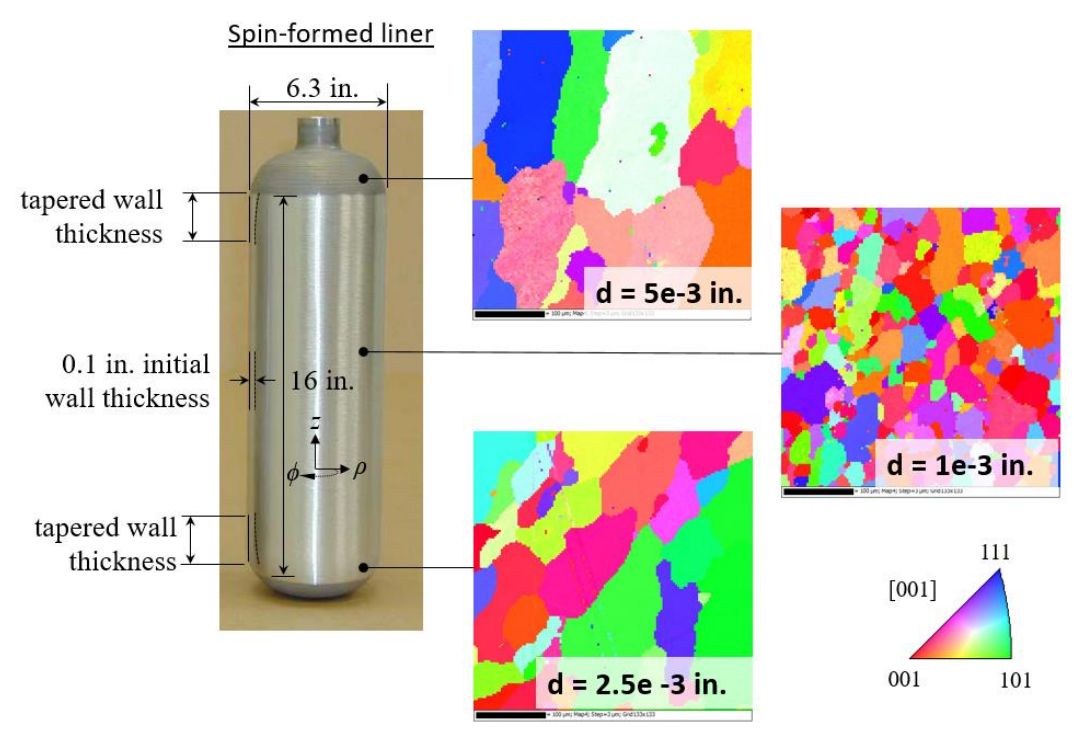


Figure 7.2.1.1-1. (left) AA6061-T6 liner with (middle) upper and lower dome EBSD results and (right) cylinder EBSD results.

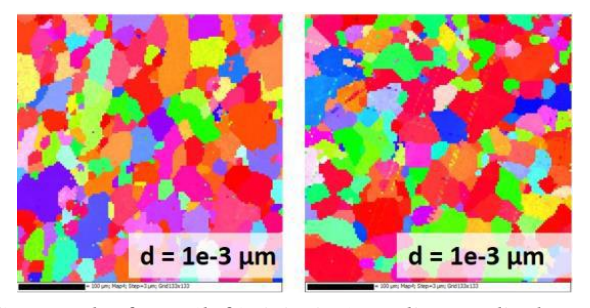


Figure 7.2.1.1-2. EBSD results from (left) AA6061-T6 liner cylinder and (right) rolled sheet.

The distribution of second-phase particles was noticeably different among samples extracted from the dome, cylinder, and rolled sheet materials, as shown in Figure 7.2.1.1-3. Comparison of the histograms in Figure 7.2.1.1-3 illustrates that the liner material dome and cylinder regions have a higher frequency of large particles (>100 pixels) than the rolled sheet material. These large, brittle second phases are known to induce fatigue crack initiation. Furthermore, particles in SEM images were observed to follow the flow lines produced during liner processing; this

was separately confirmed objectively using two-point statistics. The particles were observed to congregate along grain boundaries more often in the liner samples than in the rolled sheet samples.

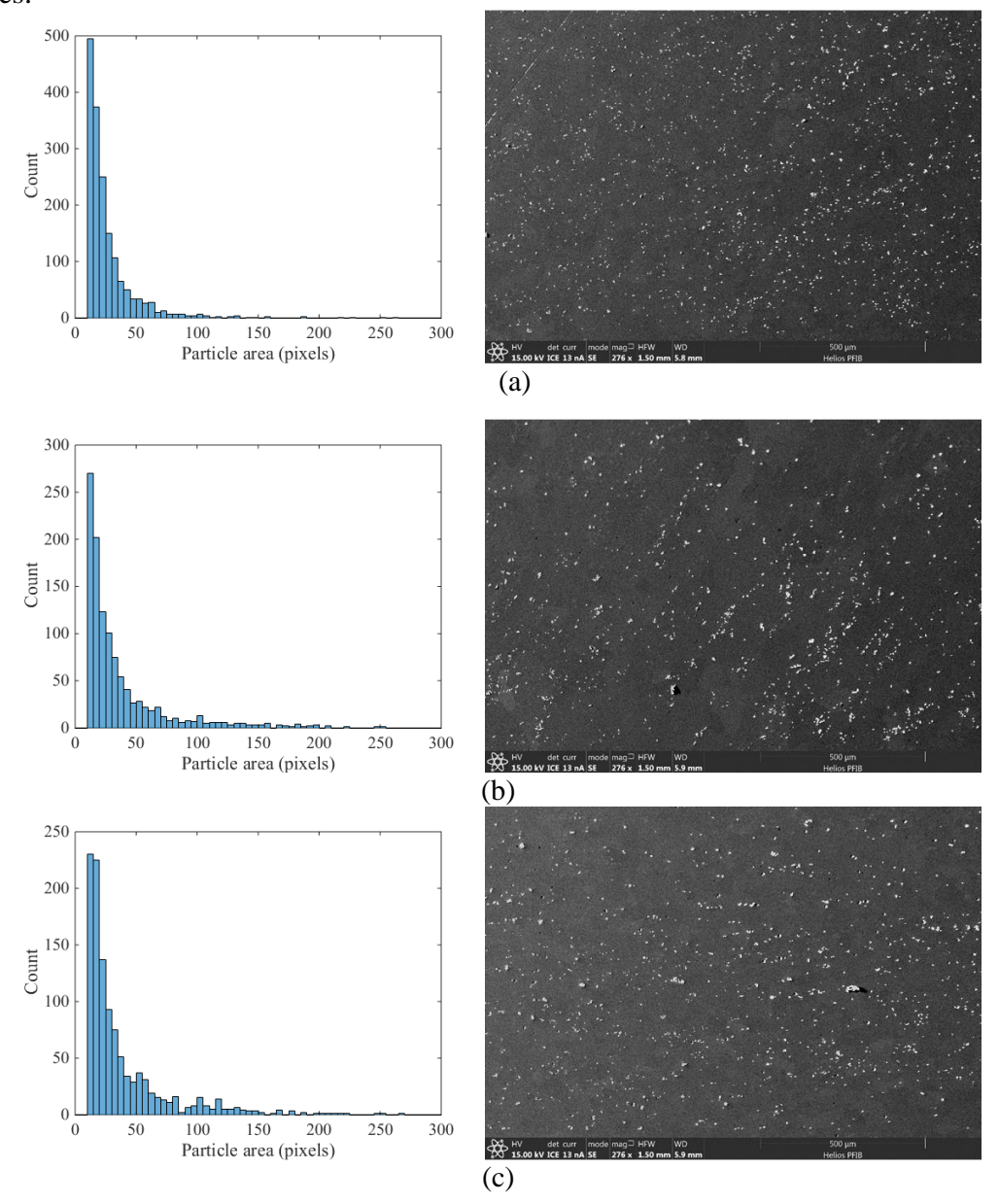


Figure 7.2.1.1-3. Second-phase particle distribution and SEM image from (a) rolled sheet (b) liner dome and (c) liner cylinder.

Ultimately, these observations suggest that differences in mechanical behavior could be present and dependent on the location within the dome. The enlarged grains in the dome region would be expected to enlarge plastic zone sizes (due to the lack of grain boundaries to constrain plastic deformation) and be a major source of increased variability in the elastic-plastic behavior. Larger and increased density of second-phase particles would be expected to have a detrimental influence on the initiation of fatigue cracks and growth rates [ref. 25]. Quantification of the impact that these visually-observed features have on fatigue cracking must currently be made through mechanical testing. In other words, neither similarities nor differences in the

microstructural features (as compared to more standard sheet material) are sufficient to conclude a disparity in elastic-plastic behavior or fatigue da/dN.

Similar surface-based microscopy measurements were completed for additional processed liner and sheet materials considered in this small-scale study. Next, a second AA6061-T6 liner with the dome region thickness of >0.5 inch allowed coupons with a thicknesses up to 0.2 inch to be extracted. This second liner was observed to have grain sizes that varied significantly (several orders of magnitude) through the thickness of the dome. This was in addition to microstructure variation throughout the entire liner (as shown in Figure 7.2.1.1-1). One IPF image for a representative dome sample is provided in Figure 7.2.1.1-4 where the grain size and texture is in comparable to the dome samples of the first generation AA6061-T6 tank discussed above.

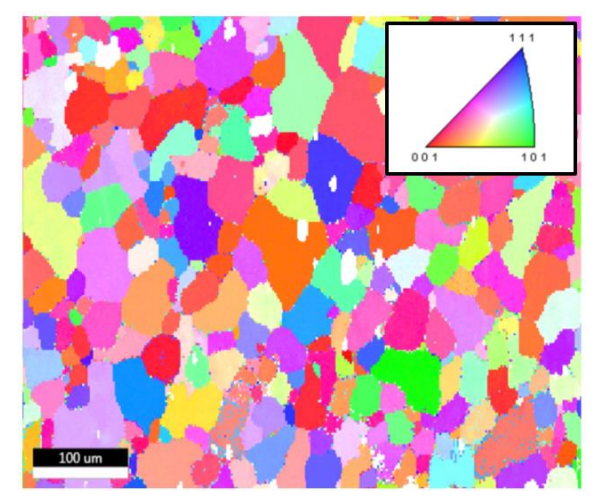


Figure 7.2.1.1-4. AA6061-T6 EBSD result from dome of second, thicker liner.

Small-scale IN718 coupons were also studied in this assessment. Similar to the comparative study for AA6061-T6 coupons, small-scale IN718 coupons were extracted from manufactured, forged liner domes and rolled sheet material. Similarly, the objective was to acquire data for elastic-plastic constitutive behavior and fatigue crack growth rates for IN718 from these two processing methods. Acquisition of this data provides evidence to guide decisions in support or discouragement of the acceptance of large-scale testing data from materials that have equivalent composition but different (even if slightly) processing steps (i.e., rolled sheet vs. forged domes). As illustrated in Figure 7.2.1.1-5, EBSD demonstrates clearly quantitative differences between the rolled sheet, Figure 7.2.1.1-5 (left), and dome, Figure 7.2.1.1-5 (right).

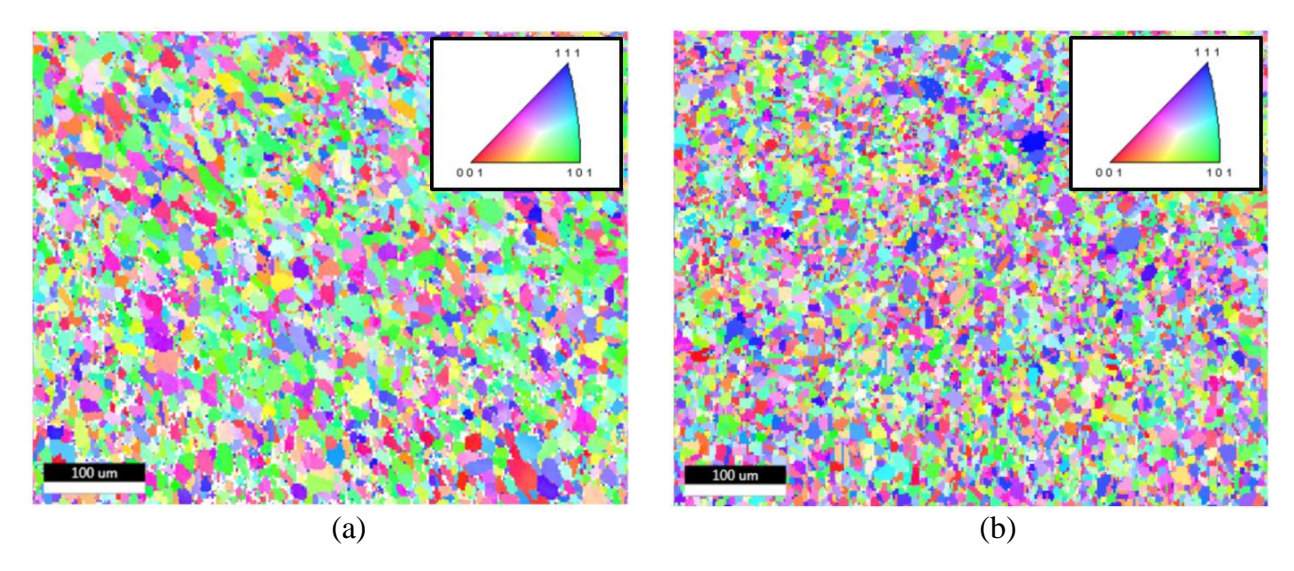


Figure 7.2.1.1-5. EBSD result from IN718 (a) sheet material on TL surface and (b) dome material extracted in radial direction (radial is vertical in the image).

7.2.1.2 Small-Scale Specimen Design, Fabrication, and Test Procedure

Small-scale specimens were extracted from both the various liner and sheet materials using EDM. See Figure 7.2.1.1-6 for an illustration of first AA6061-T6 liner after coupon extraction. The liner coupons were extracted along the entire length and oriented in the circumferential, C, direction such that cracks would grow in a manner consistent with the hoop stress in an inservice liner. Coupon identification begins with C and is followed by a number indicating its original location in the tank: 1 being the bottom dome and 30 being the top dome (near the boss). While the transition of microstructure characteristics between the dome and cylinder was gradual, it was generally observed that C1-C8 and C25-C30 were characterized best as dome microstructure and C9-C24 were characterized best as cylinder. The curvature of the liner limited the thickness of the coupons, so the extracted coupons were 0.032-inch thick. As such, the coupons are representative of the mid-thickness liner wall. Similar coupons were removed from a 0.090-inch thick sheet that was mechanically milled to 0.032-inch thick.

The small-scale test coupons were designed to be extracted from the available liner and provide a (near) 2:1 stress state at the center of the coupon due to uniaxial loading, as shown in Figure 7.2.1.1-7. This biaxial stress state was achieved as a result of the coupon geometry and limited gage length upon gripping. Uniaxial coupon designs permit the material to contract freely in the off-axes (i.e., not loading) directions. In contrast, these small-scale coupons constrain deformation in the off-axes directions, resisting the Poisson effect and thereby imposing a horizontal stress component in the vicinity of the coupon center. This added constraint also results in a stiffer response (higher stress per strain) of the small-scale coupons. Furthermore, the semi-circular edge shapes help ensure that cracking does not occur near the grips. This coupon geometry has the advantages that: 1) as-manufactured coupons can be extracted from thin product forms; 2) imposes similar bi-axial stress state, but with the ease of uniaxial loading; and 3) are easily machined using common EDM methods. The fatigue-crack-initiating notch was subsequently located at this central location. This small scale coupon design does have some disadvantages that require extra caution. First, the edge-notched design imposes a local stress concentration at the edges of the coupon. In the 0.032-inch thick coupons, the cracks approach the back surface (when the test is stopped) well before reaching these edge localizations.

However, for thicker coupons, increased driving forces should be quantified through FEA and monitored during testing. Second, the 0.032-inch thickness makes the coupon sensitive to any misalignment in the test stand. Small misalignment can result in undesirable bending and torsional effects on state-of-stress in the gage section of the coupon and influence fatigue crack growth behavior. In this study, DIC measurements were performed to ensure adequate alignment.

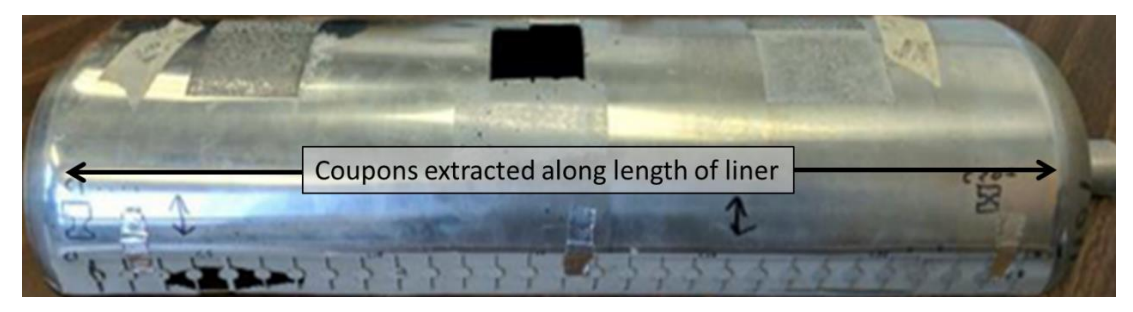


Figure 7.2.1.1-6. AA6061-T6 liner with coupons extracted along entire length.

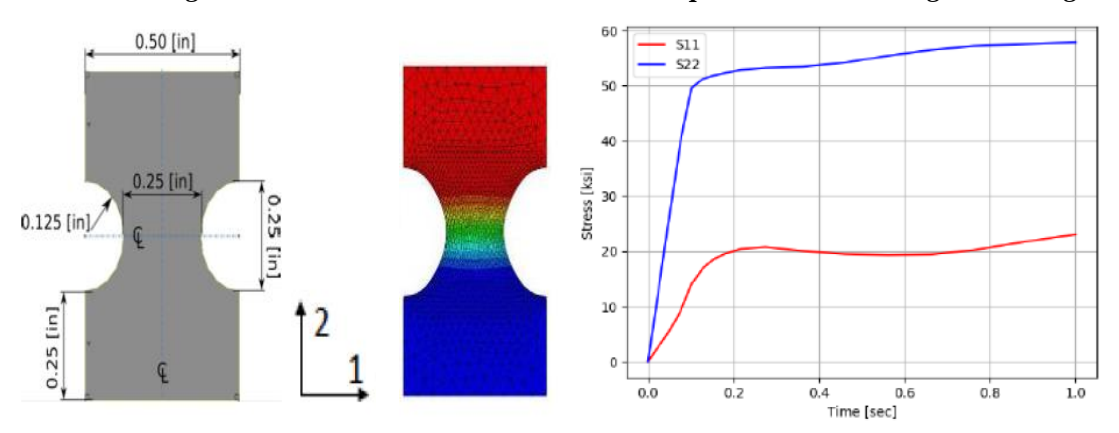


Figure 7.2.1.1-7. The small-scale coupon (left) geometry (middle) displacement contour under uniaxial load and (right) the resulting horizontal (S11) and vertical (S22) components of stress.

The reduced size of the coupons (e.g relative to ASTM E8 standard coupons cut from sheet material) required special considerationsfor the design of these tests: (1) Increased magnification was required to acquire requisite DIC data, and (2) extended grips were required to provide space between the hydraulic grips such that the coupon could be observed during tests. A detailed description of the developed test setup for the small-scale coupon is provided in Appendix G.

7.2.1.3 Small – Scale Tensile Tests

Tensile tests were performed on sub-sized coupons from both liner and rolled sheet material. The tests were conducted under displacement control with a displacement rate of 0.1 inch/minute. The reaction force was acquired from the load cell, and was used to compute the engineering stress at the center of the gage length. DIC images were captured at 200 ms intervals and a virtual extensometer was used to measure the strain, as illustrated in Figure 7.2.1.1-8. The biaxial stress state of the small-scale coupons was expected to slightly increase (~10%) the yield and ultimate strengths of the material over that measured in uniaxial tests. This biaxial effect could be accounted for using FEA to determine an equivalent uniaxial stress-strain relationship. However, the objective of these tensile tests was to determine any major differences in this

relationship upon comparing the behavior of liner and sheet materials. Next, results of the AA6061-T6 and IN718 coupon tests are discussed separately.

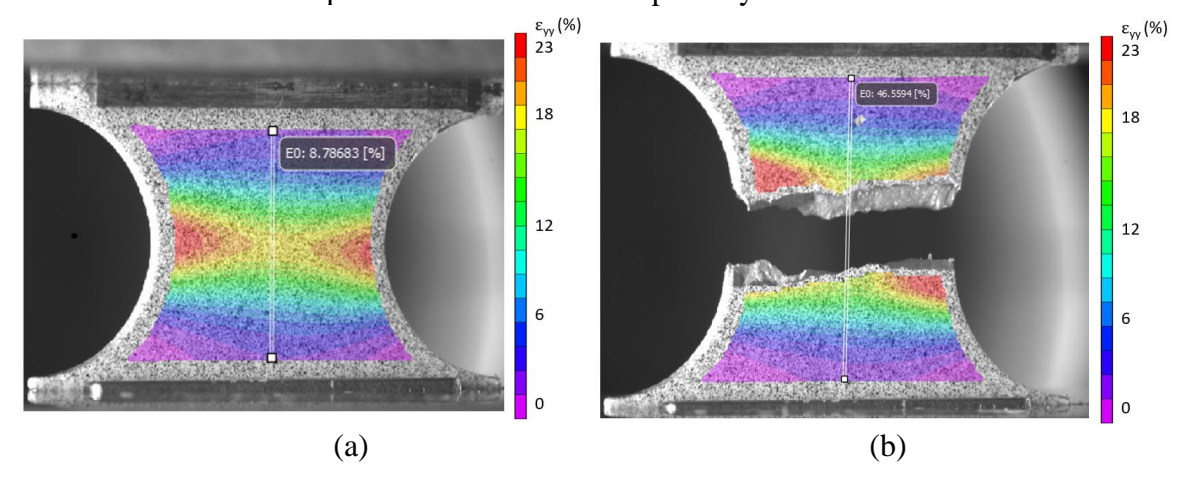


Figure 7.2.1.1-8. DIC results with virtual strain gage during testing (a) edge localization effect and (b) failed coupon.

Tensile testing of AA6061-T6 demonstrated similar behavior in the 0.032-inch thick small-scale liner and sheet coupons. Four coupons from the liner and two from the sheet were tested. As shown in Figure 7.2.1.1-9 the sheet material coupons, A3 and B3, enveloped the test results from the liner material: C7 and C8 (dome microstructure), C22 and C23 (cylinder microstructure). While this represents an insufficient data set to draw correlations or statistical conclusions, it is worthwhile noting that the C22 and C23 coupon results (both characterized by cylinder microstructure) were closely grouped and the C7 and C8 coupons were not as closely grouped, as expected due to the significantly larger grain size (with respect to coupon thickness) in the dome. Even though this is a small data set, it served to demonstrate that tensile testing, alone, does not raise any concern regarding any variation in behavior between the dome, cylinder, and sheet material. Further, the measured stress-strain relationship was in good agreement with measured structure scale tensile data, after accounting for the biaxiality of the small-scale coupons. Structure scale tensile data are included in Appendix D. In addition to the tensile tests, fatigue crack growth tests were performed, as described in Section 7.2.1.4.

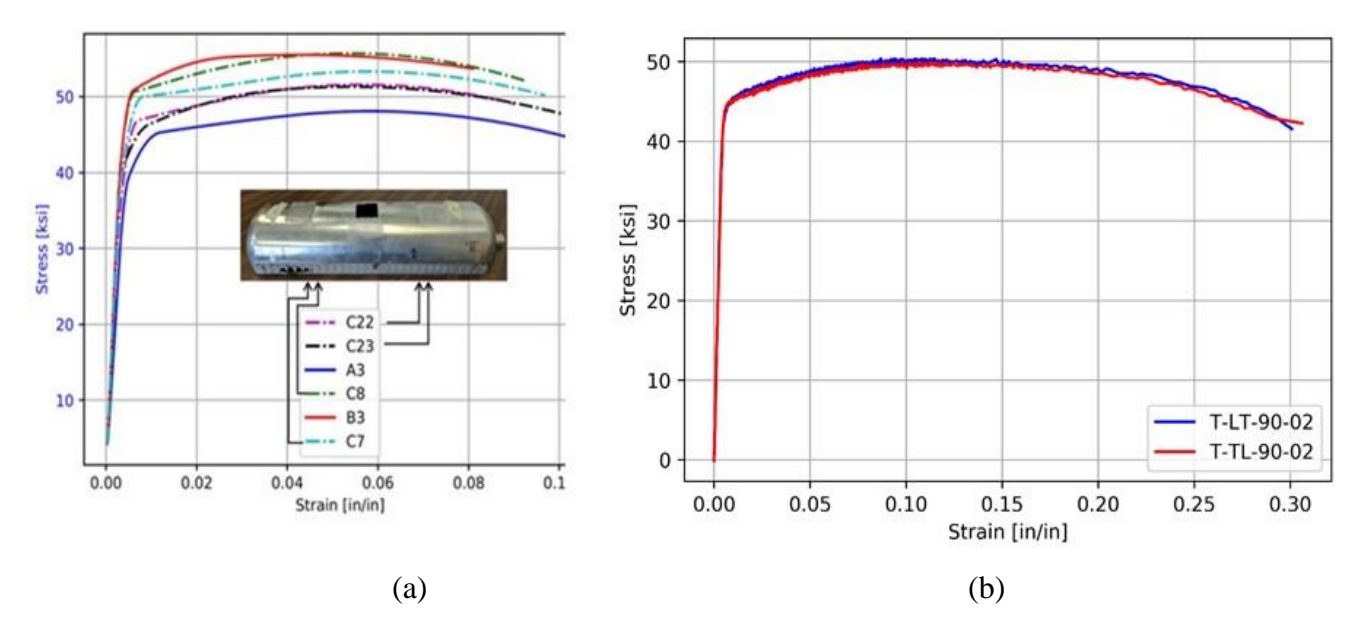


Figure 7.2.1.1-9. (a) Tensile test results for small-scale liner and sheet coupons. (b) Uniaxial tensile data for similar material and heat-treatment available in Appendix D.

Small-scale IN718 coupons were extracted from the domes of two liners, #34 and #35, and from three orientations in each dome: radial, axial, and tangential directions. In all cases, the extracted coupons were nominally 0.032-inch thick. Multiple measurements of the width and thickness were taken for each tested coupon to understand the effect this uncertainty had on the reported stress results. From these repeated measurements, a $\pm 3\%$ variation was found as indicated by the vertical error bars in Figure 7.2.1.1-10, showing this uncertainty does not have a significant effect on the reported results.

In each of the results to follow, solid lines indicate results from liner #35 coupons and dashed lines indicate #34 coupons: axial coupons are shown in green, radial coupons are shown in blue, and tangential coupons are shown in red. Figure 7.2.1.1-11, illustrates the combined results of all small-scale IN718 testing. From this combined result, it is clearly seen that coupons from the #35 liner in the radial direction have reduced yield and and ultimate strengths, as shown in Figure 7.2.1.1-12. Figure 7.2.1.1-12a clearly shows this reduction of yield strength for the #35 radial coupons. Furthermore, this observation holds true in Figures 7.2.1.1-13 and 7.2.1.1-14, corresponding to the ultimate strength and modulus, respectively.

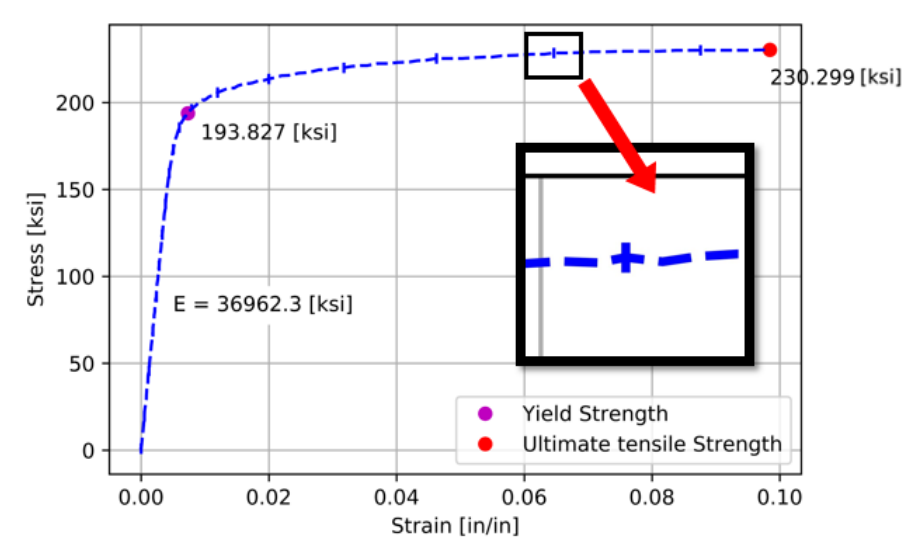


Figure 7.2.1.1-10. Engineering stress-strain curve with uncertainty bars for small-scale IN718 tensile test.

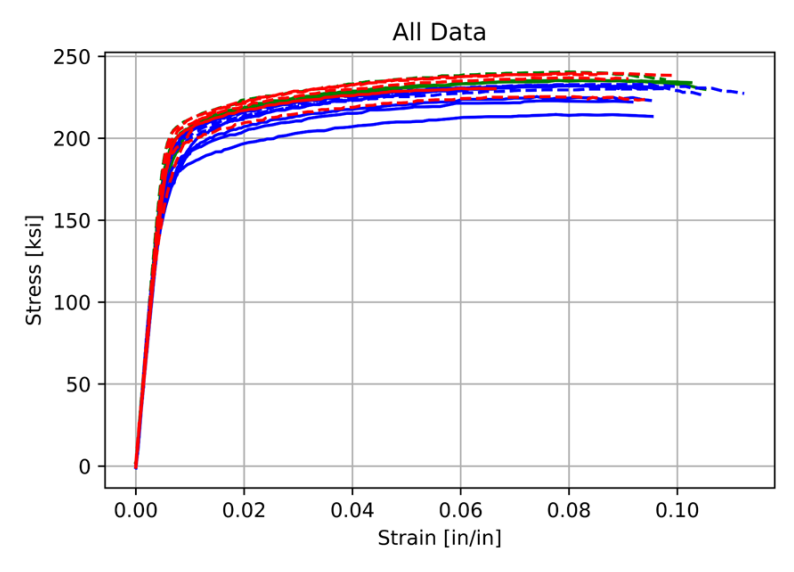


Figure 7.2.1.1-11. Engineering stress-strain curve for all IN718 tensile tests.

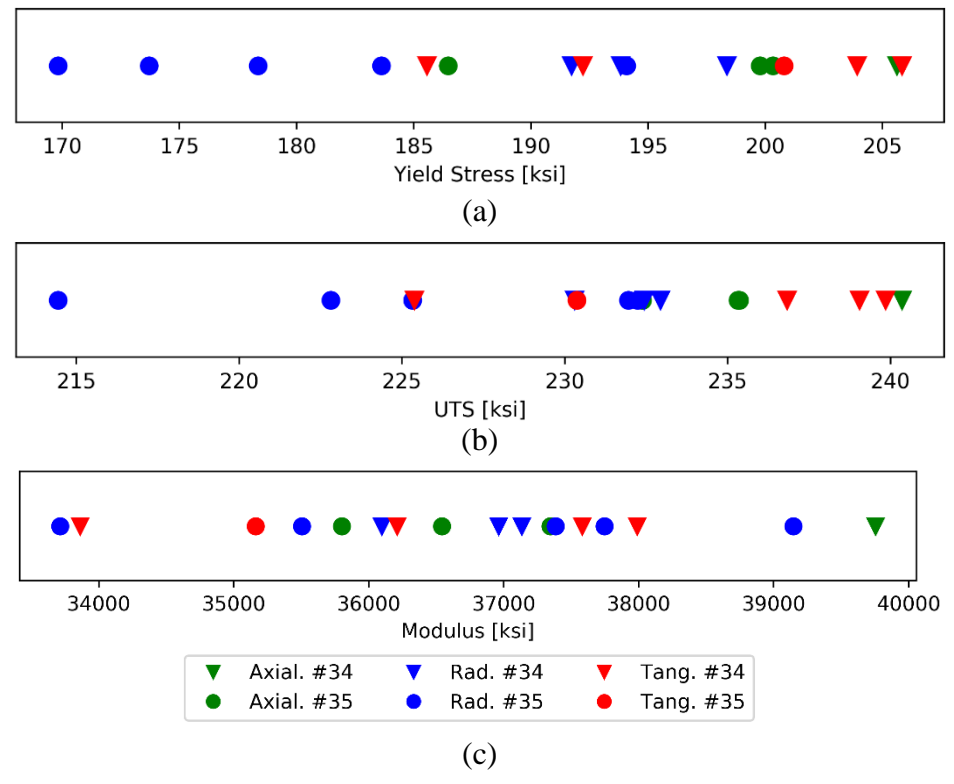


Figure 7.2.1.1-12. Line plots for summarizing the IN718 tensile test results for (a) yield stress, (b) ultimate tensile strength, and (c) modulus.

7.2.1.4 Small-Scale Fatigue Crack Growth Tests

This section provides results and example plots to illustrate data processing. The full test and analysis procedure is provided in Appendix H.

AA6061-T6 Fatigue Crack Growth Results

The image in Figure 7.2.1.1-13 shows a post-mortem fracture surface of a 0.032-inch thick AA6061-T6 coupon with the initial precrack a=0.0194 inch and the final fatigue a=0.0233 inch. Similarly, the image in Figure 7.2.1.1-14 shows a post-mortem fracture surface of a 0.140-inch thick AA6061-T6 coupon with the initial a=0.0395 inch and the final fatigue a=0.0878 inch. The crack shape at the end of precracking is clearly demarcated by the Sharpie[®] pen marker that was pressed into and allowed to dry on the crack surface, following the procedure identified in Section 7.1.1.1. The final crack shape is clearly demarcated by the change in surface morphology: from fatigue crack to ductile failure. These lengths were obtained either in a scanning electron microscope or an optical microscope. In all of the small-scale fatigue crack growth tests, the initial precrack a/c was consistently around a/c=1 and ended at a/c=0.9.

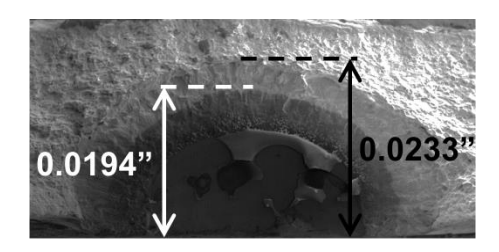


Figure 7.2.1.1-13. Thin AA6061 coupon fracture surface with measurements of initial and final crack depths.

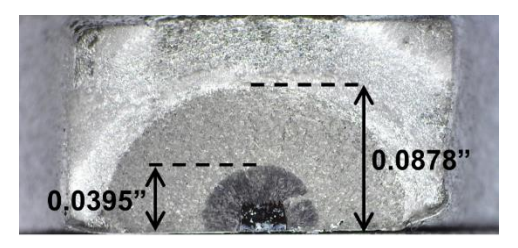


Figure 7.2.1.1-14. Thick AA6061-T6 coupon fracture surface with measurements of initial and final crack depths.

Next, Figure 7.2.1.1-15 illustrates a *CMOD* vs. cycle count, *N*, data that was obtained from a thin AA6061-T6 coupon using DIC and the virtual strain gage illustrated in Figure 7.2.1.1-15. The red data points in Figure 7.2.1.1-15, indicate where there were known values for *a* (i.e., after precracking and at conclusion of test, c.f. Figure 7.2.1.1-14), see Figure 7.2.1.1-13. In each of the small-scale tests a simliar nonlinear relationship between *CMOD* and *N* was determined.

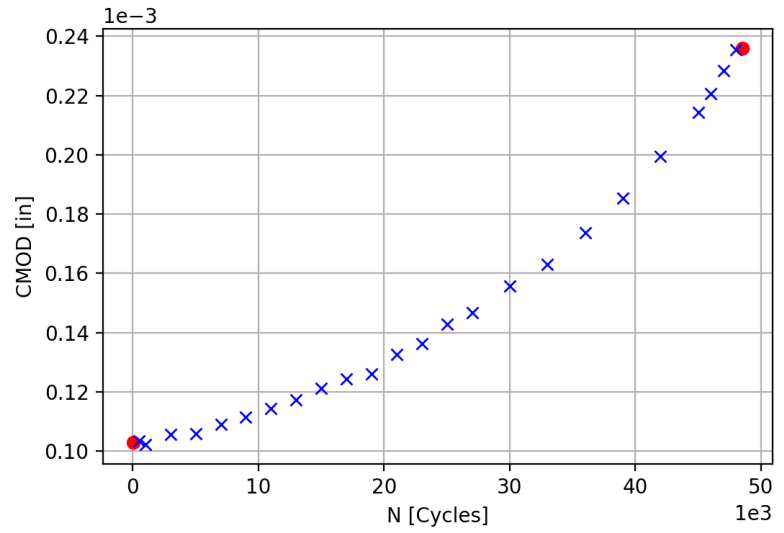


Figure 7.2.1.1-15. Analyzed CMOD from the virtual gage at periodic cycle counts during the test.

Recall that for each test, two data points for a are obtained and CMOD data are obtained at the same cycle counts. Consequently, 14 data points for a vs. CMOD from seven thin AA6061-T6 coupon tests are illustrated in Figure 7.2.1.1-16. Similarly, 10 data points obtained for a vs. CMOD from five thick AA6061-T6 coupon tests are illustrated in Figure 7.2.1.1-17. The target a/c for each test was a/c = 1, but a variation was observed. From these data, one of two possible

approaches can be taken. First, a single linear fit can be made to these data and applied to the post-processing of da/dN for each coupon. Alternatively, a linear fit can be made for each individual test and applied to the post-processing of da/dN for each coupon. In the results presented here, the latter approach was chosen for the thick AA6061-T6 coupons because the variation in a/c influenced the CMOD and resulted in the large scatter.

The da/dN vs. ΔK data for thin AA6061-T6 coupons in Figure 7.2.1.1-18 were obtained using the data in Figures 7.2.1.1-15 and 7.2.1.1-16, along with numerical differentiation from the moving 5-point Lagrange polynomial. A clear distinction is visible where growth rates in coupons extracted from the liner cylinder (C9, C12, and C20) are significantly higher than coupons extracted from the dome (C2), as seen in Figure 7.2.1.1-18. This observation is in agreement with observations made during a preliminary round of testing that imposed higher ΔK values, and were more indicative of autofrettage strain levels.

The da/dN vs. ΔK data in Figure 7.2.1.1-18 for the 0.14-inch thick AA6061-T6 coupons was obtained in an analogous manner to the 0.032-inch thick AA6061-T6 coupon data. However, for the thick AA6061-T6 case, coupons were only extracted from the dome and consequently, no similar comparison between cylinder and dome could be made. Coupons were extracted in two orientations, axial (AX) and circumferential (C), and there was no discernible difference in growth rates between these two sets of growth rate data.

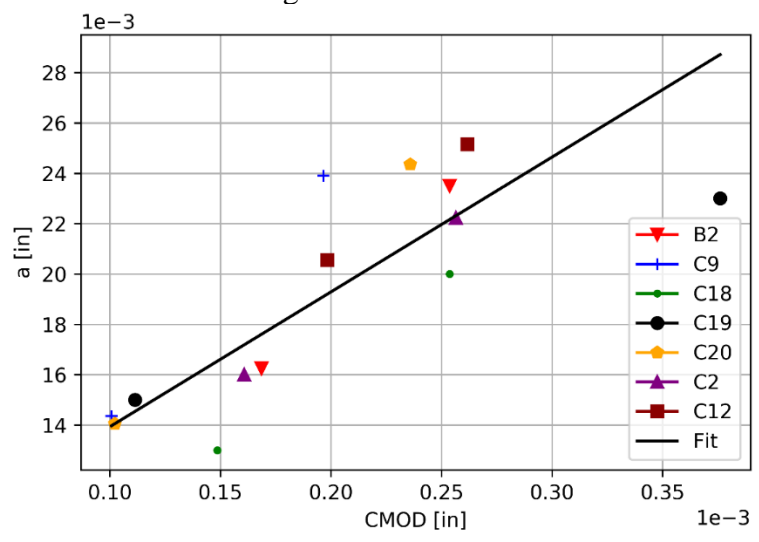


Figure 7.2.1.1-16. Thin AA6061 aggregated initial and final as with corresponding CMOD.

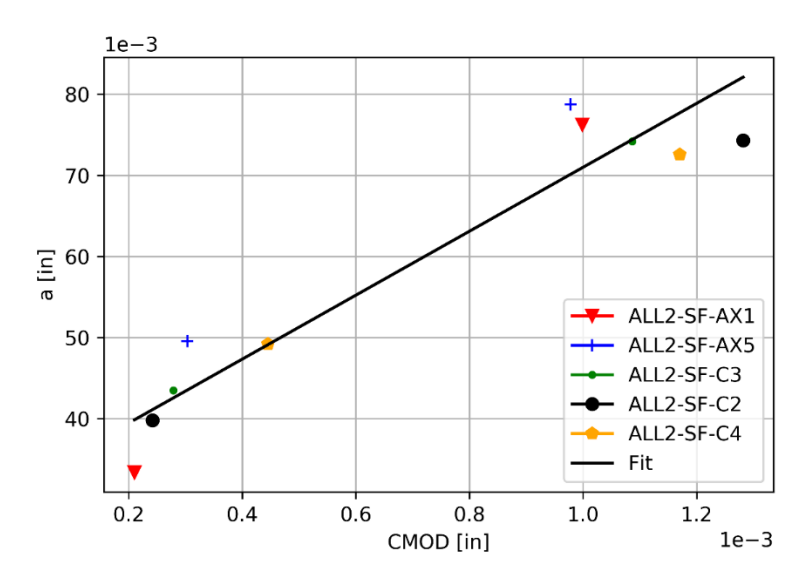


Figure 7.2.1.1-17. Thick AA6061 aggregated initial and final as with corresponding CMOD.

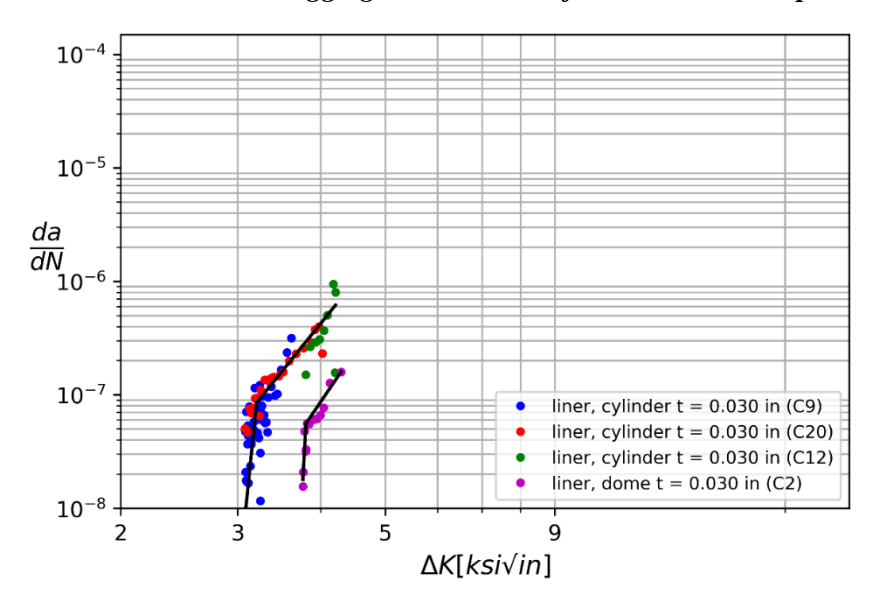


Figure 7.2.1.1-18. Thin AA6061 processed crack growth data.

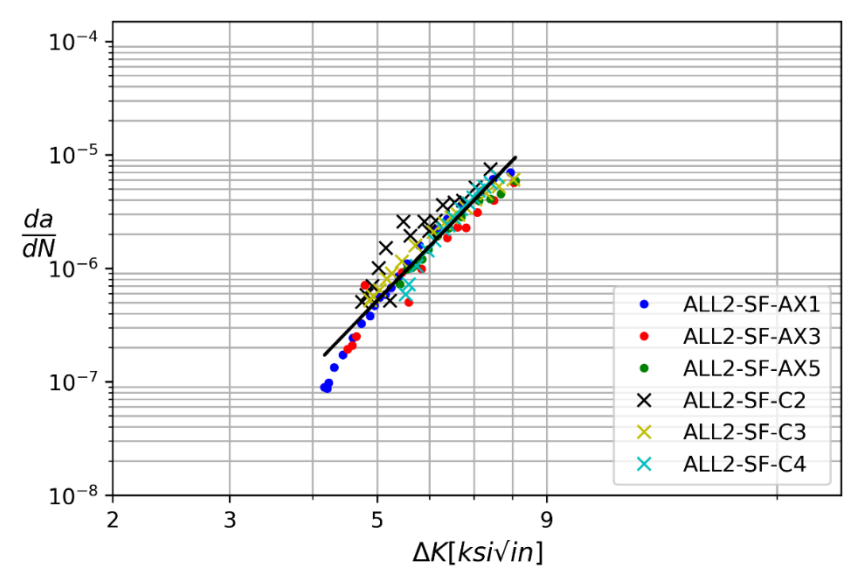


Figure 7.2.1.1-19. Thick AA6061 processed crack growth data.

Finally, Figure 7.2.1.1-20 contains all of the *da/dN* vs. ΔK data from the small-scale AA6061-T6 liner coupons presented above. The figure also includes results from small-scale and large-scale sheet data. The results demonstrated that all AA6061-T6 coupon data, except for the liner cylinder coupons, have similar crack growth rates. However, even for the liner cylinder coupons, the major difference is near threshold and several of the large-scale coupon results overlap with the small-scale cylinder data. Additional coupon data and uncertainty quantification would be required to make a more quantitative distinction among materials at this near-threshold initiation stage. However, differences in crack growth mechanism, among the small-scale coupons were observed. This further motivates understanding the effect of microstructure variation. First, it was observed that coupons extracted from the cylindrical region demonstrated intergranular (along grain boundaries) crack growth while transgranular (across grain boundaries) occurred in the dome regions. Additionally, it was often observed that secondary cracking, as seen in Figure 7.2.1.1-21, occurred in the dome and cylinder regions of the liners, but not in the rolled sheet coupons. Such changes in mechanism are likely underlying causes for any disparities in crack growth rates.

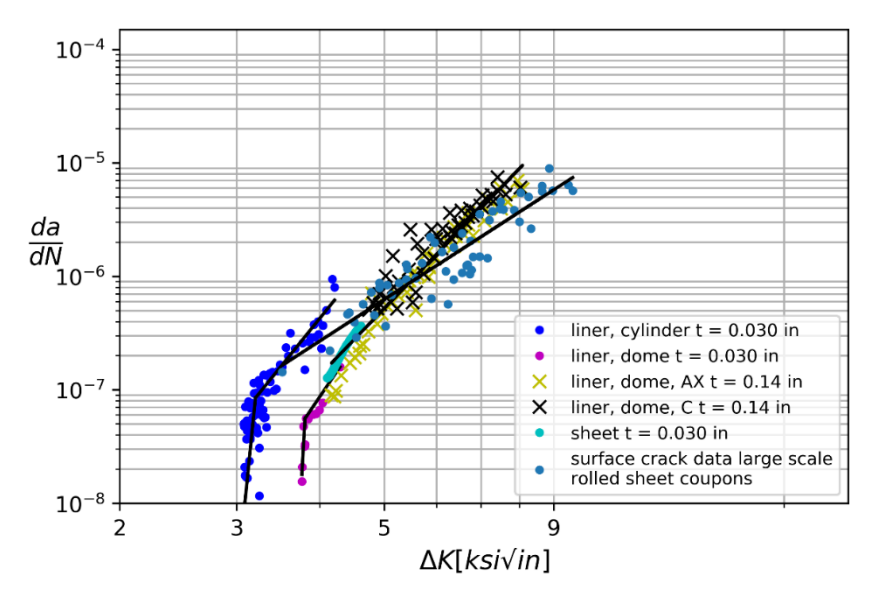


Figure 7.2.1.1-20. All AA6061-T6 processed crack growth data with large-scale surface crack results.

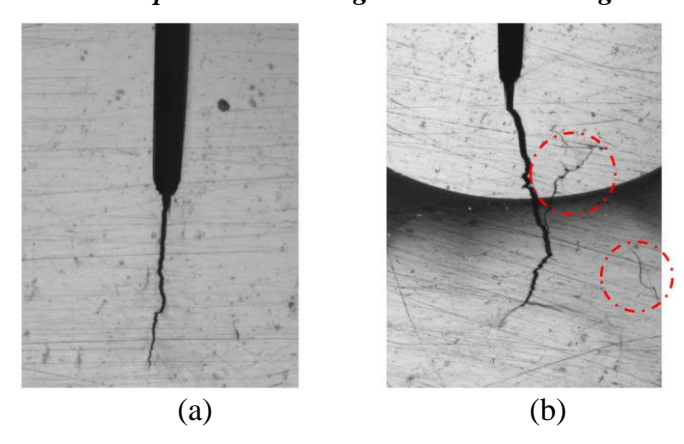


Figure 7.2.1.1-21. AA6061-T6 fatigue crack growth observations from (a) rolled sheet and (b) AA6061-T6 liner.

IN718 fatigue crack growth results

Coupon testing and data processing of the IN718 coupons followed the same procedure outlined above. Similar to the AA6061-T6 coupons, the Sharpie® pen ink method for demarcating the initial crack shape worked well on the IN718 coupons, See Figure 7.2.1.1-22. Also, the transition in fracture surface morphology from fatigue cracking to ductile failure clearly demarcated the final crack shape.

Throughout the test, CMOD vs. *N* data were acquired, see Figure 7.2.1.1-23 where the two red data points indicated known corresponding values for the *a* (initial and final). These initial and final *a* were used along with the corresponding CMOD data to generate the data illustrated in Figure 7.2.1.1-24. Figure 7.2.1.1-25 illustrates the resulting da/dN vs. ΔK data from the IN718 coupons extracted from the dome of liner #35. This result indicates that the crack growth rates are independent of the orientation that the coupon was extracted from the liner as the radial, axial, and tangential results are closely grouped. However, this is not the case for the liner #34 data, illustrated in Figure 7.2.1.1-26. In this case, each orientation experienced significantly

disparate crack growth rates, and none of them matched the behavior of liner #35 (shown in the same figure for comparison).

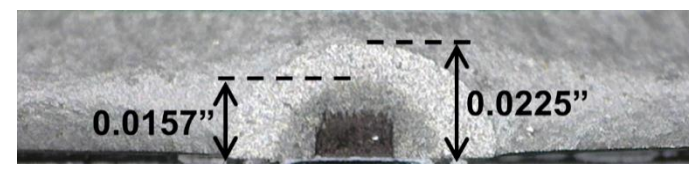


Figure 7.2.1.1-22. Thin IN718 coupon fracture surface with measurements of initial and final crack depths.

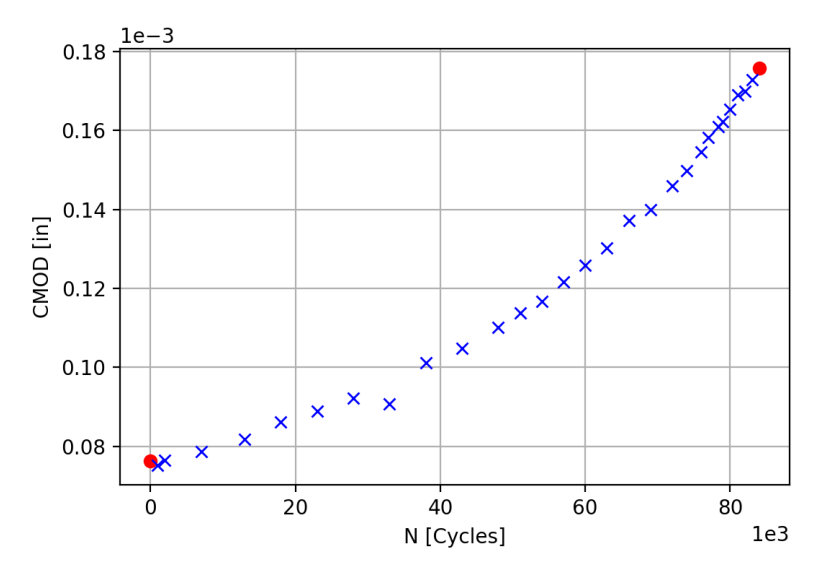


Figure 7.2.1.1-23. Analyzed CMOD from the virtual gage at periodic cycle counts during the test.

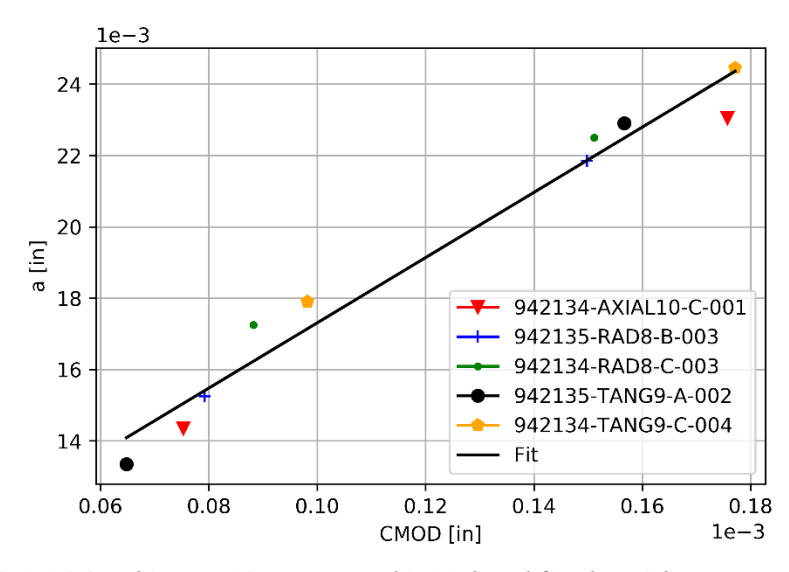


Figure 7.2.1.1-24. Thin IN718 aggregated initial and final a with corresponding CMOD.

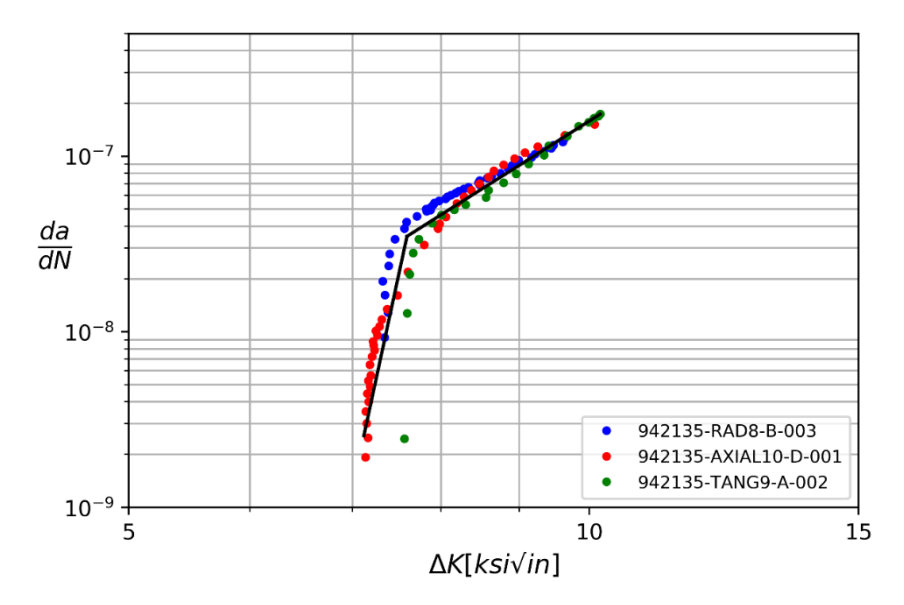


Figure 7.2.1.1-25. Liner #35 IN718 processed crack growth data.

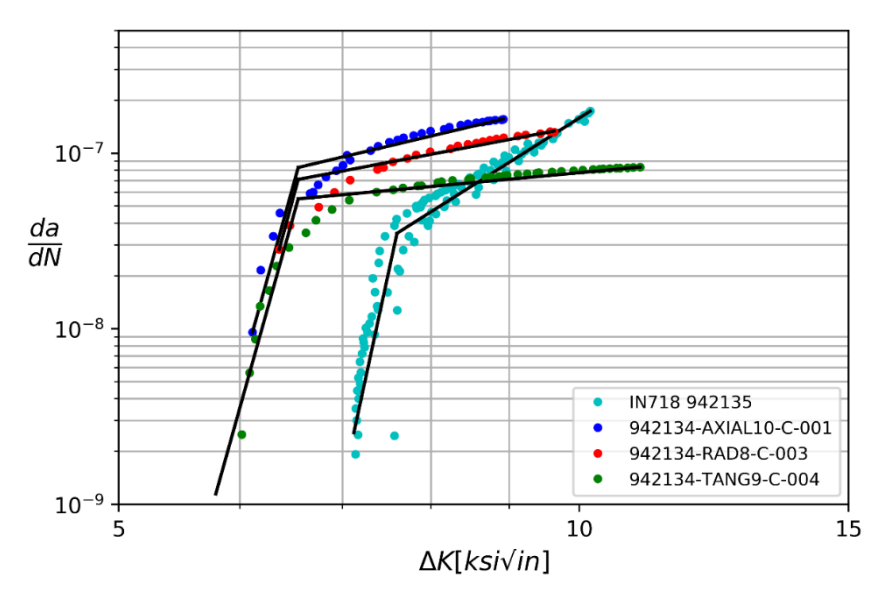


Figure 7.2.1.1-26. All IN718 processed crack growth data.

In summary, microstructure variations throughout a tank or liner should be expected to be significant, given the presently used materials and processing methods. However, these variations do not necessarily imply conformance nor disparity with mechanical behavior of more standard product forms, such as rolled sheet materials or amongst various locations within the liner. Microstructure variation can have a significant influence and executing fatigue crack growth tests are the only current way to quantify any impact on damage tolerance. As demonstrated for the thin AA6061-T6 coupons, tensile testing for the sake of demonstrating equivalence of stress-strain behavior is not adequate to understanding fatigue crack growth behavior. Finally, a main point of concern upon introducing a new material or process for these structures should be the identification of crack growth mechanisms. Microstructure variations will cause variability in behavior, but those that induce changes in mechanism can cause entire shifts in the behavior that must be understood through testing and observation.

- **F-5.** Microstructure variations are observed between different COPV liner regions, and between liner and rolled sheet material.
- **F-6.** In comparing material regions of different microstructure, fatigue crack growth tests quantified impact of damage mechanism to damage tolerance life (i.e., da/dN) while microscopy and tensile tests did not.

7.2.2 Autofrettage Crack Growth Tests

The first cycle applied to a COPV is intended to be the highest pressure that the vessel will ever experience. This cycle is called the autofrettage and is at a pressure that will cause the metal liner to yield, but the overwrap composite remains elastic. Post-autofrettage, the metal liner will experience compressive hoop stresses at zero pressure. The subsequent operating pressure cycles will result in a peak liner tensile stress that is reduced over what would have been generated without the autofrettage cycle. One objective of the autofrettage cycle is to increase the fatigue life of COPVs without preexisting cracks [ref. 12]. The damage tolerance requirements for flight COPVs [ref. 3] requires that the largest crack that can be missed by the NDE inspection must survive four service lifetimes without "sustained load crack growth, detrimental deformation, leakage, or rupture." COPVs are considered elastically responding if all of the operational cycles, other than the autofrettage cycle, remain elastic. The autofrettage cycle is elastic-plastic and must be assessed using EPFM analyses or through experimental measurements.

The objectives addressed in this section are:

- (1) develop techniques for the experimental measurement of the amount of crack growth during autofrettage,
- (2) provide experimental measurements of crack growth during autofrettage for commonly used COPV liner materials (AA6061-T6, IN718, and Ti Al-4V), and
- (3) provide experimental measurements to determine if 4 repeated autofrettage cycles result in more or less crack growth than the amount of crack growth in a single autofrettage cycle multiplied by a factor of 4.

LEFM damage tolerance life assessments of COPVs require that the amount of crack growth during autofrettage be measured or estimated. Thus, the results of this study can be used to design and conduct tests to determine the amount of crack growth during the autofrettage cycle of a specific tank. Alternatively, the data generated could be used to estimate of the amount of autofrettage crack growth for tanks with liners manufactured with the materials evaluated or to validate EPFM analyses.

7.2.2.1 Autofrettage Crack Growth Measurement Approach

This section will discuss the experimental techniques developed to characterize the crack growth during the elastic-plastic autofrettage cycle and provide examples of the measured crack growth. Tests were conducted on uniaxial coupons subjected to simulated autofrettage cycles. The crack growth during autofrettage was determined by SEM examination of the separated post-test fracture surfaces. The commonly used COPV liner materials of AA6061-T6, Ti 6Al-4V, and IN718, were examined. The results of this study can be used to provide improved estimates of the elastic-plastic autofrettage crack growth for COPV damage tolerance life qualification.

Single Cycle Autofrettage Measurements

The single cycle autofrettage measurements were made using test coupons, as illustrated in Figure 7.2.2-1. The AA6061-T6 and IN718 coupons were extracted from flat sheets with a 2-inch width. The Ti 6Al-4V coupons were extracted from the COPV liner dome region and machined flat (i.e., the liner geometry limited the coupon size). The Ti 6Al-4V coupon width was 0.5 inch for the semi-circular cracks (i.e., a = 0.025 inch and 2c = 0.05 inch, or a/c = 1) and 1-inch wide for the coupons with long, shallow cracks (a = 0.0125 inch and 2c = 0.125 inch, or a/c = 0.2). The effect of coupon width on crack behavior was modeled and is detailed in Appendix C. It was found that CMOD and J converged to <1% at a width of 9 times the precrack 2c.

F-7. A test coupon width of 9 x precrack 2c mitigates edge on crack growth behavior (i.e., CMOD and J convergence to <1%).

Cracks were introduced into the center of the coupons by creating small (i.e., \sim 0.02 inch by 0.01 inch) notches using lasers or EDM. The notched coupons were fatigue cycled at a peak stress that was no more than 80% of the material tensile yield and R = 0.1. The cyclic frequency was 5 to 10 Hz. Fatigue cracks under tensile loading tend to grow to a/c = 0.8 to 1.2. The AA6061-T6 and IN718 coupons tended to develop cracks with an $a/c = \sim$ 1, but the cracks in Ti 6Al-4V coupons tended to grow more in the depth direction and had an $a/c = \sim$ 1.2. The target a was typically 0.025 inch and was obtained by growing the cracks in the AA6061-T6 coupons to a 2c= 0.05 inch. Some of the Ti 6Al-4V coupons were fatigue cycled to 2c=0.04 inch under tensile loading and loaded under three-point bend to of 2c=0.05 inch. The maximum depth region was closer to the neutral axis than the surface under three-point bend loading, so the lower stresses at the maximum depth location resulted in more crack growth at the surface than in the interior. This crack is closer to the target size and shape.

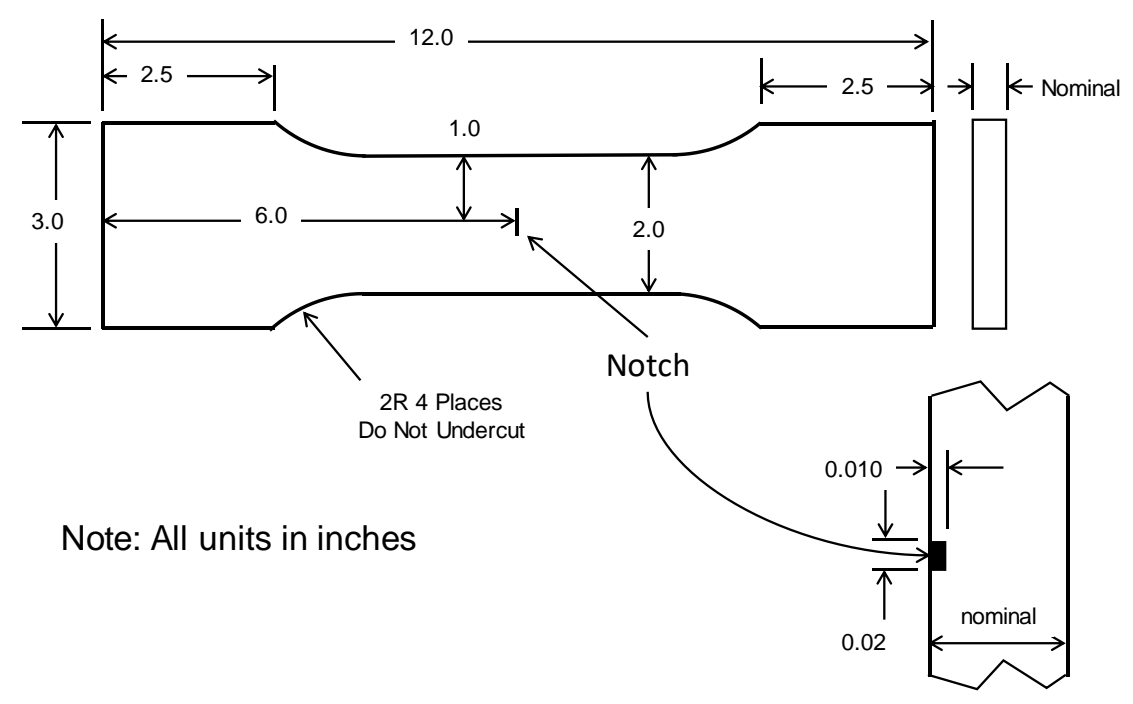


Figure 7.2.2-1. Illustration of a test coupon used for autofrettage testing.

The cracked test coupons were loaded in displacement control (i.e., 0.01 inch/minute ramp) to specific strain values for the simulated autofrettage (AF) tests. The strain measurements were made using DIC with virtual extensometers with a gage length L = 1 inch placed on the left and right edges of both the front and back surfaces, as shown in Figure 7.2.2-2. The choice of strain measurement technique and placement of the strain measurements can influence the understanding of conditions at the crack tip. An evaluation on the use of extensometers and area gages (i.e., foil gages) for strain measurements is provided in Appendix H. The results indicate the gages placed above the crack have a strong sensitivity to the distance from the crack plane while placing strain gages near the edges and in-line with the cracks would provide the most consistent strain measurements. The evaluation of edge extensometers show they produce far-field strains that are largely insensitive to the length of the extensometer.

F-8. Multiple edge physical and virtual extensometers/strain gages located at the coupon edges provide consistent far-field strain measurements.

The displacement control ramp was stopped and reversed when the desired strain level was achieved. The unloading ramp was stopped at about 70% of the previous peak load and fatigue cycled to failure at R=0.8. A fractographic examination of the failed surfaces using a SEM revealed several distinct regions: notch, elastic fatigue precracking, crack extension due to the autofrettage loading, and elastic post-cracking, as illustrated in Figure 7.2.2-3 for an AA6061-T6 test coupon to an AF strain of 1.5%.

F-9. Fracture surface (i.e., precrack, autofrettage crack growth, stable tearing, and post-cracking) regions can be distinguished with selection of precracking and post-cracking stress and R.

The AF crack growth length was determined from a higher magnification photograph of the maximum depth region of the crack, as shown in Figure 7.2.2-4 for the fracture surface shown in Figure 7.2.2-3. The results from an IN718 coupon that was tested to an autofrettage strain of 1.72% is shown in Figure 7.2.2-5, and a higher magnification photograph is shown in Figure 7.2.2-6. The results from a Ti 6Al-4V coupon that was tested to an autofrettage strain of 2.65% is shown in Figure 7.2.2-7 and a higher magnification photograph is shown in Figure 7.2.2-8. The marking of the autofrettage crack growth was generally more distinct in the AA6061-T6 fracture surfaces than in the IN718 and Ti 6Al-4V fracture surfaces.

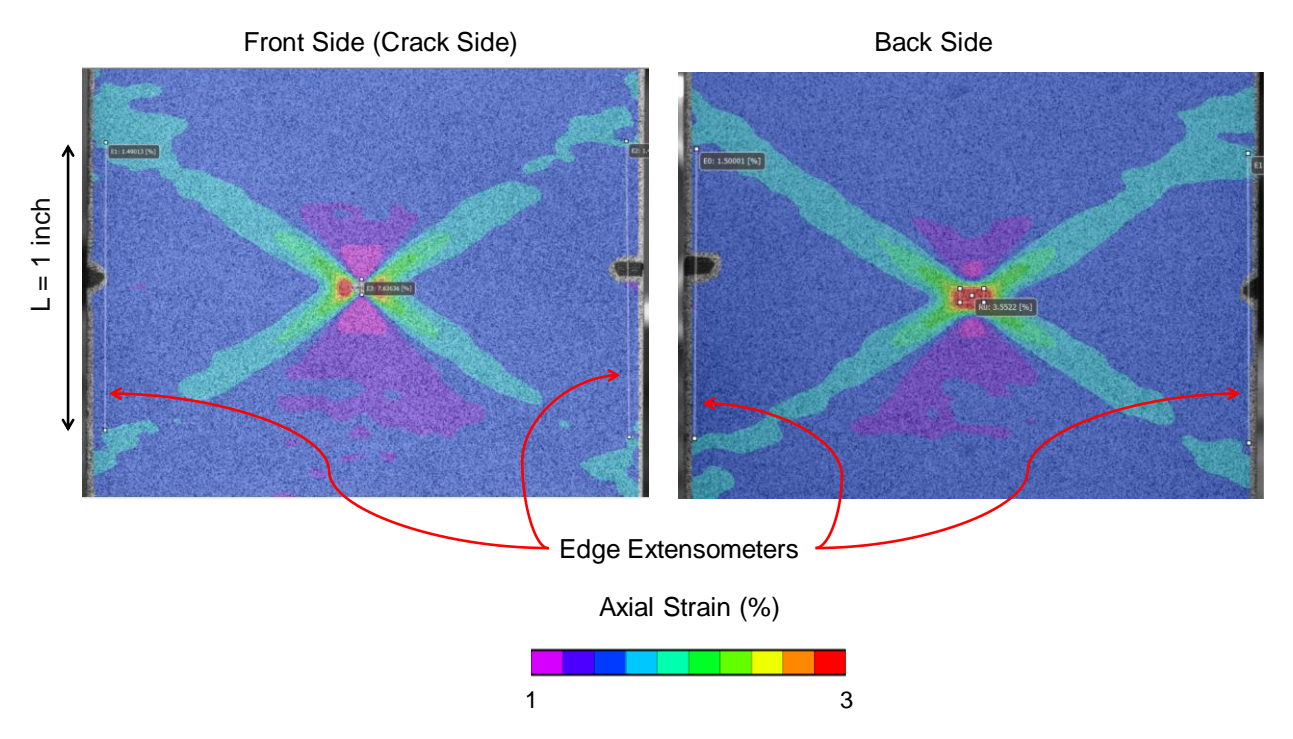


Figure 7.2.2-2. Example of strain measurements (DIC virtual extensometers on edges) for an AA6061-T6 autofrettage test at 1.5% far-field strain.

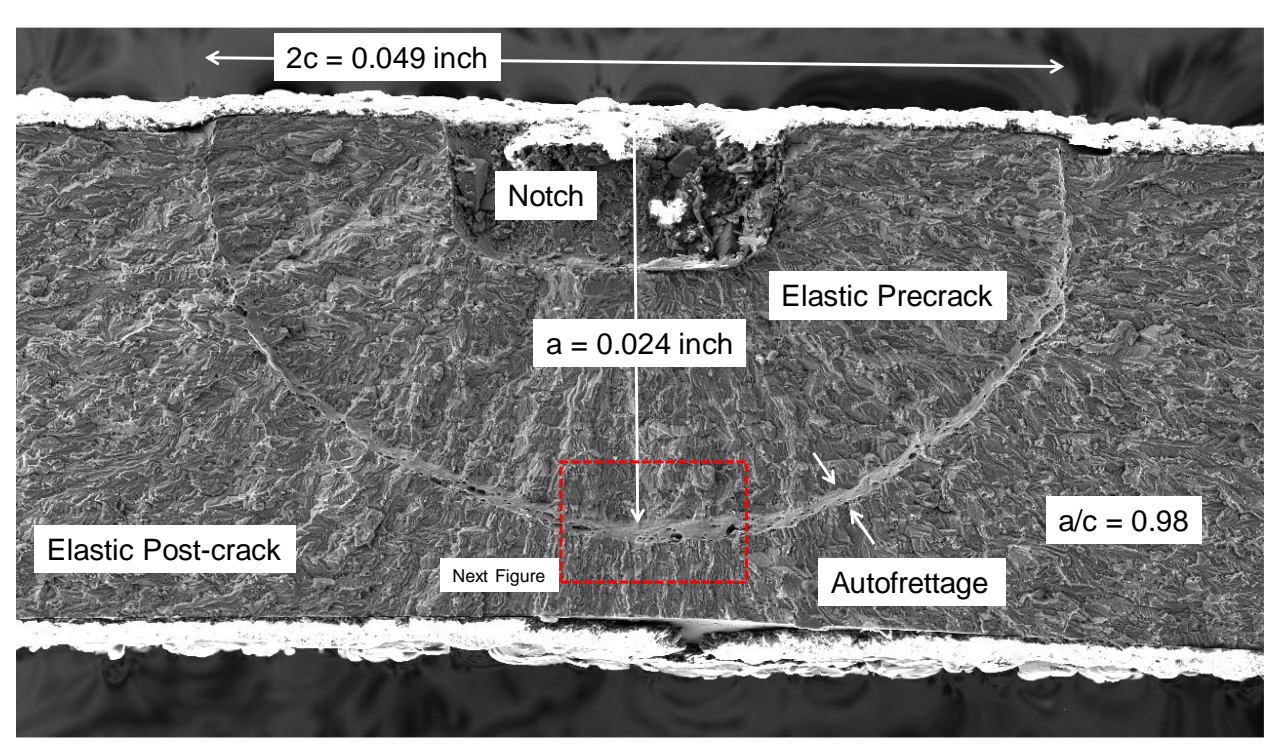


Figure 7.2.2-3. SEM photograph of the fracture surface of an AA6061-T6 single autofrettage cycle test (1.5% strain).

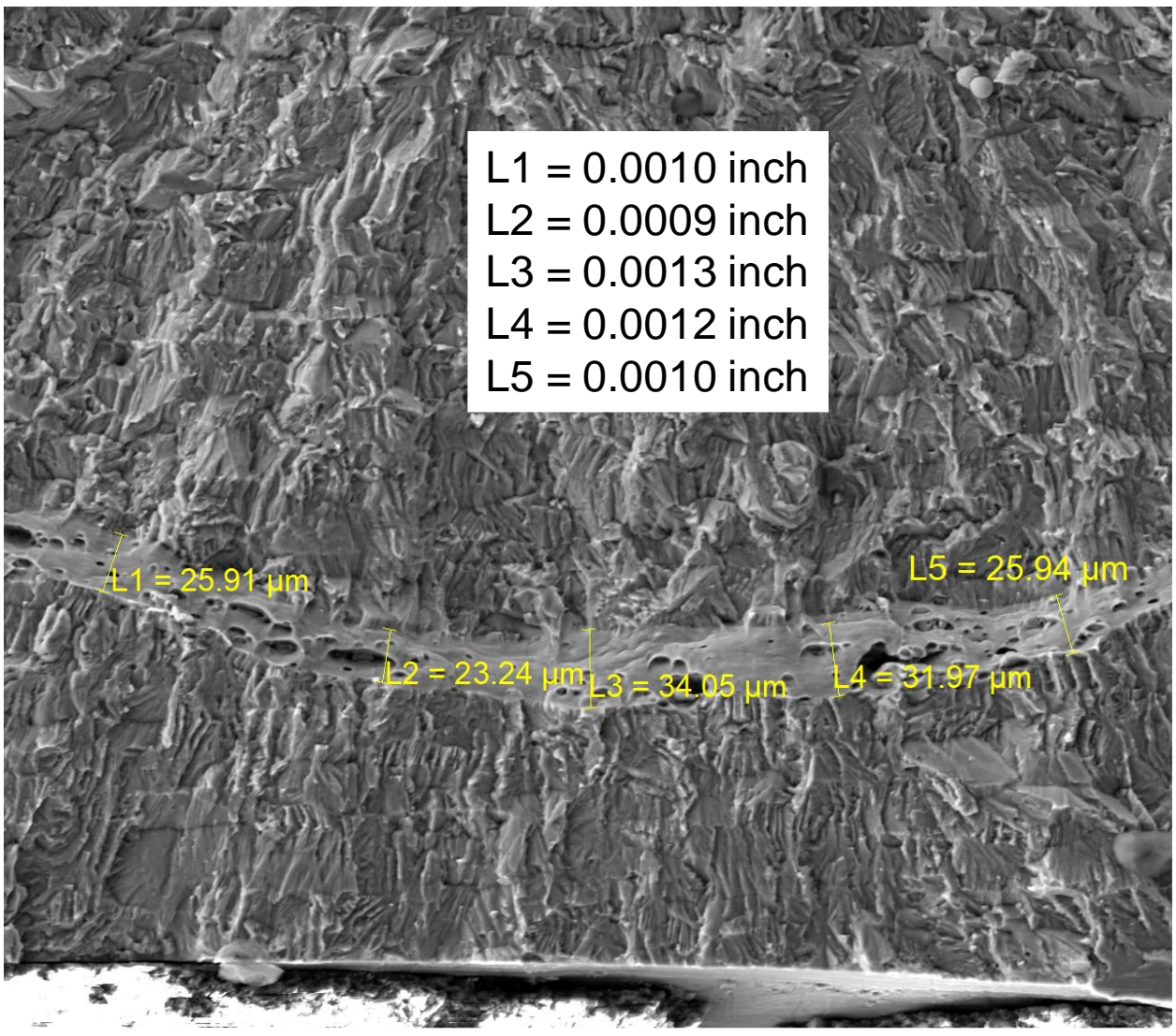


Figure 7.2.2-4. High magnification SEM photograph of the autofrettage region of an AA6061-T6 single autofrettage cycle test (1.5% strain).

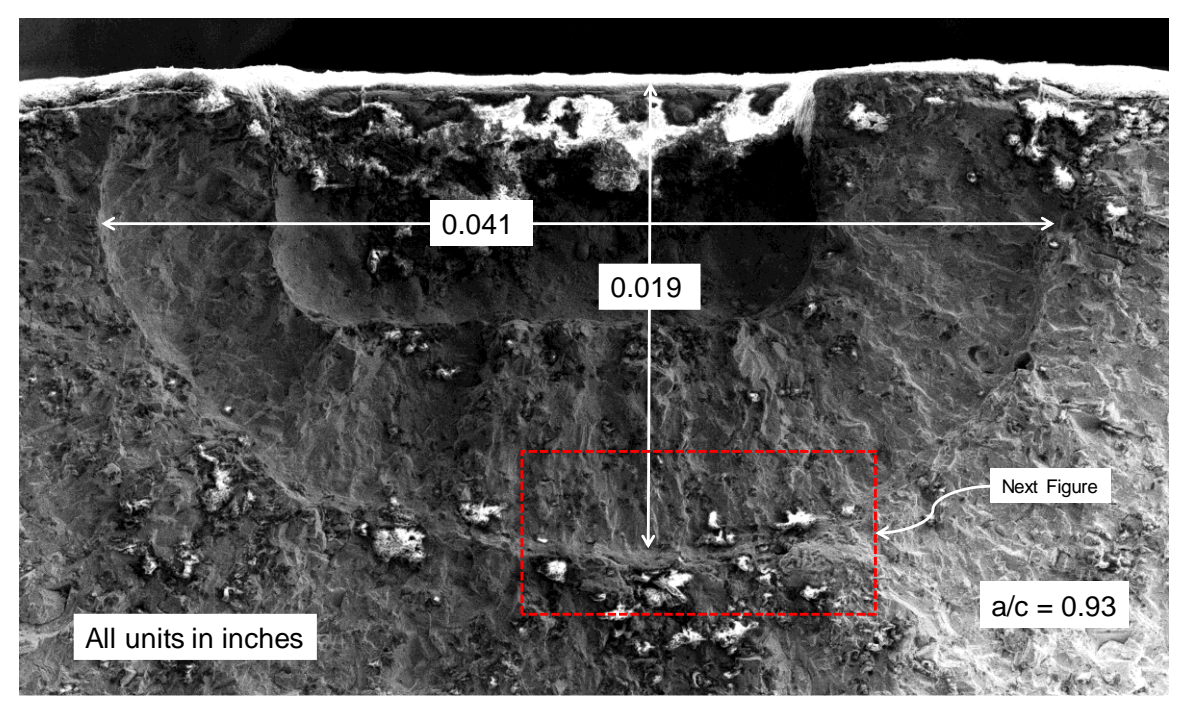


Figure 7.2.2-5. SEM photograph of the fracture surface of an IN718 single autofrettage cycle test (1.72% strain).

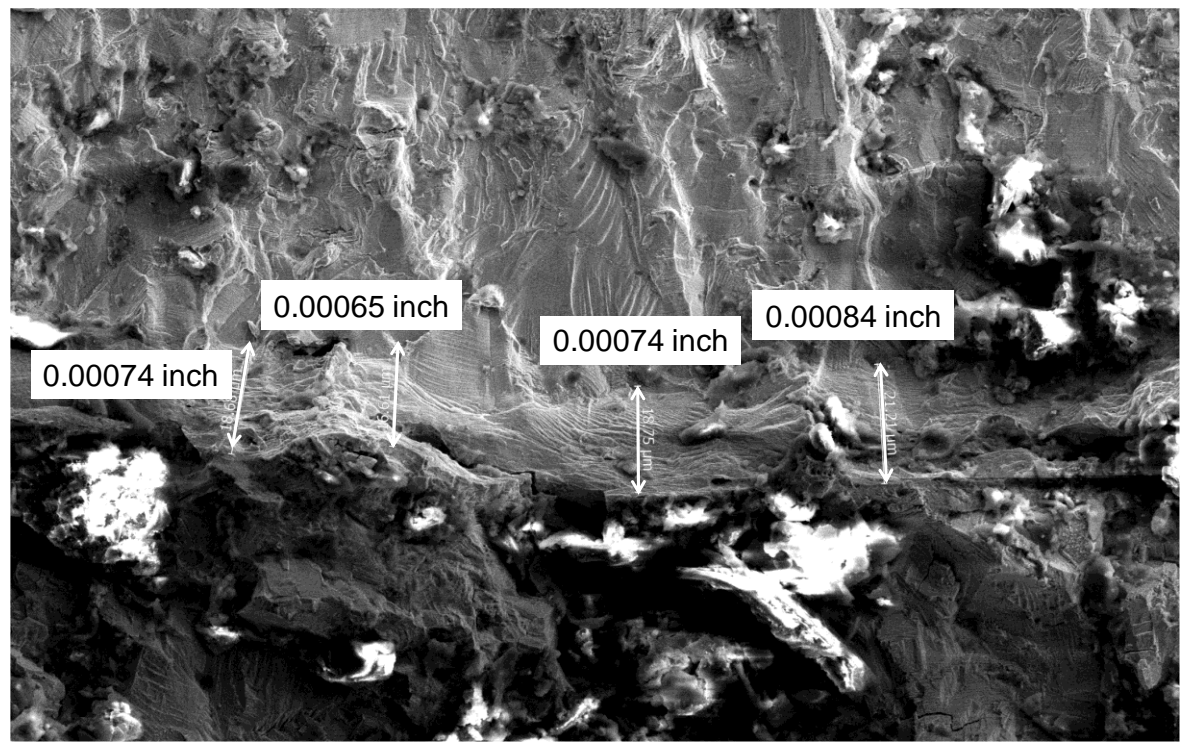


Figure 7.2.2-6. High magnification SEM photograph of the autofrettage region of an IN718 single autofrettage cycle test (1.72% strain).

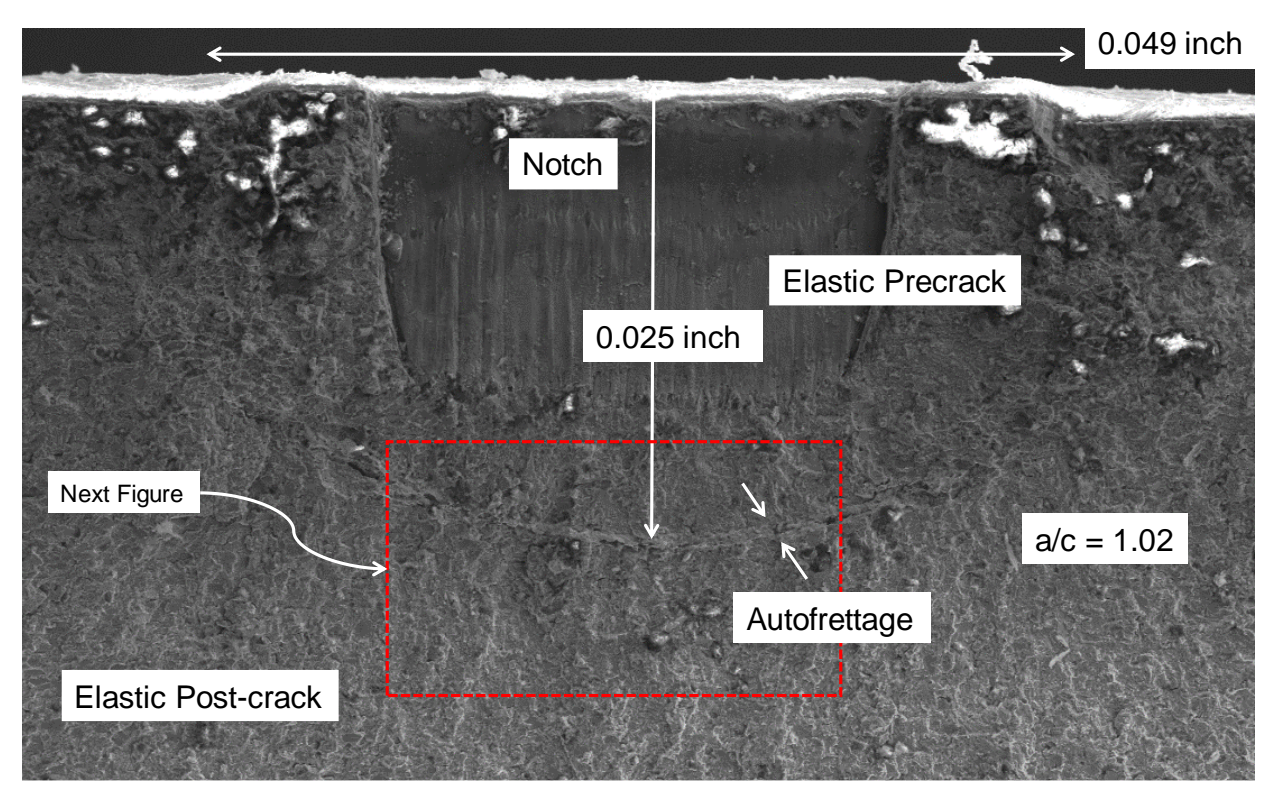


Figure 7.2.2-7. SEM photograph of the fracture surface of a Ti single autofrettage cycle test (2.65% strain).

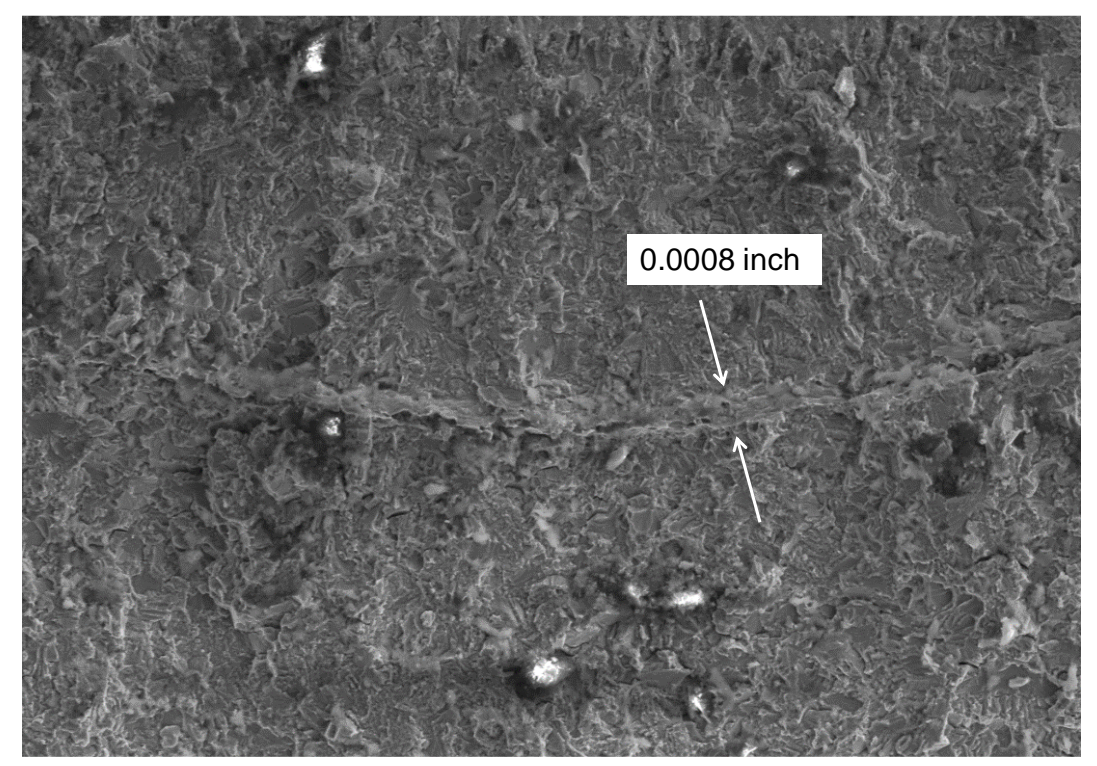


Figure 7.2.2-8. High magnification SEM photograph of the autofrettage region of a Ti single autofrettage cycle test (2.65% strain).

The ductile materials used for COPV liners appear to have two different mechanisms present during the autofrettage cycle: ductile blunting and stable tearing. Crack blunting occurs as the material at the crack tip yields and crack opens without significant crack extension. This generally appears as a narrow (<0.002 inch) region that is often near featureless. Stable tearing occurs when the crack begins to advance as the loading continues to open the crack. This generally has a ductile dimpled crack surface that is characteristically different from elastic crack growth, as shown in Figure 7.2.2-9 for an AA6061-T6 fracture surface and Figure 7.2.2-10 for a Ti 6Al-4V fracture surface.

A Wyko NT1100 Optical Profiler was used to acquire three dimensional (3D) topographical images of the fracture surfaces. The system uses non-contact interferometry to generate high resolution 3D surface measurements. Vertical scanning interferometry was used to image the fatigue crack faces. The out-of-plane resolution of this method was about 1×10^{-7} inch for a single measurement, with a scan length to 0.04 inch. Topographic measurements were made of the fracture surfaces as shown in Figure 7.2.2-11 for an AA6061-T6 coupon test shown in loaded to 1.75% strain. The topographic measurements indicate that the fatigue precrack region was relatively flat and was followed by a sharp increase in the surface height where the AF cycle was applied. The surface becomes flat again after the AF. The topography and the optical photographs of the fracture surface suggest a change in plane of crack growth as illustrated in the crack edge schematic shown in Figure 7.2.2-12.

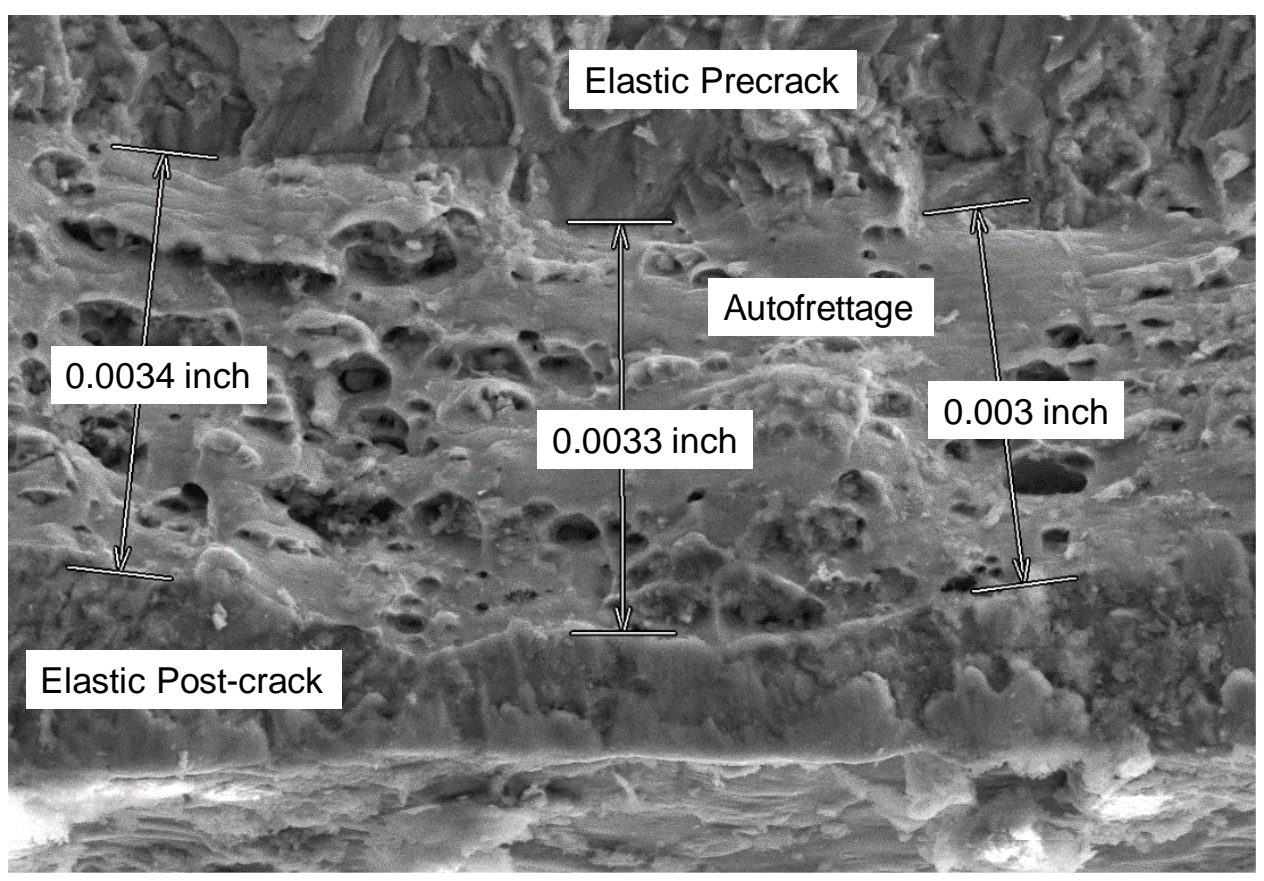


Figure 7.2.2-9. High magnification SEM photograph of the autofrettage region of an AA6061-T6 single autofrettage cycle test (2% strain).

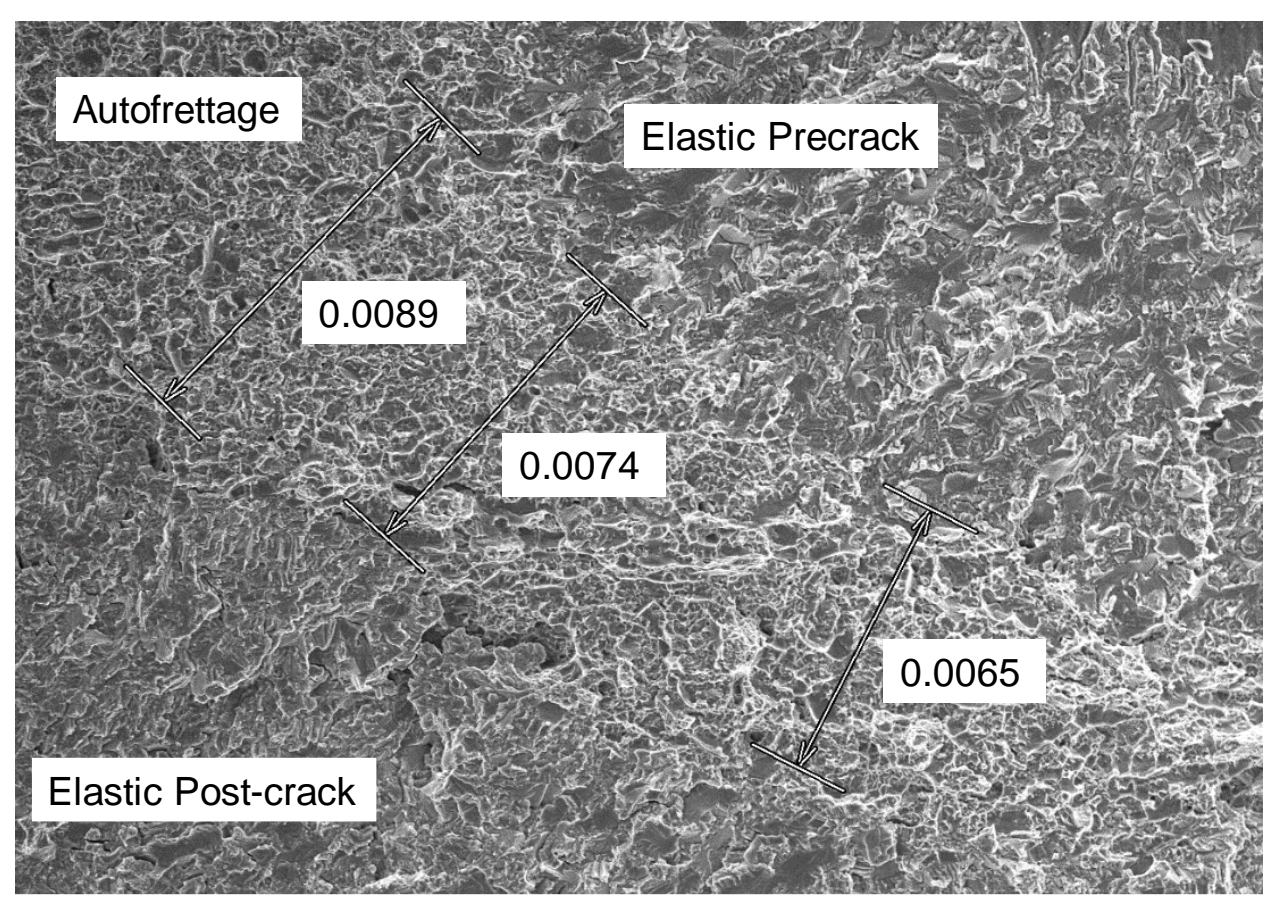


Figure 7.2.2-10. High magnification SEM photograph of the autofrettage region of a Ti 6Al-4V single autofrettage cycle test (2.65% strain).

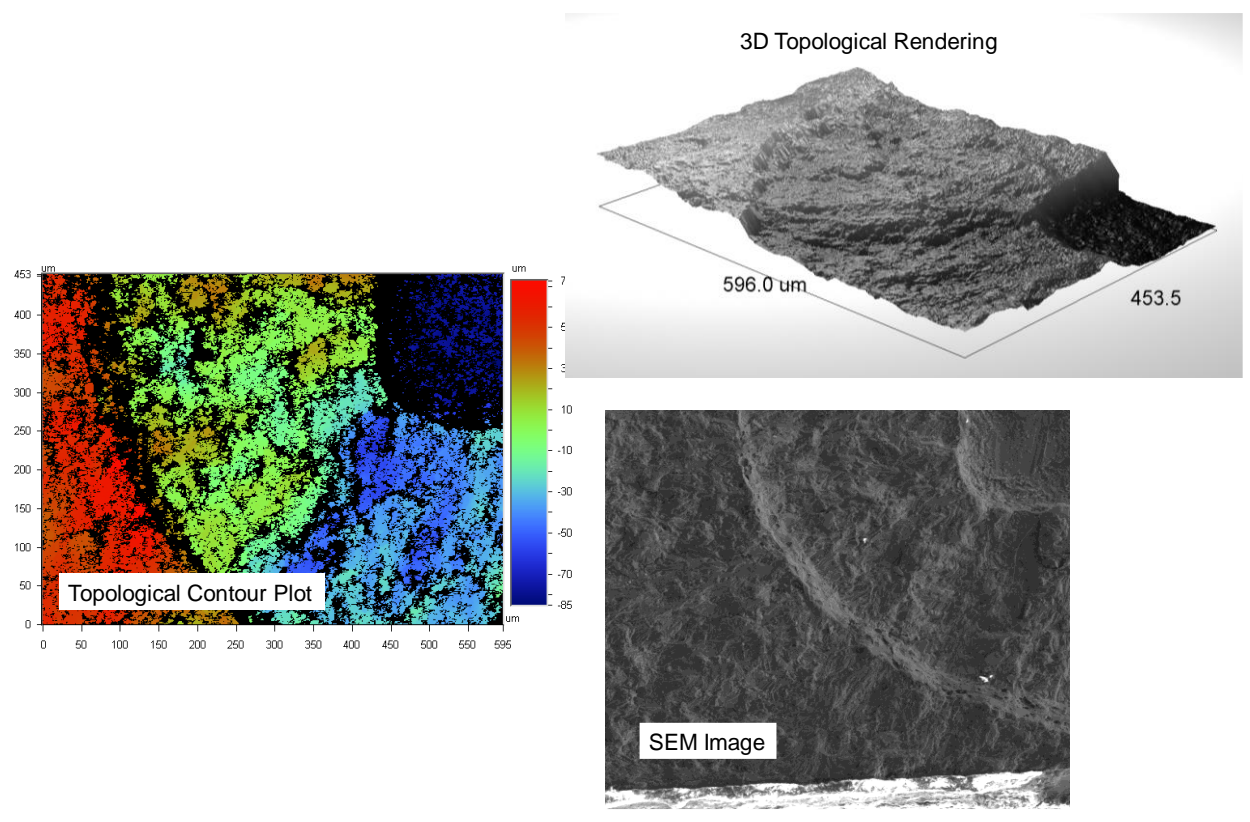


Figure 7.2.2-11. Topography measurements of the fatigue and blunted regions of two AA6061-T6 autofrettage tests (1.75% strain).

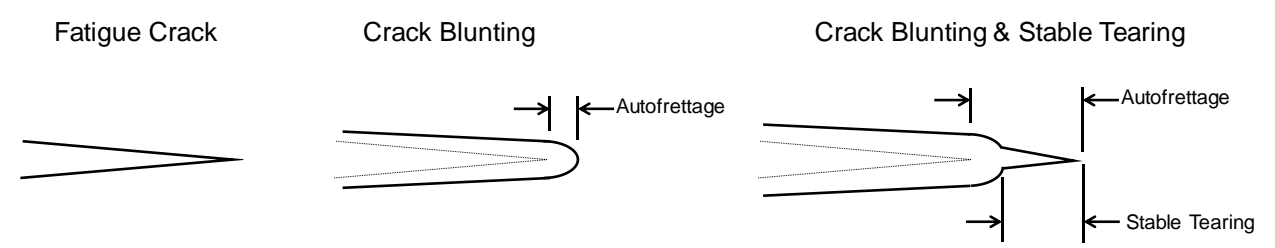


Figure 7.2.2-12. Edge view schematic based on interpretation of the topographic measurements and fracture surface photographs.

Four Consecutive Autofrettage Cycles (4xAF)

The influence of multiple, consecutive autofrettage cycles was examined by following the procedures described for the single autofrettage test with three differences: (1) The strains were measured with edge extensometers versus DIC measurements with virtual extensometers; (2) The minimum strain that follows the peak autofrettage strain is required to define the complete cycle; and (3) The minimum strain in the autofrettage cycle will necessitate compressive loads, so guide plates are required to prevent the thin coupons from buckling. An example of guide plates and edge extensometers is shown in Figure 7.2.2-13. Details on the use of guide plates are provided in Appendix I. The guide plates sandwich the coupon to prevent out-of-plane displacements. Teflon[©] tape was used on the guide plate mating surfaces to minimize friction between the plates and coupon (i.e., prevent load transfer through the guide plates). The minimum strains used in the tests were determined from pressure vs. strain data from specific or

generic liner designs. A representative stress-strain curve from a 4xAF test is shown in Figure 7.2.2-14.

F-10. Guide plates provided anti-buckling support when compressive loads were applied in coupon tests, while allowing strain and surface crack length measurements.

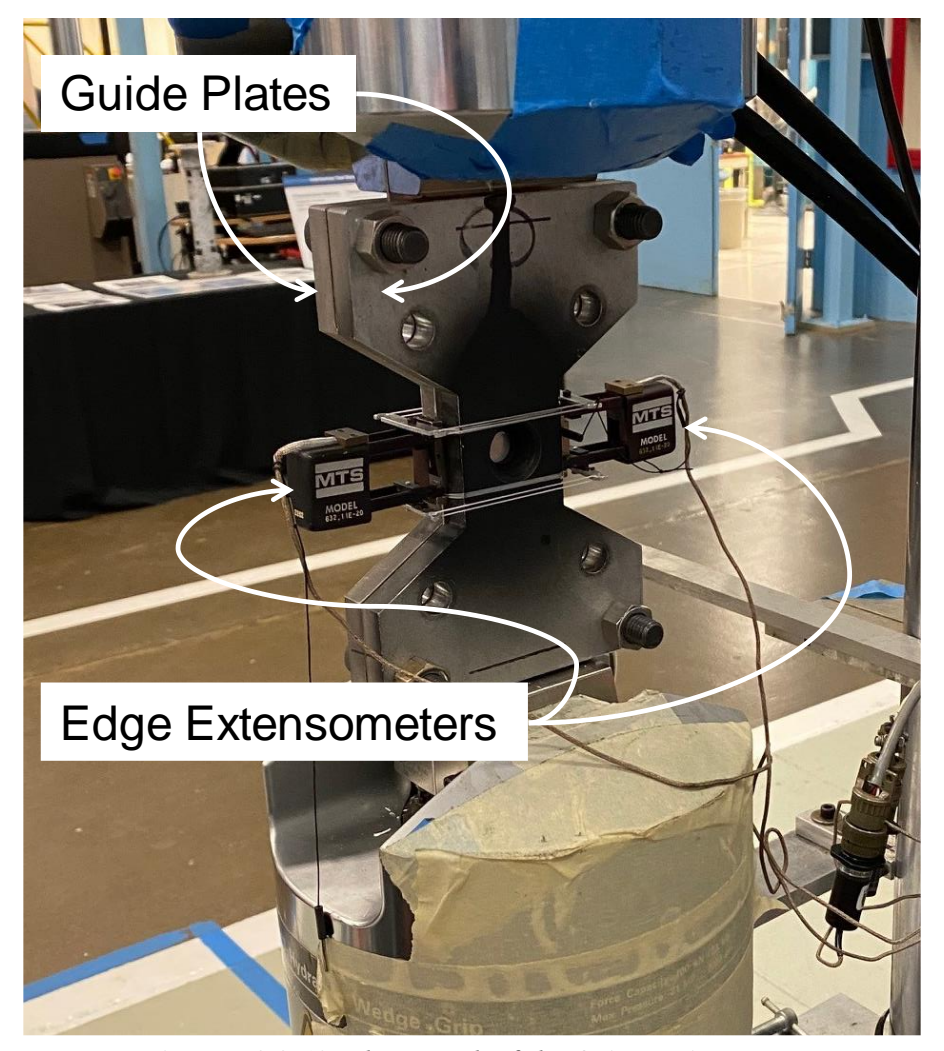


Figure 7.2.2-13. Photograph of the 4xAF testing setup.

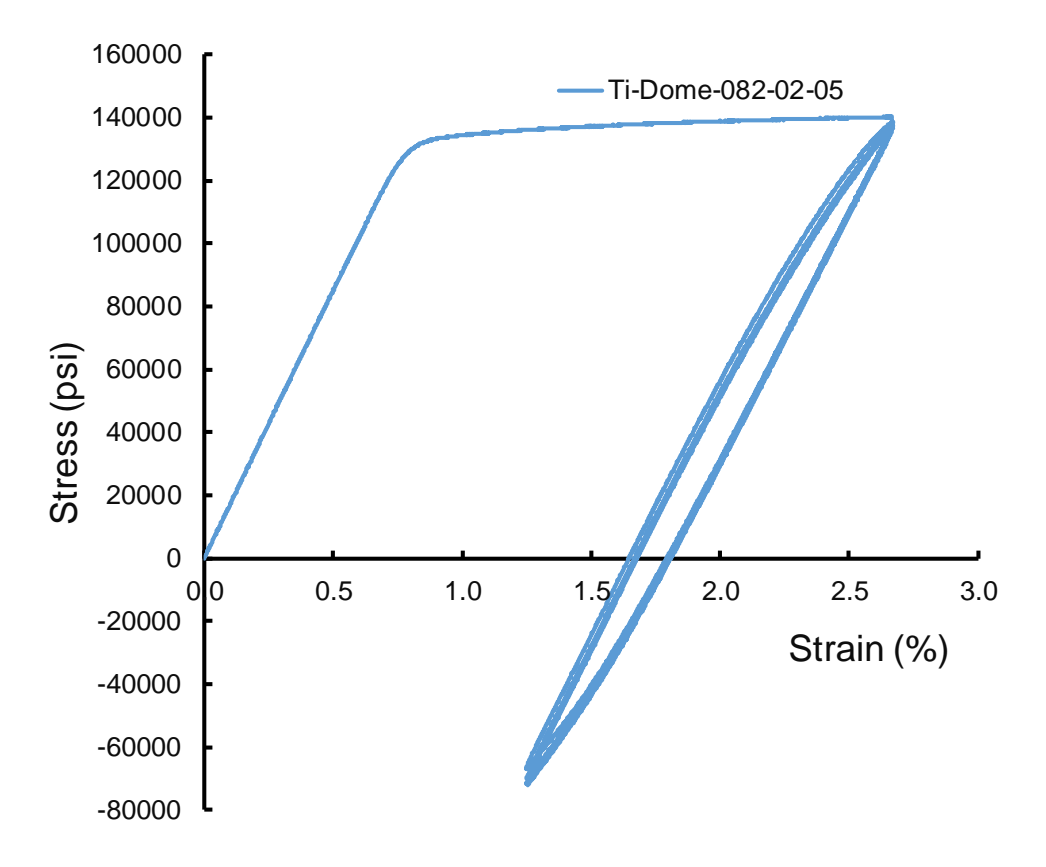


Figure 7.2.2-14. Stress-strain curve from a 4xAF test of a 0.082-inch thick Ti6Al-44 coupon.

7.2.2.2 Effect of Autofrettage on Eddy Current NDE response

Application of NDE crack screening after autofrettage could provide a means to determine the largest potential crack in the liner such that only the subsequent elastic operational cycles would need to be considered in damage tolerance analysis. Barriers to applying NDE to the liner after autofrettage include inspection in the presence of the composite overwrap and analysis of the effect of the liner compressive stress on the NDE technique. An automated scanning system for NDE of COPVs was developed and characterized, including eddy current inspection of wrapped COPVs [refs. 13, 14]. This work showed that an eddy current probe could be deployed through the port of a COPV for inspection of fatigue cracks. From Reference 14, it was found that EDM notches roughly equivalent to a 0.017 x 0.003-inch surface crack could be reliably detected by this method. As the effect of compressive stress induced crack closure and the potential corresponding loss in eddy current response was not studied in this reference, a test procedure was applied to address this unanswered question.

The procedure described in Section 7.2.2.1, with some modifications, was used to grow fatigue cracks in specimens and apply an autofrettage cycle for the eddy current crack closure experiments. First, the sample geometry as shown in Figure 7.2.2-1 was changed to eliminate the narrower gage region and maintain a constant 3-inch sample width. Second, the starter notch was removed after the completion of sample precracking. Finally, the guide plate was modified

to provide a larger area around the flaw. These changes allowed an area of 0.5 inch by 0.375 inch centered on a surface fatigue crack to be scanned with the eddy current probe during a simulated autofrettage cycle. All tests were performed on AA6061-T6 with a thickness of 0.090 inch that was approximately 0.078 inch after notch removal.

A modified version of the technique described in NASA/TM-2012-217782 was used to perform the eddy current inspections, using an equivalent eddy current probe to that applied for IML and OML COPV surface crack inspections [refs. 13 and 14]. The precracked coupons with starter notches removed were fitted with the anti-buckling guide plates and loaded into the test system. Eddy current scanning was performed in situ, with a 2-axis scanning system mounted to the frame. Eddy current data were acquired over the crack area at varying load levels, beginning in the unloaded state, increasing to 80% yield, decreasing to -80% yield, and then increasing back to zero load. Two coupons with different crack sizes were inspected. The results, shown in Figure 7.2.2-15, show very little change in eddy current signal level as a function of load on the sample. For both samples, the change in the signal between the peak tensile and compressive loads is within 2 standard deviations of the multiple zero load measurement points. A detailed description of these results is included in Appendix K.

O-4. Eddy current measurements of cracks subject to compressive loading (i.e., closed cracks), to 80% of the compressive yield, demonstrated no statistically significant loss in detectability relative to that obtained from the same crack loaded in tension (i.e., open cracks).

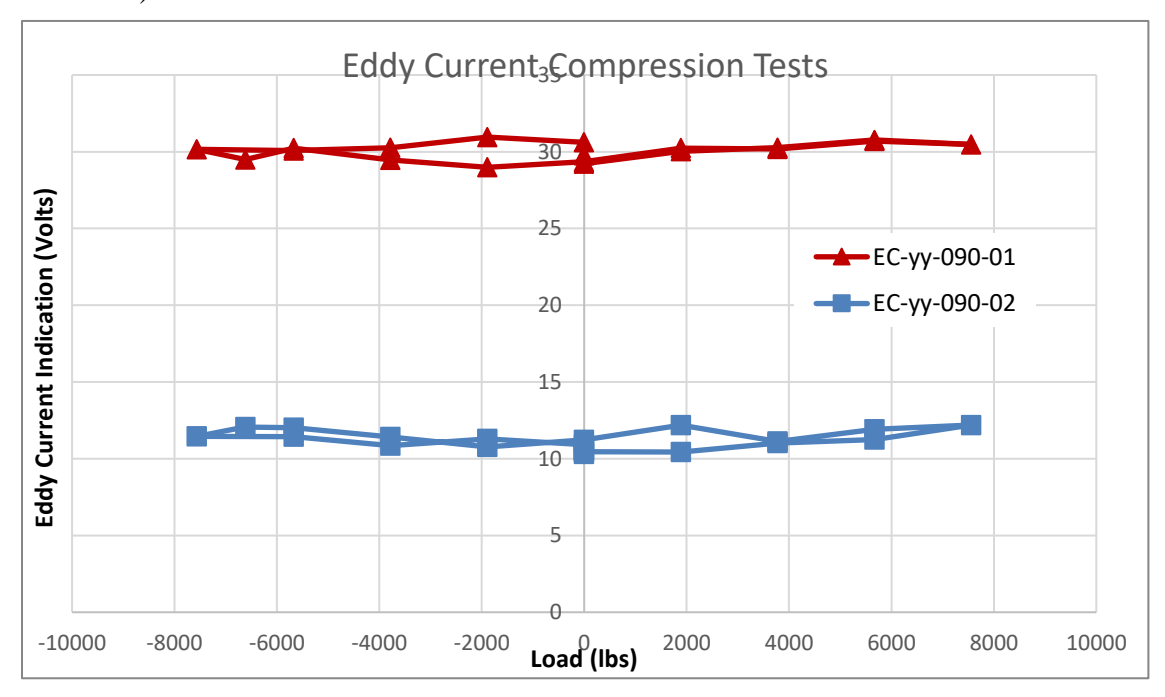


Figure 7.2.2-15. Eddy current response vs. load for surface cracks in 3" wide x .078" thick Al6061 sheets. Crack in EC-yy-090-01 is approximately .04" long x .015" deep and crack in EC-yy-02 is .027" long x .010" deep.

7.2.2.3 Autofrettage Crack Growth Results

Two types of tests were conducted to characterize autofrettage crack growth: (1) the crack size was held constant and the autofrettage strain level was increased and (2) the autofrettage strain

level is held constant and the crack size is changed. The first type of test is useful if there is a characteristic crack size (e.g., the penetrant NDE a of 0.025 inch with an a/c = 1, for the COPV liner) and different designs are under consideration (i.e., different strain levels or different thicknesses). The second type of test is useful to determine how close a specific design is to failure during the autofrettage cycle. The AA6061-T6 coupons were tested using the first test approach and the Ti 6Al-4V and IN718 materials were tested using the second approach.

AA6061-T6 Autofrettage Results

The autofrettage crack length was measured for AA6061-T6 sheet material at thicknesses of 0.09, 0.05, and 0.032 inch and from the pressurized COPV tests (see Section 7.2.3.2). The coupons had a 2-inch gage section and tested as described in Section 7.2.2.1. Target crack size was a depth of a = 0.025 inch and a surface length of 2c = 0.05 inch (a/c = 1). The measured autofrettage crack growth as a function of the autofrettage strain is plotted in Figure 7.2.2-15. The cracks extracted from the pressurized COPV tests were generally smaller than the coupon target size. One of the COPVs was subjected to four repeated autofrettage cycles (4xAF) and the others were subjected to a single initial autofrettage cycle.

The results indicate that 0.09-inch thick coupons experience less than 0.001-inch of crack growth during autofrettage strains to 2.25%. The autofrettage region appeared to be mostly featureless for all of the 0.09-inch thick coupon fracture surfaces, suggesting more of a crack blunting influence than stable tearing, as illustrated in Figure 7.2.2-16 for a coupon with an autofrettage strain of 2.25%. Conversely, the 0.032-inch thick coupons experienced an increase in amount of autofrettage crack growth at strains above 1.5%. Below 1.5% strain, the fracture surfaces of the 0.032-inch thick coupons exhibited little or no evidence of stable tearing, as illustrated in Figure 7.2.2-17. The amount autofrettage crack growth increased dramatically in the 0.032-inch thick coupons as the autofrettage strain level increased greater than 1.5% strain, as illustrated in Figure 7.2.2-18. A summary of the AA6061-T6 autofrettage tests is provided in Table 7.2.2-1. All fracture surfaces are provided in Appendix M.

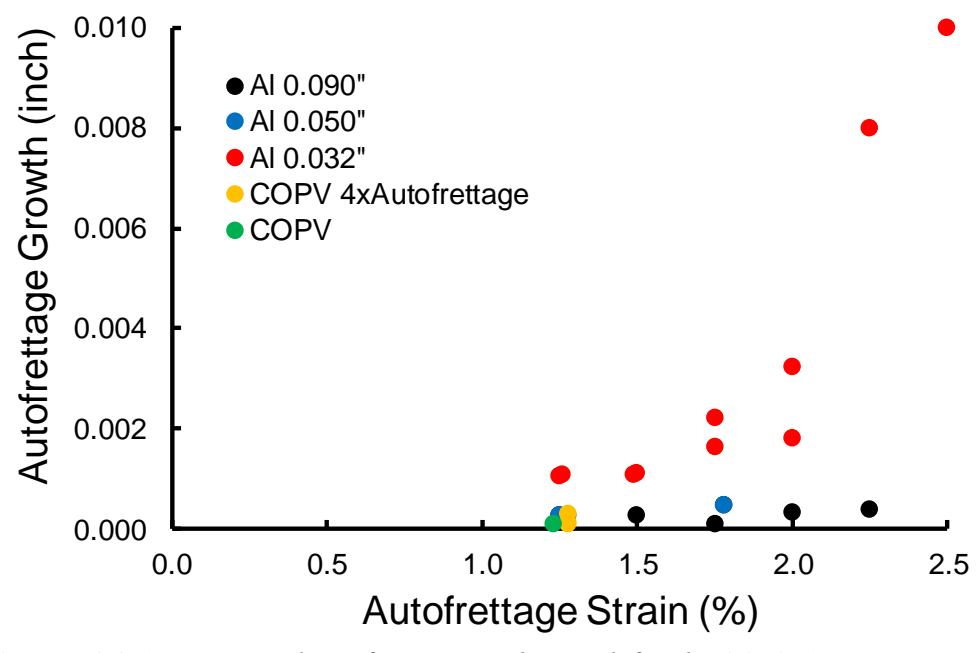
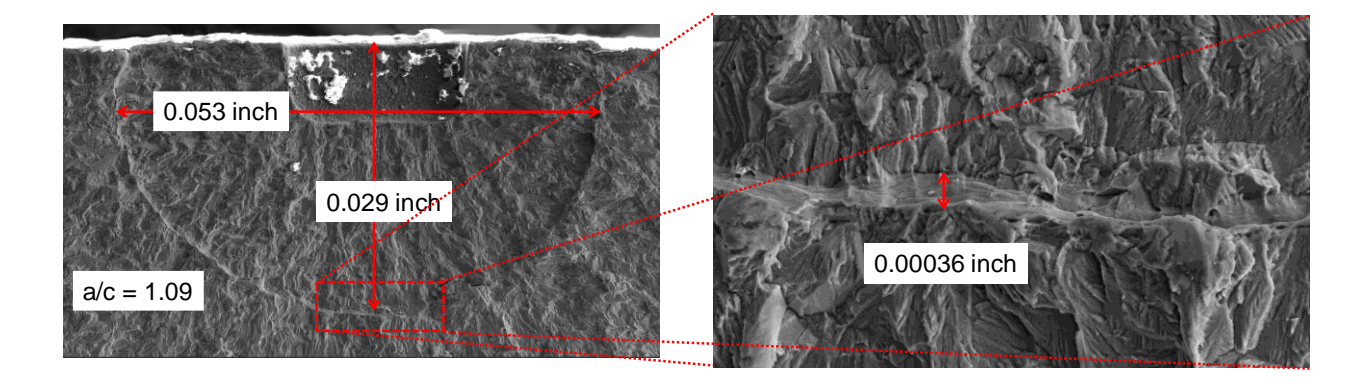


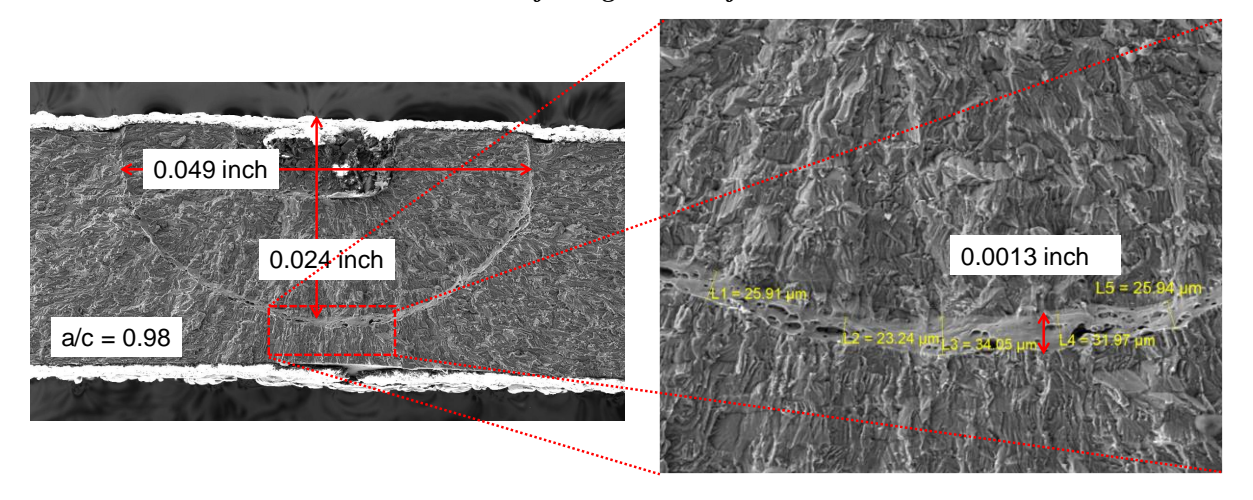
Figure 7.2.2-15. Measured autofrettage crack growth for the AA6061-T6 coupons.



A) Coupon FL-LT-090-17 at low magnification

B) Coupon FL-LT-090-17 at higher magnification

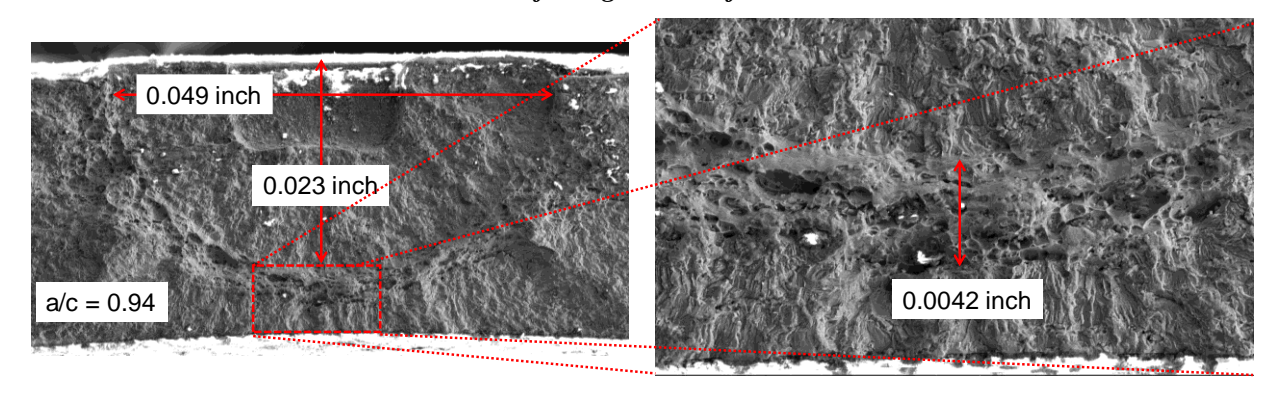
Figure 7.2.2-16. Fracture surface photographs for a 0.09-inch thick AA6061-T6 coupon subjected to an autofrettage strain of 2.25%.



A) Coupon FL-LT-032-002Aat low magnification

B) Coupon FL-LT-032-002Aat higher magnification

Figure 7.2.2-17. Fracture surface photographs for a 0.032-inch thick AA6061-T6 coupon subjected to an autofrettage strain of 1.5%.



A) Coupon FL-LT-032-07 at low magnification

B) Coupon FL-LT-032-07 at higher magnification

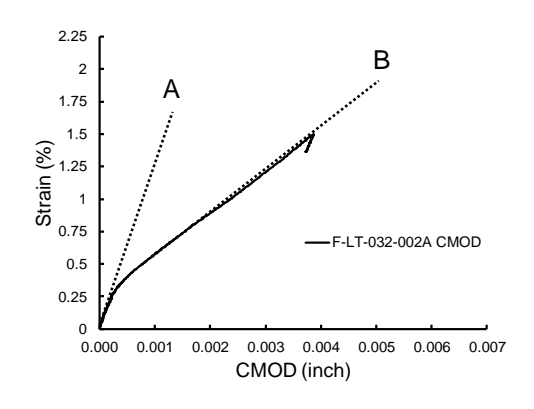
Figure 7.2.2-18. Fracture surface photographs for a 0.032-inch thick AA6061-T6 coupon subjected to an autofrettage strain of 2%.

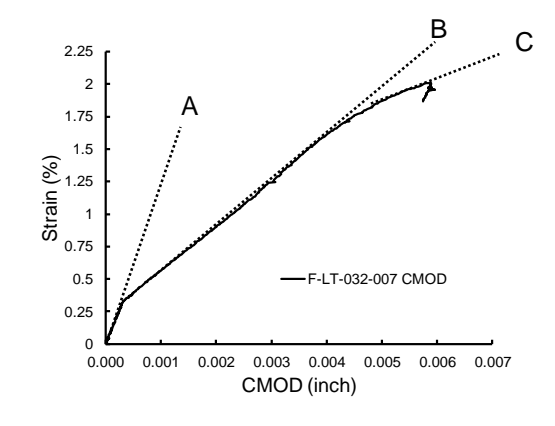
Table 7.2.2-1. Summary of AA6061-T6 Autofrettage Results

ID	Thickness	а	a/c	Strain	Delta-a	
	(inch)	(inch)		(%)	(inch)	
F-LT-032-002A	0.0305	0.024	0.98	1.5	0.00110	
F-LT-032-003A	0.031	0.027	0.74	2	0.00323	
F-LT-032-004A	0.031	0.023	0.88	1.25	0.00107	
F-TL-032-003A	0.0325	0.024	0.94	1.75	0.00223	
F-TL-032-002A	0.0325	0.026	1.06	2	0.00180	
F-LT-032-007	0.0325	0.023	0.94	2	0.03825	
F-LT-032-17	0.0315	0.023	0.92	2.25	0.00800	
F-LT-032-009	0.0315	0.027	0.9	2.5	0.01000	
F-TL-032-016_or_LT	0.0315	0.023	0.94	1.75	0.00163	
F-TL-032-002_or_LT	0.0315	0.025	1.06	1.26	0.00109	
F-TL-032-003_or_LT	0.0315	0.023	1.02	1.489	0.00108	
F-LT-050-011	0.049	0.024	1.04	1.25	0.00028	
F-LT-050-012	0.05	0.024	1.04	1.25	0.00028	
F-LT-090-018	0.0885	0.027	1	1.5	0.00028	
F-LT-090-009	0.0895	0.028	1.04	2	0.00032	
F-LT-090-011	0.0885	0.024	1	1.75	0.00010	
F-TL-090-17	0.0875	0.029	1.09	2.25	0.00038	

The amount of autofrettage crack growth did not appear to be influenced by the crack orientation relative to the rolling direction. The crack in the LT orientation coupons was perpendicular to the rolling direction and the crack in the TL orientation coupons was parallel to the rolling direction. However, the CMOD measurements made at the crack center and 0.025 inch above and below the crack indicated differences between the LT and TL orientations. The CMOD measurements for the LT coupons exhibited two linear regions (A and B) and, if the autofrettage strain was high enough, a third region (C), as shown in Figure 7.2.2-19. It is postulated that the initial linear region is due to elastic loading. The transition between region A and B is postulated to be the start of yield and blunting. The linear region B is due to additional loading after blunting. Finally, the region C is postulated to be due to stable tearing. The CMOD measurements for the TL coupons appeared to have an exaggerated blunting effect compared to the LT coupons, as shown in Figure 7.2.2-20.

F-11. CMOD measurements appear to be sensitive to the onset of yielding, blunting, and stable tearing.





- A) Coupon F-LT-032-002A (no stable tearing)
- B) Coupon FL-LT-032-07 (with stable tearing)

Figure 7.2.2-19. CMOD vs. strain curves for coupons that did and did not exhibit stable tearing.

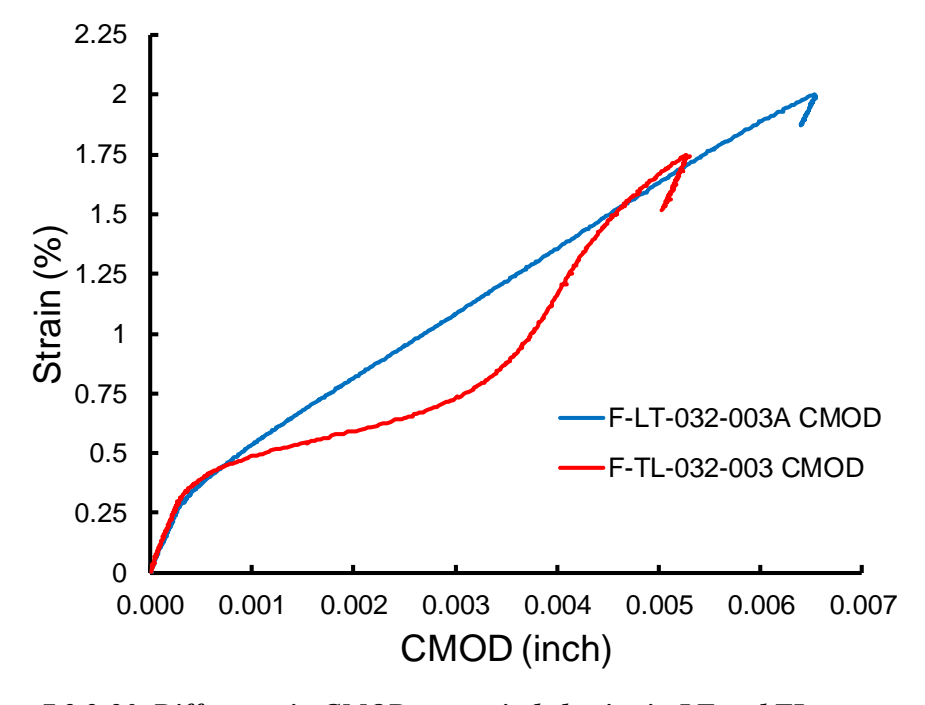


Figure 7.2.2-20. Difference in CMOD vs. strain behavior in LT and TL coupons.

IN718 Autofrettage Results

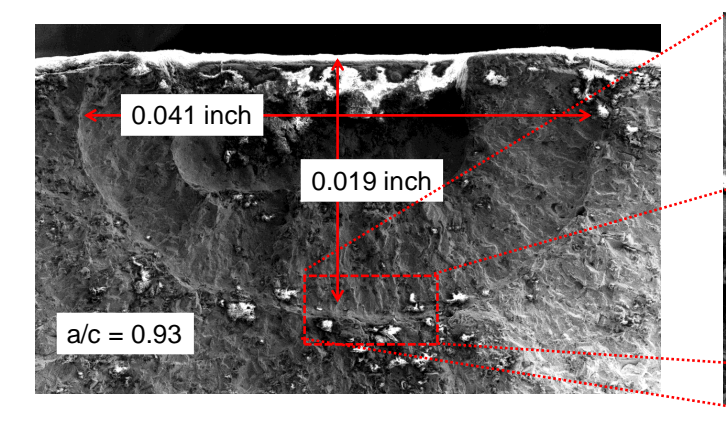
The autofrettage crack length was measured for IN718 material extracted from 0.03-inch thick flat AMS 5596 [ref. 16] sheets. The coupons were the same configuration as the AA6061-T6 coupons shown in Figure 7.2.2-1. Half of the coupons were solution treated and aged following the AMS 5663 standard [ref. 3] and the other half were solution treated following the AMS 5596 standard [ref. 3] (i.e., same solution treatment as AMS 5663, but not aged)¹⁰. The crack depth for the aged coupons ranged from 0.019 to 0.028 inch and had a target a/c = 1. The autofrettage strain target was 1.72%. The unaged coupons were 0.05-inch thick had a target 2c=0.04 inch-

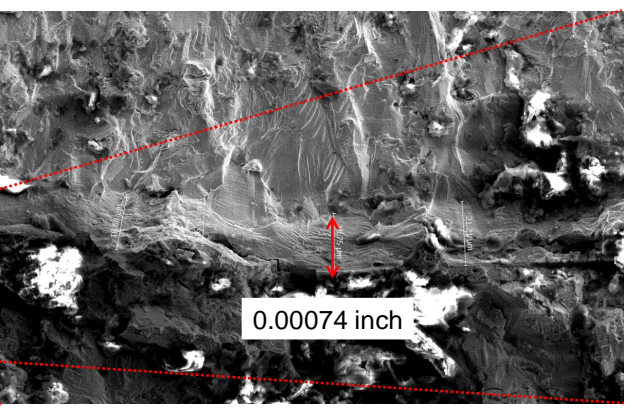
¹⁰ AMS 5596 and AMS 5662 follow heat treatments to achieve the solid solution state for sheet and forging/bar, respectively.

long and a=0.02-inch (i.e., a/c = 1). The simulated autofrettage strain level ranged from 1.5% to 3.5%. The crack growth during autofrettage exhibited behavior that indicated crack blunting for shallower cracks and blunting and stable tearing for deeper cracks.

IN718 AMS 5663 (Solution Treated and Aged) Results

The IN718 coupons that were solution treated and aged following the AMS 5663 standard [ref. 3] were loaded to an autofrettage strain level of 1.72%. The autofrettage crack growth region was not as distinct as observed in the AA6061-T6 coupons, as shown in Figure 7.2.2-21 for a coupon that did not exhibit stable tearing. Crack depths of a=0.022 inch and above experienced stable tearing, as shown in Figure 7.2.2-22. Crack depths at a=0.024 inch and above experienced stable tearing that progressed through to the back surface. This can be demonstrated by comparing the response of a coupon with an a = 0.022 inch with that of a coupon with an a =0.024 inch. The CMOD behavior for the two coupons follow the typical pattern of an initial linear region (i.e., to about 0.4% strain) followed by a change in slope that has been postulated to be crack tip blunting, as shown in Figure 7.2.2-23. A black dashed line is used to identify the slope of the second linear region. The behavior of these coupons was nearly identical until the curves begin deviate from the slope of the second linear region and separate above 1.4% strain. The F-LT-030-02 coupon with the 0.022 inch initial a deviated a small amount from the second linear region slope and experience about 0.003 inch of stable tearing, as shown in Figure 7.2.2-22. The F-LT-030-19 coupon with the 0.024 inch initial a had stable tearing that went through the 0.006-inch ligament. This breakthrough can be demonstrated by looking at the back face, directly opposite of the crack. The F-LT-030-19 coupon back face did not show any sign of back surface breakthrough at 1.4% strain. However, a 0.07 inch long back surface crack had broken the DIC pattern before reaching the 1.72% peak strain, as shown in Figure 7.2.2-24. The back side breakthrough behavior of the coupon F-LT-030-19 was contrasted with the F-LT-030-02 coupon with the 0.022-inch deep crack by looking at the back surface axial strain fields. The strain fields at the applied strain of 1.4% were nearly identical, as shown in Figure 7.2.2-25. However, the strains in coupon F-LT-030-19 was significantly higher than in coupon at F-LT-030-02 at the peak strain of 1.72%, as shown in Figure 7.2.2-26. Unlike coupon F-LT-030-19, the visual evidence suggests that the crack in F-LT-030-02 did not grow through to the back surface. A summary of the amount of autofrettage crack growth as a function of a is shown in Figure 7.2.2-27. The results suggest that the amount of crack growth due to the autofrettage cycle is relatively small and nearly constant with a as long as stable tearing is not present. Back surface breakthrough occurs at crack depths just beyond the depth that is sufficient to result in the onset of stable tearing.

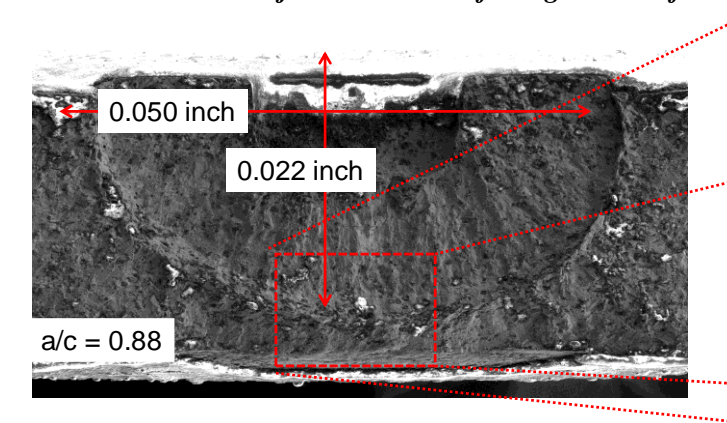


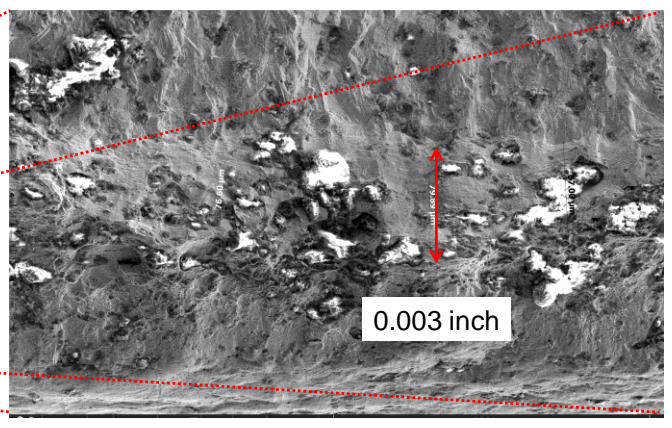


A) Coupon F-LT-030-01 at low magnification

B) Coupon F-LT-030-01 at higher magnification

Figure 7.2.2-21. Fracture surface photographs for a 0.030-inch thick IN178 (AMS 5663) coupon subjected to an autofrettage strain of 1.72% without stable tearing.





A) Coupon F-LT-030-02 at low magnification

B) Coupon F-LT-030-02 at higher magnification

Figure 7.2.2-22. Fracture surface photographs for a 0.030-inch thick IN178 (AMS 5663) coupon subjected to an autofrettage strain of 1.72% with stable tearing.

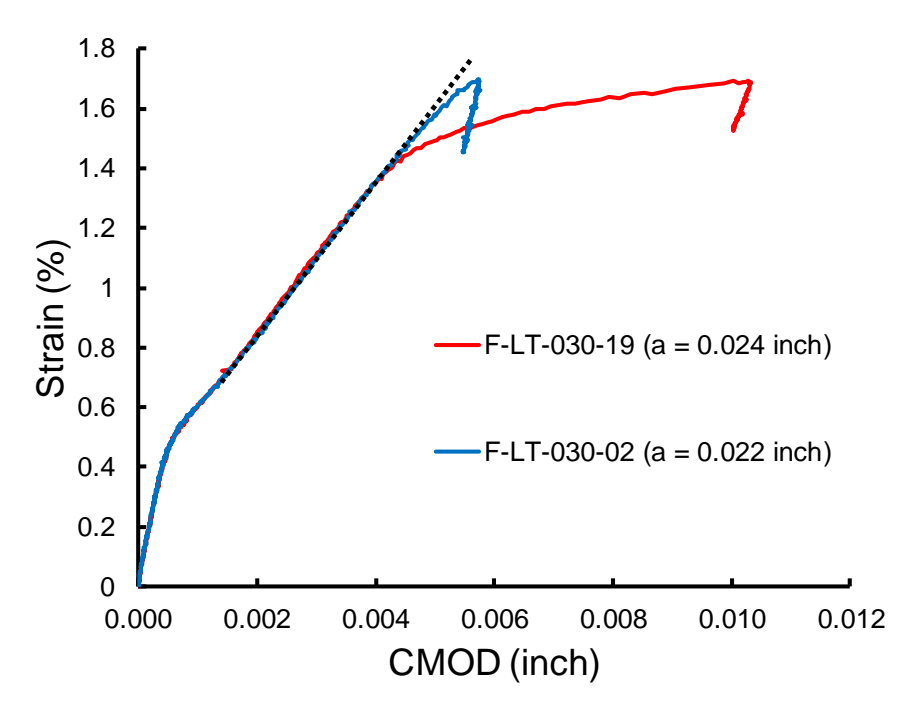
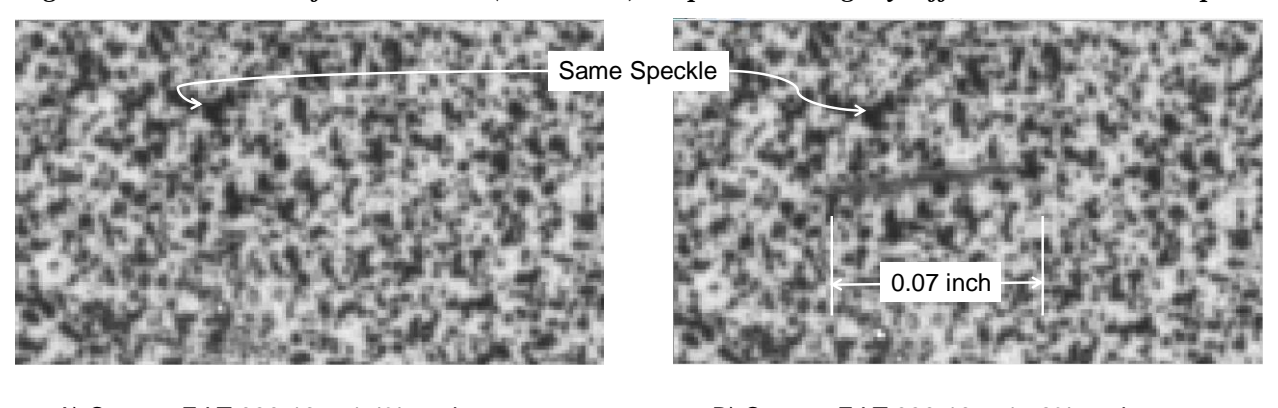


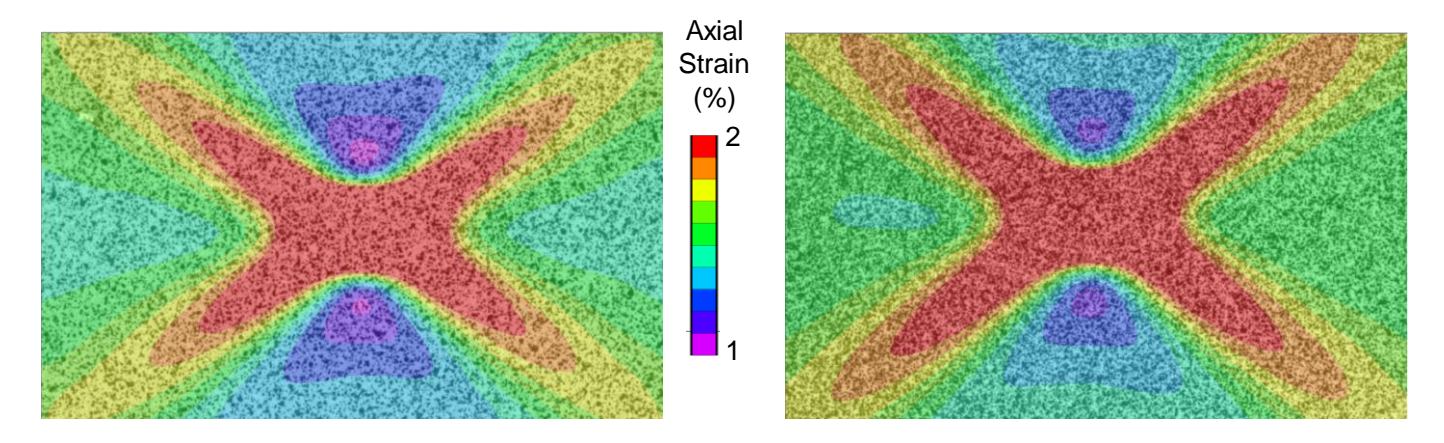
Figure 7.2.2-23. CMOD for two IN718 (AMS 5663) coupons with slightly different initial crack depths.



A) Coupon F-LT-030-19 at 1.4% strain

B) Coupon F-LT-030-19 at 1.72% strain

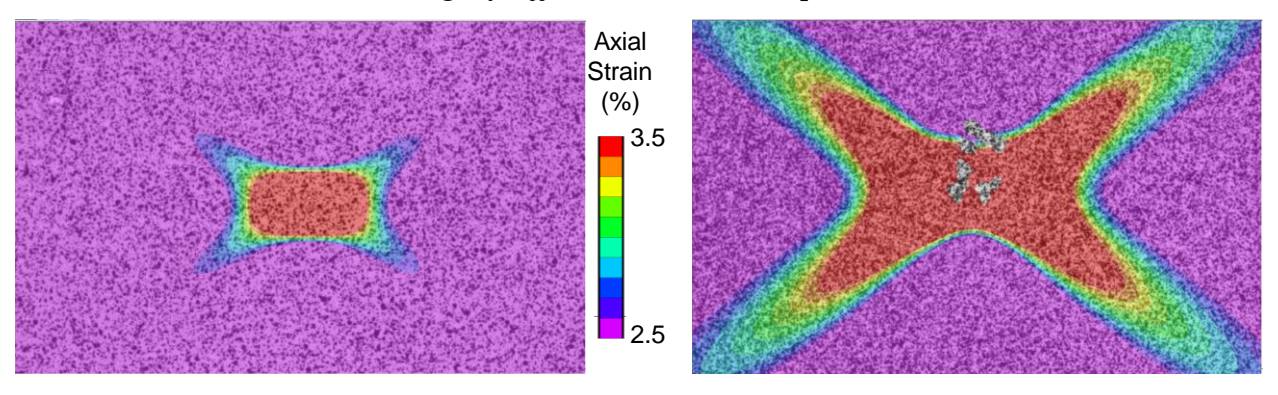
Figure 7.2.2-24. DIC speckle pattern on the back face (side opposite the crack) for coupon F-LT-030-19.



A) Coupon F-LT-030-02 at 1.4% strain

B) Coupon F-LT-030-19 at 1.4% strain

Figure 7.2.2-25. Axial strain field at 1.4% far-field strain for two IN718 (AMS 5663) coupons with slightly different initial crack depths.



A) Coupon F-LT-030-02 at 1.72% strain

B) Coupon F-LT-030-19 at 1.72% strain

Figure 7.2.2-26. Axial strain field at 1.72% far-field strain for two IN718 (AMS 5663) coupons with slightly different initial crack depths.

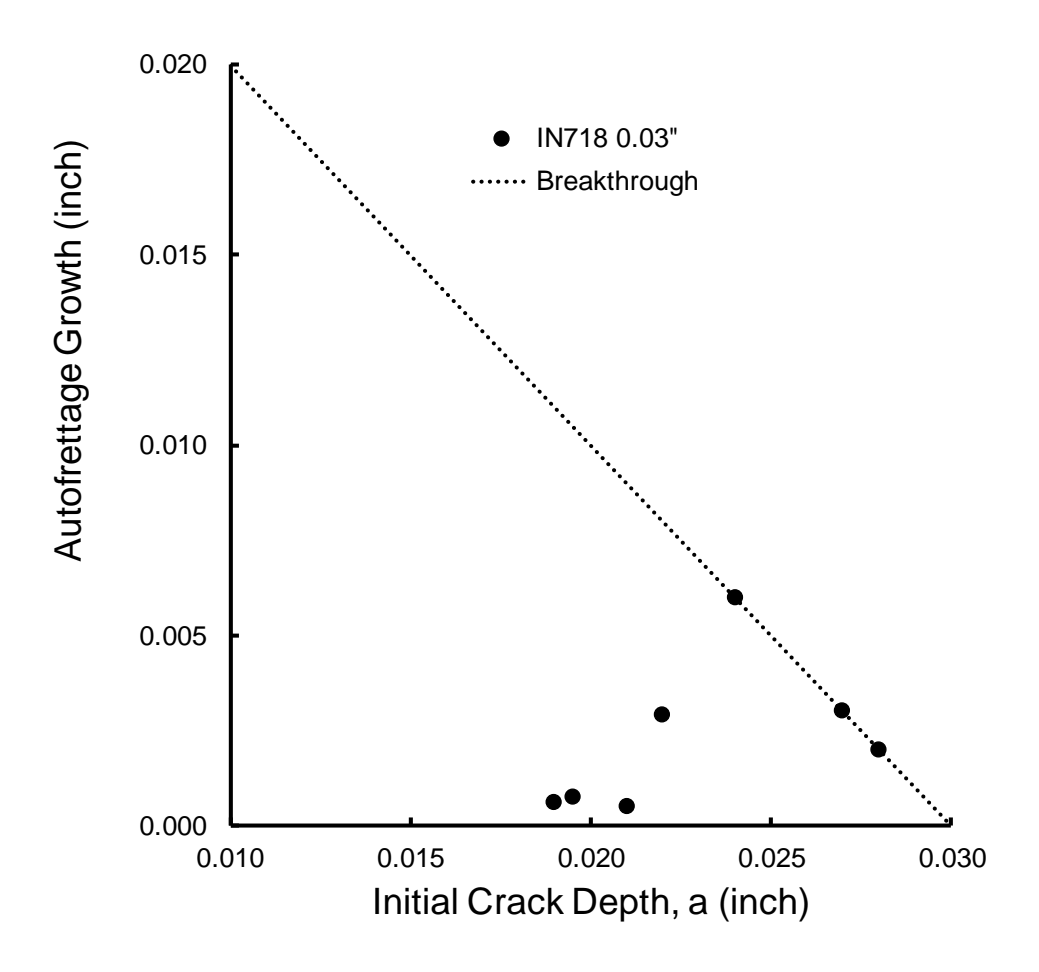


Figure 7.2.2-27. Autofrettage crack growth in the 0.03-inch thick IN718 (AMS 5663) coupons subjected to a strain level of 1.72%.

IN718 AMS 5596 (Solution Treated and no Aging) Results

The IN718 coupons that were solution treated following the AMS 5596 standard [ref. 3] were loaded to three different autofrettage strain levels: 1.5%, 2.5%, and 3.5%. The coupons were 0.05-inch thick and the target crack size was 2c = 0.04 inch and a = 0.02 inch (i.e., a/c = 1). Multiple coupons were tested to determine the variability in the amount of autofrettage crack growth. The fracture surfaces appeared to be similar to the described tests on coupons that were heat treated and aged following the AMS 5663 standard [ref. 3]. One coupon was tested with 4xAF where stable tearing was not present in any of the fracture surfaces (i.e., the coupon was thicker and the cracks smaller than the AMS 5663 coupons). The autofrettage crack growth was small (i.e., <0.0005 inch) and showed a slight increasing trend with increasing autofrettage strain level, as shown in Figure 7.2.2-28. The test with 4xAF at 2.5% strain experienced about three times the average autofrettage crack growth of the tests at a similar strain level.

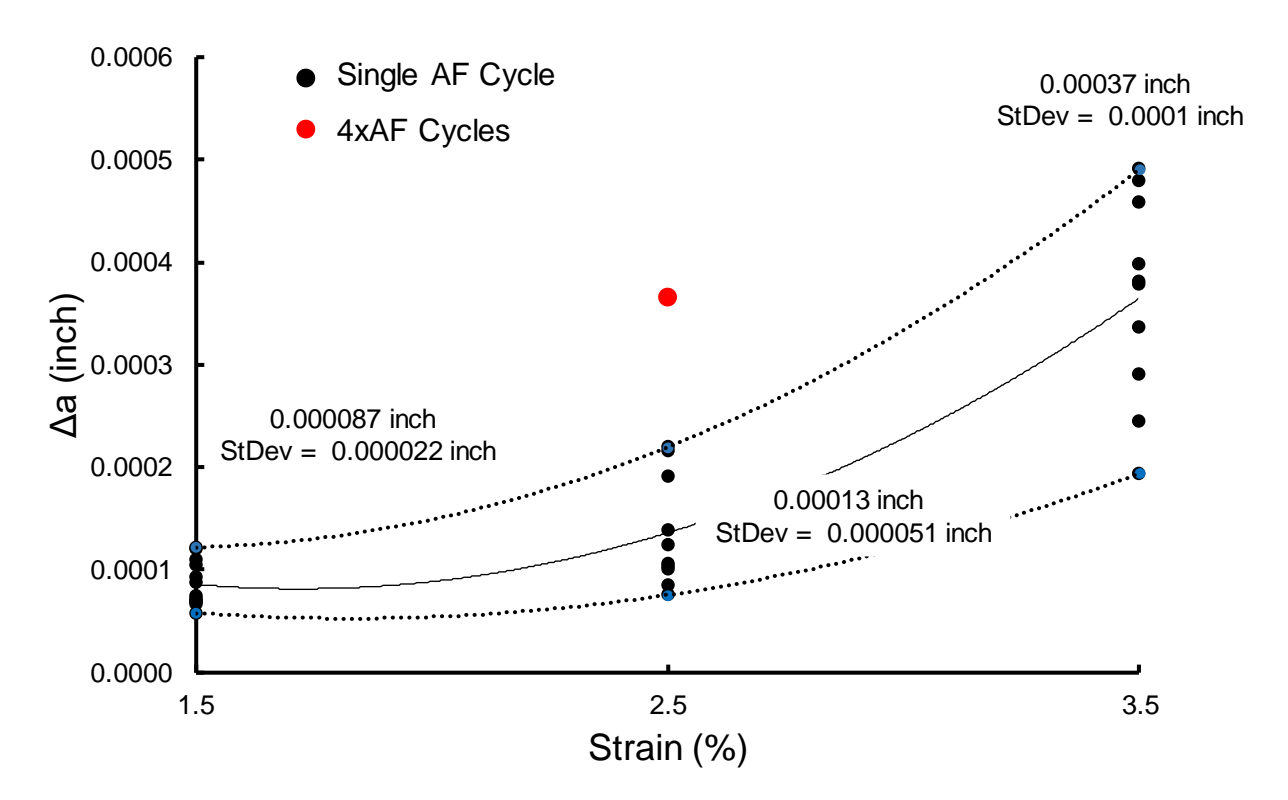


Figure 7.2.2-28. Autofrettage crack growth in the 0.05-inch thick IN718 (AMS 5662) coupons.

Ti 6Al-4V Autofrettage Results

The autofrettage crack length was measured for Ti 6Al-4V material that was extracted from the dome region of COPV liners and machined flat. Coupons that were 0.082-inch thick were manufactured from the dome top material where the material was thickest. The 0.082-inch thick coupons were machined with 1 inch and 0.5-inch widths. The 1-inch wide coupons were for cracks with a/c = 0.2 (i.e., a = 0.0125 inch and 2c = 0.125 inch). The 0.5-inch wide coupons were for cracks with a/c = 1 (i.e., a = 0.025 inch and 2c = 0.05 inch). The thickness decreases as the distance from the top of the dome increased, so other coupons were machined flat to a thickness of 0.06 inch. These coupons were 0.5-inch wide and had cracks with a/c = 1. A schematic of the dome coupon extraction sites are shown in Figure 7.2.2-29. The coupons were tested as described in Section 7.2.2.1.

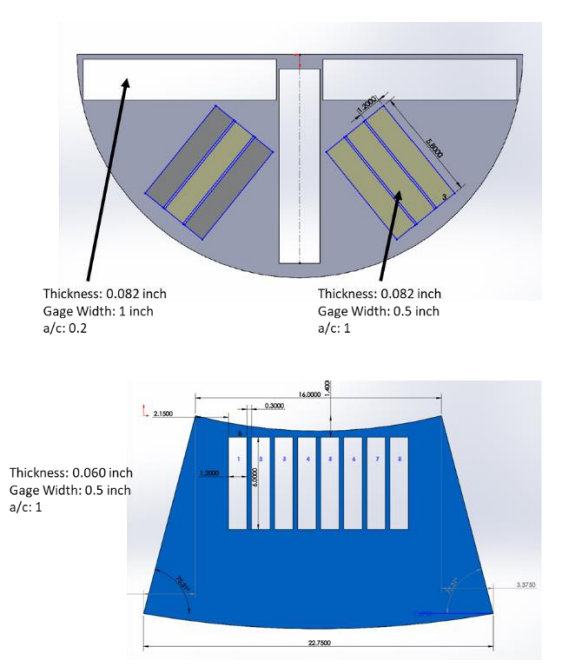


Figure 7.2.2-29. Location on the tank dome where the coupons were extracted.

Ti 6Al-4V 0.082-inch thick Coupons (a/c = 1)

The 0.082-inch thick Ti 6Al-4V coupons were tested to an autofrettage strain level of 2.65%. The autofrettage strain was held constant as was the aspect ratio (a/c = 1), but the crack depth ranged from 0.023 to 0.039 inch. Two tests were conducted with four repeated autofrettage cycles, each with the minimum strain of 1.5% (loading previously shown in Figure 7.2.2-14). As observed in the AA6061-T6 and IN718 coupons, the amount of crack extension during the autofrettage cycle was small (i.e., <0.002 inch) until stable tearing was detected, as shown in Figure 7.2.2-30. Figure 7.2.2-31 contains the coupon fracture surface that achieved the 2.65% strain with minimal crack extension. A coupon with a deeper initial crack experienced stable tearing, but did not fail at 2.65%, as shown in Figures 7.2.2-32 and 7.2.2-33.

Stable tearing was first observed at a depth = 0.029 inch and failures occurred at depths >0.032 inch in this set of tests. The dashed line in Figure 7.2.2-30 represents the amount of autofrettage crack growth that was needed for the crack to grow through the thickness (i.e., failure). The two tests that were conducted with four repeats of the autofrettage cycle had crack growth during autofrettage that was similar in magnitude to the single autofrettage tests where stable tearing was not observed. The strain at failure was measured for the tests that did not reach the 2.65% autofrettage level and plotted as a function of initial a, as shown in Figure 7.2.2-34. This plot shows a drop off in failure strain as stable tearing develops at the deeper initial cracks.

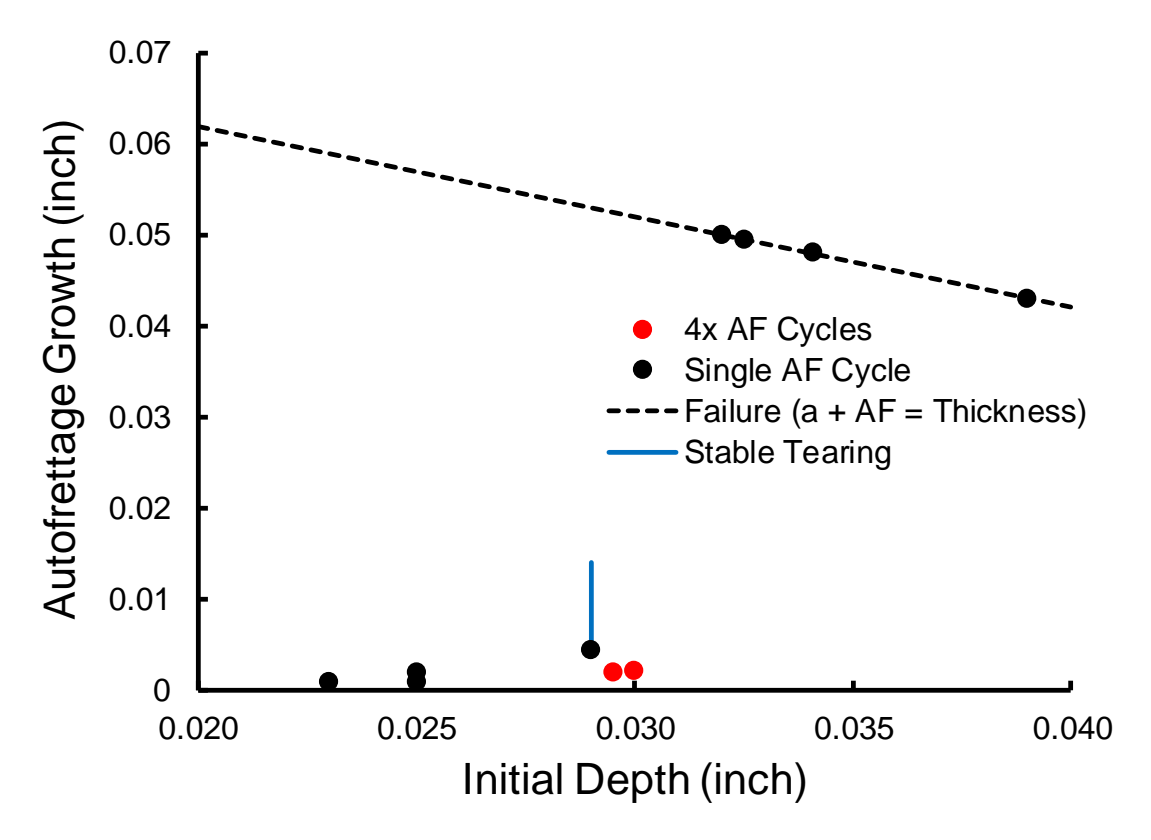


Figure 7.2.2-30. Amount of autofrettage crack growth in the 0.082-inch thick Ti 6Al-4V coupons subjected to a strain level of 2.65%.

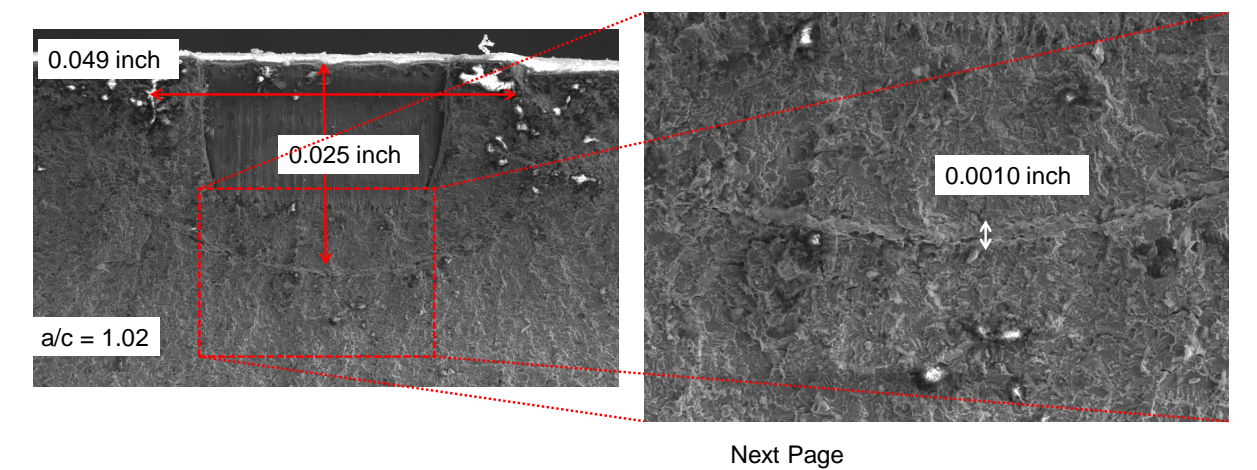
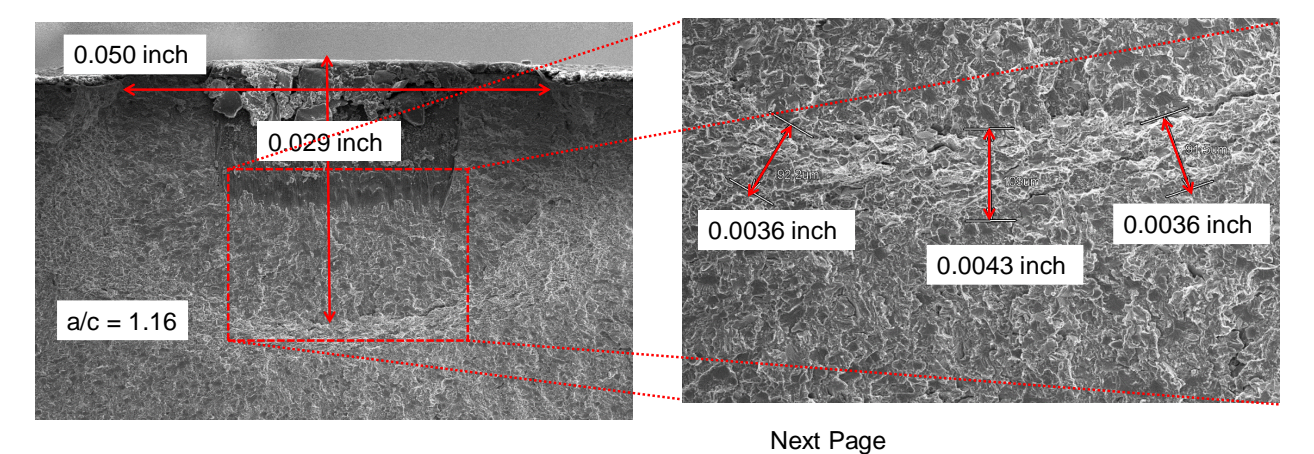


Figure 7.2.2-31. Fracture surface photographs for a 0.082-inch thick Ti 6Al-4V coupon subjected to an autofrettage strain of 2.65% (without stable tearing).

A) Coupon Ti-Dome-01-05-082 at low magnification

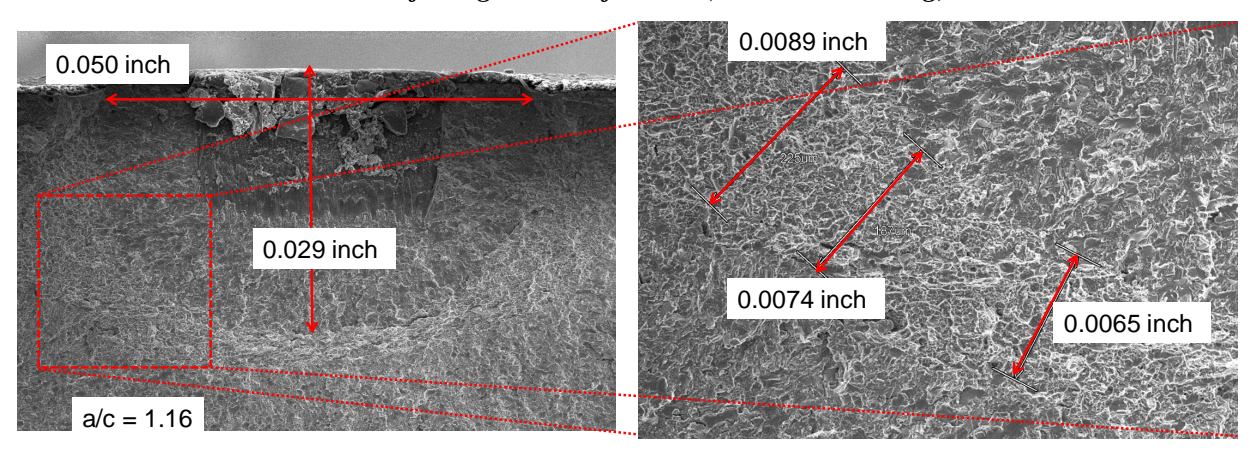
B) Coupon Ti-Dome-01-05-082 at higher magnification



A) Coupon Ti-Dome-082-01 at low magnification

B) Coupon Ti-Dome-082-01 at higher magnification

Figure 7.2.2-32. Fracture surface photographs for a 0.082-inch thick Ti 6Al-4V coupon subjected to an autofrettage strain of 2.65% (with stable tearing).



- A) Coupon Ti-Dome-082-01 at low magnification
- B) Coupon Ti-Dome-082-01 at higher magnification

Figure 7.2.2-33. Fracture surface photographs for a 0.082-inch thick Ti 6Al-4V coupon subjected to an autofrettage strain of 2.65% (with stable tearing).

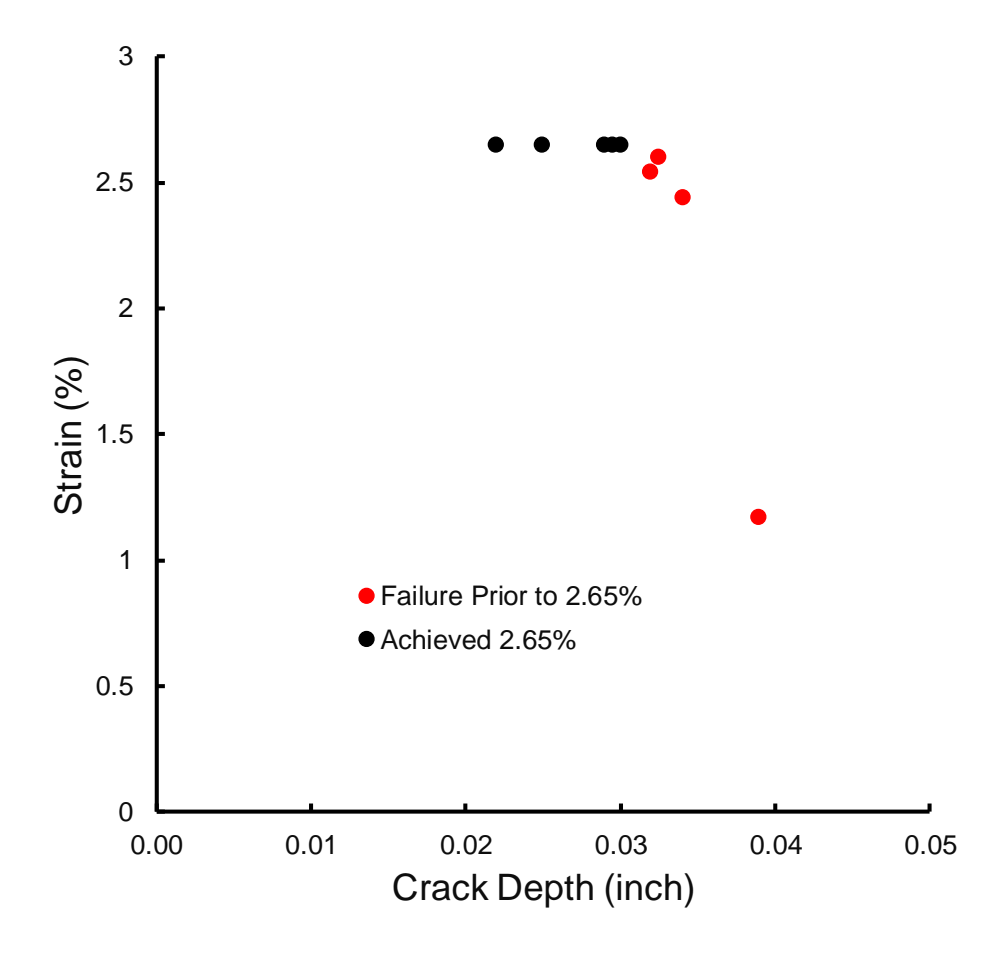


Figure 7.2.2-34. Strain at failure as a function of a for the a/c = 1, 0.082-inch thick Ti 6Al-4V autofrettage tests.

Ti 6Al-4V 0.082-inch thick Coupons (a/c = 0.2)

Part-through cracks will tend to grow at an aspect ratio of a/c = 0.8 to 1.2 when loaded under tensile loading. This creates difficulties when trying to nucleate long, shallow cracks without the cracks growing too much in the depth direction. This natural tendency was overcome by using multiple co-linear notches to nucleate the cracks to the desired size and shape. Semi-circular cracks nucleated at each notch and linked without growing too deep, as illustrated in Figure 7.2.2-35. The coupons with co-linear notches were fatigue precracked in tension until link-up of the ligaments between the notches. Typically, this left the surface crack length shorter than the target value, so the coupons were cycled under 3-point bending until the desired surface length was achieved. The crack tip region was close to the neutral axis, so most of the subsequent crack growth was in the length direction. The resulting crack surfaces achieved the desired length and depth, but were not semi-elliptical, as shown in Figure 7.2.2-36. The crack markings in the Ti 6Al-4V material were faint, so the approximate shape of the initial fatigue crack was highlighted in red. Two of the a/c = 0.2 tests achieved the targeted depth and length and were loaded to the required 2.65% autofrettage strain. The resulting autofrettage crack growth was less than 0.002 inch, as illustrated in Figure 7.2.2-37.

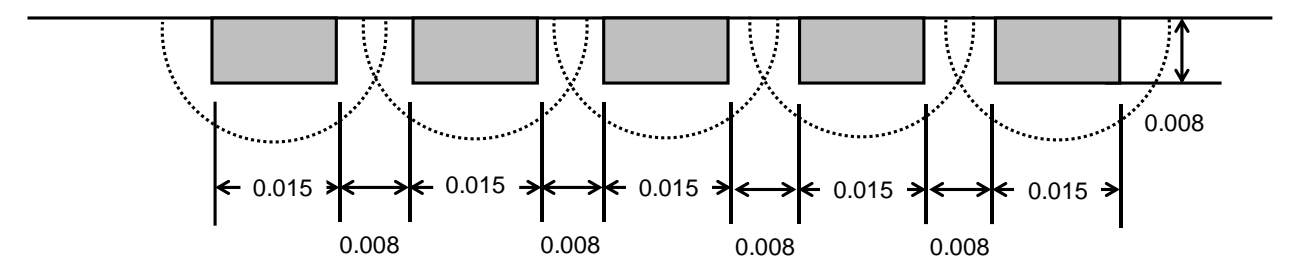


Figure 7.2.2-35. Schematic of the notch pattern used for the a/c = 0.2 cracks (dashed lines indicated expected crack nucleation and link-up).

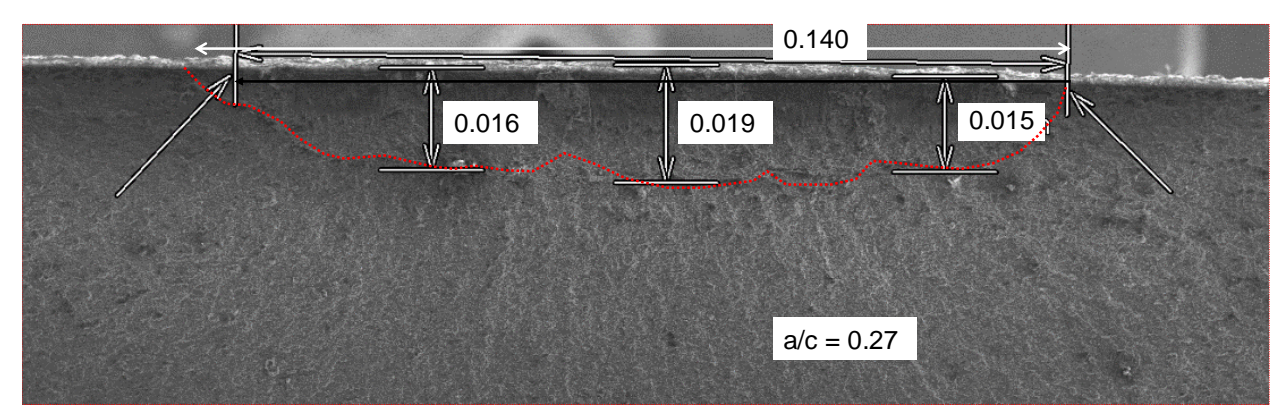


Figure 7.2.2-36. Long, shallow crack that was nucleated from 5 co-linear notches.

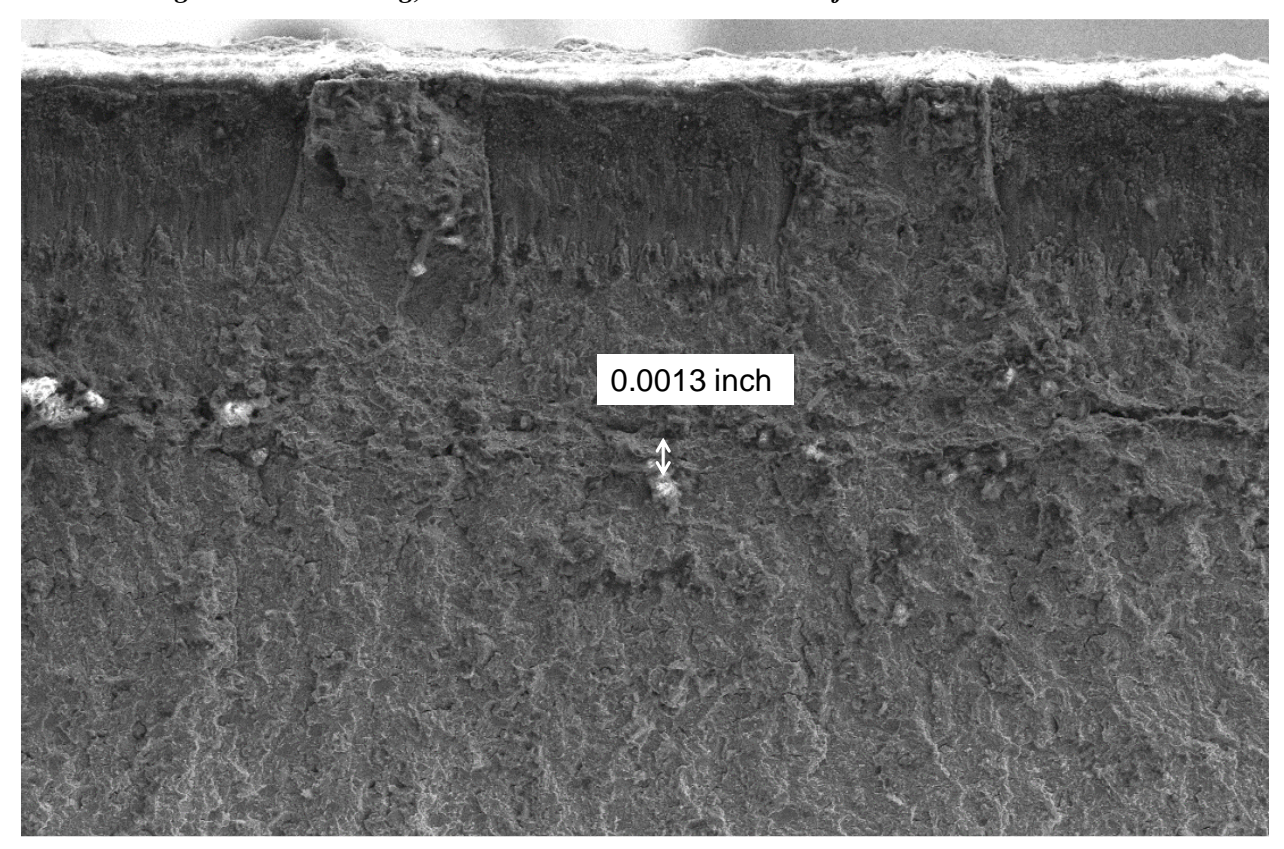


Figure 7.2.2-37. Region of autofrettage crack growth in Ti 6Al-4V coupon Ti-Dome-02-02-82.

Ti 6Al-4V 0.06-Inch Thick Coupons (a/c = 1)

The 0.06-inch thick Ti 6Al-4V coupons were tested to an AF strain level of 1%. The autofrettage strain was held constant as was the aspect ratio (a/c = 1), but the initial crack depth ranged from 0.021 to 0.039 inch. One test was conducted with 4xAF with the minimum strain of 0%, as shown in Figure 7.2.2-38. As with the 0.082-inch thick Ti 6Al4V materials, the 0.06-inch thick Ti6Al-4V material did not show a strong influence between the crack size and the amount of crack growth due to the autofrettage strain until the crack was large enough for stable tearing to occur, as shown in Figure 7.2.2-39. Stable tearing was not observed for initial crack depths less than 0.036 inch and a typical 0.06-inch thick Ti 6Al-4V fracture surface without stable tearing is shown in Figure 7.2.2-40. Stable tearing was observed for the 0.06-inch thick Ti 6Al-4V coupons with cracks deeper than 0.036 inch, as shown in Figure 7.2.2-41. The stable tearing appeared to start, or at least become the greatest, at an angle of about 30-degrees from the surface, as shown by the white dashed lines in Figure 7.2.2-42 that represent an outline of the stable tearing region. The 4xAF loading of the 0.06-inch thick Ti 6Al-4V coupon did not exhibit significantly more crack growth than the single cycle tests of similar crack depths, as shown by Figure 7.2.2-43.

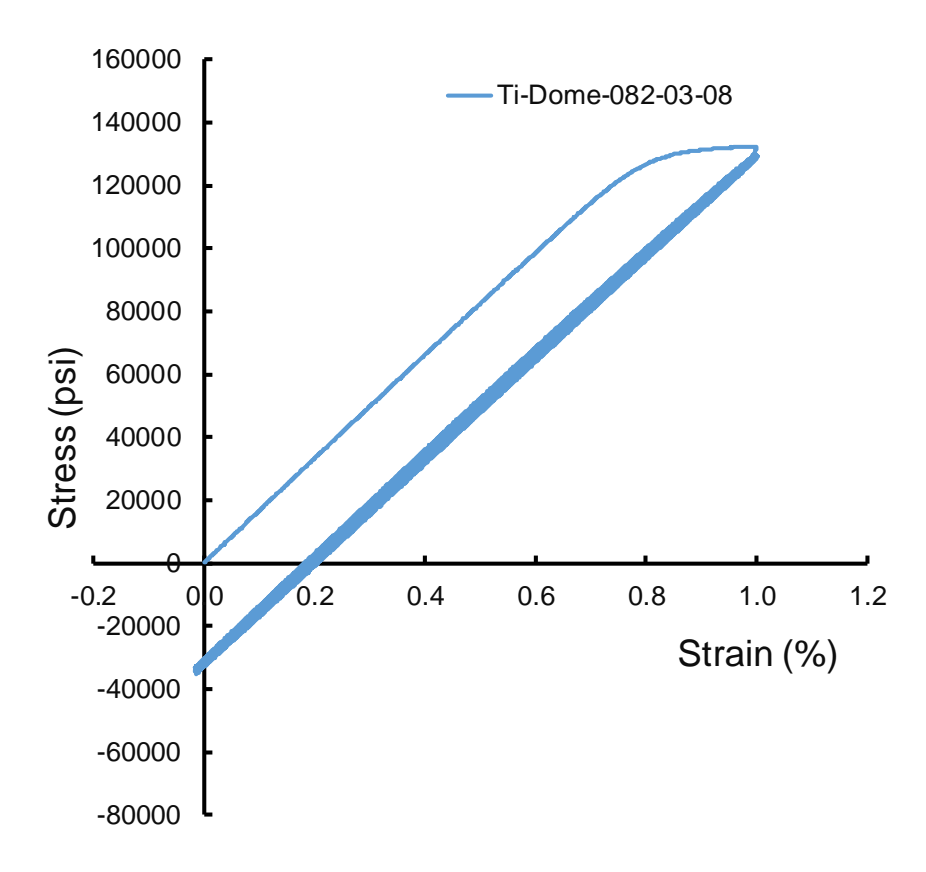


Figure 7.2.2-38. Stress-strain curve from a 4xAF test of a 0.06-inch thick Ti 6Al-4V coupon.

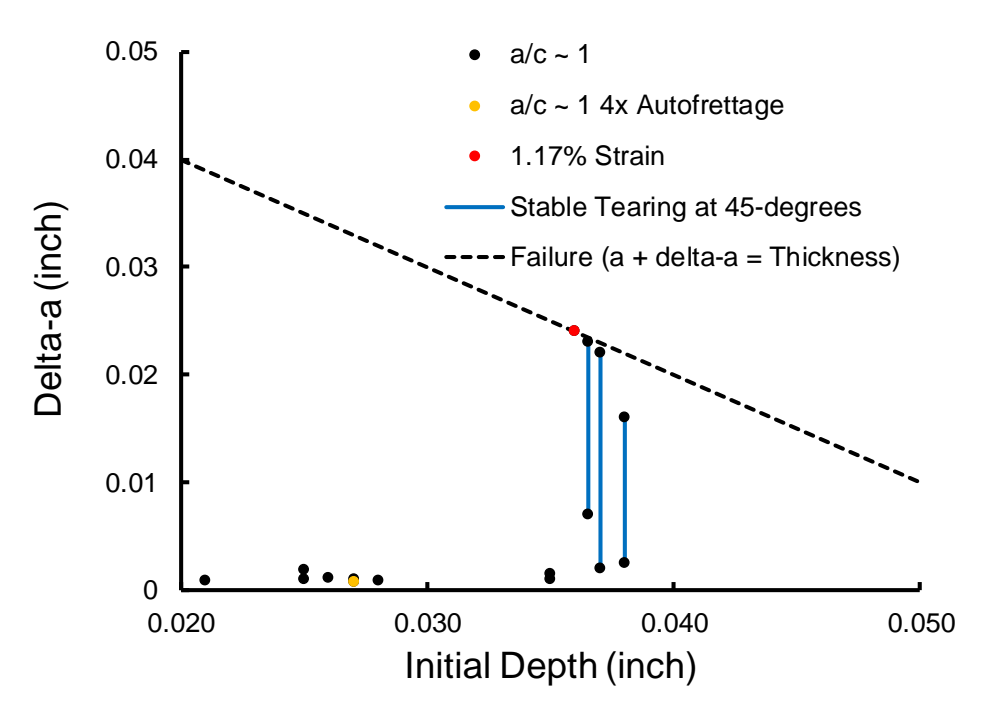
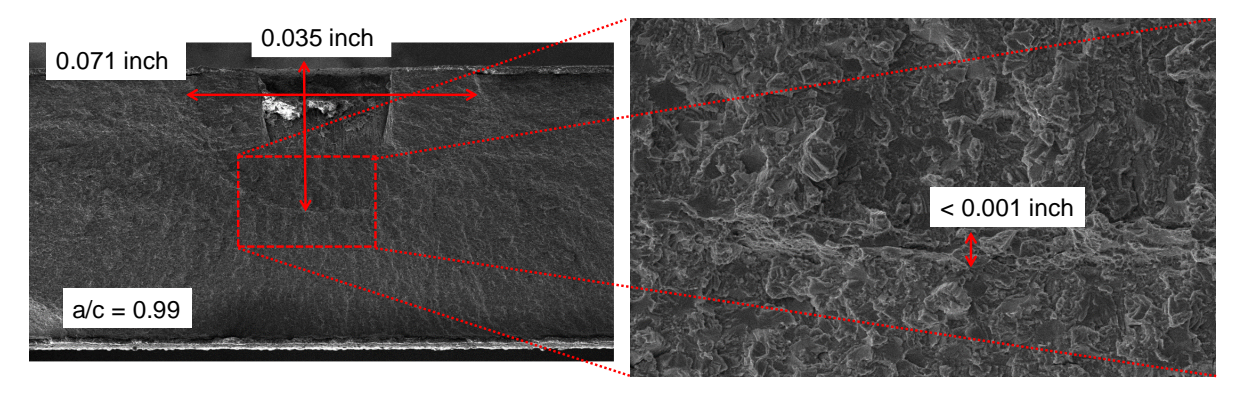
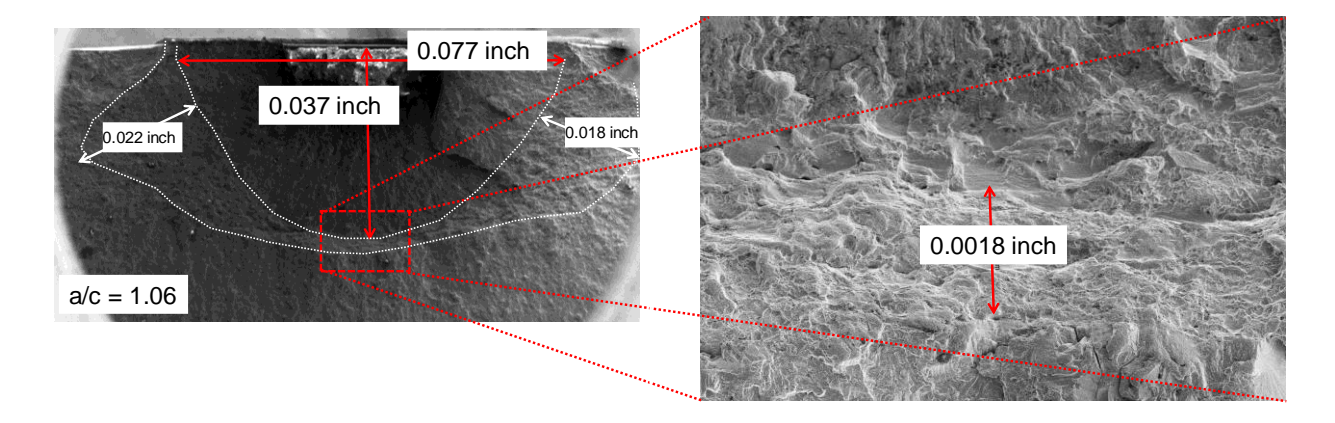


Figure 7.2.2-39. Amount of autofrettage crack growth in the 0.06-inch thick Ti 6Al-4V coupons subjected to a strain level of 1%.



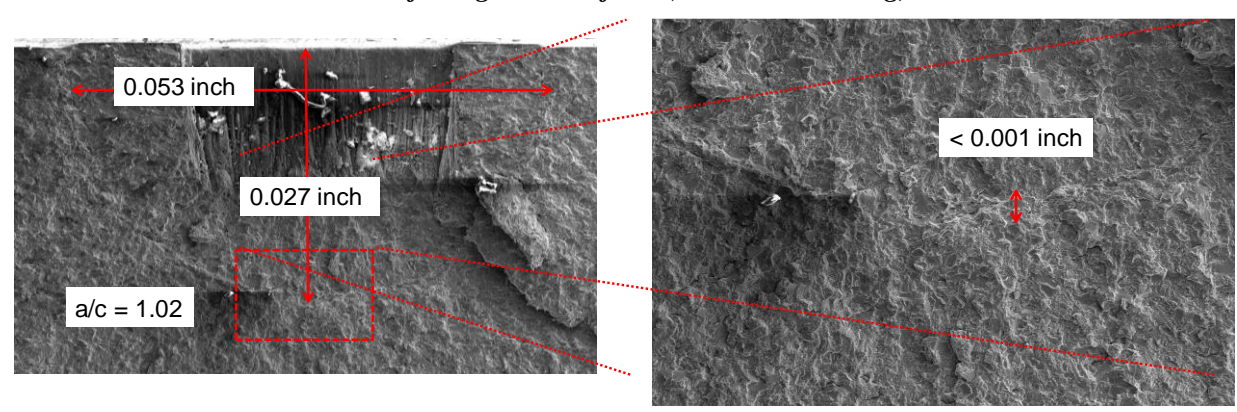
- A) Coupon Ti-Dome-060-03-01 at low magnification
- B) Coupon Ti-Dome-060-03-01 at higher magnification

Figure 7.2.2-40. Fracture surface photographs for a 0.06-inch thick Ti6Al-4V coupon subjected to an autofrettage strain of 1% (without stable tearing).



- A) Coupon Ti-Dome-060-03-07 at low magnification
- B) Coupon Ti-Dome-060-03-07 at higher magnification

Figure 7.2.2-41. Fracture surface photographs for a 0.06-inch thick Ti 6Al-4V coupon subjected to an autofrettage strain of 1% (with stable tearing).



- A) Coupon Ti-Dome-060-03-08 at low magnification
- B) Coupon Ti-Dome-060-03-08 at higher magnification

Figure 7.2.2-42. Fracture surface photographs for a 0.06-inch thick Ti 6Al-4V coupon subjected to four consecutive autofrettage cycles of 1% to 0% strain.

- **F-12.** The amount of crack growth during autofrettage was small (i.e., <0.002 inch) and relatively independent of crack depth and strain level provided that the crack tip conditions were below the onset of stable tearing.
- **F-13.** Stable tearing leading to failure (i.e., crack growth to the back surface) was observed at conditions just beyond the onset of stable tearing.
- **F-14.** The stable tearing was observed to be greater at an angle of about 30-degrees to the surface rather than at the maximum depth location (90-degrees to the surface), that appears to be in agreement with the simulations based on ASTM E2899.
- **F-15.** The amount of crack growth due to 4 consecutive autofrettage cycles was never measured to be greater than the amount of crack extension in a single autofrettage cycle, multiplied by four, provided stable tearing was not present.

7.2.3 Damage Tolerance Tests

Tests were conducted on COPVs with cracks in the liners subjected to pressure loading that simulated four operational lifetimes. Uniaxial tests were conducted on cracked coupons subjected to tensile strains that represented the hoop strains expected in the COPV tests. The goal was to demonstrate a test-based methodology for validating safe-life requirements for COPVs with thin-wall liners. The crack growth measurements will be used to complement the autofrettage testing (Section 7.2.2) and best practices (Section 7.3). This section describes the test methodology and presents test data from the COPVs and uniaxial coupons.

7.2.3.1 COPV Pressurization Test Methodology

The pressurization tests were conducted on wrapped AA6061-T6 liners with a volume of about 550 in³, as shown schematically in Figure 7.2.3-1. The 0.09-inch thick liners were chemically milled to a target thickness of less than or equal to 0.036 inch. However, post-test measurements indicated that the thickness was at least 0.04 inch in some locations. Nine EDM notches were placed in the cylindrical section of each of the reduced thickness liners, as illustrated in Figure 7.2.3-2. The notches were orientated along the axis of the liners to orientate the crack opening direction with the hoop stress. The bare liners were cycled elastically and the cracked liners were wrapped with the composite. The cyclic pressure history was applied to the COPVs. The following sub-sections will describe each step in the process.

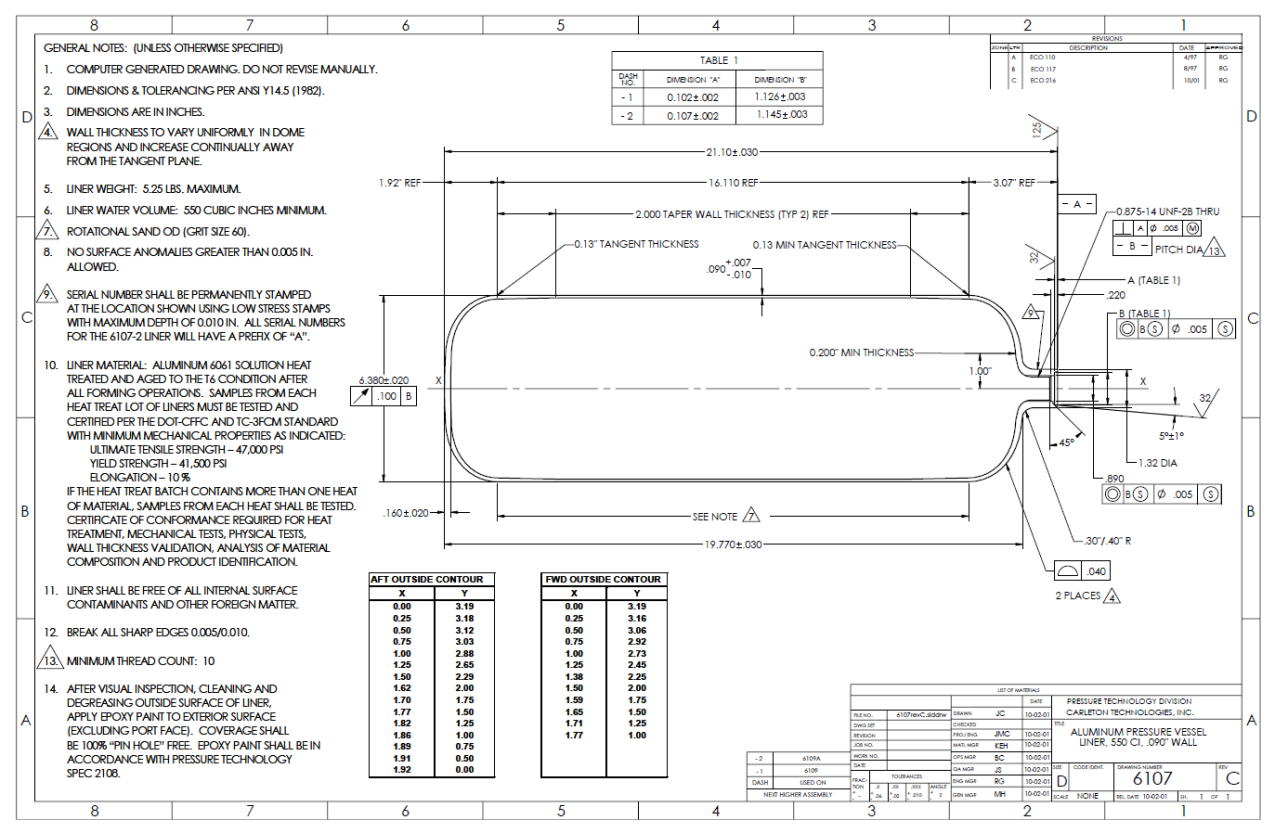


Figure 7.2.3-1. Schematic of AA6061-T6 liners.

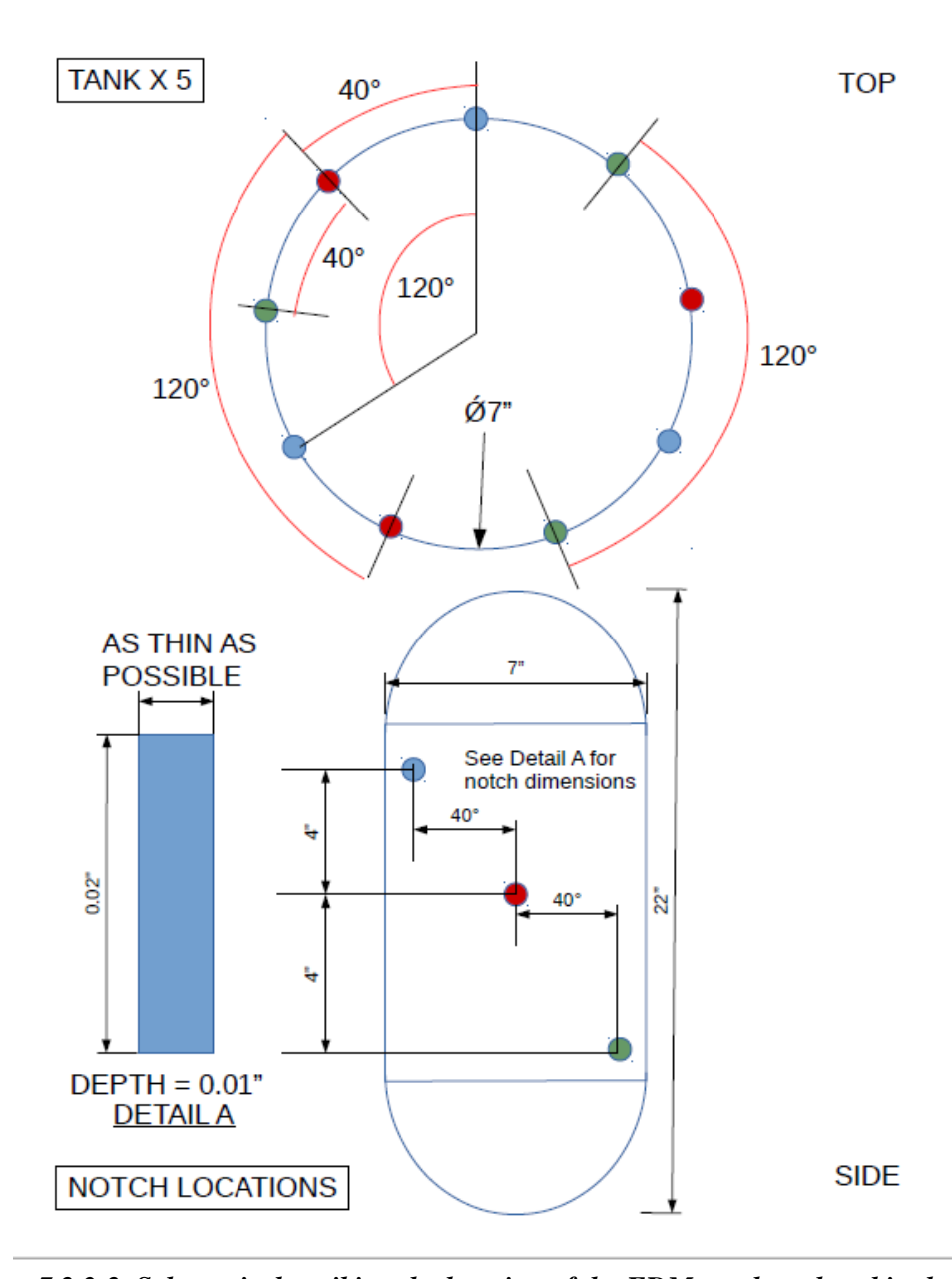


Figure 7.2.3-2. Schematic describing the location of the EDM notches placed in the liners.

Elastic Precracking of the Bare Liners

Fatigue cracks were introduced into the bare liners by pressure cycling the notched tanks elastically. The hoop stress during cyclic pressure needed to be below the material yield stress and the liner hoop stress due to the maximum design pressure (MDP). The yield stress of the material was about 41 ksi and the expected liner hoop stress at MDP was 29 ksi, so a target precrack hoop stress of 28 ksi was selected. The Young-Laplace equation for estimating the hoop stress in a pressurized cylinder (Equ. 7.2.3.1) was used to estimate the required precrack pressure. The radius of the liner was estimated to be 3.2 inches and the thickness was estimated to be 0.035 inch, thus a hoop stress of 28 ksi would require a pressure of 300 psig.

$$S = \frac{Pr}{t}$$
 Equ. 7.2.3.1

Where:

S = hoop stress

P = Internal pressure

r = liner radius

t = liner thickness

The precracking was performed by applying pressure cycles between 0 and 300 psi at a rate of about 6 cycles/minute. Periodic surface crack length measurements using a 20x optical scope were taken to determine when the longest crack has reached the target length. Uniaxial coupons of AA6061-T6 sheet material with a similar notch were fatigue cycled at a maximum stress of 28 ksi and R = 0.1 to determine the number of cycles required to nucleate a fatigue crack (i.e., \sim 20,000 cycles). Based on the uniaxial coupon results, the initial crack length measurement was taken after 10,000 cycles and subsequent measurements were made at smaller cycle increments as the longest crack approached the target length. The cycling was planned to stop when the longest crack reached the target length.

The liners used were susceptible to cracks nucleating at manufacturing induced defects on the inner mold line (IML), while optical measurement could only be made on the outer mold line (OML) The largest IML cracks nucleated from long shallow defects and, once nucleated, grew faster in the depth direction than the semi-circular notches. Periodic eddy current inspection was performed to determine if cracks were nucleating on the IML and stop the precracking before the crack growth through the thickness, as described in Appendix K. This precracking process is derived from Reference 8.

- **O-5.** Test coupon precracking process via inserting EDM notches and pressure cycling was demonstrated to grow flaws to the target initial flaw size.
- **F-16.** Long, shallow cracks nucleating from naturally occurring IML defects were reliably detected from the OML using eddy current inspection.

Composite Wrapping

Liners with precracks were overwrapped as shown in Figure 7.2.3-3. The wrap consisted of the Hexagon MasterWorks wrap pattern [ref. 22] that contained hoop and helical layers. The COPV manufacturing information and constituents of the composite [ref. 23] are summarized in Table 7.2.3-1.

Table 7.2.3-1. COPV Manufacturing Information

Liner:

Manufacturer: SamtechOriginal thickness: 0.09 inch

• Baseline PN 6107 chem-milled to 0.032 inch minimum sidewall thickness

Resin System

• Epoxy Resin System

Carbon Fiber

• T1000-12000-40D

• Lot Number J6117C1

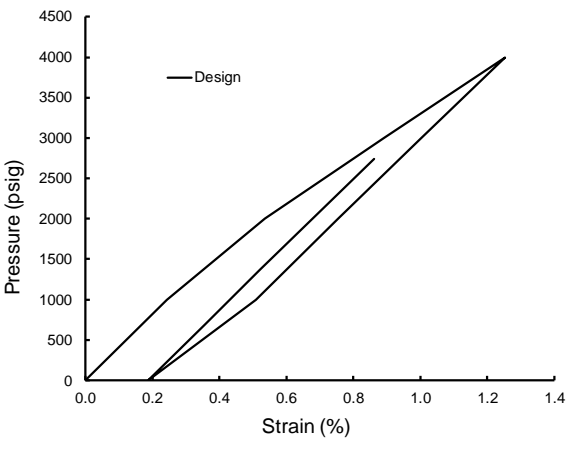
Winding Cell Setup and Verification

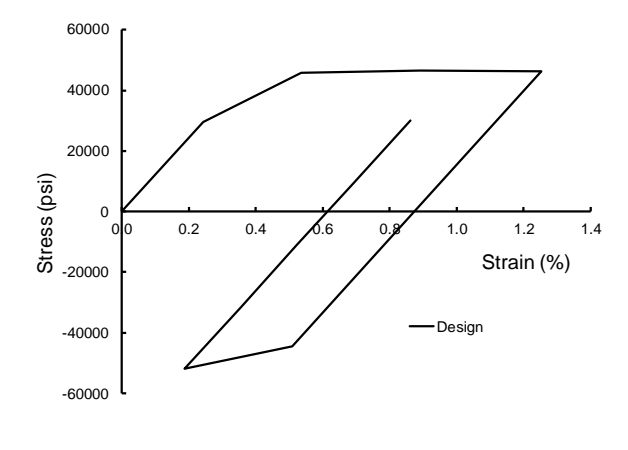
• Verified IAW-MWI_00021_A

The COPVs had a demonstrated burst pressure of about 6,200 psig. The estimated autofrettage strain was 1.25% and was achieved at a pressure of 4,000 psi. Upon unloading from the autofrettage pressure, the residual strain in the liner was 0.2%. The subsequent MDP pressure was 2,745 psig and resulted in an estimated strain of 0.85%. The design pressure vs. strain and stress vs. strain are shown in Figure 7.2.3-4. Additional details of the test COPV development are provided in [ref. 15].



Figure 7.2.3-3. Wrapping of the liners with the composite [ref. 15].





A) Design pressure and strain response

B) Design stress vs. strain behavior

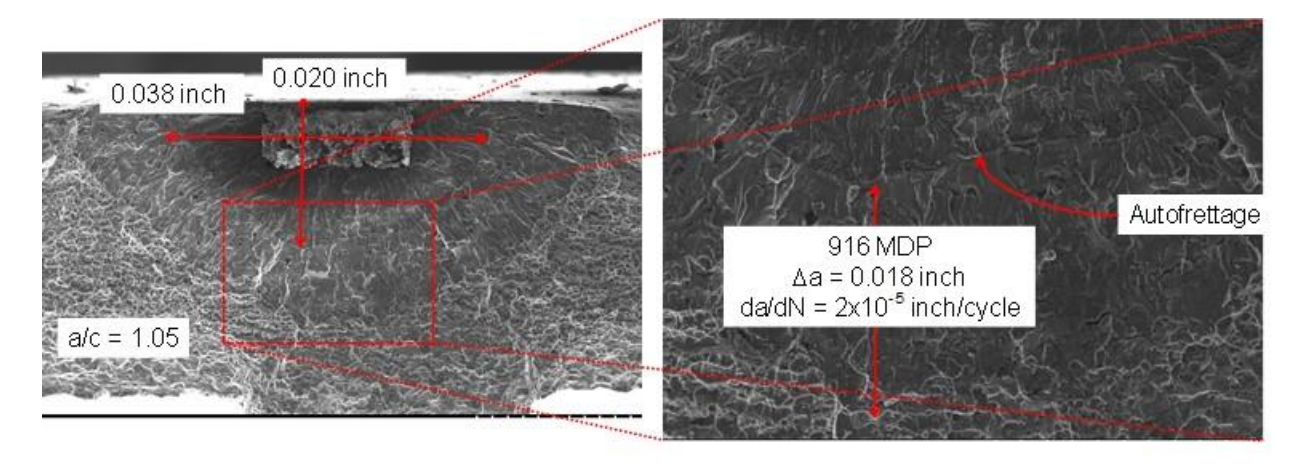
Figure 7.2.3-4. Design behavior of the COPV liner.

7.2.3.2 Pressure Testing

Five COPVs with liner fatigue cracks were pressure tested. COPV 18074 had one autofrettage cycle to 4,000 psig followed by 916 MDP cycles to 2,745 psig (AF&916xMDP). The liner leaked at a crack that nucleated on the IML on cycle 917 and cycling stopped. The nine OML cracks that nucleated from the EDM notches produced fracture surfaces that generated da/dN information from markings on the surface. The autofrettage cycle provided an interface between the precrack and the fatigue regions, and the end of the fatigue region was bounded by the ductile fracture, as shown in Figure 7.2.3-5. The extent of crack growth due to MDP cycles was measurable as the difference between the autofrettage marking and the ductile fracture. The crack growth due to the autofrettage cycle was measurable, as shown in Figure 7.2.3-6. The number of MDP cycles for the other COPVs was selected to be 200 based on the number of cycles required for COPV 18074 to leak.

COPV 18086 leaked during the initial autofrettage cycle. A crack on the IML was detected during precracking by eddy current inspection (see Appendix K) and was observed to rapidly grow in intensity, as shown in Figure 7.2.3-7. The precracking was halted before the cracks nucleating from the surface notches reached the target sizes. The COPV leaked during the initial autofrettage cycle and the failure site was a long, shallow crack (i.e., $a/c \sim 0.04$) that was at least 0.45 inch long and about 0.010-inch deep, as shown by the photograph of a portion of the crack in Figure 7.2.3-8.

COPV 18099 had four consecutive autofrettage cycles followed by 800 MDP cycles (4xAF & 800xMDP). Six of the nine OML notches yielded cracks with measurable growth. The amount of crack growth during the four autofrettage and 800 MDP cycles could be measured and the average da/dN calculated as shown in Figure 7.2.3-9a. The four individual autofrettage cycles were visible and the total autofrettage crack growth was measured, as shown in Figure 7.2.3-9b.



A) Crack N9 of COPV 18074

B) Crack N9 of COPV 18074 at higher magnification

Figure 7.2.3-5. Fracture surface of OML crack N9 for COPV 18074.

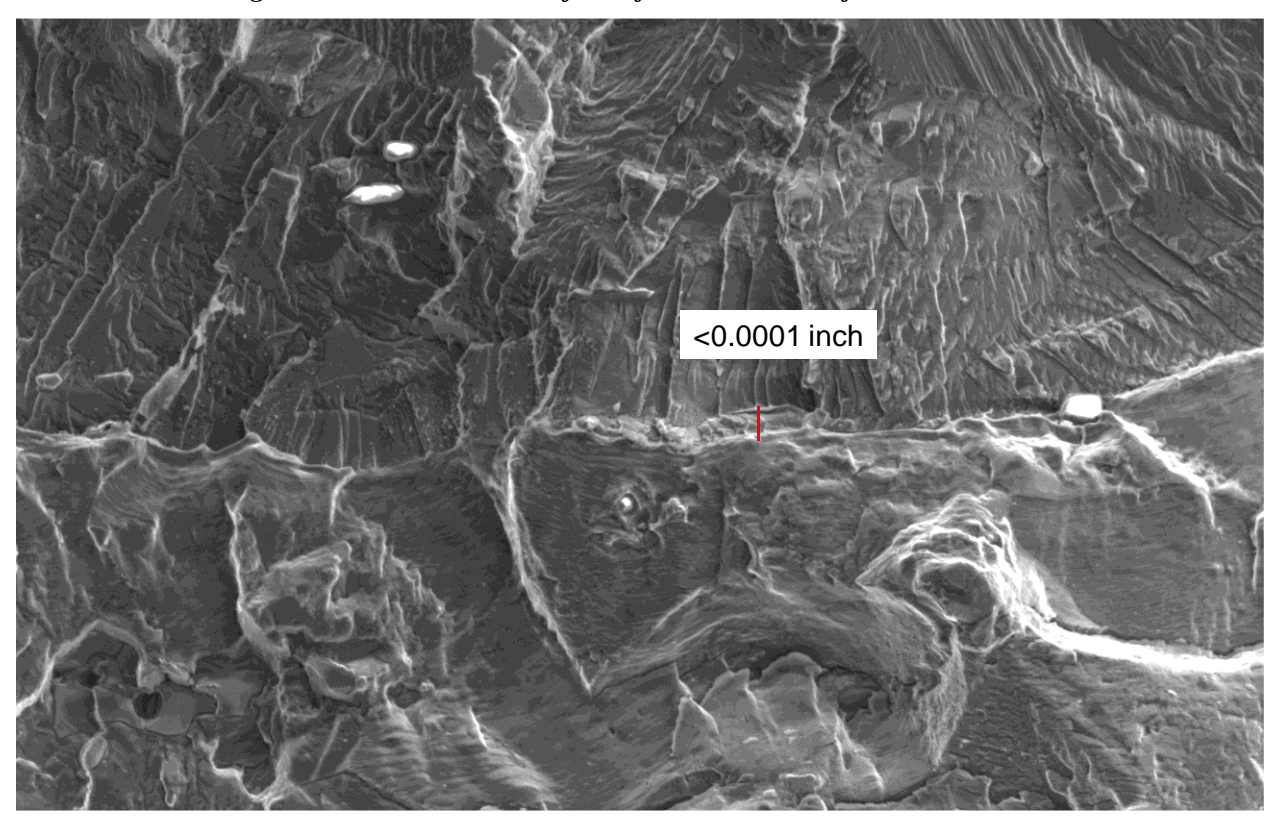


Figure 7.2.3-6. Autofrettage crack growth in crack N1 of COPV 18074.

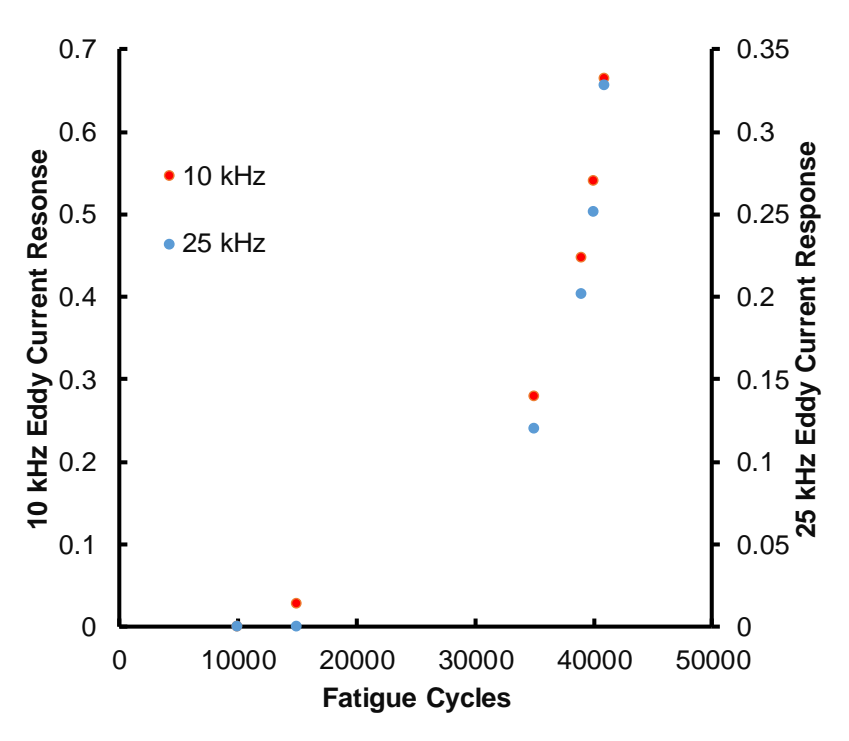


Figure 7.2.3-7. Eddy current response for the IML crack that leaked during the COPV 18086 autofrettage cycle.

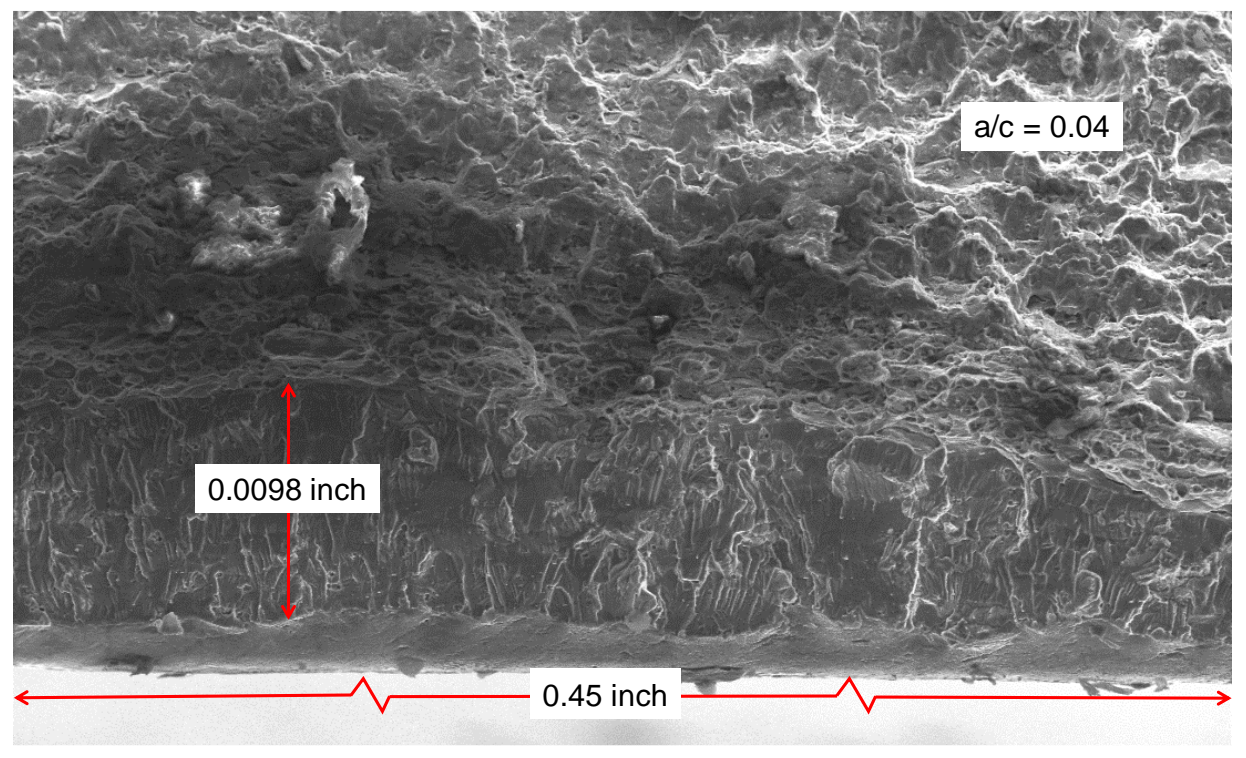
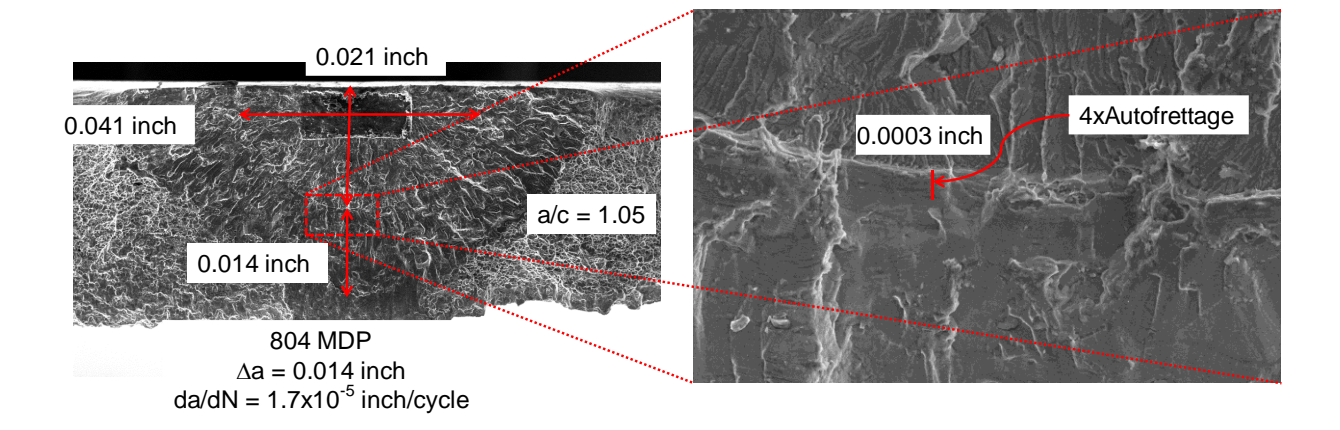


Figure 7.2.3-8. Deepest section of the long, shallow crack that leaked during the autofrettage of tank 18086.



A) Crack C4 of COPV 18099

B) Crack C4 of COPV 18099 at higher magnification

B) Crack C4 of COPV 18072 at higher magnification

Figure 7.2.3-9. Crack growth for an OML crack in COPV 18099 (4xAF & 800 MDP).

COPVs 18072 and 18092 were tested with 4 repeats of an autofrettage cycle followed by 200 MDP cycles, or (4x(AF & 200 MDP)). The COPV 18072 did not complete all four sets with leaking detected after 116 of the last 200 MDP cycles. The initial autofrettage cycle resulted in the most pronounced fracture surface marking, but the other three autofrettage cycles created faint markings, as shown in Figure 7.2.3-10. The amount of crack growth during the initial autofrettage cycle of crack C4 of COPV 18072 was less than 0.0002 inch, as shown in Figure 7.2.3-11. A summary of all of the COPV pressurization tests in provided in Table 7.2.3-2. The cracks were used to correlate the fracture surfaces with the NDE measurements. The crack location was specified as growing from the OML from a notch or nucleating from an IML naturally occurring defect. Additional images of COPV test fracture surfaces are found in Appendix N.

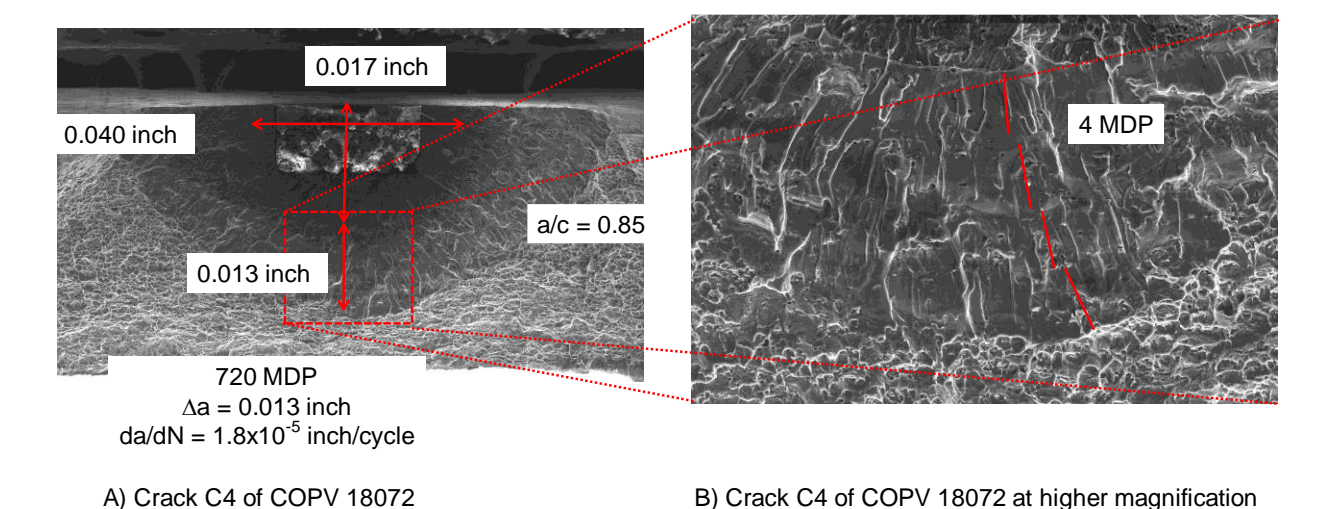


Figure 7.2.3-10. Fracture surface for crack C4 of COPV 18072.

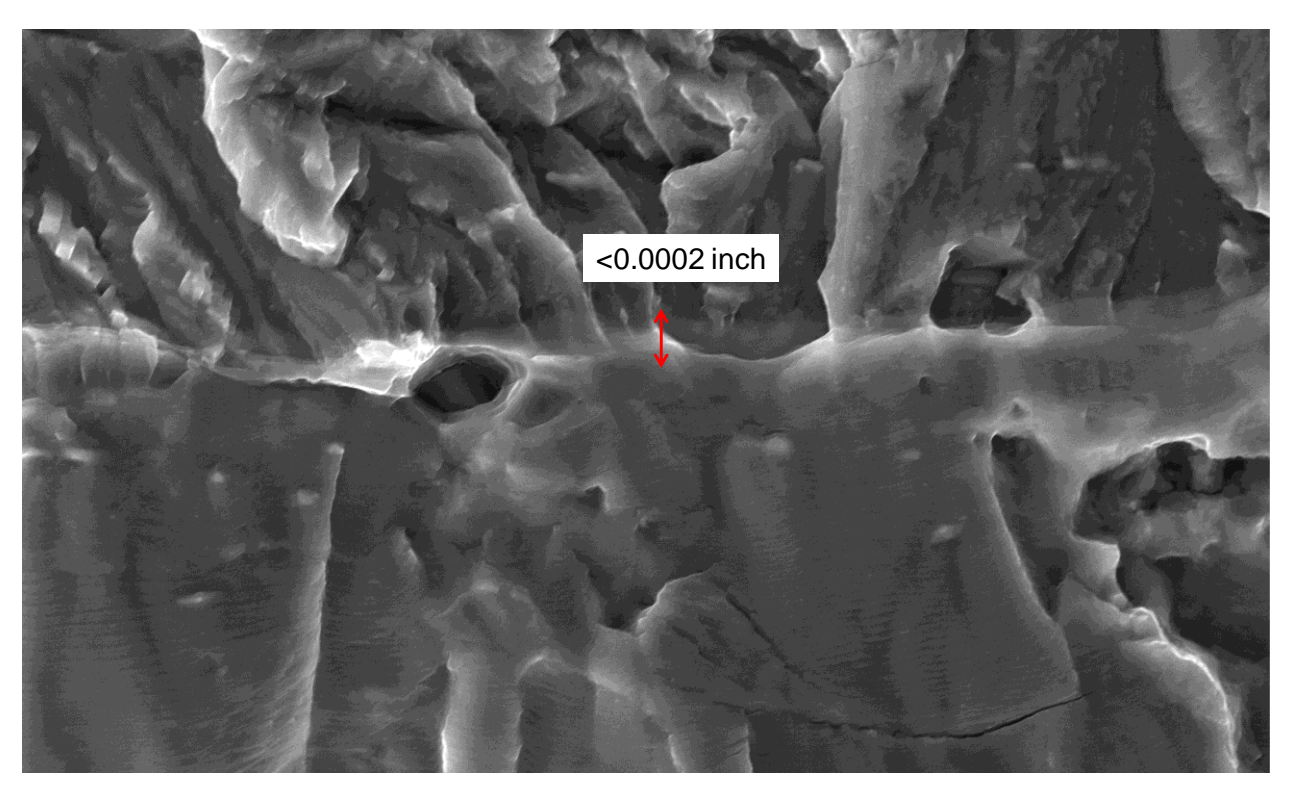


Figure 7.2.3-11. Autofrettage crack growth region in crack C4 of COPV 18072.

Table 7.2.3-2. Summary of Pressurized COPV Tests

COPV 18074 - 1AF and 916 MDP Cycles						COPV 18092 – 4x(AF & 200MDP)										
Crack IML	Location	a _{initial} (inch)	2c _{initial} (inch)	a _{final} (inch)	2c _{final} (inch)	Cycles	da/dN (inch/cyc le)	Crack IML	Location	a _{initial} (inch)	2c _{initial} (inch)	a _{final} (inch)	2c _{final} (inch)	Cycles	da/dN (inch/cycl e)	
C2	OML	0.0123	0.0251	0.0162	0.0312	917	4.25E-06	C1	OML	0.0176	0.0381	0.026	0.0614	804	1.04E-05	
C3	OML	0.0109	0.0257	0.0148	0.034	917	4.25E-06	C2	OML	0.01	0.0239	0.0144	0.028	804	5.47E-06	
C4	OML	0.0206	0.0401	0.0343	0.0787	917	1.49E-05	C3	OML	0.0214	0.0406	0.0369	0.0725	804	1.93E-05	
C5	OML	0.0112	0.022	0.0137	0.028	917	2.73E-06	C4	OML	0.018	0.0301	0.0252	0.0524	804	8.96E-06	
C7	OML	0.0147	0.0335	0.021	0.0518	917	6.87E-06	C5	OML	0.0179	0.0394	0.0278	0.0704	804	1.23E-05	
C8	OML	0.0145	0.0297	0.0195	0.0518	917	5.45E-06	C6	OML	0.0216	0.039	0.0323	0.0804	804	1.33E-05	
C9	OML	0.0147	0.0286	0.0204	0.0419	917	6.22E-06	C7	OML	0.014	0.0333	0.022	0.0543	804	9.95E-06	
N2	OML	0.0225	0.0509	0.0352	0.0871	917	1.38E-05	C8	OML	0.0126	0.0287	0.0188	0.0407	804	7.71E-06	
34	IML	0.0169	0.0583	0.0367	0.133	917	2.16E-05	C9	OML	0.0169	0.0373	0.029	0.0681	804	1.50E-05	
					1	IML	0.0024	0.099	0.0066	0.111	804	5.22E-06				
COPV 18086 – Failed on First Autofrettage Cycle					4	IML	0.0082	0.0338	0.0171	0.0661	804	1.11E-05				
COPV 18099 – 4AF and 800 MDP Cycles								COPV 18072 – 3x(AF & 200MD) + AF & 116MDP								
Crack IML	Location	a _{initial} (inch)	2c _{initial} (inch)	a _{final} (inch)	2c _{final} (inch)	Cycles	da/dN (inch/cyc le)	Crack IML	Location	a _{initial} (inch)	2c _{initial} (inch)	a _{final} (inch)	2c _{final} (inch)	Cycles	da/dN (inch/cycl e)	
N1	OML	0.0127	0.0298	0.0174	0.0424	804	5.85E-06	C1	OML	0.0194	0.0413	0.029	0.0646	720	1.33E-05	
N2	OML	0.0219	0.0386	0.0325	0.0796	804	1.32E-05	C2	OML	0.0193	0.0398	0.0252	0.0614	720	8.19E-06	
N3	OML	0.019	0.0418	0.0307	0.0715	804	1.46E-05	C4	OML	0.0203	0.0401	0.0295	0.065	720	1.28E-05	
N4	OML	0.0227	0.043	0.0331	0.0756	804	1.29E-05	C5	OML	0.0197	0.0436	0.0305	0.0718	720	1.50E-05	
N5	OML	0.014	0.0327	0.0179	0.0437	804	4.85E-06	C6	OML	0.0157	0.0343	0.02	0.0475	720	5.97E-06	
N6	OML	0.0242	0.0441	0.0323	0.0833	804	1.01E-05	C9	OML	0.0216	0.0364	0.0297	0.0571	720	1.13E-05	
N7	OML	0.0227	0.0496	0.037	0.114	804	1.78E-05	C7	OML	0.0116	0.0284	0.0161	0.0393	720	6.25E-06	
N8	OML	0.0118	0.0326	0.0173	0.0424	804	6.84E-06	C8	OML	0.0132	0.0253	0.018	0.0379	720	6.67E-06	
N9	OML	0.019	0.0393	0.0288	0.0685	804	1.22E-05	12	IML	0.0177	0.0347	0.041	0.094	720	3.24E-05	

7.2.3.3 Uniaxial Fatigue Tests

Dogbone-shaped coupons were fatigue cycled to the strain levels determined by the analysis used to design the COPVs [ref. 15]. The coupons had a 2 inch gage section, as shown in Figure 7.2.3-12. The testing was performed by loading the coupons in displacement control to the strains that the design analyses predicted for the autofrettage and MDP cycles of the COPVs. The strains in the coupon were measured with edge extensometers, as shown in Figure 7.2.3-13. The minimum strains require that the uniaxial coupons be subject to large compressive loads without buckling, so guide plates were used to "sandwich" the coupon. The inside surfaces of the guide plates were covered with Teflon[©] tape to minimize any load transfer due to friction. The bolts that held the guide plates together were finger tightened to allow the guide plates to slide easily along the coupon. The full strain history was applied to the coupons, as determined by analysis. The influence of the compressive stresses that follow the autofrettage cycle can have a significant influence on the subsequent da/dN behavior, so truncation at zero stress to eliminate the need for guide plates will usually result in unconservative results. Appendix L provides additional data to support the requirement of replicating the entire strain history.

The stress-strain behavior measured for an autofrettage cycle and a subsequent MDP cycles is shown in Figure 7.2.3-14 with the predicted stress-strain behavior from the analysis of the COPVs. Loading up to autofrettage produced similar behavior in the analysis and uniaxial coupons, but the slope of the initial linear portion of the analysis curve, or stiffness, was about 20% greater than measured uniaxial behavior (i.e., 12 Msi for analysis vs. 10 Msi from test). The slope of the uniaxial curve was the elastic modulus and was identical to the value used in the design analysis. The higher initial stiffness of the design analysis was due to the biaxial stress reducing the strain in the hoop direction. Consider Hooke's Law with the hoop direction being the x-direction and the circumferential direction being the y-direction.

$$e_{xx} = \frac{1}{E} \left(\sigma_{xx} - v \sigma_{yy} - v \sigma_{zz} \right)$$
 7.2.3.2

Where:

 e_{xx} = strain in the hoop direction

E = Elastic modulus determined from uniaxial tensile tests

 σ_{xx} = Hoop stress

 σ_{yy} = Circumferential stress = $\sigma_{xx}/2$ (for a cylindrical COPV liner)

 σ_{zz} = Through-thickness stress = 0

 $\upsilon = Poisson's ratio$

Therefore, the apparent elastic modulus based on the hoop stress and strain is:
$$\frac{\sigma_{xx}}{e_{xx}} = \frac{E}{(1-v/2)}$$
 7.2.3.3

A value of v = 0.33, as used in the design analysis, would produce the difference in stiffness observed in Figure 7.2.3-14. Thus, the uniaxial coupon tests of crack growth at the COPV liner strain levels achieved the same hoop strain and peak stresses (both at autofrettage and MDP), but not the minimum stresses after autofrettage and MDP. Additional discussion of using uniaxial coupons to simulate crack growth in a biaxial COPV liner is included in Appendix O.

The uniaxial coupons were notched using the technique used on the liners, but with only a single notch per coupon. The coupons were fatigue precracked with a maximum stress of 28 ksi and R = 0.1 with a target 2c=0.05 inch. The coupons were loaded in displacement control at rates of 0.01 to 0.05 inch/minute to specific strain values as measured by the edge extensometers. The

guide plates had a hole that allowed CMOD DIC measurement, as shown in Figure 7.2.3-15. Two types of loading spectra were applied: (1) 4xAF & 800xMDP, and (2) 4x(AF & 200xMDP). The strain range for the autofrettage cycles was 1.25% and 0.2% and the strain range for the MDP cycles was 0.85% to 0.2%. The resulting applied stresses are shown in Figure 7.2.3-16. As shown in Figure 7.2.3-16, the uniaxial tests included the full compression cycles. The CMOD was measured for the autofrettage cycles for these spectra and was plotted with the applied stress, as shown in Figure 7.2.3-17. The CMOD vs. stress curves for the autofrettage cycles of 4xAF & 800xMDP spectrum were nearly identical, while those of the 4x(AF & 200xMDP) spectrum exhibited an increase in the amount of CMOD for each subsequent cycle. This suggests that the crack is growing during the 200 MDP cycles and the autofrettage cycles in the 4x(AF & 200xMDP) spectrum may be more damaging than those in the 4xAF & 800xMDP spectrum. The coupons were monotonically loaded to failure after the completion of the spectrum cycles. The post-test fracture surface examinations of tests conducted with the two loading spectra are shown in Figures 7.2.2-18 and 7.2.2-19. The initial autofrettage cycle provided a mark that indicated the end of the precrack and the start of the fatigue crack growth. The ductile fracture of the monotonic loading marked the end of the fatigue crack growth region. The F-TL-090-13 uniaxial coupon that was loaded with the 4xAF &800xMDP spectrum had a slightly larger initial crack than the F-TL-090-07 coupon loaded with the 4x(AF& 200xMDP) spectrum. However, even with a smaller initial crack, the specimen loaded with the 4x(AF & 200xMDP) spectrum experienced more than 20% more crack growth in the depth direction than the coupon that was loaded with the 4xAF and 800 MDP spectrum.

- **F-17.** The autofrettage cycles provided a distinct mark on the fracture surface that was used to determine the amount of crack growth.
- **F-18.** The crack depth measurements demonstrated that the coupon that was truncated (i.e., excluding the compressive loading following the autofrettage cycle) grew slower than the coupon with the full loading history.
- **F-19.** Uniaxial coupon tests of crack growth at the COPV liner strain levels achieved the same hoop strain and peak stresses (both at autofrettage and MDP), but not the minimum stresses after autofrettage and MDP.

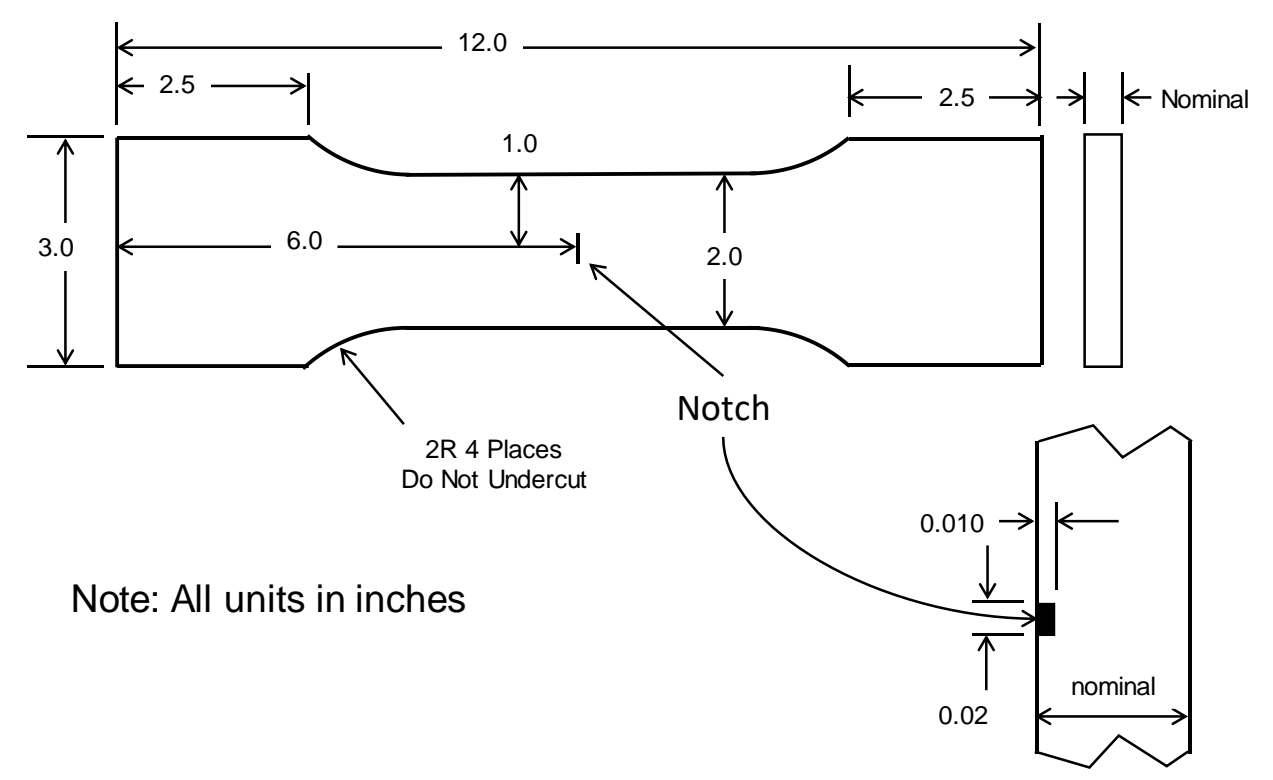


Figure 7.2.3-12. Coupon design for the uniaxial fatigue crack growth tests.

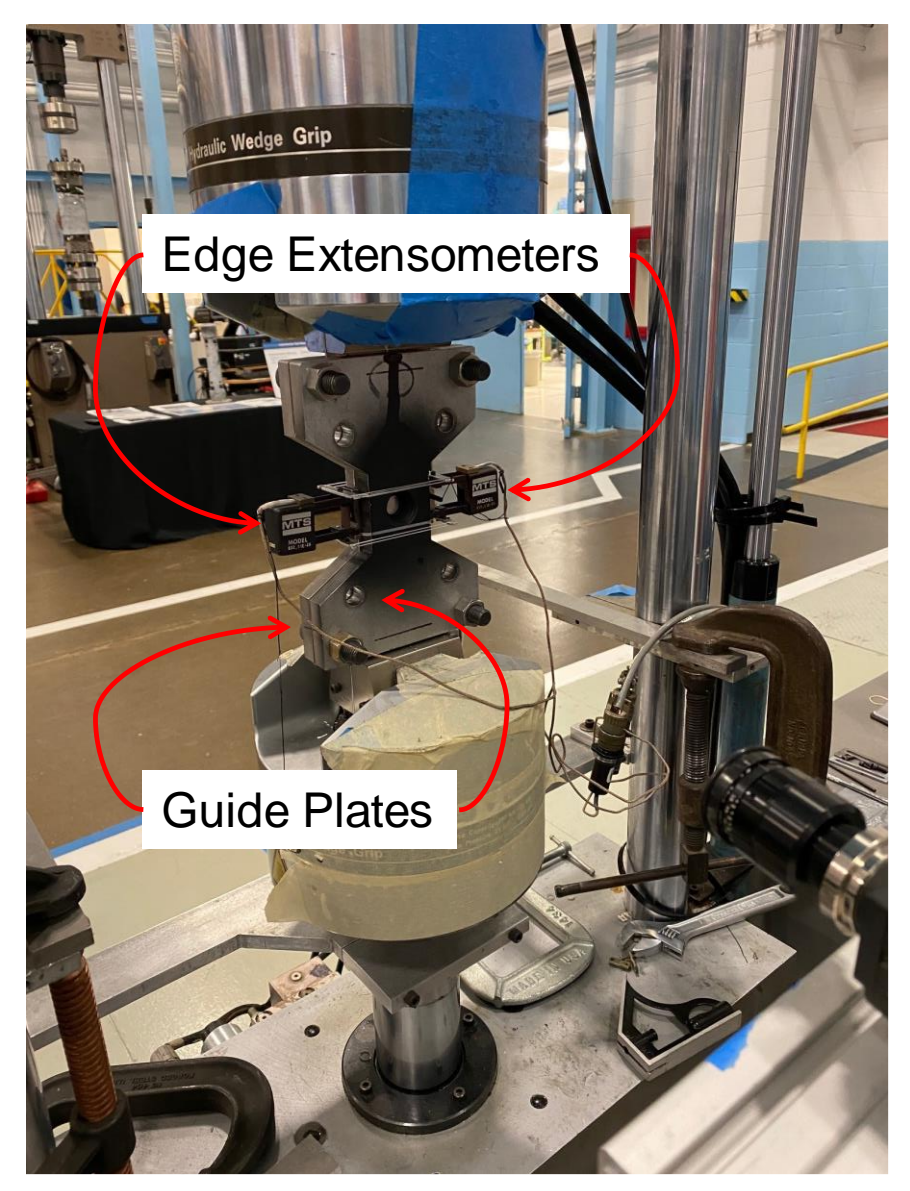


Figure 7.2.3-13. Uniaxial coupon testing setup.

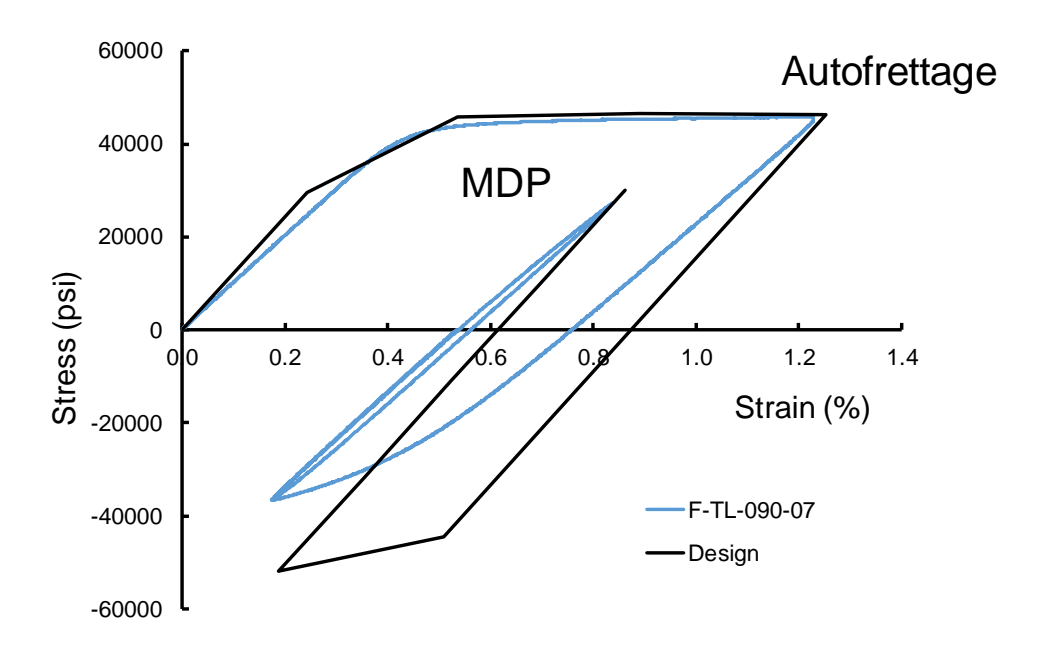


Figure 7.2.3-14. Predicted stress-strain behavior for the COPVs and the measured stress-strain behavior for the uniaxial coupons.

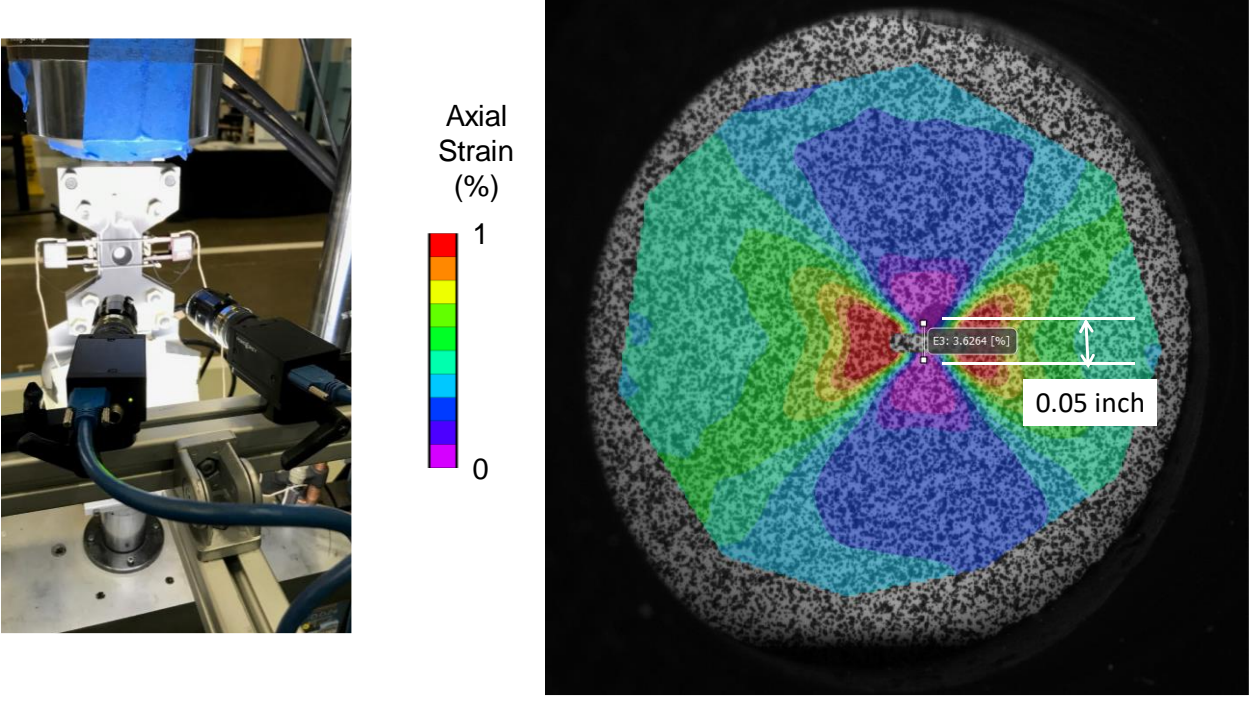


Figure 7.2.3-15. DIC measurement of the CMOD for the uniaxial coupons.

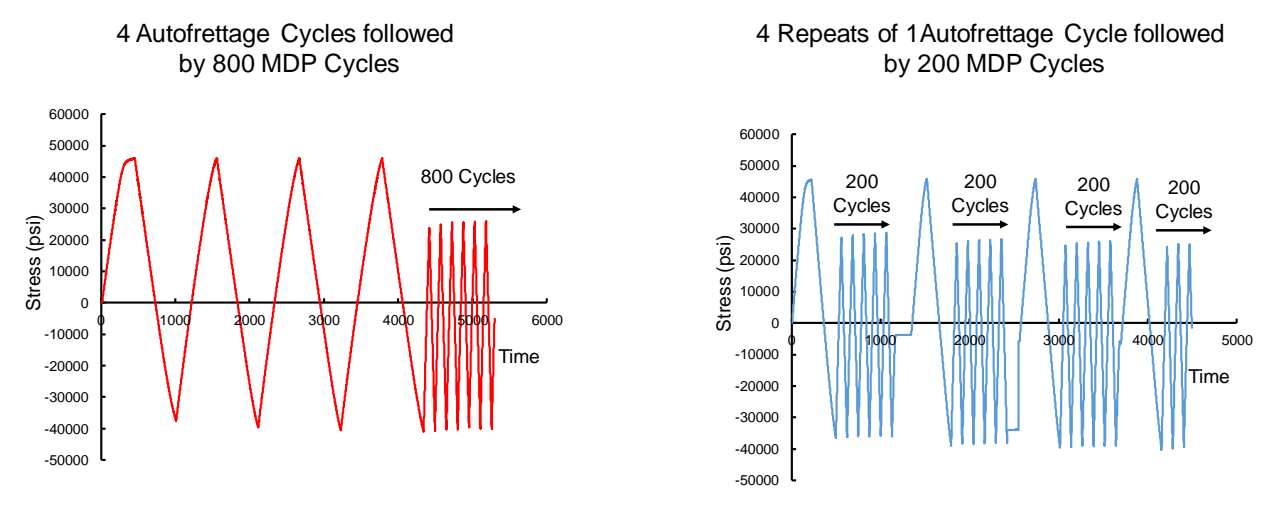


Figure 7.2.3-16. Applied stresses for the two uniaxial coupon loading spectra.

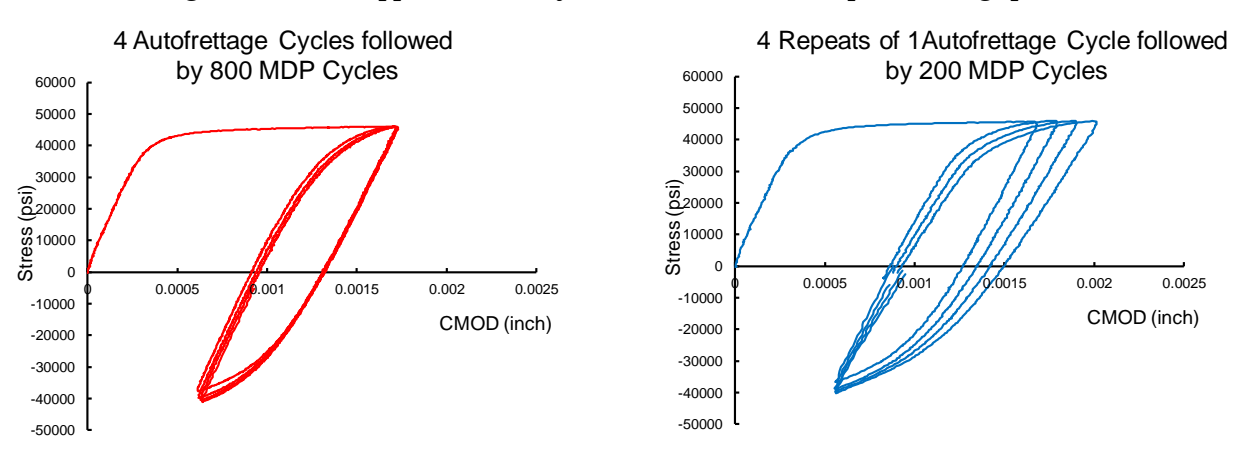


Figure 7.2.3-17. CMOD measurements for the autofrettage cycles of the two spectra.

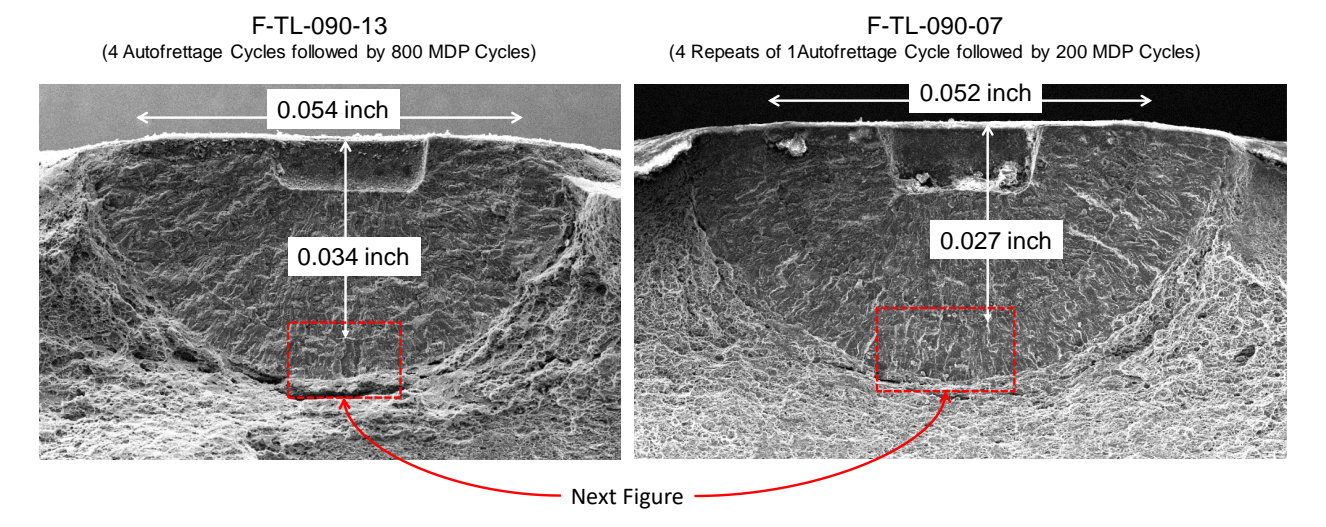
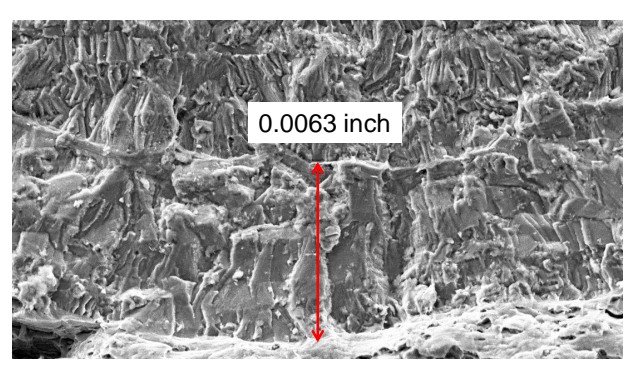


Figure 7.2.3-18. Fracture surfaces for two uniaxial coupon tests.



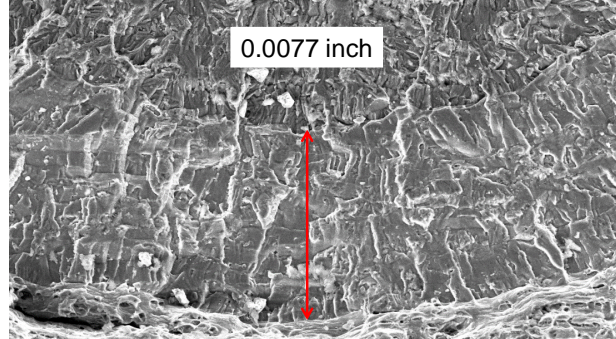


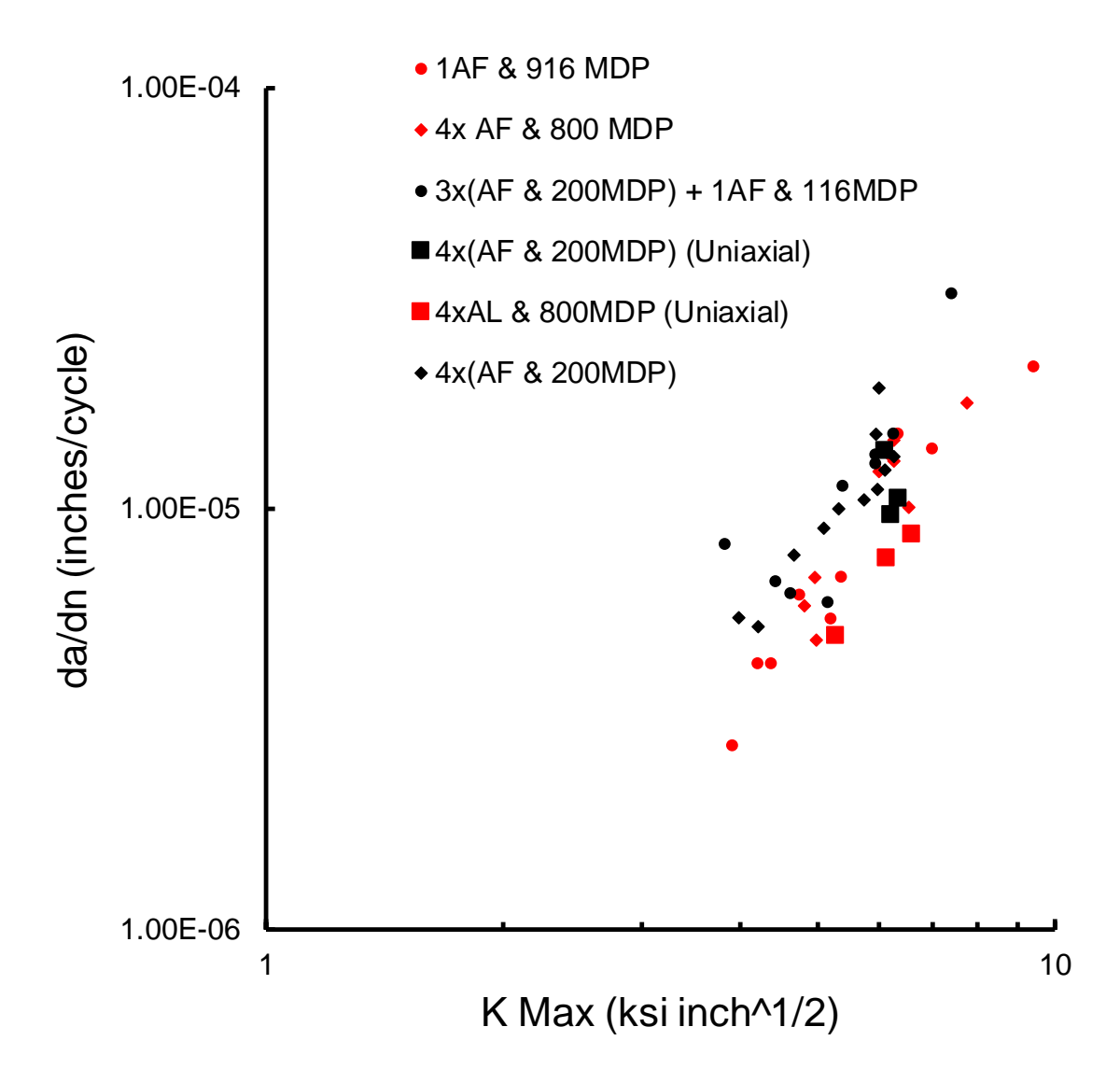
Figure 7.2.3-19. Higher magnification images of the fracture surface.

7.2.3.4 da/dN Results

Examination of the fracture surfaces provided the crack size and shape at the end of fatigue precracking and spectrum loading. The average da/dN in the depth direction was obtained by dividing the difference between the *a* at the end of the spectrum loading and the *a* at the end of precracking by the total number of cycles applied. Likewise, the average K was determined from the average of the starting and ending crack lengths and widths. The stress used in the K calculation was 29 ksi, representing the stress of the MDP cycles. The K of the IML cracks was influenced by the internal pressure loading acting on the crack faces. An estimate of the influence was obtained from the solution of a pressure loaded crack in an infinite body, as given by Equ. 7.2.3.4 [ref. 8]. The total K was the superposition of the stress intensity factor due to the hoop stress (Khoop) and the influence of the MDP pressure loading (PMDP). The plot of the average da/dN as a function of the average stress intensity factor is shown in 7.2.3.20. Also plotted in 7.2.3.20 are the results the uniaxial coupon tests for the two loading histories. The comparison between the 4xAF and 800 MDP da/dN (red points) and the 4x(AF & 200xMDP) da/dN (black points) suggests that the 4x(AF & 200xMDP) results in a faster crack growth.

$$K = K_{hoop} + P_{MDP}\sqrt{\pi a}$$
 (Equ. 7.2.3.4)

- **O-6.** Liner IML and OML crack da/dN correlated when the K solution for the IML cracks included the influence of crack face pressure.
- **F-20.** The average da/dN from coupons and liners with the 4x(AF & 200 MDP) load spectrum were faster than those measured from coupons and liner with 4xAF and 800 MDP load spectrum.



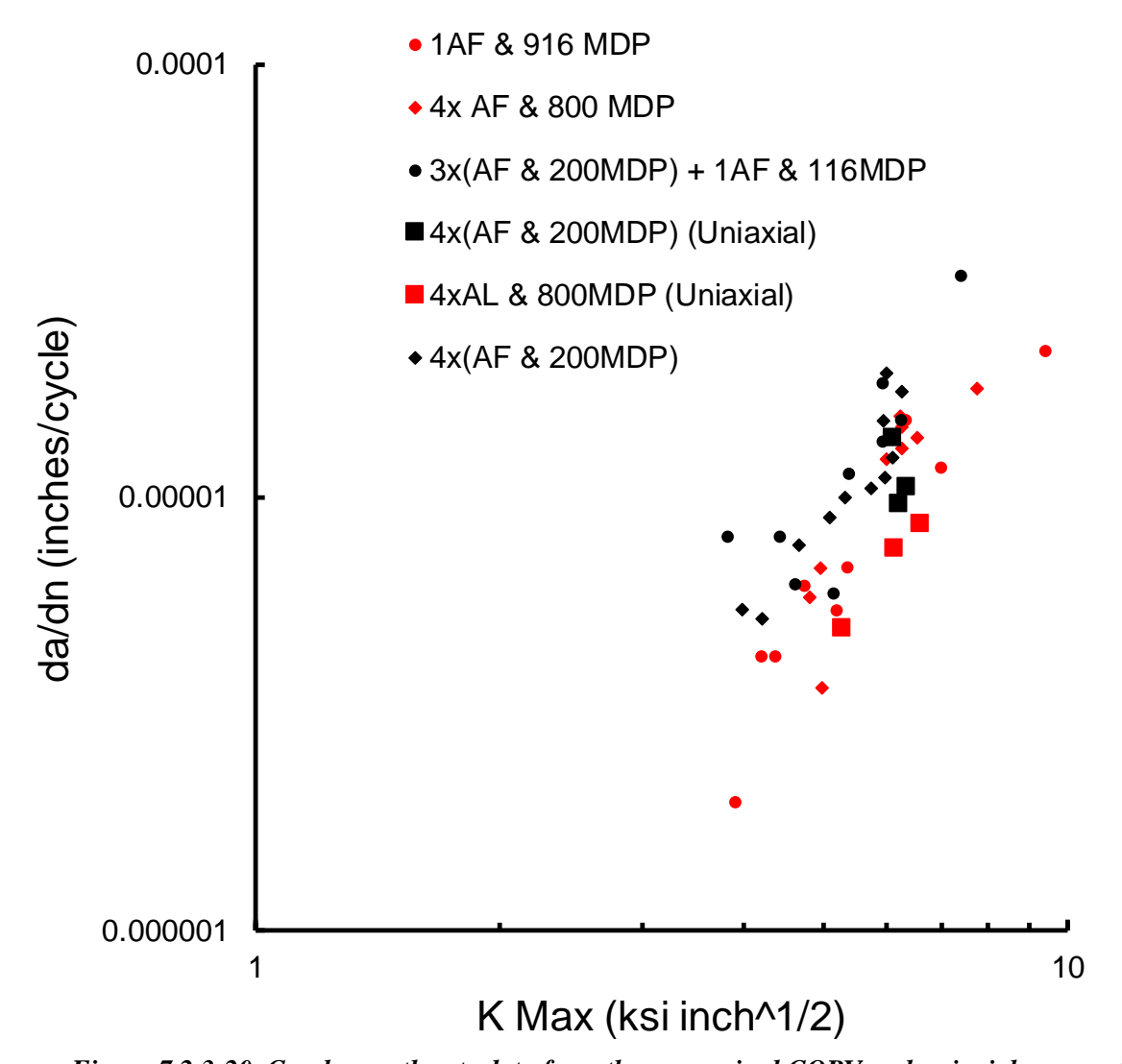


Figure 7.2.3-20. Crack growth rate data from the pressurized COPV and uniaxial coupon tests.

7.3 Best Practices for Complying with AIAA/ANSI S-081B Damage Tolerance Life Requirements

This section provides an overview of best practices for complying with AIAA S-081B damage tolerance life requirements. These best practices were identified during the NESC COPV Life Test Assessment of elastically responding COPV liners that generated:

- Data to evaluate the limitation of the LEFM computational methods used to predict crack growth behavior
- Tests to demonstrate methodology for validating COPV damage tolerance life requirements

Each best practice is summarized in a table with:

- Identification of the relevant section of AIAA S-081B
- Requirement text from AIAA S-081B
- Best practice text

- Summary of evidence supporting the best practice
- Reference to more detailed data in this report describing the evidence for the best practice
- Notes

In AIAA S-081B, damage tolerance life requirement, verification, analysis, and test requirements are listed in sections 5.2.13.1, 6.2.1, 7.5.1, and 10.1, respectively. Section 7.1 addresses the selection of material properties for analysis. The best practices do not address every requirement in these sections of AIAA S-081B.

Best Practice	DTL-1
AIAA S-081B Section	5.2.13.1

AIAA S-081B Requirement

The region(s) of the COPV to which damage tolerance is applied shall be designed such that the COPV liner possesses a minimum damage tolerance life of four (4) times the service life without sustained load crack growth, detrimental deformation, leakage, or rupture.

Best Practices

Demonstrate by test and/or validated elastic-plastic fracture analysis that stable tearing does not occur during the service life, including autofrettage

Ensure margin to stable tearing is characterized.

Margin to stable tearing can be identified by testing with larger crack sizes than NDE minimum detectable flaw or larger strains than identified COPV stress analysis.

A minimum of ten coupons is necessary to establish the margin; five coupons should be at crack depths near the NDE minimum detectable flaw and target strain, and five coupons should be at larger crack sizes or strain levels.

Evidence Summary	Stable tearing leading to failure (i.e., crack growth to the back surface) was observed at conditions just beyond the onset of stable tearing.
	The stable tearing was observed to be greater at an angle of about 30-degrees to the surface rather than at the maximum depth location (90-degrees to the surface), which appears to be in agreement with the simulations based on ASTM E289.
	CMOD measurements appear to be sensitive to the onset of yielding, blunting, and stable tearing.
TI-16-01183 Data Reference	7.2.2 F-11, F-13, F-14
Note	This best practice also applies to AIAA S-081B Sections 10.1.1 and 10.1.2 on Damage Tolerance Life Test: The size of each precrack shall be greater than or equal to the minimum flaw size associated with the NDT inspection technique(s).
1	

The following three criteria shall be met for verification of damage tolerance life:	
1.	The cracks have not grown to through-cracks in test.
2.	The precrack size has been verified for conformance to liner NDT thresholds.
3.	The testing confirms that no sustained load crack growth has occurred during the test.

Best Practice	DTL-2
AIAA S-081B Section	6.2.1

The damage tolerance life requirement may be verified by analysis only if both of the following conditions are met:

- 1) The liner (or region of the liner) is shown to be elastically responding and characterized by linear elastic fracture mechanics (LEFM) throughout proof testing and the operational portion of the service life.
- 2) The fracture properties of the liner materials are determined in accordance with Section 7.1.

Best Practice

When NASGRO analysis is used for damage tolerance life verification, COPV designers should use the following analysis procedure to address the potential violation of LEFM plasticity assumptions:

- Simulate crack growth to failure (i.e., breakthrough) using NASGRO
- Identify the predicted a after M-lifetimes, a_F
- Identify the limits a_i , a_L , and a_i^*
- Verify that $a_F < a_i^*$, otherwise the design does not meet recommended requirement for damage tolerance life by analysis

- Report a_F , a_i , a_L , and a_i^* to fracture control engineering technical authority

$\mathbf{Report} \ a_F, a_l, a_l$	L, and a ₁ to mactate control engineering technical authority
Evidence Summary	LEFM plasticity assumptions are violated before the transition from a surface crack to a through-crack (i.e., before COPV liner leakage).
	There is a gradual divergence between LEFM predicted behavior and measured crack behavior as cracks grow through the uncracked ligament.
	Measured crack growth in 0.032-, 0.048-, and 0.090-inch thick AA6061-T6 sheet material (i.e., representative of COPV liner thickness) was predominantly higher than predicted by common practice LEFM-based computational methods (e.g., NASGRO).

	LEFM plasticity assumption violations are not always flagged in a NASGRO analysis allowing users to mistakenly continue analysis.
	The COPV Life LEFM limit and knockdown failure criteria is a more conservative damage tolerance life analysis approach than the state-of-practice damage tolerance life analysis approach.
TI-16-01183 Data	7.1
Reference	F-1, F-2, F-3, F-4, O-2
Note	This best practice also applies to AIAA S-081B Section 7.5.1 on Damage Tolerance Life Analysis:
	The analysis shall show that the COPV liner meets the damage tolerance life. The analysis may be performed using a crack growth software package.
	At all times in the service life, the applied stress intensity factor shall be less than the surface or embedded crack fracture toughness (see ASTM E2899) and KIEAC for the applicable environment (such as embrittlement).
	The stress in the uncracked ligament (the remaining cross-sectional area at the crack plane) shall remain below the flow stress throughout the analysis of the damage tolerance life.

Best Practice	DTL-3		
AIAA S-081B Section	7.1		
	AIAA S-081B Requirement		
The test program shall include the effects of all plastic deformation throughout the service life, for example, during autofrettage (if one is performed) and any other plastic cycles.			
Best Practice			
Use coupon or tank testing to characterize the amount of crack growth observed during autofrettage or plastic cycles.			
Evidence Summary	Fracture surface (i.e., precrack, autofrettage crack growth, stable tearing, and post-cracking) regions were distinguished with selection of precracking and post-cracking stress and R.		
	The amount of crack growth during autofrettage was small (i.e., <0.002 inch) and relatively independent of a and strain level provided that the crack tip conditions were below the onset of stable tearing.		
	The amount of crack extension due to 4 consecutive autofrettage cycles was never measured to be greater than the amount of crack		

	extension in a single autofrettage cycle, multiplied by four, provided stable tearing was not present.
	The autofrettage cycles provided a distinct mark on the fracture surface that was used to determine the amount of crack growth.
	CMOD measurements appear to be sensitive to the onset of yielding, blunting, and stable tearing.
TI-16-01183 Data	7.2.2, 7.2.3
Reference	F-9, F-11, F-12, F-15, F-17
Note	This best practice also applies to AIAA S-081B Section 7.5.1 on Damage Tolerance Life Analysis:
	Autofrettage may be assessed using elastic/plastic fracture mechanics (EPFM). The data used for the EPFM analysis shall conservatively represent the material alloy, condition, thickness, and autofrettage cycle as validated through testing.

Best Practice	DTL-4
AIAA S-081B Section	7.1

Sufficient data shall be obtained either from conducting tests or other available sources so that meaningful nominal values can be established. The test program shall establish these properties for the parent metal, weld joints, and heat-affected zones, all taking into account the fluid contents, service life, and expected operating and test environments, as appropriate.

Best Practice

Demonstrate by test that da/dN vs. ΔK data from a surrogate material (i.e., rolled sheet in place of as-manufactured tank) is equivalent to or conservative to liner material. Upon modification of the material composition or processing, ensure the equivalency check is repeated.

Complete fatigue crack growth tests using coupons extracted from a representative COPV liner and with the minimum reliably detectable surface precrack. These coupons should be extracted from a variety of regions throughout the tank, where the number of regions or extraction should be guided by EBSD or other microscopy observations. To form a baseline comparison, coupons should be extracted from the desired surrogate material (e.g., rolled sheet) with the same geometry as the liner coupons. Equivalency or conservatism can then be demonstrated by measuring fatigue crack growth rates. Fatigue crack growth testing at this scale should apply loads that induce the expected peak net section stress in the liner.

Evidence	Microstructure variations are observed between different COPV liner
Summary	regions, and between liner and rolled sheet material.

	In comparing material regions of different microstructure, fatigue crack growth tests quantified impact of damage mechanism to damage tolerance life (i.e., da/dN) while microscopy and tensile tests did not.
TI-16-01183 Data Reference	Section 7.2.1 F-5, F-6
Notes	This best practice also applies to AIAA S-081B Section 7.5.1 on Damage Tolerance Life Analysis and 10.1.1 on Damage Tolerance Life Test by Coupon:
	Section 7.5.1:
	For the cycles in the service life during which the liner remains elastic, the analysis shall use nominal or conservative values of fracture properties (fracture toughness, stable crack extension resistance, KIEAC, and fatigue crack growth rate data) (Section 7.1) associated with each alloy, heat-treat condition, thickness, and product form in the applicable thermal and chemical environments.
	Section 10.1.1:
	If coupon testing is used, then verification by test shall be performed on coupons that are representative of the liner material at the worst-case or relevant location(s) based on material, weld procedure, weld thickness, geometry and/or product form.
	Section 10.1.2:
	If COPV specimen testing is used, then verification by test shall be performed on test specimens that are representative of the flight COPV. The test specimens shall represent liner and overwrap configuration and properties.

Best Practice	DTL-5	
AIAA S-081B Section	7.5.1	
AIAA S-081B Requirement		
The analysis shall show that the COPV liner meets the damage tolerance life. The analysis may be performed using a crack growth software package.		
Best Practice		
In damage tolerance life analysis, apply service lives in sequence.		
Evidence Summary The average da/dN from coupons and liners with the 4x(AF & 200 MDP) load spectrum were faster than those measured from coupons and liner with 4xAF and 800 MDP load spectrum		
TI-16-01183 Data Reference		

	F-20
Notes	This best practice also supports existing requirements in AIAA S-081B Section 10.1 to apply strains in sequence for coupon tests and to apply load cycles in sequence for COPV tests.
	Section 10.1.1:
	After precracking, all strains in the damage tolerance life shall be applied in sequence to each coupon.
	Section 10.1.2:
	After precracking, all load cycles in the damage tolerance life shall be applied in sequence to each test specimen.

Best Practice	DTL-6
AIAA S-081B Section	7.5.1

For analysis of the autofrettage cycle (if one is performed), the factor of four may be waived provided conservative crack growth properties and methodology are used in the determination of crack growth for autofrettage.

EXAMPLE The autofrettage cycle might be approached through analysis of a single event predicting the potential extension in a conservative manner using a lower bound crack extension resistance curve or equivalent technique, rather than a nominal resistance curve. This extended defect size thus derived might then be used as the starting defect size in the damage tolerance life analysis.

damage to retained into unaryons.	
Best Practice Evaluate margin to stable tearing before waiving scatter factor of four for autofrettage.	
Lvaluate margin to stable	tearing before warving scatter factor of four for autoffettage.
Evidence Summary	Stable tearing leading to failure (i.e., crack growth to the back surface) was observed at conditions just beyond the onset of stable tearing.
	The stable tearing was observed to be greater at an angle of about 30-degrees to the surface rather than at the maximum depth location (90-degrees to the surface), which appears to be in agreement with the simulations based on ASTM E2899.
TI-16-01183 Data Reference	Section 7.2.2 F-13, F-14

Best Practice	DTL-7
AIAA S-081B Section	7.5.1

The analysis shall account for changes in the flaw (crack) a/c and the effects of all environment(s) on the crack growth rate.

Best Practice

For flaws on the inner diameter of a COPV liner, include the contribution of pressure on IML crack faces to the applied stress intensity factor in damage tolerance life analysis.

Evidence Summary	Liner IML and OML crack da/dN correlated when the K solution for the IML cracks included the influence of crack face pressure.
TI-16-01183 Data	7.2.3
Reference	O-6

Best Practice	DTL-8	
AIAA S-081B Section	10.1.1	
AIAA S-081B Requirement		
The coupons shall meet the specimen configuration and size requirements of ASTM E740.		
Best Practice		
Ensure the width of damage tolerance life test coupon is at least 9 times 2c.		
Evidence Summary	A test coupon width of 9 x precrack 2c mitigates edge on crack growth behavior (i.e., CMOD and J convergence to <1%).	
TI-16-01183 Data Reference	7.2.2, Appendix C F-7	

Best Practice	DTL-9
AIAA S-081B Section	10.1.1

AIAA S-081B Requirement

Each coupon shall be precracked.

Best Practice

Precrack at R=0.1 at 80% of yield or MDP whichever is lower.

Precracks of a/c other than 0.5 can be accomplished using multiple closely-spaced notches.

Grow the precrack beyond the influence of the notch. Notches are half the size of the target precrack size.

Evidence Summary	Fracture surface (i.e., precrack, autofrettage crack growth, stable tearing, and post-cracking) regions were distinguished with selection
	of precracking and post-cracking stress and R.
TI-16-01183 Data Reference	7.2.2 F-9

Best Practice	DTL-10
AIAA S-081B Section	10.1.1

The size of each precrack shall be greater than or equal to the minimum flaw size associated with the NDT inspection technique(s).

Best Practice

Demonstrate precracking procedure on sample coupons prior to starting test. The number of cycles required to consistently grow the precrack to the NDE length and depth should be demonstrated (post precracking fractography) by precracking and examining the precrack using SEM prior to precracking the test specimens. The notch procedure for inserting a flaw from which to grow a precrack should also be demonstrated.

Evidence Summary	Fracture surface (i.e., precrack, autofrettage crack growth, stable tearing, and post-cracking) regions were distinguished with selection of precracking and post-cracking stress and R.
TI-16-01183 Data	7.2.2
Reference	F-9

AIAA S-081B Section	10.1.1
AIAA S-081B Section	10 1 1

AIAA 5-081B Requirement

Strains equal to or greater than those associated with each load cycle, including the compressive liner strains at zero pressure, shall be tested.

Best Practice

Use strains that represent the entire cyclic history (i.e., no truncation at zero stress).

Guide plates can be used to prevent buckling during compressive strain tests.

Evidence Summary	Crack depth measurements demonstrated that the coupon that was truncated, excluding the compressive loading following the
	autofrettage cycle, grew significantly slower than the coupon with the full loading history.

	Guide plates provided anti-buckling support when compressive		
	loads were applied in coupon tests, while allowing strain and surface		
	crack length.		
TI-16-01183 Data	7.2.3, Appendix L, and Appendix I		
Reference	F-18, F-10		

Best Practice	DTL-12				
AIAA S-081B Section	10.1.1				

Test strains and strain rate shall be verified by measurement.

Best Practice

Strain measurements for uniaxial tests should be performed using physical or virtual edge extensometers or strain gages at the edge. The strain measurement location should be centered about the plane of the crack. Physical extensometers should be placed on both edges. Virtual extensometers and strain gages should be placed on the both edges of both sides (i.e., 4 locations).

Evidence Summary	Multiple edge physical and virtual extensometers/strain gages located at the coupon edges provide consistent far-field strain measurements.
TI-16-01183 Data	7.2.2 and Appendix H
Reference	F-8

Best Practice	DTL-13
AIAA S-081B Section	10.1.1

AIAA S-081B Requirement

After completion of cyclic strain testing, the following procedures and measurements on the coupons shall be performed.

- 1) The crack faces will be separated in a way that will allow examination of the fracture surfaces produced during testing.
- 2) The fracture surface will be examined to verify that the crack has not grown to become a through-crack.
- 3) The initial and final crack sizes will be measured.

Best Practice

Identify and measure regions of notching, precracking, autofrettage growth, cyclic loading, and monotonic loading to failure in the SEM, a slight microscopy is not adequate. At least a small ligament of material that failed during monotonic loading should exist between the back surface and cyclic crack growth region.

Evidence Summary	Fracture surface (i.e., precrack, autofrettage crack growth, stable tearing, and post-cracking) regions were distinguished with selection of precracking and post-cracking stress and R.
TI-16-01183 Data	7.2.2
Reference	F-9

Best Practice	DTL-14
AIAA S-081B Section	10.1.2

At least two liner cracks shall be tested for each condition (location and a/c). Each location shall contain a surface crack. Each location shall be precracked. The size of each precrack shall be greater than or equal to the minimum flaw size associated with the NDT inspection technique(s).

Best Practice

Perform precracking on an unwrapped liner so that crack length can be measured prior to test. Use coupons and/or a non-test liner and extract the cracks to confirm NDE minimum crack size.

Use NDE (e.g., eddy current inspection) to identify IML cracks during the precracking process if cracks nucleate at locations other than the notches.

Evidence Summary	Liner precracking process via inserting EDM notches and pressure cycling was demonstrated to grow flaws to the target initial flaw size.			
	Long, shallow cracks nucleating from naturally occurring IML defects in an AA6061-T6 liner were reliably detected from the OML using eddy current inspection.			
TI-16-01183 Data Reference	7.2.3			
	O-5, F-16			

7.4 Other Considerations

Several topics arose during the testing and analyses that could influence the damage tolerance analysis of COPV liners, but were either not directly related to the scope of this assessment. The following sub-sections describe these topics and discuss the importance relative to damage tolerance analyses.

Analysis Limit for Grain Size Relative to Crack Size and Remaining Ligament

Section 7.2 discusses the influence of grain structure variations on the damage tolerance behavior of COPV liner materials. da/dN tests on part-through cracks were conducted in support of this study. However, sufficient data were not found on the analysis limit of the grain size relative to the crack or remaining ligament. The crack in some of the tests was deep enough for the ligament

to consist of only one or two grains, as shown in Figure 7.4-1. The grains in this, and other similar cracks were large relative to the ligament, but small relative to the overall crack size.

From the post-test fractography, it was observed that semi-elliptical crack shapes were often not maintained throughout crack growth. Frequently, increased crack growth rates along directions of approximately 30- and 150-degrees along the front were observed. However, these increased local rates are due to increased local driving force and are not a direct result of the specific microstructure in the region. Grain size dependent crack growth rates would typically demonstrate local crack growth rate variations that coincide with individual grains along the crack front. These variations are most notable during the crack initiation stage. However, in the tests conducted, an initial crack was inserted using EDM or plasma focused ion beam (PFIB) to mimic threshold detectable indications and, consequently, the crack initiation stage was surpassed before starting the test.

Because of the variation in driving force along the crack front and sizes of the inserted initial cracks, these tests do not provide adequate data for quantifying grain-scale effects on crack growth rates. However, it is important to note that these tests were designed to mimic in-service conditions. Consequently, they demonstrate for the materials tested that the initial crack size and inherent variation in driving force along the crack are more significant to the crack growth behavior than individual grains. If initial crack sizes were to decrease or grain sizes were to increase, in comparison to the tests accomplished herein, then the governance of grain-specific crack growth rates would become increasingly prevalent. Correspondingly, as fewer grains populate the remaining ligament, the uncertainty in plastic zone size and crack growth rates would increase. In such cases, mechanical testing of as-manufactured materials becomes more important and sufficient testing and support analysis or simulation should be completed to quantify uncertainty and worst-case microstructures in the remaining ligament. Such analysis methods are heavily researched and not applied in a usual engineering methodology. However, they are technically feasible and can be used to support higher-fidelity analyses when needed.

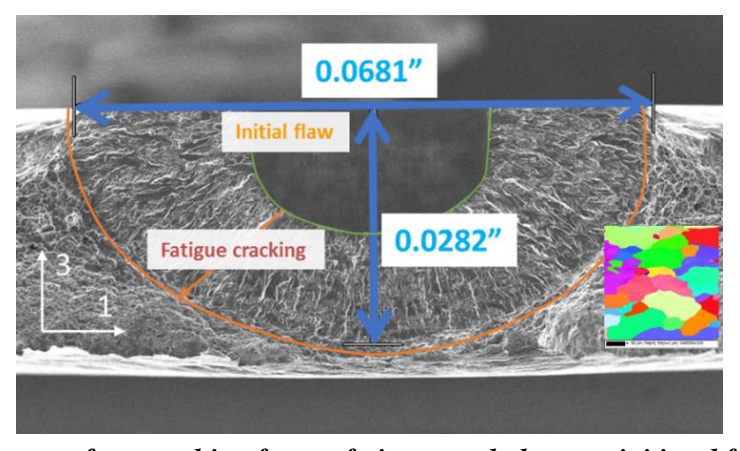


Figure 7.4-1. Fracture surface resulting from a fatigue crack that was initiated from a surface notch and grown almost to the back face of the thin-walled coupon.

Uniaxial Coupon Simulations of Biaxial COPV Liners

Measurements of the axial stress-strain behavior in the uniaxial coupons and design analyses of the hoop and axial stress-strain behavior in the COPV liners indicate a difference in the stresses, as discussed in Section 7.2.3.3. The impact of these differences on the crack tip driving force

along the crack front were examined in Appendix O. These investigatory analyses suggest that a uniaxial coupon may be unconservative relative to the biaxial stress state in the liner for autofrettage simulations. A likely overly conservative, approach was suggested of the following: (1) Perform elastic-plastic FEA on the uniaxial coupon and biaxial liner for the crack size/shape and strain levels required in the damage tolerance life qualification; (2) Select a crack tip driving force parameter (i.e., J-integral) and evaluate the parameter along the perimeter of the crack in the biaxial liner analysis; (3) Increase the strain level in the uniaxial analysis until the peak value of the crack tip driving force parameter is equal to that in the biaxial analysis, and (4) Conduct the uniaxial tests at the increased strain level. Additional elastic-plastic analyses and tests on cracks under biaxial loading would be required to evaluate and understand the influence of the different stress states when using uniaxial coupons to determine the onset of stable tearing in a biaxial COPV liner.

Prediction of a/c Changes in NASGRO

Differences in the measured and NASGRO predicted changes in a/c was observed and described in Section 7.1.1.1. These differences were consistently in the direction of NASGRO predicting smaller a/c that experimentally measured, as shown in Figure 7.1.1-9. This indicates that NASGRO is predicting either less crack growth in the depth direction or more growth in the surface crack length direction. Four possible causes have been postulated: (1) The K solutions used in NASGRO do not accurately calculate the actual stress intensity factor at the surface and/or depth; (2) The crack growth rate behavior is different in the surface and depth directions; (3) The crack shapes may not be accurately represented as a semi-ellipse; and (4) The constraint (i.e., plane stress to plane strain) differences at the surface and depth may influence the crack growth rates. Results presented in Appendix C.3 suggest that (1) is unlikely. However, further analysis is required to determine cause and effect of the observed a/c behavior.

Prediction of Fatigue Crack Growth Following Autofrettage

The influence of the compressive loading after the autofrettage cycle is not accounted for in a traditional LEFM damage tolerance life analysis. This influence can have a significant influence on the subsequent fatigue crack growth behavior if the liner material yields in compression. Tests conducted on uniaxial coupons indicated that the compressive loading following the autofrettage cycle can make LEFM damage tolerance life predictions unconservative.

A uniaxial test was conducted with a simulated COPV liner strain history that consisted four autofrettage cycles followed by 800 MDP cycles. The autofrettage peak strain was 1.25% and the strain at the simulated depressurization was 0.18%. The MDP peak strain was 0.85% and the strain at the simulated depressurization was 0.18%. The measured crack tip opening displacement located 0.015 inch above and below the center of the crack, and applied stress is shown in Figure 7.4-2. The MDP cycles were essentially constant amplitude loading between 25,000 and -40,000 psi.

A second test was conducted with the same constant amplitude loading that represents the MDP cycles, but no autofrettage cycles, as shown in Figure 7.4-3 along with the measurements from the test conducted with the autofrettage cycle. The Δ CMOD was defined as the change in CMOD from the value at the minimum stress of the first MDP cycle. The Δ CMOD vs. load behavior for the MDP cycles that followed the autofrettage were nearly linear with load. The test with MDP cycles without the autofrettage were stiffer from -40,000 psi to near zero load, then experienced a slope change that matched that of the test with the autofrettage cycle.

Plasticity induced fatigue crack closure [refs. 19-21] is one possible explanation of the behavior observed in the uniaxial tests. This theory suggests that the crack in the test without the autofrettage cycle experienced residual stresses that forced the crack shut at minimum load. These residual stresses had to be relieved during the subsequent loading, reducing the effective stress range that develops crack tip damage. The test with the MDP cycles that followed the autofrettage cycle had the residual stresses relieved when the material compressive yielding occurred at the first depressurization. This resulted in a larger portion of the stress range contributing to crack tip damage.

NASGRO LEFM damage tolerance life predictions were made for three tests conducted with MDP cycles following an autofrettage cycle and one tests with MDP cycles without an autofrettage cycle, as shown in Figure 7.4-4. Only the initial and final crack sizes were known for the four tests (i.e., round symbols). The fracture surfaces indicated that the amount of crack growth due to the autofrettage cycle was less than 0.0005 inch. The NASGRO predictions (i.e., solid lines) used a peak stress of 25,000 psi, a minimum stress of -40,000 psi, and the crack growth rate was calculated from the tabular data described in Appendix E. The NASGRO predictions were unconservative for each of the three tests with MDP cycles that followed an autofrettage cycle, but were in good agreement with the test that was conducted with the 800 MDP cycles without an autofrettage cycle. Similar NASGRO predictions were made for the OML cracks in the COPV tests. The ratio of predicted crack depth to measured crack depth as a function of the initial crack depth is shown in Figure 7.4-5. The prediction for all of the tests that were conducted with autofrettage cycles were unconservative (i.e., %Predicted/Measured <100). The only test with the predicted crack depth within 15% of the measured value was the coupon test conducted without the autofrettage cycle.

- O-7 AIAA S-081B damage tolerance life analyses are permitted to evaluate the elastic MDP cycles without accounting for the potentially detrimental influence of the autofrettage cycle.
- F-21 Fatigue crack growth tests conducted with and without an autofrettage cycle suggest that the compressive unloading of the liner that follows the autofrettage cycle can increase the crack growth rate in the liner and ignoring this influence can result in unconservative damage tolerance life predictions.

The results discussed were for a limited number of tests, but suggest that NASGRO LEFM damage tolerance life analyses can be unconservative in predicting the damage tolerance life of cracks in COPV liners. An approach to fully investigate this behavior could include:

- 1. Long crack da/dN tests at positive and negative R
- 2. Uniaxial surface crack tests with multiple repeats with different autofrettage and MDP strain levels
 - a. Measure the autofrettage crack growth
 - b. Measure the starting and ending crack sizes
 - c. Measure the CMOD
 - d. The autofrettage levels should have different levels of strain at depressurization (with compressive yielding and without compressive yielding)
- 3. Repeat #2 for uniaxial surface crack tests without the autofrettage cycles
- 4. NASGRO predictions for surface crack tests with and without autofrettage cycles
- 5. Pressure test six COPV liners

- a. Introduce laser notches in six liners
- b. Pressure cycle the bare liners elastically to nucleate fatigue cracks to the NDE limit
- c. Design two wrapping patterns
 - i. Keep the peak autofrettage strain level and MDP peak strain level constant
 - ii. One design will have the liner yielding in compression at the depressurization after autofrettage
 - iii. The other design will have the liner experience stresses about half the yield stress in compression at the depressurization after autofrettage
- d. Wrap the liners (3 with each design)
- e. Test the COPVs
- f. Examine the fracture surfaces to determine the amount of crack growth
- 6. Elastic-plastic FEA simulations
 - a. Simulate autofrettage peak strains and contact at minimum strain
 - b. Simulate subsequent MDP cycles
 - c. Examine the separation of the crack surface during the loading portion of the MDP cycle
 - d. Perform the same analysis for MDP loading without the autofrettage cycle
 - e. Validate the analyses with the CMOD measurement

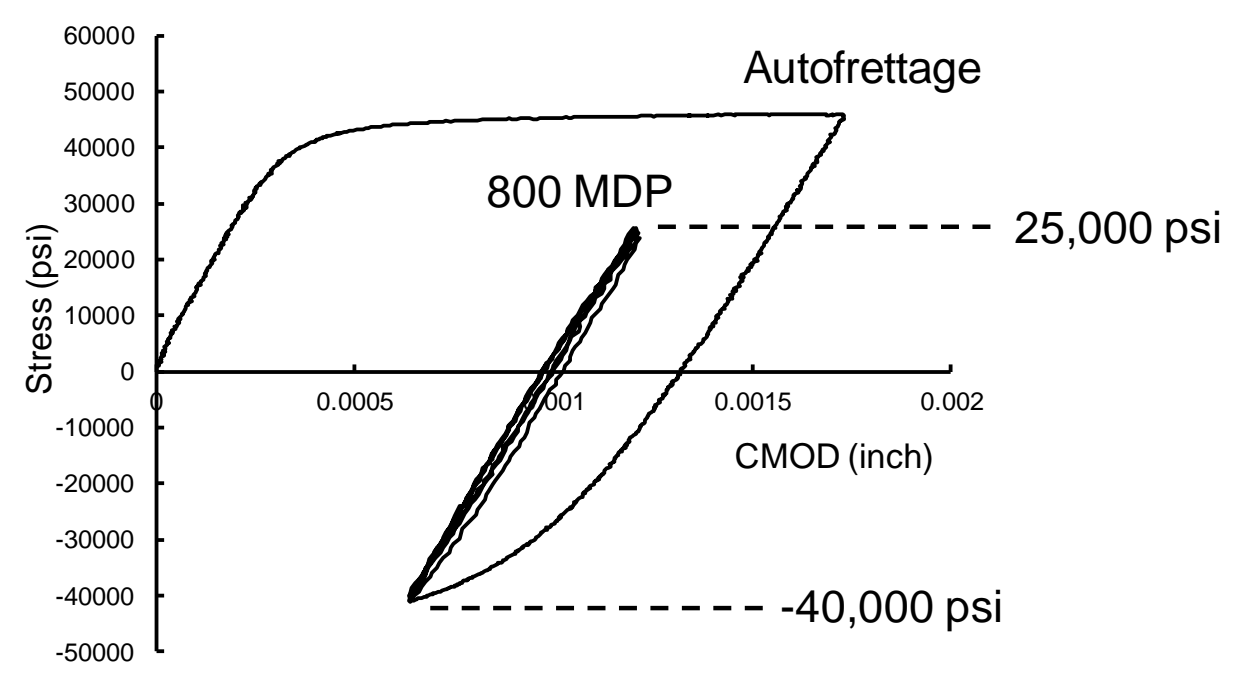


Figure 7.4-2. Measured CMOD as a function of applied strain for a uniaxial simulation of a COPV liner strain history.

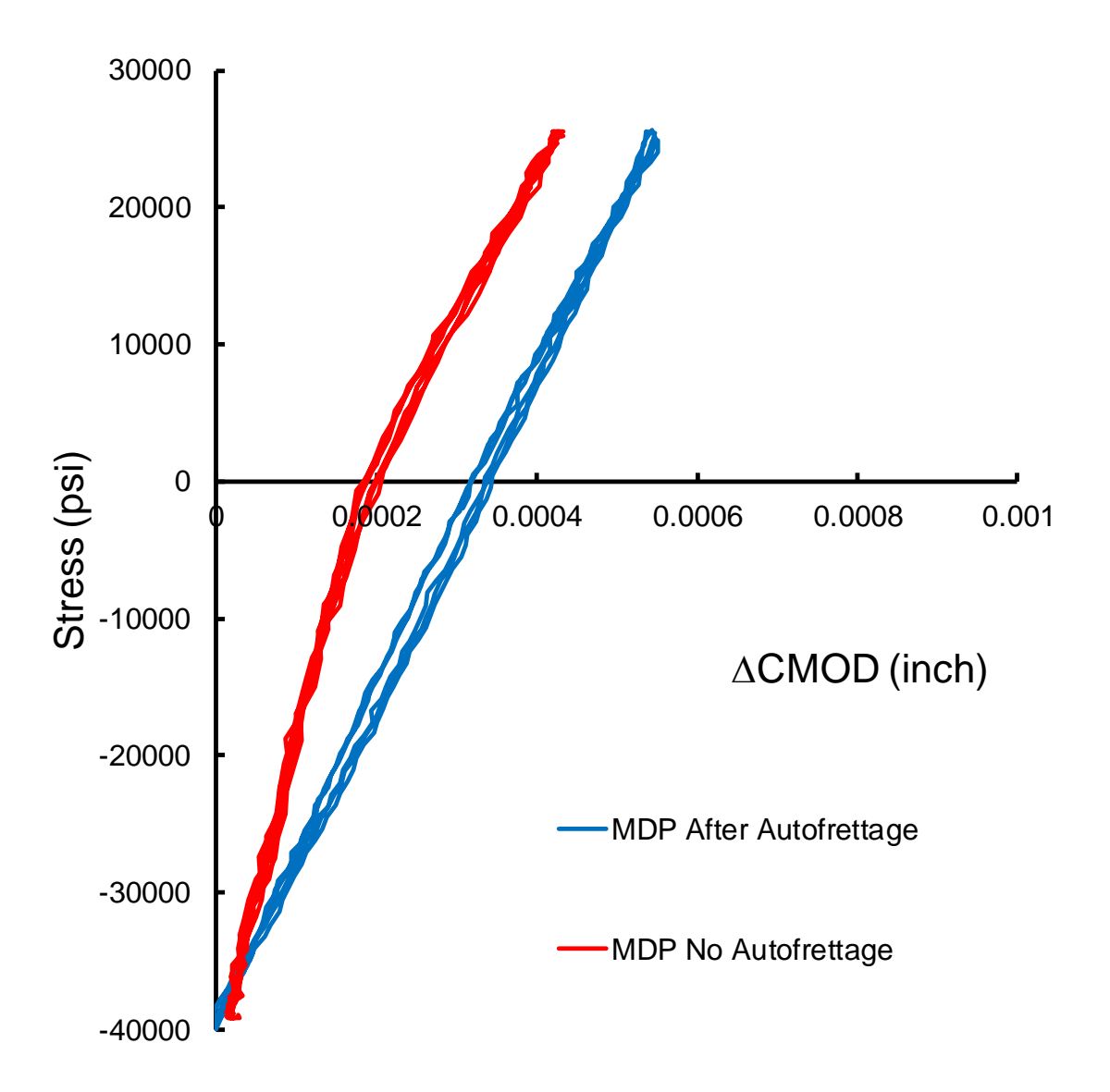


Figure 7.4-3. Measured \triangle CMOD as a function of applied strain for MDP cycles with and without autofrettage.

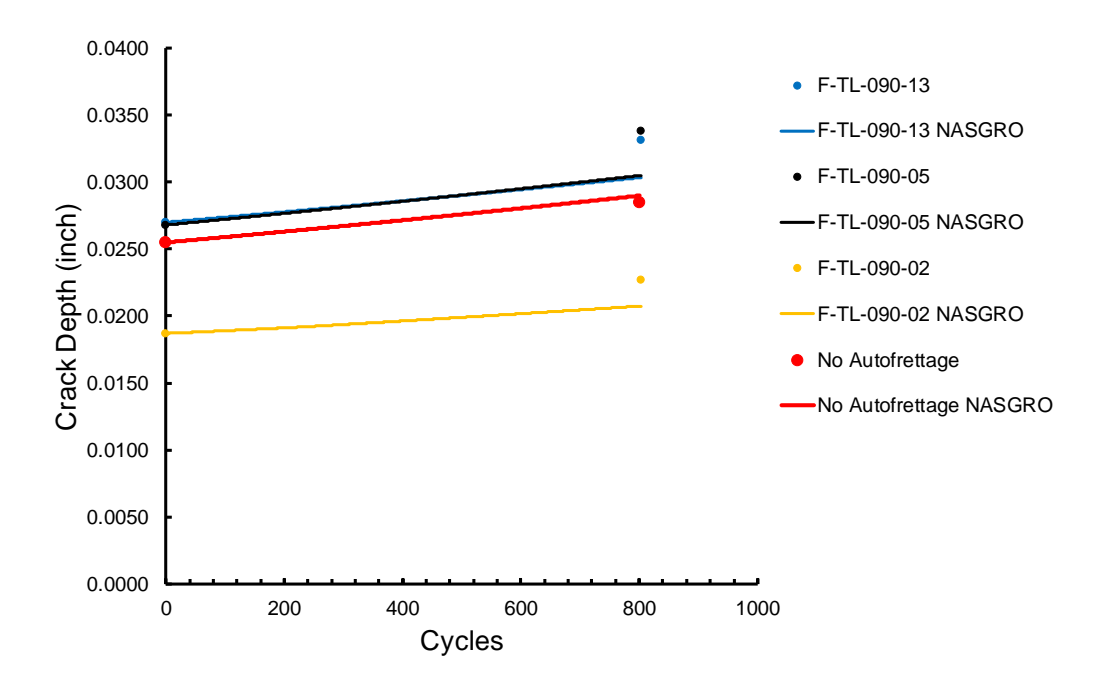


Figure 7.4-4. Measured crack length and NASGRO predictions for three tests with 800 MDP cycles following autofrettage cycles and one test with 800 MDP cycles without an autofrettage cycle.

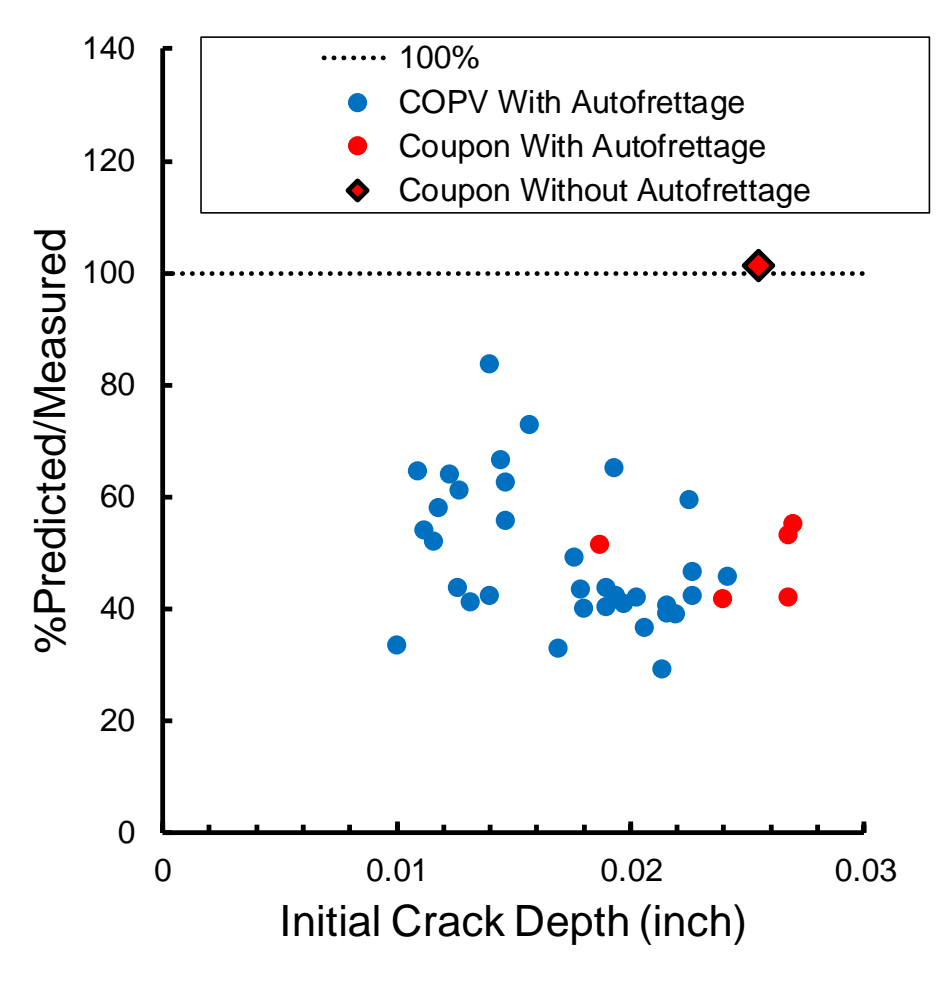


Figure 7.4-5. The ratio of predicted final crack depth to measured crack depth as a function of initial crack depth is plotted for the COPV and coupon tests.

8.0 Findings, Observations, and NESC Recommendations

8.1 Findings

The following findings were identified:

Understanding Limitations of LEFM and Damage Tolerance Analysis

- **F-1.** LEFM plasticity assumptions are violated before the transition from a surface crack to a through-crack (i.e., before COPV liner leakage).
- **F-2.** There is a gradual divergence between LEFM predicted behavior and measured crack behavior as cracks grow through the uncracked ligament.
- **F-3.** Measured crack growth in 0.032-, 0.048-, and 0.090-inch thick AA6061-T6 sheet material (i.e., representative of COPV liner thickness) was predominantly higher than predicted by common-practice LEFM-based computational methods (e.g., NASGRO).
- **F-4.** The COPV Life LEFM limit and knockdown failure criterion is a more conservative damage tolerance life analysis approach than the state-of-practice damage tolerance life analysis approach.

Material Evaluation

- **F-5.** Microstructure variations are observed between different COPV liner regions, and between liner and rolled sheet material.
- **F-6.** In comparing material regions of different microstructure, fatigue crack growth tests quantified impact of damage mechanism to damage tolerance life (i.e., da/dN) while microscopy and tensile tests did not.

Coupon Crack Growth Testing

- **F-7.** A test coupon width of 9 x precrack 2c mitigates edge on crack growth behavior (i.e., CMOD and J convergence to <1%).
- **F-8.** Multiple edge physical and virtual extensometers/strain gages located at the coupon edges provide consistent far-field strain measurements.
- **F-9.** Fracture surface (i.e., precrack, autofrettage crack growth, stable tearing, and post-cracking) regions were distinguished with selection of precracking and post-cracking stress and R.
- **F-10.** Guide plates provided anti-buckling support when compressive loads were applied in coupon tests, while allowing strain and surface crack length measurements.
- **F-11.** CMOD measurements appear to be sensitive to the onset of yielding, blunting, and stable tearing.
- **F-12.** The amount of crack growth during autofrettage was small (i.e., <0.002 inch) and relatively independent of crack depth and strain level, provided that the crack tip conditions were below the onset of stable tearing.
- **F-13.** Stable tearing leading to failure (i.e., crack growth to the back surface) was observed at conditions just beyond the onset of stable tearing.

- **F-14.** The stable tearing was observed to be greater at an angle of about 30-degrees to the surface rather than at the maximum depth location (90-degrees to the surface), which appears to be in agreement with the simulations based on ASTM E2899.
- **F-15.** The amount of crack extension due to 4 consecutive autofrettage cycles was never measured to be greater than the amount of crack extension in a single autofrettage cycle, multiplied by four, provided stable tearing was not present.

Damage Tolerance Life Testing

- **F-16.** Long, shallow cracks nucleating from naturally occurring IML defects in an AA6061-T6 liner were reliably detected from the OML using eddy current inspection.
- **F-17.** The autofrettage cycles provided a distinct mark on the fracture surface that was used to determine the amount of crack growth.
- **F-18.** The crack depth measurements demonstrated that the coupon that was truncated (i.e., excluding the compressive loading following the autofrettage cycle) grew slower than the coupon with the full loading history.
- **F-19.** Uniaxial coupon tests of crack growth at the COPV liner strain levels achieved the same hoop strain and peak stresses (both at autofrettage and MDP), but not the minimum stresses after autofrettage and MDP.
- **F-20.** The average da/dN from coupons and liners with the 4x(AF & 200 MDP) load spectrum were faster than those measured from coupons and liner with 4xAF and 800 MDP load spectrum
- **F-21.** Fatigue crack growth tests conducted with and without an autofrettage cycle suggest that the compressive unloading of the liner that follows the autofrettage cycle can increase the crack growth rate in the liner and ignoring this influence can result in unconservative damage tolerance life predictions.

8.2 Observations

The following observations were identified:

- **O-1.** The NASGRO user's manual discusses its limitations and provides guidance on its use.
- **O-2.** LEFM plasticity assumption violations are not always flagged in a NASGRO analysis allowing users to mistakenly continue analysis.
- **O-3.** The crack growth scatter for a/c ranging from 1.1 to 0.8, with NASGRO consistently predicting smaller than observed a/c, was greater than expected given the test coupons were extracted from the same material lot using the identical cracking process.
- **O-4.** Eddy current measurements of cracks subject to compressive loading (i.e., closed cracks), to 80% of the compressive yield, demonstrated no statistically significant loss in detectability relative to that obtained from the same crack loaded in tension (i.e., open cracks).
- **O-5.** Liner precracking process via inserting EDM notches and pressure cycling was demonstrated to grow flaws to the target initial flaw size.

- **O-6.** Liner IML and OML crack da/dN correlated when the K solution for the IML cracks included the influence of crack face pressure.
- **O-7.** AIAA S-081B damage tolerance life analyses are permitted to evaluate the elastic MDP cycles without accounting for the potentially detrimental influence of the autofrettage cycle.

8.3 NESC Recommendations

The following NESC recommendations are directed towards programs that use COPVs required to comply with damage tolerance life requirements:

- **R-1.** When NASGRO analysis is used for damage tolerance life verification, COPV designers should use the following analysis procedure to address the potential violation of LEFM plasticity assumptions: (*F-1*, *F-2*, *F-3*, *F-4*, *O-2*)
 - Simulate crack growth to failure (i.e., breakthrough) using NASGRO
 - Identify the predicted crack depth after M-lifetimes, a_F
 - Identify the limits a_i , a_L , and a_i^*
 - Verify that $a_F < a_i^*$, otherwise the design does not meet recommended requirement for damage tolerance life by analysis
 - Report a_F , a_i , a_L , and a_i^* to fracture control engineering technical authority
- **R-2.** Require reporting of the LEFM limit and failure criteria evaluation to their fracture control engineering technical authority. (*F-3*)
- **R-3.** Demonstrate by test and/or validated elastic-plastic fracture analysis that stable tearing does not occur during the service life, including autofrettage. (*F-13*, *F-14*)
- **R-4.** Use Best Practices for Complying with Damage Tolerance Life Requirements of AIAA S-081B. (*F-1 through F-20, 0-2, 0-5, 0-6*)
- **R-5.** NASA-STD-5019 and NASA-HDBK-5010 Office of Primary Responsibility should update these documents to incorporate the COPV Life LEFM limit and modified failure criteria evaluation in damage tolerance life analysis. (*F-1*, *F-2*, *F-3*, *F-4*, *O-2*)
- **R-6.** AIAA Aerospace Pressure Vessel Committee on Standards should modify ANSI AIAA S-081B Section 5.2.13.1 "Damage Tolerance Life Design" to require that stable tearing shall not occur at any time in the service life, including autofrettage. (*F-13*, *F-14*)

9.0 Alternative Viewpoint(s)

There were no alternative viewpoints identified during the course of this assessment by the NESC assessment team or the NRB quorum.

10.0 Other Deliverables

No unique hardware, software, or data packages, outside those contained in this report were disseminated to other parties outside this assessment.

11.0 Lessons Learned

No additional lessons learned with identified in this assessment.

12.0 Recommendations for NASA Standards and Specifications

Recommendations R-5 and R-6 address updates to NASA Standards and Specifications.

- R-5. NASA-STD-5019 and NASA-HDBK-5010 Office of Primary Responsibility should update these documents to incorporate the COPV Life LEFM limit and modified failure criteria evaluation in damage tolerance life analysis. (*F-1*, *F-2*, *F-3*, *F-4*, *O-2*)
- R-6. AIAA Aerospace Pressure Vessel Committee on Standards should modify ANSI AIAA S-081B Section 5.2.13.1 "Damage Tolerance Life Design" to require that stable tearing shall not occur at any time in the service life, including autofrettage. (*F-15*, *F-16*)

13.0 Definition of Terms

Corrective Actions Changes to design processes, work instructions, workmanship practices,

training, inspections, tests, procedures, specifications, drawings, tools, equipment, facilities, resources, or material that result in preventing, minimizing, or limiting the potential for recurrence of a problem.

Finding A relevant factual conclusion and/or issue that is within the assessment

scope and that the team has rigorously based on data from their independent analyses, tests, inspections, and/or reviews of technical

documentation.

Lessons Learned Knowledge, understanding, or conclusive insight gained by experience

that may benefit other current or future NASA programs and projects. The experience may be positive, as in a successful test or mission, or

negative, as in a mishap or failure.

Observation A noteworthy fact, issue, and/or risk, which may not be directly within the

assessment scope, but could generate a separate issue or concern if not

addressed. Alternatively, an observation can be a positive

acknowledgement of a Center/Program/Project/Organization's operational

structure, tools, and/or support provided.

Problem The subject of the independent technical assessment.

Recommendation A proposed measurable stakeholder action directly supported by specific

Finding(s) and/or Observation(s) that will correct or mitigate an identified

issue or risk.

14.0 Acronyms and Nomenclature List

a Crack Deptha/c Aspect RatioAA Aluminum Alloy

ACT Absorption Contrast Tomography

Al Aluminum

ASTM American Society for Testing and Materials

AX Axial

CMOD Crack Mouth Opening Displacement

COPV Composite Overwrapped Pressure Vessel

DOT Department of Transportation
DCT Diffraction Contrast Tomography

DIC Digital Image Correlation

EPFM Elastic/Plastic Fracture Mechanics
EDM Electrical Discharge Machining
da/dN Fatigue Crack Growth Rate
FEA Finite Element Analyses
FEM Finite Element Model
HAZ Heat Affected Zone
ID Inside Surface

L Length

IPF

LEFM Linear Elastic Fracture Mechanics

Inverse Pole Figure

MAPTIS Materials and Processes Technical Information System

MDP Mean Design Pressure

MMPDS Metal Materials Properties Development Standardization

NESC NASA Engineering and Safety Center

NDT Nondestructive Testing
NDE Nondestructive Evaluation

OD Outside Surface

PFIB Plasma Focused-ion Beam POD Probability Of Detection

R R-ratio

SEM Scanning Electron Microscope

SG Strain Gage Ti Titanium

TASC Tool for Analysis of Surface Cracks UHMW Ultra High Molecular Weight

15.0 References

- 1. McDowell, DL, Gall, K, Horstemeyer, MF, Fan, J; Microstructure-based fatigue modeling of cast A356-T6 alloy; Engineering Fracture Mechanics Volume 70, Issue 1, January 2003.
- 2. Piascik and Knight, Re-Tooling the Agency's Engineering Predictive Practices for Durability and Damage Tolerance.
- 3. "Space Systems Composite Overwrapped Pressure Vessels," ANSI/AIAA S-081B-2018.
- 4. ASTM E2899-15, "Standard Test Method for Measurement of Initiation Toughness in Surface Cracks Under Tension and Bending," ASTM International, West Conshohocken, PA, 2015.
- 5. Grimes-Ledesma, Lorie Dr., COPV Webcast SLAMS, https://appel.nasa.gov/2017/10/26/human-spaceflight-knowledge-sharing-mitigating-the-high-risk-of-copvs/
- 6. McLaughlan, P, Forth, S, Grimes-Ledesma, L; Composite Overwrapped Pressure Vessels, A Primer, NASA SP-2011-573, March 2011.

- 7. Russell, R., Dawicke, D., Hochhalter, J., Composite Overwrapped Pressure Vessel Life Test, NF1676L-28435, European Conference on Spacecraft Structures, Materials and Environmental Testing (ECSSMET), May 28, 2018.
- 8. Piascik, R, Raju, I, Dawicke, D, Lewis, J.; Fracture Mechanics Based Methods Development for Composite Overwrapped Pressure Vessels with Metal Liners, NESC Assessment TI-06-065.
- 9. NASGRO, Fracture Mechanics and Fatigue Crack Growth Analysis Software, Reference Manual, v9.0, May 2018.
- 10. Tool for Analysis of Surface Cracks (TASC).
- 11. MAPTIS
- 12. Kyo-Min Lee, Ji-Sang Park, Hak-Gu Lee, and Sang-Tae Kim, "A Study on the Correlation of Autofrettage Pressure with Cycling Life of Type3 Composite Pressure Vessel," Int. J. of Precision Engineering and Manufacturing, Vol. 17, No. 12, pp. 1685-1691, December 2016.
- 13. COPV Liner Inspection Capability Development Assessment", NESC-RP-14-00954, 2019, NESC Assessment TI-14-00954.
- 14. Additional Characterization and Improvements of the Multi-Purpose COPV Liner Inspection System, NESC-RP-16-01191.
- 15. Harris, J., "NASA Crack Growth Study Development Tank 1 Test Results and Correlation to FEA Results," Contract Update October 8, 2018, Hexagon MasterWorks, Inc.
- 16. Society of Automotive Engineers Aerospace Materials Specifications, SAE International.
- 17. Irwin, G. R., "Crack-Extension Force for a Part-Through Crack in a Plate," Journal of Applied Mechanics, vol. 29, no. 4, Dec. 1962, pp. 651-654.
- 18. Orange, T. W., Sullivan, T. L., and Calfo, F. D., "Fracture of Thin Sections Containing Through and Part-through Cracks," Fracture Toughness Testing at Cryogenic Temperatures, ASTM STP 496, American Society for Testing and Materials, Philadelphia, 1970, pp. 61-81
- 19. Elber, W. "Fatigue crack closure under cyclic tension". Engineering Fracture Mechanics. Vol. 2: 37–45, 1970.
- 20. Elber, W. "The Significance of Fatigue Crack Closure". Damage Tolerance in Aircraft Structures. pp. 230–230–13, 1971.
- 21. J.C. Newman, Jr., "A Crack-Closure Model for Predicting Fatigue-Crack Growth under Aircraft Spectrum Loading", NASA TM-81941, January 1981.
- 22. Harris, J., "NASA Crack Growth Study Development Tank 1 and Correlation to FEA Results," Hexagon MasterWorks, Inc., October 8, 2018.
- 23. Harris, J., "NASA Crack Growth Study COPV Manufacturing Report," Hexagon MasterWorks, Inc., October 9, 2018.
- 24. NASGRO, Fracture Mechanics and Fatigue Crack Growth Analysis Software, Reference Manual, v8.2, October 2017.
- 25. Some studies on fatigue crack growth rate of aluminum alloy 6061, B.F.JogiaP.K.BrahmankaraV.S.NandabR.C.Prasadb.

Appendices (Volume II)

- Appendix A. Excerpts from AIAA S-081B on Damage Tolerance
- Appendix B. Surface Crack Testing
- Appendix C. Surface Crack Finite Element Model Verification and Validation
- Appendix D. Tensile Testing
- Appendix E. Long Crack Data
- Appendix F. Calculation of LEFM Limit and Derivation of Modified Failure Criteria
- Appendix F.1. Calculation of LEFM Limit
- Appendix F.2. Derivation of Modified (Knockdown) Irwin Limit
- Appendix G. Small-Scale Testing and Microstructure Evaluation
- Appendix H. Strain Measurement in Uniaxial Coupon Testing
- Appendix I. The Use of Guide Plates
- Appendix J. N/A
- Appendix K. Eddy Current Inspection of COPV Liners and Coupons
- Appendix L. Truncation
- Appendix M. Fracture Surfaces from the Uniaxial Coupon Autofrettage Tests
- Appendix N. Fracture Surfaces from the COPV Pressure Tests
- Appendix O. Uniaxial Coupons for Damage Tolerance Life Testing

REPORT DOCUMENTATION PAGE

Form Approved OMB No. 0704-0188

The public reporting burden for this collection of information is estimated to average 1 hour per response, including the time for reviewing instructions, searching existing data sources, gathering and maintaining the data needed, and completing and reviewing the collection of information. Send comments regarding this burden estimate or any other aspect of this collection of information, including suggestions for reducing the burden, to Department of Defense, Washington Headquarters Services, Directorate for Information Operations and Reports (0704-0188), 1215 Jefferson Davis Highway, Suite 1204, Arlington, VA 22202-4302. Respondents should be aware that notwithstanding any other provision of law, no person shall be subject to any penalty for failing to comply with a collection of information if it does not display a currently valid OMB control number. PLEASE DO NOT RETURN YOUR FORM TO THE ABOVE ADDRESS.

1. REPORT DATE (DD-MIM-YYYY)	2. REPORT TYPE		3. DATES COVERED (From - 10)	
08/25/2020	Technical Memorandum			
4. TITLE AND SUBTITLE			5a. CONTRACT NUMBER	
	sure Vessel (COPV) Damage Tolerance Life			
Analysis Methodology and Tes	t Best Practices	5b. GR	ANT NUMBER	
		5c DD	OGRAM ELEMENT NUMBER	
		JC. 1 K	OGNAM ELEMENT NOMBER	
6. AUTHOR(S)		5d DD	OJECT NUMBER	
` '	Richard W.; Dawicke, David S.;	Ju. Tik	OULOT NOMBER	
Leser, William; Leser, Patrick E		- TA		
Hochhalter, Jacob D.; Grimes Ledesma, Lorie R.; Imtiaz, Kauser S.			5e. TASK NUMBER	
		5f. WO	RK UNIT NUMBER	
		86902	1.05.07.02.16	
7. PERFORMING ORGANIZATION N	• • • • • • • • • • • • • • • • • • • •		8. PERFORMING ORGANIZATION	
NASA Langley Research Cent	er		REPORT NUMBER NESC-RP-16-01183	
Hampton, VA 23681-2199			NESC-RP-10-01163	
9. SPONSORING/MONITORING AGI	ENCY NAME(S) AND ADDRESS(ES)		10. SPONSOR/MONITOR'S ACRONYM(S)	
National Aeronautics and Space	* *		NASA	
Washington, DC 20546-0001				
			11. SPONSOR/MONITOR'S REPORT NUMBER(S)	
			NASA/TM-2020-5006765/Volume I	
12. DISTRIBUTION/AVAILABILITY S	STATEMENT			
Unclassified - Unlimited				

Subject Category Space Transportation and Safety Availability: NASA STI Program (757) 864-9658

13. SUPPLEMENTARY NOTES

14. ABSTRACT

The NASA Engineering and Safety Center (NESC) Deputy Director requested an independent assessment to develop data to understand the limitations of linear elastic fracture mechanics (LEFM) computational methods used to predict fatigue crack growth rate (da/dN) behavior of small detectable cracks in thin metal liners for composite overwrapped pressure vessels (COPVs). The NESC assessment team was also requested to demonstrate a test-based methodology for validating damage tolerance requirements for COPVs with elastically responding metal liners where LEFM methods are not appropriate. This report contains the outcome of the NESC assessment.

15. SUBJECT TERMS

Composite Overwrapped Pressure Vessels; Linear Elastic Fracture Mechanics; Damage Tolerance; NASA Engineering and Safety Center

16. SECURITY CLASSIFICATION OF:		17. LIMITATION OF		19a. NAME OF RESPONSIBLE PERSON	
a. REPORT	b. ABSTRACT	c. THIS PAGE	ABSTRACT	OF PAGES	STI Help Desk (email: help@sti.nasa.gov)
					19b. TELEPHONE NUMBER (Include area code)
U	U	U	UU	133	(443) 757-5802